Nanostructured hybrid interfaces for supramolecular electronics

Thomas Mosciatti

UNIVERSITÉ DE STRASBOURG

ÉCOLE DOCTORALE DES SCIENCES CHIMIQUES

UMRS 7006 – Institut de science et d'ingénierie Supramoléculaires

THÈSE

présentée par :

Thomas MOSCIATTI

soutenue le : **24 Juillet 2015**

pour obtenir le grade de : **Docteur de l'université de Strasbourg**

Discipline/ Spécialité : Chimie

Nanostructured Hybrid Interfaces for Supramolecular Electronics

THÈSE dirigée par :

M. SAMORÌ Paolo	Professeur, Université de Strasbourg, France
M. ORGIU Emanuele	Maitre de Conférence, HDR, Université de Strasbourg, France

RAPPORTEURS :

M. BISCARINI Fabio	Professeur, Université de Modena et Reggio nell'Emilia, Modena, Italie
M. CALAME Michel	Privat-Docent (MdC-HDR), Université de Basel, Suisse

AUTRES MEMBRES DU JURY :

M. WÖLL Christof	Professeur, Karlsruhe Institute of Technology, Karlsruhe, Allemagne
M. BAUDRON Stéphane	Chargé de Recherches 1ère classe, Université de Strasbourg – Examinateur Interne

Resumé

Cette thèse est centrée autour de l'utilisation de la chemisorptions et de physisorption de molécules ad hoc afin de fonctionnaliser des interfaces avec pour objectif la fabrication de dispositifs multifonctionnels pour des applications logiques. En particulier, des efforts ont été fournis sur la fonctionnalisation de nanoparticules d'or (AuNP) ou des électrodes d'or ainsi que des surfaces de SiO2. Ces interfaces fonctionnalisées ont été étudiées pour de multiples raisons. La première étant d'explorer les effets électroniques de surfaces métalliques couvertes une fois introduites dans des matrices polymériques semi-conductrices en tant que couche active pour des transistors organiques à effet de champ. La seconde étant d'exploiter ces nanostructures comme des plateformes pour la modification de propriétés modulables, et le chauffage afin de modifier les interactions entre solvant et graphène.

AuNP sont des objets à l'échelle nanométrique ayant des propriétés chimiques et physiques uniques dues à leur isolement spatial. Compte tenu de leur structure bien définie, elles représentent des structures populaires qui peuvent être décorées avec des fonctions ad hoc. Parmi leurs diverses applications, dans l'électronique ils sont utilisés comme éléments de memristors, dispositifs à grille flottante et onduleurs. Au cours de mes travaux, j'ai observé comment l'ajout de AuNPs à un semi-conducteur de type p, le polymère Poly(3-hexylthiophène), P3HT, par mélange, influe sur le transport de charge dans le matériau, en particulier en mettant l'accent sur le rôle de la taille et le revêtement des AuNP. A cette fin, j'ai employé des AuNP de diamètre 1,3 nm et 3 nm, recouvertes d'oligophénylènes thiolés de longueur croissante, à savoir le thiophénol, le biphényl-4 -thiol et 1, 1', 4', 1"-terphényle-4- thiol. Les deux tailles ont été choisies car les nanoparticules métalliques subissent une transition entre comportement métallique et comportement semi-conducteur lorsque leur diamètre est inférieur à 1,5 nm tandis que les fragments oligophénylène ont été sélectionnés car leur géométrie moléculaire et leur fonction de travail sont similaires une fois chemisorbés sur Au(111).

L'étude électrique comparative a été réalisée en incorporant les mélanges AuNP-P3HT comme composant actif dans les OFET et en mesurant les

paramètres pertinents tels que la mobilité, la tension de seuil et courant maximal pour des quantités différentes de NP dans les mélanges pour chaque combinaison taille/revêtement. Afin d'expliquer les résultats obtenus, l'effet de la taille et du revêtement sur la structure cristalline P3HT a été analysé dans un cadre théorique développé par F. Spano. Ce modèle permet d'extraire la bande passante de l'exciton des agrégats P3HT-H à partir des spectres d'absorption UV-Vis des films et en tenant compte de l'agrégation des différentes NP dans les mélanges en raison de la longueur du revêtement. En outre, nous avons étudié l'interaction électronique entre les deux composants, à savoir AuNP et P3HT, en quantifiant leur énergie d'ionisation par la spectroscopie photo-électronique ambiante et en effectuant une analyse minutieuse de dispositifs plans à deux terminaux dans le cadre du modèle du courant limité par la charge d'espace (SLCL) afin d'obtenir une estimation de la densité de pièges de surface pour différentes conditions expérimentales. De plus, le comportement dans le temps a été étudié, démontrant la corrélation entre le stress et le nombre de pièges dans les dispositifs. Concrètement, les analyses effectuées ont révélé que la taille AuNP est un facteur crucial pour moduler la mobilité à effet de champ, les petites nanoparticules améliorant la mobilité, tandis que les plus grandes agissent comme des impuretés de diffusion. Une grande aide pour comprendre l'effet

mesuré sur les performances électriques vient de mesures SLCL, pour la première fois utilisées dans un système hybride nanoparticules/P3HT, où une diminution du nombre de piège dans la couche active est directement liée à la mobilité sous l'effet de l'amélioration par de petites AuNP. D'autre part, il a été établi comment les différents revêtements affectent l'agrégation des NP dans les films minces de P3HT, la cristallinité du polymère ainsi que l'effet de modulation dans le décalage de la tension de seuil.

Les mêmes AuNP peuvent être utilisées comme aide pour la génération de nanostructures réactives, quand leur enrobage est réalisé en utilisant des molécules qui modifient leur état lorsqu'elles sont exposées à un stimulus externe bien défini. À cette fin, nous avons revêtu les AuNPs avec des molécules photochromiques par chemisorption Nous avons choisi des diaryléthènes avec pour but ultime de développer des dispositifs électroniques intelligents commutables. Les diaryléthènes photochromiques sont des systèmes qui présentent une résistance à la fatigue élevée et une stabilité thermique des deux isomères ouverts et fermés et qui sont associés à des propriétés électroniques radicalement différentes. L'isomère à cycle ouvert, c'est à dire hexatriène, est généralement incolore, tandis que le cycle fermé, c'est à dire l'isomère cyclohexadiène est de couleur jaune, rouge ou bleue, en fonction des substituants.

En collaboration avec le groupe du professeur Stefan Hecht à l'Université Humboldt de Berlin, nous avons conçu des fragments diaryléthènes avec un groupe fonctionnel thiolé (t-DAE) dans la position α, et un des groupes di-ter-butyle dans la position ω-. Le premier permet la chemisorption moléculaire efficace sur des surfaces métalliques formant une monocouche auto-assemblée (SAM), par exemple, à la fois sur Au plan et sur les AuNP. Le deuxième rend possible de conférer un caractère hydrophobe à une surface tout en tirant parti de l'encombrement stérique afin d'éviter l'agrégation des AuNP. Notre molécule possède une bande d'absorption à 313 nm lorsqu'elle est sous forme ouverte, et deux bandes d'absorption à 365 et 540 nm lorsqu'elle est sous forme fermée. En irradiant à ces longueurs d'onde il est possible d'activer la commutation entre les deux formes isomères. J'ai étudié et mis en œuvre deux systèmes différents dans des OFET avec t-DAE. Dans le premier système, des AuNP fonctionnalisés avec DAE ont été employés dans une matrice polymère semi-conductrice. Dans ce cas, nous avons tiré profit de la modulation de la lumière entre les deux formes afin d'étudier l'effet du revêtement de ligand conjugués (fermés) et non-conjugués (ouvert) sur le transport de charge lorsqu'ils sont utilisés dans un OFET. P(NDI2OD-T2), un polymère semi-conducteurs de type n, a été choisi en raison de ses hautes performances, sa solubilité dans les mêmes

solvants que les AuNP et ses propriétés bien connues. L'insertion d'AuNP dans la matrice polymère diminue les performances, mais permet de conférer un caractère responsif à la lumière pour le transport de charge. En fait, lorsque les revêtements DAE couvrant les AuNP sont dans leur forme fermée la mobilité de charge augmente, mais les tensions de seuil se décalent vers des valeurs plus positives supérieures à 10V. Ce changement est réversible par irradiation par des UV et par de la lumière visible, et aucune fatigue n'a été observée suite à l'enregistrement de plusieurs cycles, avec une bi-stabilité parfaite du système et une hystérésis réduite. L'interaction avec la lumière a également été testée pour prouver le rôle critique des NP seules dans l'augmentation du nombre d'excitons dans le dispositif sous irradiation. Le transfert de charge a été étudié entre les AuNP revêtues de DAE et le semi-conducteur, et la façon dont elle est modifiée par les différentes conjugaisons du revêtement et l'effet de l'irradiation de lumière. Une deuxième approche était de s'appuyer sur la fonctionnalisation des électrodes d'or planes avec un SAM de t-DAE afin de moduler l'injection de charge par irradiation lumineuse dans les OFET. Ce système est supérieur aux systèmes similaires étudiés dans la littérature.

Par rapport à les études employant des fragments azobenzène pour fonctionnaliser les électrodes, les DAE présentent de nombreux avantages.

La première est que les deux formes de DAE sont thermiquement stables avec une isomérisation à haute efficacité, alors que les AZO en forme cis, peuvent retourner dans leur forme trans thermiquement, car elle est plus favorable énergétiquement. Le second avantage, est que l'isomérisation du DAE concerne la conjugaison moléculaire et non la géométrie moléculaire. Une faible contrainte géométrique est donc prévue dans les cycles d'isomérisation améliorant la résistance à la fatigue. Inversement, l'isomérisation des Azos nécessite qu'un déplacement physique de l'interface se produise, avec un réarrangement du semi-conducteur moléculaire, provoquant une baisse de rendement d'isomérisation avec le temps. Le troisième aspect est que le changement de DAE induit par la lumière est lié à la formation d'une liaison chimique qui conduit à une conjugaison étendue. Cela se reflète sur une bande interdite réduite qui se traduit par une augmentation de la conductance d'au moins deux ordres de grandeur, alors que le commutateur Azo module la distance tunnel avec une sortie de modulation inférieure.

D'autre part en ce qui concerne des jonctions moléculaires bien connus utilisant (t)DAE, la conception d'un OFET complet permet de réaliser des appareils multifonctionnels de haute performance potentiellement intégrables dans les circuits électroniques, et d'étudier profondément la

modulation de l’injection de charges en raison de l’isomérisation. Afin d’obtenir ce résultat la formation d'une SAM sur la surface de l'or a été étudiée.

La nature sensible à la lumière de la SAM sur des surface d’or plates, en raison de l'isomérisation entre les deux formes, a été étudiée par spectroscopie UV-vis et XPS. Après avoir prouvé que l'or n’empêche pas la réaction d'isomérisation, j’ai étudié l'effet de la commutation de trois facteurs intimement liés, soit la mouillabilité, le décalage de la fonction de travail et le décalage de la conductance. La différence observée était minime en terme de mouillabilité, tandis que la fonction de travail présente une différence d’environ 100 meV entre les deux formes, confirmé à la fois par spectroscopie photo-électronique et par des mesures de sonde Kelvin macroscopique.

D'autre part, la différence de conductivité pour les deux isomères formant une SAM sur Au a été étudiée en utilisant gallium/indium liquide (E-GaIn) comme électrode afin d'empêcher la diffusion de métal indésirable à travers le SAM. L’isomère en forme fermée a une conductance 100 fois supérieure à la forme ouverte, ce changement étant réversible par irradiation lumineuse. Enfin, ce système a été mis en œuvre dans des dispositifs 3-terminaux

appropriés, un transistor à grille supérieure en utilisant P(NDI2OD-T2) comme couche active.

Ces OFET présentent des performances électriques très élevés et l'introduction de t-DAE sur l'électrode les modifient à peine. Lorsque l'on bascule vers la forme fermée, la mobilité et le courant de sortie des OFET avec t-DAE sur les électrodes augmente de plus de 70% par rapport à la forme ouverte, tandis que la tension de seuil reste constante prouvant que la conjugaison différente joue un rôle prédominant. Il est possible de basculer entre les deux formes de nombreuses fois sans signe de fatigue. Aussi après l'irradiation le dispositif reste dans la forme fermée pendant plus de 14h, démontrant un contrôle sur la performance électrique.

L'insertion de AuNP dans une matrice de polymère par mélange est une façon intelligente de moduler les propriétés et d'ajouter des nouvelles fonctions à un dispositif nanostructuré avec des revêtements photochromiques appropriés. Mais en se basant sur deux composants mixtes, il est très difficile de contrôler les phénomènes de ségrégation de phase latérale et verticale, notamment pour savoir où les AuNP se placent à l'intérieur du canal. Afin d'améliorer cet aspect et d'étudier un autre type de nanostructure et de fonctionnalisation de surface, j'ai conçu un nouveau type de dispositif basé sur le dépôt de nano-flocons de graphène sur la surface de

la grille d'un OFET avec une méthode de traitement reproductible. Le graphène a suscité beaucoup d'attention dans les dernières années en raison de ses propriétés physiques et chimiques uniques. Le graphène est une couche unique d'atomes de carbone attachés par covalence disposés en pavage hexagonal; c'est un semi-conducteur de bande interdite nulle présentant des propriétés électroniques, thermiques, optiques et mécaniques extraordinaires qui en font un candidat prometteur pour des applications pratiques dans l'(opto)électronique, la détection, le stockage de l'énergie, etc.

Pour devenir un matériau adapté aux exigences de l'industrie électronique, deux grands défis doivent encore être relevés : (i) le développement de méthodes qui peuvent être mis à l'échelle pour la production de masse du graphène de haute qualité, et (ii) l'ouverture de la largeur de la bande interdite afin de pouvoir "éteindre" les dispositifs basés sur le graphène et les rendre ainsi adaptés à une application logique. D'une part, l'exfoliation en phase liquide du graphite pour obtenir du graphène est en train de devenir une méthode à grande échelle adaptée à la production de graphène de haute qualité facile à manipuler, stocker et traiter. D'autre part, différentes stratégies ont été proposées afin d'ouvrir un intervalle de bande dans le graphène, telles que la production d'oxyde de graphène réduit ou de nano-rubans de graphène. Une autre façon d'employer le graphène exfolié en phase

liquide (LPE-G) pour l'électronique s’appuie sur l'utilisation de solutions hybrides qui combinent le graphène avec des molécules appropriées pour permettre une modification des propriétés des composants.

Cette nouvelle stratégie de fabrication d'un transistor à couches minces de polymère/graphène est basée sur un dépôt de solution de polymère au dessus de nano-îles de graphène semi-conductrices ayant une énergie d'ionisation thermique modulable (également déposées en solution). L’ingénierie du niveau d'énergie provoquant une large gamme d’IE permet de moduler les interactions électroniques entre le LPE-G et le polymère semi-conducteur. Des quantités différentes de LPE -G ont été déposées sur de l'oxyde de silicium par un procédé de déposition par goutte, de manière à obtenir une couverture différente de nano-flacons de graphène à la surface. Après le dépôt, nous avons modulé l'IE du graphène par l’interaction avec la N-méthyl-2-pyrrolidone avec un procédé de recuit. En changeant le temps de recuit et l'atmosphère dans laquelle le recuit est effectué, il est possible de contrôler l’IE du graphène déposé dans une plage de presque 1 eV. Pour ce travail, j’ai concentré mon attention sur deux cas exemplaires, soit LPE-G avec une IE se situant soit à l'intérieur soit à l'extérieur de la bande interdite d’un polymère de type p ou n.

Dans le premier cas, une extinction complète des propriétés électriques est observée, le graphène agissant comme un piège pour les charges. A l'inverse, lorsque l'IE est en dehors de la bande interdite on obtient des régimes de travail du dispositif ajustables qui dépendent de la couverture de surface LPE-G. En particulier, il a été possible d'ajuster le transport dans le film à deux composants, de semi-conducteur jusqu'à conducteur, c'est à dire ne présentant pas de modulation de grille, par l'amélioration des performances électriques, comme la mobilité et du courant de sortie, sans contrepartie. En particulier, le cas lorsque les performances sont améliorées a été étudié et il a été démontré que le LPE-G déposé sur la surface se charge, d'où la présence d'hystérésis dans le dispositif en raison d'une plus grande accumulation de charges. Ces résultats suggèrent que ce dispositif avec l'IE du graphène à l'extérieur de la bande interdite des polymères permet aussi de faire fonctionner le dispositif à trois bornes comme un élément de mémoire sans qu'il soit nécessaire de déposer une couche diélectrique intermédiaire comme rapporté précédemment dans la littérature.

Ce dispositif peut être programmé en appliquant une impulsion sur l'électrode grille, décalant la tension de seuil du dispositif vers une valeur différente. Une impulsion de tension opposée est nécessaire pour supprimer l'état, soit la reprogrammation de la tension de seuil aux valeurs initiales.

Aussi aucun effet de fatigue n'a été enregistré après de nombreux cycles. Il convient de noter que l'approche a été testée à la fois sur des semi-conducteurs de polymère n et de type p démontrant que ce mécanisme de fonctionnement général novateur est viable à la fois pour le transport de trous et d'électrons. Cette nouvelle conception du dispositif permet d'ouvrir un certain nombre de développements intéressants grâce à cette nouvelle stratégie PG-TFT : la méthode de dépôt aisée valide cette approche comme un processus applicable à grande échelle approprié pour les dispositifs graphène/polymère hybrides. De plus, l'effet de mémoire résultant d'une ingénierie contrôlée de l'énergie d'ionisation LPE-G ouvre la voie à de nouvelles et passionnantes possibilités en science des matériaux, physique de la matière molle et chimie.

En outre, la possibilité de construire un nouveau type d'élément de mémoire à deux électrodes a été explorée. Nous avons utilisé les polymères dérivés de P(M)MA azo-modifiés comme des mémoires fonctionnant optiquement, testées électriquement en mesurant leur conductance, à savoir la mesure de différence de courant de transmission avant et après l'irradiation. Afin d'atteindre cet objectif, nous faisons usage d'une géométrie du dispositif à deux bornes simple dans lequel l'azo-polymère est pris en sandwich entre deux électrodes métalliques, et nous mesurons une résistance

électrique différente en fonction de l'isomérisation du polymère méso-groupe. Nous avons démontré qu'il est possible de régler la conductance de cette matière avec la lumière et de cette manière nous avons obtenu une entrée de lumière, des éléments de mémoire de sortie électrique, dans lequel tous les échantillons sont le capteur et peuvent être ponctuellement lus avec une jonction E-GaIn.

En conclusion, ce travail de thèse démontre qu'introduire des interfaces fonctionnelles convenablement conçues dans des dispositifs organiques est une voie prometteuse et créative pour l'ajout de nouvelles fonctionnalités et propriétés de modulation, pour repenser des architectures de dispositifs établies, en ajoutant le contrôle par la lumière des propriétés électriques et l'amélioration des performances. Le contrôle de l'interaction à la surface entre la nanostructure et la matrice polymère est un outil puissant pour contrôler les propriétés si des moyens efficaces de fonctionnalisation sont employés. Etudier l'effet de la taille des AuNP et la longueur de leur revêtement a été une première étape pour mieux comprendre le système. Cela a permis d'explorer en profondeur cette approche par fonctionnalisation des interfaces Au avec une molécule photochromique, permettant de contrôler les propriétés électriques avec de la lumière et de renforcer l'effet en introduisant des objets de taille nanométrique. De plus, ce principe a été

appliqué en utilisant les flocons de graphène afin de mieux contrôler le dépôt de nanostructures dans le dispositif et d'exploiter les interactions graphène/solvant et graphène/polymères au sein d'OFET. Cela a permis de repenser des dispositifs de mémoire en éliminant le diélectrique et donc d'ouvrir de nouvelles voies pour optimiser les performances et améliorer les éléments de mémoire.

Abstract

This thesis is centered around the use of chemisorption and physisorption of ad hoc molecules to decorate interfaces in order to fabricate multifunctional devices for logic applications. In particular, efforts have been devoted to the functionalization of gold nanoparticles (AuNPs) or gold flat electrodes as well as SiO2 surfaces. These functionalized interfaces have been studied for different reasons. The first is to explore the electronic effect of coated metallic nanostructures when embedded into polymeric semi-conductive matrix as active layer for Organic Field-Effect Transistor (OFET); the second is to exploiting such nanostructures as platforms for tunable properties modification, by using as external stimuli either light when photo-switchable molecules are employed, or heat in order to modify solvent-graphene interactions.

AuNPs are nanoscale objects possessing unique chemical and physical properties as a result of the space confinement. In view of their well-defined

structure, they represent popular structures that can be decorated with *ad hoc* functions. Among their various applications, in electronics they are employed as elements in memristor, floating gate devices and inverters. In my work I have explored how the addition of AuNPs to a p-type polymer semiconductor Poly(3-hexylthiophene) (P3HT) via blending influences the charge transport within the material, in particular by focusing on the role of their AuNP's size and coating. Towards this end, I employed AuNPs with 1.3 nm and 3 nm diameter, coated with thiol-exposing oligophenylenes with increasing length, i.e. thiophenol, biphenyl-4-thiol and 1, 1', 4', 1''-terphenyl-4-thiol. The two sizes have been chosen because metallic nanoparticles undergo a transition between metallic and semiconducting behaviour when their diameter is lower than 1.5 nm while the oligophenylene moieties have been selected in view of their similar molecular geometry and work function once chemisorbed on Au (111). The comparative electrical study have been carried out by incorporating the AuNP-P3HT blends as active component in OFETs and extracting the relevant parameters such as mobility, threshold voltage and maximum current for different amount of NPs in the blends for each combination of size/coating. To explain the findings the effect of the size and the coating on the P3HT crystalline structure has been analyzed in the theoretical framework developed by F.

Spano. This model allows to extract the exciton bandwidth for P3HT H-aggregates from UV-Vis absorption spectra on films and by taking into account the different aggregation of NPs in the blends due to the length of the coating. Furthermore, we have investigated the electronic interaction between the two components, i.e. AuNPs and P3HT, by quantifying their ionization energy with ambient photoelectron spectroscopy and by performing a careful analysis of planar two-terminal devices within the framework of the Space-Charge-Limited Current (SLCL) model in order to get an estimate of the surface trap density upon different experimental conditions. In addition, the behavior under time has been studied, demonstrating the correlation of stress with number of traps in devices. All together, performed analysis revealed that AuNPs size is a crucial factor for modulating the field-effect mobility, with small nanoparticles enhancing it, while the bigger ones acting just as scattering impurities. A great help to understand measured effect on electric performances comes from SCLC measures, for the first time used in a hybrid system nanoparticles/P3HT, where a decrease in the number of trap in the active layer is directly related to mobility enhancing effect of small AuNPs. On the other hand has been established how different coatings affect the aggregation of NPs in P3HT

thin films thus the crystallinity of the polymer, and finally modulation effect in threshold voltage shift.

The very same AuNPs can be used as scaffolds for generating responsive nanostructures, when their coating is performed using molecules that change their state when exposed to a well-defined external stimulus. Towards this end, we have coated the AuNPs with photochromic molecules via chemisorption. We have chosen diarylethenes with the ultimate goal of developing smart, switchable electronic devices. Diarylethenes are photochromic systems that exhibit high fatigue resistance and thermal stability of both open and closed isomers, which (most importantly) are associated with radically different electronic properties. The open-ring isomer, i.e. hexatriene, is generally colorless, whereas the closed-ring, i.e. the cyclohexadiene isomer, exhibit yellow, red and blue color, depending on the substituents.

In collaboration with the group of Prof. Stefan Hecht at Humboldt University Berlin we designed diarylethenes moieties exposing a thiolated functional group (t-DAE) in the α-position, and a di-tert-butyl groups in the ω-position. The former enables efficient molecular chemisorption on metallic surfaces forming Self Assembled Monolayer (SAM), e.g. both on planar Au and on AuNPs. The latter it makes possible to impart a

hydrophobic nature to a surface and at the same time taking advantage from the steric hindrance to avoid AuNPs aggregation. Our molecule have an absorption band at 313 nm when in open form, and two absorption bad at 365 and 540 nm when in closed form. Irradiating at those wavelengths it is possible to activate the switching between the two isomeric forms. I studied and implemented two different systems in OFET with t-DAE.

In the first system AuNPs functionalized with DAEs have been employed in a polymeric semiconducting matrix. In this case it has been taken advantage of light modulation between the two forms in order to investigate the different effect of conjugated (closed) and not-conjugated (open) ligand coating AuNPs on charge transport when employed in an OFET. P(NDI2OD-T2) a n-type polymeric semiconductor, has been chosen due to its high performance, solubility in the same AuNPs solvent and its well know properties. Inserting AuNPs in the polymeric matrix decreases performance, but allowed confer a light responsive nature to the charge transport. In fact, when the DAEs coating the AuNPs are in their closed form the charge mobility increases but the threshold voltage shifts towards more positive values exceeding 10 V. This shift is reversible by irradiation with UV and visible light, and no fatigue has been observed when recording several cycles, along with a perfect bi-stability of the system and a reduced

hysteresis. Interaction with light has also been tested proving dramatic role of just NPs in increasing excitons in device under irradiation. Finally charge transfer has been studied between DAE coated AuNPs and the semiconductor, how it is mediated by the different conjugation of coating and the effect of light irradiation.

A second approach relied on the functionalization of planar gold electrodes with a SAM of t-DAE in order to modulate charge injection by light irradiation in OFET. This system offers a great advantage with respect to similar systems studied in literature.

With respect to studies employing azobenzene moieties to functionalize electrodes present many advantages. The first is that both DAEs form are thermally stable with a high efficient isomerization, while AZO cis form thermally recover to trans more energetically favorable form.20 The second advantage, is that for DAEs isomerization concern the molecular core conjugation and not molecular geometry. Low geometrical stress is hence expected in isomerization cycles improving fatigue resistance. Conversely AZOs isomerization needs to physical move the interface to occur, with subsequent molecular semiconductor rearrangement, causing a decrease of isomerization yield as function of time. The third aspect is that DAEs induced light change is related to a chemical bond formation that drives to

an extended conjugation. This is reflected on lowered band gap which is reflected in an increased conductance of at least two order magnitude, while AZOs switch modulates tunneling distance with lower modulation output.

On the other hand with respect of well-known molecular junctions employing (t-)DAE, designing a full OFET allows to achieve high performance multifunctional devices potentially integrables in electronic circuits and to study deeply charge injection modulation due to isomerization. To achieve this result the formation of a SAM on gold surface has been studied.

The light responsive nature of the SAMs on flat Au surfaces, due to the isomerization between the two forms, has been monitored by UV-vis spectroscopy and with XPS. After proving that gold does not quench the isomerization reaction I investigated the effect of switching on three intimately linked factors, *i.e.* wettability, work function shift and conductance shift. Difference has been found to be minimal in wettability, while work function has a difference of ca. 100 meV between the two forms, as confirmed both by Ambient Photoelectron Spectroscopy and macroscopic Kelvin Probe measurements. On the other hand, difference in conductivity has been recorded for both isomers forming SAM on Au by using a liquid compliant Gallium/Indium (E-GaIn) electrode in order to prevent the

undesired metal diffusion across the SAM. Closed form isomer has a conductance 100 times greater than the open-form; importantly, this change is reversible by light irradiation. Finally this system has been implemented in proper 3-terminal devices, *a* top gate transistor using P(NDI2OD-T2) as active layer.

These OFETs present a very high electric performances and the introduction of t-DAEs on electrode barely affect them. When switched to the closed-form, OFET with t-DAEs on electrodes increases their mobility and output current of over 70% with respect to the open-form, while the threshold voltage remains constant proving that different conjugation plays a predominant role. It is possible to cycles back and forth between the two forms numerous times with no evidence of fatigue. Also after irradiation device stays in the closed form for over 14h, demonstrating a full-light gate control on the electrical performance.

While inserting AuNPs into a polymer matrix via blending is a smart way to modulate properties and impart new functions to a nanostructured device with appropriate photochromic coatings, being based on two mixed components it is very difficult to control phenomena of lateral and vertical phase segregation, and in particular to know where AuNPs sit inside the channel. In order to improve this aspect and to explore a different kind of

nanostructure and surface functionalization, I devised a new type of device, depositing graphene nano-flakes on the gate surface of an OFET with a reproducible processing method. Graphene has garnered a great deal of attention in those last year because of its unique chemical and physical properties. Graphene is constituted by a single layer of covalently tethered carbon atoms arranged in a honey-comb lattice; it is a zero band-gap semiconductor exhibiting extraordinary electronic, thermal, optical and mechanical properties which make it a promising candidate for practical applications in (opto-)electronics, sensing, energy storage *etc.*

To become a material suitable for the electronic industry, two greatest challenges need still to be addressed: *(i)* developing methods that can be up scaled for mass production of high quality graphene, and *(ii)* opening a band gap to "switch off" graphene devices and thus make them suitable for logic application. On the one hand, liquid phase exfoliation of graphite into graphene is emerging as a suitable up-scalable method for the production of high quality graphene easy to handle, deposit and processing. On the other hand, different strategies have been proposed in order to open a band gap in graphene such as the production of reduced graphene oxide or graphene nano-ribbons.

A different way of employing liquid phase exfoliated graphene (LPE-G) for electronics relies on the use of hybrid solutions that combine graphene with suitable molecules to enable reciprocal modification of the component properties. This new strategy for fabricating a multifunctional polymeric-graphene thin film transistor (PG-TFT) relied on solution processing of semiconducting polymers on the top of solution processed graphene nanoscale patches having thermally tunable ionization energy. This graphene's energy level engineering resulting in a broad range of IEs makes it possible to modulate the electronic interactions between the LPE-G and the semiconducting polymer. Briefly, different amounts of LPE-G have been deposited on silicon oxide with a drop casting procedure, in order to obtain different coverage of graphene nano-patches on surface.

After deposition we tuned the IE of graphene with interaction with N-Methyl-2-pyrrolidone upon annealing. By changing annealing time and atmosphere in which annealing is carried out it is possible to control deposited graphene IE in a range of almost 1 eV. For this work I focused my attention on two exemplary cases, *i.e*. LPE-G with an IE laying either inside or outside the band-gap of either a p- or an n-type polymer active layer. In the former case a complete shutting off electrical properties is recorded due to graphene acting as a trap for charges. Contrary when the IE is outside the

polymer band-gap one obtains tunable device's working regimes which depend on LPE-G surface coverage. In particular, it was possible to adjust the transport in the bi-component film from semiconducting to truly conductive, i.e. exhibiting no gate modulation, by improving electrical performance, like mobility and output current in exchange for no drawbacks. In particular, the case when performance are improved has been studied and has been demonstrate that LPE-G deposited on the surface charges itself, hence introducing hysteresis in the device due to greater accumulation of charges in the devices. Those findings suggested that this device with IE of graphene outside polymers band gap makes it possible also to operate the three-terminal device as a memory element without the need of depositing a further dielectric interlayer as previously reported in literature. This device can be programmed by applying a pulse on the gate electrode o charge graphene, shifting the threshold voltage of the device in a different value.

A pulse of opposite voltage is necessary to delete the state, hence reprogramming the threshold voltage to the initial values. Also no fatigue effect has been recorded after numerous cycle. Noteworthy, the approach has been tested with both n- and p-type polymer semiconductor demonstrating that this novel and general working mechanism is viable for both hole and electron transport. Those new device design open a number of interesting

future developments using this new PG-TFTs strategy: while the easy deposition method qualifies this approach as a suitable large scale process for hybrid graphene/polymer device, the special memory effect arising from a controlled engineering of the LPE-G ionization energy paves the way for novel and exciting routes in materials science, soft matter physics and chemistry.

Also the possibility of building a new type of two electrode memory element has been explored. We employed azo-modified derived polymers of P(M)MA as optically driven, electrically detectable memories by gauging their conductance, *i.e.* measuring athwart transmitted current difference before and after irradiation. In order to achieve this goal, we make use of a simple two-terminal device geometry in which the azo-polymer is sandwiched between two metallic electrodes, and we record different electrical resistance depending on the polymer meso-group isomerization. We demonstrated that is possible to tune the conductance of this material with light and in this way we obtained a light input, electric output memory elements, in which all the samples is the sensor and can be punctually read with a soft E-GaIn junction.

In conclusion this thesis work demonstrates how introducing suitably designed functional interfaces in organic devices is a promising and creative

way for adding new functionalities, tuning properties, redesign established device architecture, adding light control to electrical properties and improving performances. The subtle interplay at the surface between the nanostructure and the polymeric matrix is a powerful tool to control properties if effective ways of functionalizing it are employed.

Starting from the effect of the size of AuNPs and length of their coating has been an initial step to better understand the system. This helped to deeply explore this approach by functionalizing Au interfaces with photochromic molecule, allowing to control electrical properties with light and enhancing the effect by introducing nano-sized object. On the other hand, this principle has been applied using graphene nano- flakes in order to better control deposition of nanostructures in device and exploiting interactions between graphene and its solvent and graphene and polymers in OFET. This allowed to redesign memory device eliminating the gate dielectric hence opening complete new ways to tune performance and to build memory element.

Table of Contents

*

Abbreviation list

a	inverse of localization radius
AFM	atomic force microscopy
Ambient-PS	ambient photoelectron spectroscopy
AuNPs	gold nanoparticles
AZO	Azobenzene
BD	bond dipole
BPT	biphenyl-4-thiol
c-DAE	o-diarylethene
$\mathbf{C_{insulator}}$	dielectric capacitance
D	AuNPs diameter
DAE	diarylethene
DDT	dodecanethiol
$\mathbf{E_f}$	Fermi level
$\mathbf{E_g}$	band gap
E-GaIn	eutectic gallium-indium
$\mathbf{E_p}$	intramolecular vibration
$\mathbf{E_{vac}}$	vacuum level
g	paracristallinity parameter
$\mathbf{HAuCl_4}$	Chloroauric acid
HOMO	highest occupied molecular orbital
$\mathbf{I_{ds}}$	drain current
$\mathbf{I_E}$	ionization energy
$\mathbf{I_e}$	mean free path of conduction electrons
IIDDT-C3	poly[1,1'-bis(4-decyltetradecyl)-6-methyl-6'-(5'-methyl-[2,2'-bithiophen]-5-yl)-[3,3'-biindolinylidene]-2,2'-dione]
$\mathbf{J_0}$	transfer integral
k	boltzman constant
$\mathbf{K_f}$	Fermi wavenumber
KP	kelvin probe
L	Channel length
LI/EO memories	Light input/electronic output memory
LPEG	liquid phase exfoliated graphene
LUMO	lowest unoccupied molecular orbital
MPT	thiophenol
N	number of atoms
NPs	nanoparticles
$\mathbf{N_{trap}}$	number of traps in the active layer
ODA	octadecylamine

o-DAE	c-diarylethene
OTFT	Organic Thin Film Transistor
OTS	octadecyltrichlorosilane
P(NDI2OD-T2)	poly[N,N'-bis(2-octyldodecyl)-naphthalene-1,4,5,8-bis(dicarboximide)-2,6-diyl]-alt-5,5'-(2,2'-bithiophene)
P3HT	poly (3-Hexylthiophene)
PANI	polyaniline
PEDOT:PSS	poly(3,4-ethylenedioxythiophene) polystyrene sulfonate
PEN	polyethylene naphthalate
PET	polyethylene terephthalate
PG-TFT	polymeric-graphene thin-film transistor
PMA-AZO1	poly 2-(metha-hexyloxy-2-methyl-4'-pentyloxy-azobenzene)
PMMA	poly(methylmethacrylate)
PMMA-AZO2	2(methyl-metha-hexyloxy-4'-ethoxyazobenzene)
PS	polystyrene
PVP	Polyvinylpyrrolidone
q	elementary charge
$\mathbf{R_0}$	effective contact resistance
$\mathbf{R_{rms}}$	root mean square roughness
$\mathbf{R_t}$	tunnelling resistance
RT	room temperature
SAM	self-assembled monolayer
SEM	scanning electron microscopy
SPR	surface plasmon resonance
TEM	transmission electron microscopy
TOAB	tetraoctylammonium bromide
TPT	1,1′,4′,1″-terphenyl-4-thiol
UPS	ultraviolet photoelectron spectroscopy
UV-VIS	ultraviolet-visible spectroscopy
ν_0	attempt to hop frequency
$\mathbf{V_a}$	applied potential
$\mathbf{V_{ds}}$	drain-source voltage
$\mathbf{V_g}$	gate voltage
$\mathbf{V_{th}}$	threshold voltage
W	Channel width
W	exciton bandwidth
$\mathbf{W_f}$	work function
XPS	x-ray photoelectron spectroscopy
β	exponential prefactor of tunnelling
$\mathbf{\Delta U_{vac}}$	shift of vacumm level
ε(λ)	dielectric malue of the metal
ε_i	energy of electronic state *i*
λ	reorganization energy

μ	field effect mobility
φb.	Schottky barrier

1. Introduction

The first interfaces generated by self-assembly in the primordial broth introduced order in a disorder-dominated world.[1] Nature, with its most sophisticated product, i.e. life, relies on myriad of perfect micro and nanostructures[12] to battle against inexorable universe's time arrow pointing towards entropy and thus death.[3] From Democritus deduction guess of intrinsic grainy nature of matter[4] to Richard Feynman world famous speech,[5] more than 2000 years passed by, in which the nano-world remained concealed from mankind attention. Yet, other 20 years were necessary to bring to the consideration of scientists the importance of manipulating matter directly at the very nanoscale to build and envision about nanoscopic devices.[6] The development of scanning probe microscopies provided direct access to the nanoworld and paved the way towards the first electrical nanodevice, being a true proof-of-concept on the potential of thinking small.[7] The last 20 years science, and the society overall, has witnessed a true nanoscale revolution which led to the emergence nanotechnology.[8-10]

While physicists always follow in their approaches the motto of Richard Feynman "there is plenty of room at the bottom", the chemical approach more wisely relies on the concept that "there is even more room at the top".[11] Such a room is the room reserved for the nanoscale control over a structural complexity at the supramolecular level, which necessarily leads to functional complexity.[12] Despite playing a key role in nature and for example having been a fundamental factor in the emergence of life, the concept of supramolecular interactions has been recognized for the first time by Lehn in 70s and described as the intramolecular bond occurring between molecular building blocks.[13] Control over supramolecular interactions has been the tool embraced by the bottom-up approach towards the controlled formation of nanostructures.[14] Supramolecular interactions combine reversibility, directionality, specificity and cooperativity therefore they are versatile means for assembling molecules under thermodynamic control to form highly ordered 2D or 3D architectures.

The supramolecular approach, through its subtle control over the interaction between molecules, has been of pivotal importance to the field of organic semiconductors.[15] The way molecules interact and organize is strictly connected with the properties possessed by the ensemble, being necessarily different from those of single molecules. Among various properties, charge transfer and transport in poly-molecular structures occurs.

[1] Nano prefix derived from Greek "νᾶνος".

Such process is fundamental when dealing with organic semiconductors.[16] Organic or polymeric semiconductors have been first introduced in 1976; they are formed by sp^2 conjugated molecules that show semiconducting properties.[17] The intense research activity during the last ten years on the design and synthesis of novel (macro)molecules programmed to undergo self-assembly forming ordered solid-state arrangements possessing high delocalization of the π-states, has led to electrical performances which make organic and polymeric semiconductors mature impact science and technology.[18] The understanding of supramolecular interactions has been necessary for reaching field-effect mobility on OFET devices exceeding 1 $cm^2V^{-1}s^{-1}$.[19] Polymeric semiconductors tend to form supramolecular aggregates that are held together by non-covalent interactions, in particular π-π stacking.[20 21] It is worth noting that most modern high performance semiconducting polymers are forming highly organized and supramolecularly engineered materials consisting of spatially extended crystalline domains featuring a good overlap of the π-orbitals belonging to adjacent molecules.[22,23] Such a winning approach opens new and exciting routes for the emergence of supramolecular electronics. In fact, organic and polymeric semiconductors share many advantages which are not in common with their inorganic counterparts, including the possibility of tuning their properties by chemical design, their easy processability on large scale, their unique mechanical properties making flexibile device a possible solution, and low power consumption.[24,25]

Organic and polymeric semiconductors can be combined with inorganic systems to form hybrid materials that express characteristics that are possessed by the individual components including the tunable functionality. It is therefore crucial attaining a full control over the process of self-assembly systems at surfaces and interfaces forming hybrid structures and integrate them in working devices.[26]

Organic and inorganic materials can be combined leading to hybrid devices. Supramolecular interactions are a powerful tool to functionalize inorganic, more specifically metallic, surfaces by self-assembling of molecular species in order to generate a bridge between the inorganic and the organic part of a hybrid interface.[27] Self-assembly is a supramolecular process driven by interactions among molecules, solvent and the surfaces, in which ordered structures spontaneously generate according to the information coded in the single molecules.[28,29]

By design, molecules can be functional. They can therefore be used to impart a supplementary function to a material or to an interface, ultimately leading to the generation of "multifunctional" devices, which can be driven by different independent stimuli.[30] Multifunctionality is a hallmark of multicomponent materials. Like in nature, the various components can be assembled at different interfaces. Interfaces, in organic electronic devices include the interface of the molecules with electrodes, dielectrics and among themselves when more than one component is present in the active material, obtained via blending. [31] Among various inorganic components, nanoparticles are clusters of atoms with a size ranging from 1 to 100 nm. The number of atoms forming the nanostructure strictly affects its optical and

electronic properties. Therefore the tuning of their size and environment is key towards their integration in hybrid device.[32] Yet, metal nanoparticles are not the only nano-sized objects that can be fruitfully employed in hybrid devices. During the last decade graphene has establish itself as golden material in virtue of its outstanding optical, thermal, electrical and mechanical properties which opens bright perspectives towards future emerging technologies based on this unique 2D material. Graphene can be produced using different bottom-up and top-down methods. Among them, a cheap and easily up scalable approach relies on the liquid phase exfoliation.[33] Devices based on such a graphene type recently showed carrier mobilities as high as 95 $cm^2V^{-1}s^{-1}$ and they combine high performances, with transparency and flexibility properties. Therefore graphene based devices are a promising alternative for both organic and inorganic electronics.

The high syncretism needed to explore supramolecular based devices can be seen as one of the reasons for the slow integration of organic semiconductor in market applications. They are still limited to niche application (but important like OLED based screen) and far away from substituting inorganic electronics in computers. However, the interest in this field is very high, both from academic and industrial point of view, because they could be employed for developing novel applications that are not accessible with inorganic semiconductors, like flexible[34], large area,[35] wearable electronics,[36] or transparent applications. [37]

This thesis work has its *raison d'être* in the framework here presented. The combination of supramolecular engineering of organic systems with inorganic components to form hybrid nanostructured materials is a viable approach towards multifunctional devices. The comprehension of how interactions at the interfaces can be tailored is at the heart of this thesis. The mastering these interactions has been instrumental towards the development of high-performances optoelectronic and flash memory devices. Different ways have been pursued in order to introduce nanostructured interfaces in organic field-effect transistors, to modulate and add properties arising from how the components are interacting among each other.

The thesis is organized as follows:

- **Chapter 1** introduces the topic of the thesis and places it in the scientific contest.
- **Chapter 2** presents the materials employed in the thesis, their properties and characteristics and as well provides a glimpse on some theoretical aspects.
- **Chapter 3** summarizes the experimental techniques and methods employed providing a brief theoretical introduction when needed.
- **Chapter 4** describes the multiscale characterization performed on nanostructured systems composed by gold nanoparticles (AuNPs) and polymeric semiconductors with a particular focus on how particle size and type of coating influence the energetic, morphological and electric properties of bi-component materials for OFETs.
- **Chapter 5** expands further the approach of blending AuNPs in bi-component OFETs by integrating photochromic SAMs as coating layer. Light modulation on charge

trapping is achieved by a careful study on the interactions between the AuNPs and the semiconducting polymeric matrix and how they are mediated by different conjugation on the coating, achieved by photo-isomerization.

- **Chapter 6** presents optoelectronic transistor employing self-assembled monolayer of photochromic molecules on the electrodes. The modulation of output current using light as a gate is reported, preceded by an in-depth study of optical, switching, energetic and surface modification characteristics of planar gold coated by SAMs of diarylethenes.
- **Chapter 7** introduces the concept of controlled deposition of liquid-phase exfoliated graphene on SiO_2 and show how one can tune the graphene's ionization potential by thermal annealing. Transistors build on these graphene platforms oxide are reported with a focus on different working regime and they are analyzed with a discussion on working principle and morphological occurring modifications. Finally they are employed as flash memory devices with a new concept of architecture design for this kind of devices.
- **Chapter 8** Describes light triggered electrical-read memory elements based on side-chain photochromic liquid crystalline polymethylmethacrylate. They exhibit nanostructured surfaces that can be induced to morphologically transform by light irradiation. The effect of these changes directly affects the electrical properties of two terminal junction for a light driven memory device
- **Chapter 9** provides a summary of the presented work and gives short and long term outlooks.

1.1 REFERENCES

1. Deamer, D. W., Origins of life: How leaky were primitive cells? *Nature* **2008,** *454*, 37-38.
2. England, J. L., Statistical physics of self-replication. *The Journal of Chemical Physics* **2013,** *139*, 121923.
3. Schneider, E. D.; Kay, J. J., Life as a manifestation of the second law of thermodynamics. *Mathematical and Computer Modelling* **1994,** *19*, 25-48.
4. Democritus, νόμωι (γάρ φησι) γλυκὺ καὶ νόμωι πικρόν, νόμωι θερμόν, νόμωι ψυχρόν, νόμωι χροιή, ἐτεῆι δὲ ἄτομα καὶ κενόν. *Fragment 9*.
5. Feynman, R., There's pleny of room at the bottom. *Engineering and Science* **1960,** *23*, 22-36.
6. Joachim, C.; Plévert, L.; Crisp, J., *Nanosciences: The Invisible Revolution*. World Scientific: 2009.
7. Joachim, C.; Gimzewski, J. K.; Schlittler, R. R.; Chavy, C., Electronic Transparence of a Single ${\mathrm{C}}_{60}$ Molecule. *Phys. Rev. Lett.* **1995,** *74*, 2102-2105.
8. Daniel, M. C.; Astruc, D., Gold nanoparticles: Assembly, supramolecular chemistry, quantum-size-related properties, and applications toward biology, catalysis, and nanotechnology. *Chem. Rev.* **2004,** *104*, 293-346.
9. Ferrari, M., Cancer nanotechnology: Opportunities and challenges. *Nat. Rev. Cancer* **2005,** *5*, 161-171.
10. Avouris, P.; Chen, Z. H.; Perebeinos, V., Carbon-based electronics. *Nat. Nanotechnol.* **2007,** *2*, 605-615.
11. Lehn, J. M., *Supramolecular Chemistry: Concepts and Perspectives*. Wiley: 1995.
12. Cademartiri, L.; Ozin, G. A., *Concepts of Nanochemistry*. Wiley: 2009.
13. Lehn, J. M., Cryptates - Inclusion Complexes of Macropolycyclic Receptor Molecules. *Pure Appl. Chem.* **1978,** *50*, 871-892.
14. Isaacs, L.; Chin, D. N.; Bowden, N.; Xia, Y.; Whitesides, G. M., Self-Assembling Systems on Scales from Nanometers to Millimeters: Design and Discovery. In *Perspectives in Supramolecular Chemistry*, John Wiley & Sons, Ltd.: 2007; pp 1-46.
15. Hoeben, F. J. M.; Jonkheijm, P.; Meijer, E. W.; Schenning, A. P. H. J., About Supramolecular Assemblies of π-Conjugated Systems. *Chem. Rev.* **2005,** *105*, 1491-1546.
16. Noriega, R.; Rivnay, J.; Vandewal, K.; Koch, F. P. V.; Stingelin, N.; Smith, P.; Toney, M. F.; Salleo, A., A general relationship between disorder, aggregation and charge transport in conjugated polymers. *Nat. Mater.* **2013,** *12*, 1038-1044.
17. Shirakawa, H.; Louis, E. J.; MacDiarmid, A. G.; Chiang, C. K.; Heeger, A. J., Synthesis of electrically conducting organic polymers: halogen derivatives of polyacetylene, (CH). *J. Chem. Soc., Chem. Commun.* **1977**, 578-580.
18. Luo, C.; Kyaw, A. K. K.; Perez, L. A.; Patel, S.; Wang, M.; Grimm, B.; Bazan, G. C.; Kramer, E. J.; Heeger, A. J., General Strategy for Self-Assembly of Highly Oriented Nanocrystalline Semiconducting Polymers with High Mobility. *Nano Lett.* **2014,** *14*, 2764-2771.

19. Venkateshvaran, D.; Nikolka, M.; Sadhanala, A.; Lemaur, V.; Zelazny, M.; Kepa, M.; Hurhangee, M.; Kronemeijer, A. J.; Pecunia, V.; Nasrallah, I.; Romanov, I.; Broch, K.; McCulloch, I.; Emin, D.; Olivier, Y.; Cornil, J.; Beljonne, D.; Sirringhaus, H., Approaching disorder-free transport in high-mobility conjugated polymers. *Nature* **2014,** *515*, 384-388.
20. Fabiano, S.; Himmelberger, S.; Drees, M.; Chen, Z.; Altamimi, R. M.; Salleo, A.; Loi, M. A.; Facchetti, A., Charge Transport Orthogonality in All-Polymer Blend Transistors, Diodes, and Solar Cells. *Advanced Energy Materials* **2014,** *4*, n/a-n/a.
21. Ciferri, A., *Supramolecular Polymers, Second Edition*. Taylor & Francis: 2005.
22. Steyrleuthner, R.; Di Pietro, R.; Collins, B. A.; Polzer, F.; Himmelberger, S.; Schubert, M.; Chen, Z.; Zhang, S.; Salleo, A.; Ade, H.; Facchetti, A.; Neher, D., The Role of Regioregularity, Crystallinity, and Chain Orientation on Electron Transport in a High-Mobility n-Type Copolymer. *J. Am. Chem. Soc.* **2014,** *136*, 4245-4256.
23. Olivier, Y.; Niedzialek, D.; Lemaur, V.; Pisula, W.; Müllen, K.; Koldemir, U.; Reynolds, J. R.; Lazzaroni, R.; Cornil, J.; Beljonne, D., 25th Anniversary Article: High-Mobility Hole and Electron Transport Conjugated Polymers: How Structure Defines Function. *Adv. Mater.* **2014,** *26*, 2119-2136.
24. Arias, A. C.; MacKenzie, J. D.; McCulloch, I.; Rivnay, J.; Salleo, A., Materials and Applications for Large Area Electronics: Solution-Based Approaches. *Chem. Rev.* **2010,** *110*, 3-24.
25. Wang, C. L.; Dong, H. L.; Hu, W. P.; Liu, Y. Q.; Zhu, D. B., Semiconducting pi-Conjugated Systems in Field-Effect Transistors: A Material Odyssey of Organic Electronics. *Chem. Rev.* **2012,** *112*, 2208-2267.
26. Oehzelt, M.; Koch, N.; Heimel, G., Organic semiconductor density of states controls the energy level alignment at electrode interfaces. *Nat Commun* **2014,** *5*.
27. Love, J. C.; Estroff, L. A.; Kriebel, J. K.; Nuzzo, R. G.; Whitesides, G. M., Self-Assembled Monolayers of Thiolates on Metals as a Form of Nanotechnology. *Chem. Rev.* **2005,** *105*, 1103-1170.
28. Palermo, V.; Samorì, P., Molecular Self-Assembly across Multiple Length Scales. *Angew. Chem. Int. Ed.* **2007,** *46*, 4428-4432.
29. Whitesides, G. M.; Grzybowski, B., Self-Assembly at All Scales. *Science* **2002,** *295*, 2418-2421.
30. Orgiu, E.; Samorì, P., 25th Anniversary Article: Organic Electronics Marries Photochromism: Generation of Multifunctional Interfaces, Materials, and Devices. *Adv. Mater.* **2014,** *26*, 1827-1845.
31. Gupta, R. K.; Ying, G.; Srinivasan, M. P.; Lee, P. S., Covalent Assembly of Gold Nanoparticles: An Application toward Transistor Memory. *The Journal of Physical Chemistry B* **2012,** *116*, 9784-9790.
32. Eustis, S.; El-Sayed, M. A., Why gold nanoparticles are more precious than pretty gold: Noble metal surface plasmon resonance and its enhancement of the radiative and nonradiative properties of nanocrystals of different shapes. *Chem. Soc. Rev.* **2006,** *35*, 209-217.
33. Ciesielski, A.; Samori, P., Graphene via sonication assisted liquid-phase exfoliation. *Chem. Soc. Rev.* **2014,** *43*, 381-398.
34. Forrest, S. R., The path to ubiquitous and low-cost organic electronic appliances on plastic. *Nature* **2004,** *428*, 911-918.
35. Dimitrakopoulos, C. D.; Malenfant, P. R. L., Organic Thin Film Transistors for Large Area Electronics. *Adv. Mater.* **2002,** *14*, 99-117.
36. Duan, X. F.; Niu, C. M.; Sahi, V.; Chen, J.; Parce, J. W.; Empedocles, S.; Goldman, J. L., High-performance thin-film transistors using semiconductor nanowires and nanoribbons. *Nature* **2003,** *425*, 274-278.
37. Ju, S. Y.; Facchetti, A.; Xuan, Y.; Liu, J.; Ishikawa, F.; Ye, P. D.; Zhou, C. W.; Marks, T. J.; Janes, D. B., Fabrication of fully transparent nanowire transistors for transparent and flexible electronics. *Nat. Nanotechnol.* **2007,** *2*, 378-384.

2. Materials and interfaces

This chapter provides a general overview over materials and interfaces used in this work.

Organic electronic devices are based on semiconducting materials that present different degrees of order according to their supramolecular interactions and their electrical properties are strictly morphological dependent. On this regard interfaces occurring in electronic devices based on polymeric semiconductors have *(i)* a role in polymer structural modifications and (ii) in charge injection, transport and accumulations processes. Hence they directly influence electrical characteristics of organic transistors and can be fruitful employed to tune properties and to add multifunctionality to the device. In this thesis, gold has been used both in planar and nanoparticle form. Gold allows the growth of self-assembled thiolated species on its surface, which are a powerful nanotechnology tool for modifying its surface properties, both for affecting charge injection and charge transport mechanism in transistor. A further step has been achieved by employing photochromic thiols to change, with a light stimulus, the isomeric form of the molecules and thereby modulating electric output of a device. The possibility of changing with light how metal/semiconductor interactions are mediated by a functionalized surface is a very promising way to obtain efficient multifunctional devices. Moreover gold is not the only materials used in this work to introduce interfaces. Liquid phase exfoliated graphene is an easy processable material, whose properties can be thermally tuned to obtain multifunctional device.

2.1 ORGANIC SEMICONDUCTORS

2.1.1 Introduction

Organic molecules are defined as compounds that contain a skeleton of carbon atoms on which are attached hydrogen, oxygen or nitrogen atoms.[1] Carbon peculiar chemistry is the main reason for the rich variety of structures and properties of organic compounds since it can form different type of bonds according to the hybridization theory of atomic orbitals. Its 6 electrons are split between inner and outer shells. In the most inner s shell $1s^2$ there are two electrons, other four are placed two in the second s orbital ($2s^2$) and two more in the p orbital. These four external orbitals can undergo hybridization forming an excited orbital state generated by a linear combination of s and p orbital wave function. This hybrid orbital called sp has a lower energy with respect to un-hybridized p orbital because electrons can be disposed in it with parallel

spins. Of particular interest is when hybridization occurs between 2p orbital, p_x and p_y, with the s orbital. This allows a bond formation where a conjugated π- electron system is formed by un-hybridized p_z orbitals of sp^2 carbon atoms in a molecule as shown in **Figure 2.1**.

In this configuration, as happens in alkenes molecules, two carbons share one electron from their sp hybrid shell resulting in σ bond, and a free p_z electron perpendicular to the plane of the C and H atoms, forming a π bond. Hence, there is a double bond between the carbons. One is a strong σ bond and another is weaker π bond. The electron conduction can occur due to the change in weak π orbital overlap.

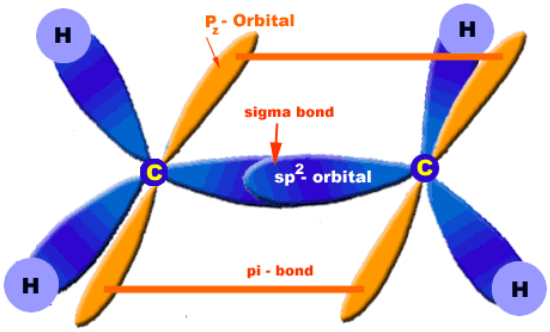

Figure 2.1 Cartoon of carbon-carbon double bond as described in the main text. A σ-bond and a π-bond formed from the un-hybridized p_z orbitals on the two carbon atoms. Reproduced from citycollegiate.com

An alkene, which contains an appreciable number of carbon-carbon sp^2 bonds and is capable of supporting electronic conduction, it is classified as organic semiconductor and it is conjugated if the adjacent carbon atoms are also sp^2 hybridized.[2] Two main categories exist of organic semiconductors, depending on their size: small molecules and polymers. In this thesis we focused on the latter since they have been extensively employed as the active layer in all nanostructured systems studied.

2.1.2 Polymeric Semiconductors

Polymeric semiconductors were for the first time reported by Heeger, MacDiarmid and Shirakawa in 1976. They reported the synthesis and analysis of conducting polymers as well as the possibility to dope the polyacetylenes moieties from insulator to metal.[3] Since this discovery, extensive research has been conducted on all aspects of the chemistry and physics of conjugated polymers

Polymeric semiconductors are polymers in which there is an alternation of single and double bonds along their backbone. Thus, the π-orbitals forms a continuous overlap of states in reason of their conjugated structure. Electrons that populate his continuum of state are delocalized and can move from one bond to another one or along the entire scaffold of the polymer.

2.1.2.1 Energetic profile in semiconducting polymers

In organic semiconductors the highest occupied molecular orbital the HOMO level represents the energetic molecular orbital where the electron charge cloud is occupied while the lowest unoccupied molecular orbital LUMO level denotes the unoccupied energy orbital. The energy of the HOMO level is lower. However, if an electron is excited to a higher energetic state, it will be promoted in the unoccupied molecular orbital and can have enough energy to play a role in electrical conduction. In this regard, sigma bond is stronger with respect to other π bond due to the weaker p_z orbital overlap and hence π electrons are more easily promoted to their anti-bond with respect to sigma ones.

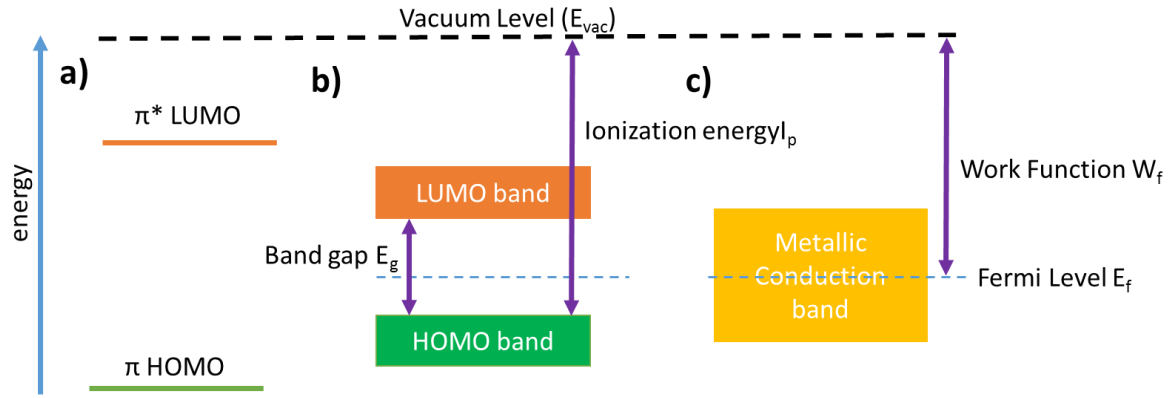

Figure 2.2 a) π energy level, bond and anti-bond, of a single molecule. b) band structure of a generic semiconducting polymer showing the band gap, and c) metallic conduction band

With respect to polymers, we must consider the linear combination of atomic orbitals. The over-position of all orbitals interacting among them, results in a farther splitting with the appearance of valence band with higher energy and conduction band with lower energy, analogous to the HOMO and LUMO respectively as seen in **Figure 2.2a** for a molecule and a polymer in **Figure 2.2b**. Difference in energy between HOMO/LUMO bands in a polymer is called band gap (E_g). E_g is the threshold energy barrier for an electron in the HOMO to be promoted to the LUMO. This energy is fundamental to define the electronic behavior of materials. Conductors, like metals in **Figure 2.2c**, have no band gap, while insulator have a large band gap. Semiconductor can be defined as materials with a narrow band gap where the Fermi level sits in between the gap. Fermi level (E_f)is defined as the energy level that has 50% probability of being occupied at any given time, if not in a forbidden gap. For metals is usually consider to sit in the middle of the metallic band. The ionization energy I_E is the energy required to extract an electron from the valence band maximum (*i.e.* the HOMO) to the vacuum level. This means that for a metal, I_E corresponds to the value of work function (W_f) where W_f corresponds to the energy required to extract an electron from the Fermi level E_f to the vacuum level (**Figure 2.2c**).

2.1.2.2 Transport models in organic semiconductors.

Various charge transport models have been proposed for polymeric semiconductors, mainly adapted from inorganic semiconductor physics. Polymeric semiconductors are anyhow very different from inorganic crystals, being weakly bonded macromolecules with partial conformational freedom, and morphology that can vary from completely amorphous to crystalline.[4]

Without losing generality, possible electronic states in a semiconductor can be divided into extended states or localized states. Extended states are those in which the charge carrier is delocalized over the entire lattice and their associated wave function range is over the whole lattice. On the other hand, localized states are those in which the charge carrier's wave function is always zero except in a finite region of the polymeric chain. The main reason for localization is the presence of disorder in the lattice.[5]

Charge transport mechanisms are largely determined by the type of states that are present. If extended state are predominant, **band-like transport** is observed as for crystalline materials.[6] Another and largely different charge transport mechanism is called **hopping** and occurs between individual localized states near the Fermi energy. Hopping is a thermally activated tunneling of carriers among localized state. This means that charge carriers occupy one state at time and hop from a state to another one with a frequency depending on temperature. In particular, for polymeric semiconductors, the most common transport model is the **variable range hopping**. In this model, charges can transfer towards to a state which is faraway with respect to the initial one, but still in the accessible energy band as sketched in **Figure 2.3a.**

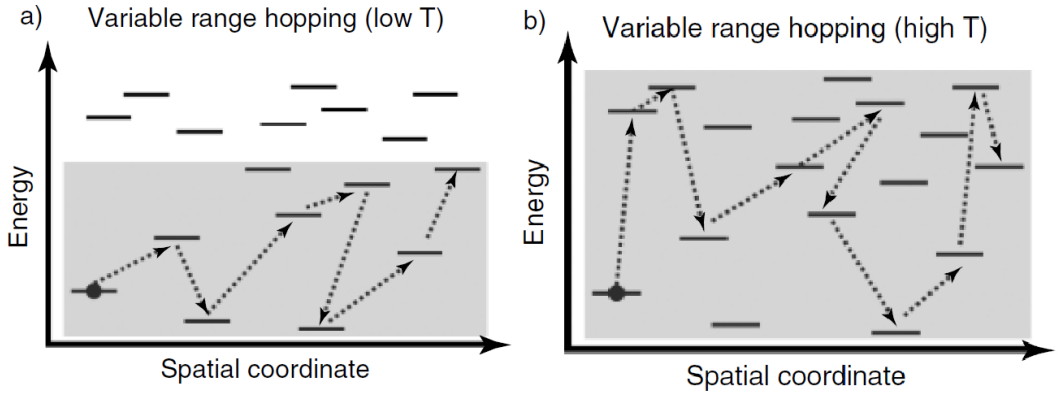

Figure 2.3 Model for variable range hopping transport in a polymer at a) low T and b) high T. Continuous grey lines represent localized state, band in dark grey represents accessible energy range. Dotted arrows indicate a hopping mechanism. Reproduced from ref [5]

The disordered system is characterized by an exponential distribution of localized states. The tunneling hopping is activated thermally and at higher T the accessible available energy range is wider (**Figure 2.3b**). An important parameter for tunneling frequency is the overlapping of states, which is directly related to polymer's crystallinity, with more crystalline polymers presenting a higher overlapping and thus higher performances. Also this model takes into

account the effect of an applied electric field on the gate of a transistor. When the device is turned on, charges fills lower energy states, and additional carriers must fill higher energy levels, resulting in a smaller activation energy to hop away from the initial state, *i.e.* there is a linear dependence of output current with gate applied voltage.[7]

A third regime, involving both extended and localized states, and mainly describing oligomers, is the one in which charge carriers are trapped in deep energetic trap levels and they are thermally promoted to an extended-state transport level from which they can move by drifting, up to when they are again trapped. This model is called **multiple trap and release model**.

Variable charge hopping is temperature dependent, and hence if energy decreases charges can hop just to close low-energy localized states. At very low T, only hops towards lower energy states are possible. The hopping frequency between two energetic sites, say *i* and *j*, can be calculated through the Miller-Abrahams model reported in **equation 2.1.**[8]

$$v_{ij} = v_0 e^{-2ar_{ij}} e^{-\frac{\varepsilon_j - \varepsilon_i + |\varepsilon_j - \varepsilon_i|}{2KT}} \qquad 2.1$$

Where v_0 is attempt to hop frequency of a charge and *a* is the inverse of localization radius, r_{ij} is the energy difference between the sites *i* and *j* and ε_i and ε_j are their respective energies.

Two considerations arise from **Equation 2.1**: first is that the energetic separation of the state exponentially decreases hopping frequency, but it does not accelerate hopping at low energetic separation. The second is that for each hopping a phonon should be emitted or absorbed to compensate the difference in energy between starting and final state Δε. This means that another limitation to this process is the presence of a phononic state with energy equal to Δε.

A model that takes into account the phonon contribution and the fact that charges induce polarization of the space around is the **polaron model**. When a charge moves a reorganization occurs in the polymer. For general charge transfer we consider that charges (positive or negative) move from state I to J [$I^{(+)/(-)}+J \rightarrow I+J^{(+)/(-)}$] and thus a shift in potential energy occurs, considering hole or electron transfer respectively.[9]

Marcus theory describes this process as (**Equation 2.2**)

$$v_{ij} = \frac{|J_o|^2}{\hbar}\sqrt{\frac{\pi}{\lambda KT}} e^{-2ar_{ij}} e^{-\frac{(\Delta\epsilon_{ij}+\lambda)^2}{4\lambda kT}} \qquad 2.2$$

J_0 is the transfer electron integral and λ is the reorganization energy associated with the charge transfer. The other variables have been already defined. Transfer frequency depend on $\Delta\varepsilon_{ij}$. A remarkable aspect for this model is that transfer rate does not increase with more favorable energy differences. Given a needed reorganization energy λ, when $-\lambda < \Delta\varepsilon < 0$ transfer rate increases with Δε, with a maximum when $\Delta\varepsilon = -\lambda$. For more negative values transfer rate decreases. In other words, there is a normal mode of transfer, which increases up to a maximum value and then decreases, in the so-called inverse region when difference in energy between

states cannot being compensate by reorganization after transfer. Transfer integral in organic semiconductor is strictly depending from electronic states overlapping. This means that it is related to supramolecular interactions that occurs between chains. Distance between stacked chains is a main factor governing the transfer integral and very strong interactions are required for high performance polymers making them less sensitive to disorder. Anyhow, these weak interactions makes the material soft and introduction of disorder in the film dramatically decreases performances. Also molecular fluctuations should be taken into account since they induce a change between initial and final state coupling affecting the transfer integral.[10] On the other hand, reorganization energy is defined as the energy required to distort the configuration of the initial state to the final state without electron transferring and it depends on the chemical structure of the employed polymer.

The effect of an external electric field is not taken into account in this model. Briefly, in an electric field (**F**) lower the activation barriers as reported in **Equation 2.3 (**vectorial terms are reported in bold)

$$\Delta\varepsilon = \varepsilon_j - \varepsilon_i - q\boldsymbol{r_{ij}}\boldsymbol{F} \qquad 2.3$$

External applied electric field increases the number of state available and it is an effect similar to increasing temperature.

Despite all the presented models, charge transport in polymers is an open question due to the complexity of the structure/transport relationship in these systems. Organic semiconducting polymers have different degree of paracrystallinity as described by *Rivnay et al*. Paracrystallinity parameter *g* is defined as a fluctuation of individual lattice spacing, and is related to difference in separation between the ideal value and the real one.[11] *G* values are lower of 1% for crystals, between 1-10% for paracrystalline materials and over 10% for glasses or amorphous materials. The effect of *g* parameter on charge transport is very important, since fluctuation of π-stacking generates traps states in the band gap of the polymer. Even for well-defined regular morphology polymeric films, has been found values of paracrystallinity higher of 5%, indicating a conformational disorder in the π-π stacking direction due to fluctuations. Henceforth the g parameter is of fundamental importance in governing charge transport in polymers.[11]

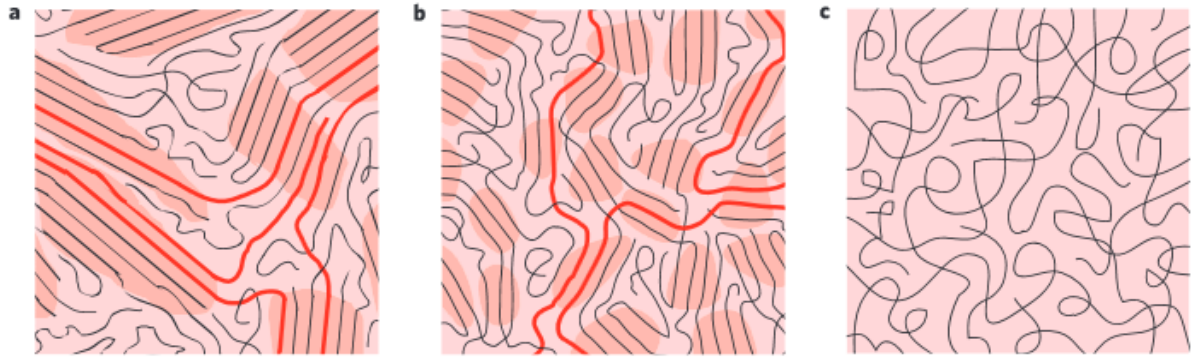

Figure 1.4 a–c, Schematics of the microstructure of P3HT a) semi crystalline polymer film, b) disordered aggregates, and c) a completely amorphous film. Figure reproduced from ref [4]

Moreover, if we consider the tendency of a polymeric semiconductor to form a semicrystalline structure consisting of microcrystalline regions embedded in spaghetti-like amorphous matrix we can assume that transport within a less aggregated phase is the bottle-neck for charge transport within the whole structure. In the case reported for semi crystalline polymers the most ordered regions are accounted for the charge transport, since higher band gap makes conduction band of amorphous region not accessible to charges. Long polymer chains connect crystallites as in **Figure 2.4a**. For polymeric films exhibiting a higher degree of disorder, ordered regions are smaller and are formed by small domains with short range order, composed by aggregates of a few molecular units as depicted in **Figure 2.4b.** Charges are usually confined in these aggregates and they are transported along fibrils that exit one crystallite and enter another one if they are a few nm far apart. This chain cannot be considered part of any crystalline aggregate and act as highway for charges linking different ordered regions.[12] Most recent findings showed that higher mobility is achieved by polymers made by monomers with an exposed rigid core, but no necessarily with a long-range order. Explanation of this must be searched in the fact that they have enough short range order due to high packing occurring between the rigid cores. This tightly π –stacked aggregates have a distance inferior than 1 nm and this distance is shorter of typical polariton wave function, which allows carriers to efficiently move towards conjugated packed cores. This is reflected in their higher disordered tolerance. Very interestingly, the paracrystallinity factor of those polymers is higher than 5% and comparable with crystalline polymers but lower with respect to amorphous polymers. This means that these aggregated material can be disordered on the nanoscale, but the tight packing between cores maintains order in the angstrom scale.[4] The most important factor for high-performance polymer is hence the presence of interconnected aggregates, while their size and how disordered they are is less important.

In this thesis we took advantage of one model compound as crystalline p-type polymer, and an n-type and a p-type poorly ordered-high performance polymers.

2.1.3 Employed semiconducting polymers

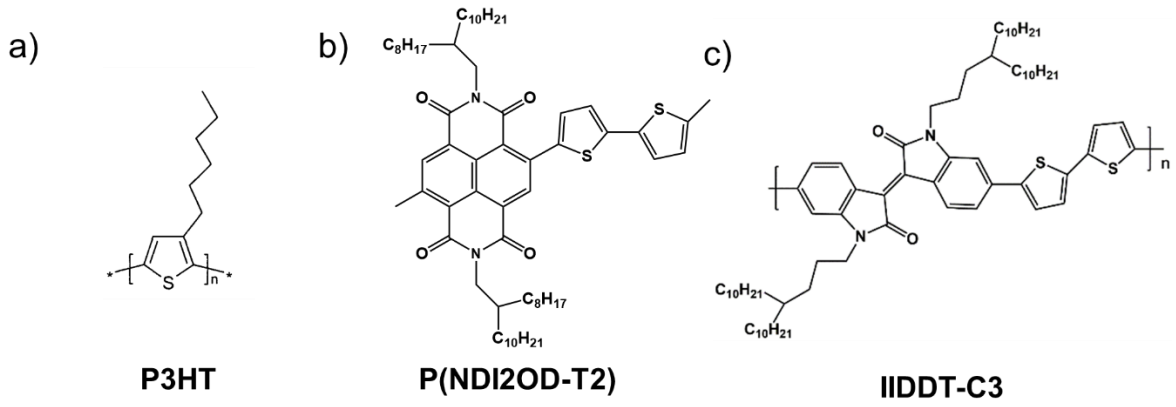

Figure 2.5 Chemical formula of repetitive unit of a) P3HT, b) P(NDI2OD-T2), and c) IIDDT-C3

2.1.3.1 Poly (3-Hexylthiophene)

Poly (3-Hexylthiophene) **P3HT Figure 2.5a** is a well-known and established polymer with mainly crystallite structure embedded in amorphous matrix. P3HT is p-type polymer that reaches maximum mobility of 0.1 $cm^2V^{-1}s^{-1}$.[13] P3HT is known to form two kind of structures, interdigitated and not interdigitated, with a spacing among its lamellar structures varying between 1.6 and 1.3 nm. Those values has been obtained by X-Ray diffraction and confirmed by theory calculations. [14] These two forms usually coexist in a P3HT film and they are embedded in an amorphous matrix that generates domain boundaries. Domain boundaries are the primary source for trap states and are a major limit for obtaining high mobility values.[15] To improve performances a common strategy is to use regio-regular P3HT with high molecular weight. Regioirregular P3HT forms high amorphous thin films due to the weak tendency of intermolecular packing. Regioregular P3HT, on the other hand, forms π-stacked aggregates in which chain bending is strongly inhibited.[16] Molecular weight is critical for having long chains interconnecting different crystalline zones of the film, diminishing the boundaries importance between crystalline and amorphous zones that otherwise results in strong charge trapping.[17] A growth of 4 order of magnitude of mobility values has been observed by increasing almost 10 times the molecular weight.[18] Nevertheless an increase of molecular weight over 10 kg/mol doesn't affect anymore electric performances, because at this molecular weight, paracrystallinity becomes close to 7% and no further increase of mobility has been observed. P3HT is commonly used as matrix in bi-component blends because it tends to expel the other components of the blend to its amorphous phase, thereby only slightly affecting overall performances.[19] The molecular structures of P3HT are strictly correlated to optical features of absorption spectra of P3HT thin films. Of particular importance to understand P3HT morphology is the Spano model on H-aggregates from which is possible to evaluate crystallinity of casted film by simple absorption spectra features of polymer thin films (see paragraph 3.6.3 for more details).[20] In this work P3HT has been used in Chapter 4 in a bi-component system with gold nanoparticles blended in it.

2.1.3.2 P(NDI2OD-T2)

Poly[N,N'-bis(2-octyldodecyl)-naphthalene-1,4,5,8-bis(dicarboximide)-2,6-diyl]-alt-5,5'-(2,2'-bithiophene),**P(NDI2OD-T2) Figure 2.5b** is n-type, slightly ambipolar polymer synthetized by Facchetti group in 2009.[21] It reaches mobility as high as 5 $cm^2V^{-1}s^{-1}$, [22] it is air stable and has a particular face-on structure that helps to maximize performances in top-gate transistor configuration.[23] .It is a particular noteworthy polymer because it has been the first n-type semiconductor reaching electron mobility close to 1 $cm^2V^{-1}s^{-1}$. High-performances for n-type mobility is usually difficult to achieve because of the sensitivity towards air and oxygen that produces strong electron trapping.[24] A very attentive synthetic design has been made to balance the order of donating and accepting units in this polymer to obtain stabilized LUMO level. Moreover a carefully choice of the branching point of the aliphatic chain with respect to the NDI core allowed to obtain a tight π-π stacking of 0.39 nm between polymer chains, which is the main reason for the so high electron mobility reported.[23] Deposited polymer from spincasting has a peculiar face-on conformation that can be changed to edge-on by slowly cooling the film from the melting point. The rearrangement anyhow doesn't change obtained mobility, suggesting that reorganization doesn't occurs at the interface.[25] Moreover increasing the molecular weight doesn't led to an increase of performance, due to the particular nature of polymer aggregates, which is not influenced by increasing of long-range order.[21] The polymer is partially ambipolar, and hole mobility is usually lower with respect to electron mobility. The reason for this behavior has been found in an higher transfer integral for electrons with respect to holes.[26] In this thesis P(NDI2OD-T2) has been used in chapter Chapters 5-6-7 as active layer in light of its high performances and stability.

2.1.3.3 IIDDT-C3

Poly[1,1'-bis(4-decyltetradecyl)-6-methyl-6'-(5'-methyl-[2,2'-bithiophen]-5-yl)-[3,3'-biindolinylidene]-2,2'-dione] **IIDDT-C3 Figure 2.5c** is a p-type polymer. It has been synthetized by Lei *et al.* in 2012.[28] It is based on an isoindigo core coupled to two thiophene groups. The reason of this design resides in the need to compensate electron deficiency nature of the isoindigo core with high electron rich units in order to increase the HOMO level of the obtained co-polymer.[29] Moreover the combination of electron rich/electron deficient block has the effect to increase π- π stacking between polymer chains.[30] Another factor playing a fundamental role in π- π stacking, and hence polymer morphology, is the distance of the branching point form the core. It has been found that a three carbons distance permits to obtain the highest electronic performances. This is due to the fact that in this isomer there is the most exposed isoindigo core, which induces a thigh π-stacking of 0.37 nm and mobility is increased up to a maximum value up to 3.62 $cm^2V^{-1}s^{-1}$.[28] It should be noticed how the stacking is tighter with respect to **P(NDI2OD-T2)** because of the different branching point. Shorter branching points increase the packing distance, thus decreasing charge transport, while longer branching points don't improve anymore performances. As expected from its tight stacking between

chains. molecular weight don't affect mobility and lower molecular weight IIDDT-C3(20kg/mol) has the same mobility of the 40 kg/mol one.[30]

IIDDT-C3 has been used in chapter 7 to evaluate different effect of nanostructuring transistor gate surface with graphene on both p-type and n-type polymers, especially considering very close HOMO/LUMO level energy values with respect to **P (NDI2OD-T2).**

2.2 GOLD NANOPARTICLES

2.2.1 Introduction

One of the first human example of nanotechnology conscious employed to modify properties of material is the Lycurgus cup.[31] In this handcrafted cup the presence of nanoparticles of silver and gold (AuNPs) in the glass confers to it a dichroic behavior. If the cup is irradiated from the front is green (**Figure 2.6a**), if irradiated from the inside is red (**Figure 2.6b**), in order to symbolize the maturation process of grapes.

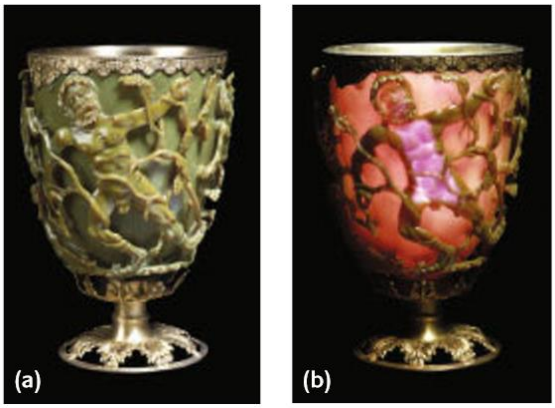

Figure 2.6 Lycurgus cup irradiated from a) front and b) back showing different coloration. Image reproduced from ref [31]

This effect arises form scattering due to the presence of AuNPs and the colors are strongly affected by the size of nanoparticles (NPs) as noted by Faraday.[32]

Nanoparticles are objects with size between 1 and 100 nm. They have attracted much interest because their unique properties, arising from their small size, are distinctively different from that of the bulk equivalent. Of great importance is the fact that AuNPs properties are dependent from their size and shape, meaning that is possible to tune at the synthetic stage desired properties. At the nanometric size, particles are composed by a reduced number of atoms, and a great amount of them are on the surface. The great surface/volume ratio can be successful used to introduce functionalization at the interface that can further modulate NPs properties. Moreover the small number of atoms composing the clusters induces a dramatic change in electronic properties with respect to bulk gold, giving rise to electrical semiconducting behavior and to electrons quantum-confinement effects. [33]

Though how changes in optical properties of NPs are related to their size have been widely studied, the same effort has not been performed to understand how in organic electronic devices, the size of AuNPs affect interactions with a semiconductor. Within the context of the present work, AuNPs will be employed in bi-component transistors to explore how they interact with charges, in view of the possibility of tuning the electric properties by changing their size, of the easy functionalization of their surface for multifunctional devices and to take advantage of their surface plasmon resonance.

2.2.2 AuNPs size - Kubo Gap

In 1962 Kubo elegantly demonstrated that with decreasing size and thus the number of gold atom in a nano-cluster, its metallic behavior is reduced, up to a formation of an energetic gap that makes clusters smaller than 2 nm non-metallic.[34]

Considerations adduced were not so different from what we already described for semiconducting molecules. Each metallic atom has its atomic-orbital. When is organized in a crystal each orbital contributes to a band with its atomic states. The formed band has a width proportional to the number of states multiplied for the number of atoms of the ensemble. We can consider this band formed by a number of states separated energy equal to E_f/N, where E_f is the Fermi level and N the number of atoms composing the cluster. When the number of atom is very high, as in microscopic or macroscopic structures, we have an infinitely small difference, and thus all states are accessible to electrons.[35] Decreasing number of atoms, usually starting from cluster under 2 nm of diameter (about 250 atoms), difference in energy increase up to the creation of a gap, called Kubo gap. When this gap is lower than KT, we have a metal, otherwise a non –metal.

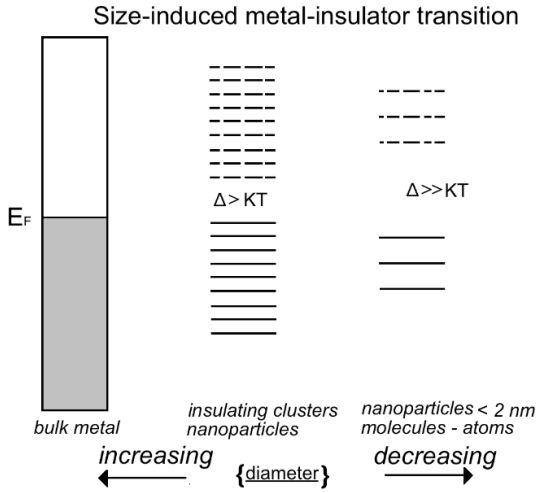

Figure 2.7 Effect of decreasing particle on the electronic structure of a metal clusters the formation of an energy Kubo gap is highlighted with respect to the decreasing size. Adapted from reference [36]

In **Figure 2.7** is reported as scheme of what discussed above. In summary, metallic regime is found in objects as small as 1000 nm, a negligibly small Kubo gap arises for size between 1000

nm and 2 nm, and a non-metal regime is observed under 2 nm.[36] From what concerns the conduction properties of NPs, the effect of size on the electronic transport was addressed by Gor'kov and Eliashberg[37]. They correlated the effect of small cluster with the de Broglie electrons wavelength λ, which in metals typically amounts to 0.5-1 nm.

When an electron is in the bulk metal its wave is delocalized on the entire crystal. Gor'kov demonstrated that when NPs approach values comparable with λ a decrease in conduction is expected up to a complete non-metallic behavior, due to confinement of the wave function of electrons.

In particular the transition is consider to happen when **Equation 2.4** is respected

$$K_f I_e \approx K_f D \approx 1 \qquad 2.4$$

Where K_f is the Fermi wavenumber of the electron wave function and I_e is the mean free path of conduction electrons. A rough interpretation is that I_e can be considered equivalent of diameter D of the NP and hence when $K_f \cdot D$ is about 1 the equation describes the condition for the cessation of metallic behavior of a NP.

2.2.3 Surface Plasmon resonance

AuNPs solutions have beautiful bright colors, even at low concentration. Faraday was the first to note this effect in 1847,[32] and a proper explanation has been given by Mie in 1908 using Maxwell's equations.[38]

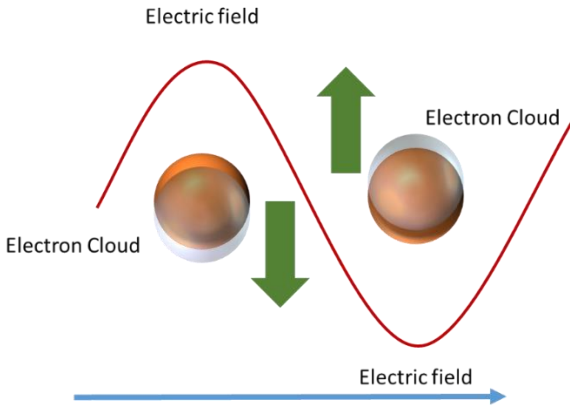

Figure 2.8 Schematic representation of Localized Surface Plasmon Resonance of gold nanoparticle by the oscillation of electrons across the nanosphere in an electromagnetic field

Schematically the origin of this wide range of colors is attributed to the collective oscillation of free conduction electrons of NP when interacting with an external magnetic field. When induced oscillation of electrons couples with the electromagnetic wave of the electric field, a resonance of the electronic cloud occurs, giving rise to plasmon waves as sketched in **Figure 2.8.**[39] Resonant excitation by the incident photons causes strong absorption band, which is called a surface plasmon band (SPR). Mie equation for energy losses in the direction of propagation of the incident light on a NP due to both scattering and absorption is the following

$$C_{est}(\lambda) = \frac{24\pi^2 R^3 \epsilon_m^{3/2}}{\lambda} \frac{\epsilon''(\lambda)}{(\epsilon'(\lambda) + 2\epsilon_m) + \epsilon''(\lambda)^2} \qquad 2.5$$

In **Equation 2.5** ε(λ) is the dielectric value of the metal, ε_m is the dielectric constant of the medium, solvent for a solution, R is NPs radius, and is the λ wavelength of incident light. It is important to observe the ε for a metal is not a fixed value and is function of cluster's size. This explain the wide range for absorption band found for AuNPs from 500 to 550 nm for different dimensions. Also SPR can change according to the material in which NPs are dispersed, their coating and eventual aggregation. Finally if AuNPs are under 2 nm as previously described, they will interact with an external electromagnetic wave in a differently way. [40] Scatter will no longer occurs, so very small NPs in solution are transparent,[41] and at the same time light promotes some electrons over the Kubo gap in an excited state. These electrons radiatively relax, causing emission in the IR range.[42]

2.2.4 Synthesis and surface functionalization

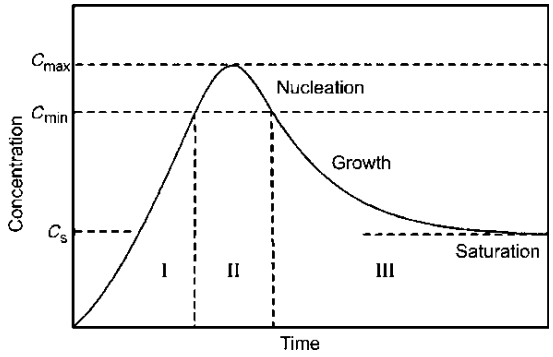

Figure 2.9 Schematic representation of the concentration of atomic reduced metallic gold before and after nucleation as a function of time. Adapted from ref [43]

Gold nanoparticles have been synthetized with various methods, in gas, solution and solid phase. Solution synthesis has been introduced by Turkevich in 1951[44] and various modifications and variations have been proposed during the years by different chemists. All these in situ synthesis have in common two factors. The first is a reducing agents that reduce gold ions in solution (usually derived from a $HAuCl_4$) to metallic gold and the second is the presence of stabilizing agents that acting as surfactant on NPs surface avoid coalescence and aggregation. Reaction mechanism is based on attraction of metallic gold atoms in order to reduce surface energy. Metallic atoms are formed by reduction of Au ions. Their concentration grows in solutions up to super-saturation, when they start to precipitate as nano-clusters, a phase called nucleation as showed in **Figure 2.9.** When precipitation rate is not compensated by reduction rate, concentration of Au(0) becomes lower of super-saturation limit. At this stage new nanoparticles are not formed anymore, and growth phase starts, with previously formed cluster that increase in size, collecting metallic atom in solution as they are reduced.[43] Gold

nanoparticles formed are naked and surfactants play a fundamental role to stabilize them thereby avoiding excessive aggregation. Without them the AuNPs will continue growing and then coalescence will occur, leading to big, not-nanometric clusters, which precipitate. Surfactants avoid coalescence by forming a self-assembled monolayer (SAM) on the surface. Varying surfactant and reducing agent gold ratio it is possible to tune AuNPs size with good precision. While amines can physisorbes on the surface giving some degree of stability and size control, thiols have more interesting properties. In particular thiols have been widely used in literature since they stabilized very well NPs by formation of a strong chemical bond (100 kJ/mol) between sulphur and gold, passing through an RS* radical specie. Thiol-capped NPs are stable in solution for years. Specific nature of the bond is still under investigation, with standard models assuming a mono-thiolated species bonding atop or hollow sites in gold surface while more modern studies suggest formation of adatom on the surface with Au(I) gold stabilized by two mono-thiols.[45] Whichever is the real description of the bond, its particular nature can be useful employed to stabilize AuNPs and to tune their size,[46] they can displace amine coating because of their stronger interaction and they allow to perform digestive ripening on already formed nanoparticles.[47] In particular this method permits to obtain very mono-disperse NPs size distribution, allowing to obtain particle with a diameter under 1.5 nm, by adding an excess of thiols in solution on bigger nanoparticles.

In this thesis the employed AuNPs synthesis are detailed in the material and methods paragraphs in Chapter 4 and 5.

2.3 INTERFACES IN ORGANIC ELECTRONICS DEVICES

2.3.1 Introduction

Polymeric semiconductors are soft solid, kept together by supramolecular interactions. They are sensitive to effects arising from interfaces with other materials. When their surface is placed in contact with a metal, the interface that is formed affects strongly the electric outcome. Various chemical-physical process take place at the interface and their understanding is of seminal importance. Electrodes interfaces play a fundamental role in organic device, since they rule charge injection and accumulation, thus they are key factor in governing the general electrical characteristics of both two and three terminals device, *i.e.* junctions and transistors. In particular, it should be noticed that, beside electronic interactions between the semiconductor and the metal, also morphological issues arises, since variation in surface energy affects packing and degrees of order of polymers.[48] Interfaces can be planar, like source-drains electrodes or generated by interactions with nano-objects. In this case, interactions at the interfaces are subtle. They rule how the nano-object (nanoparticle of nano-flakes of graphene in this thesis) can

interact or affect the charges transport, acting as traps, as doping agent, as scattering centers *etc*. In this paragraph, we focus on the three most relevant aspects for hybrid interfaces properties: charge injection mechanism, interfaces modification with self-assembled monolayer and tunneling at the interfaces.

2.3.2 Charge Injection

Charge injection is a fundamental process in organic transistor or junctions which takes place at the interfaces between electrodes and semiconducting active layers.

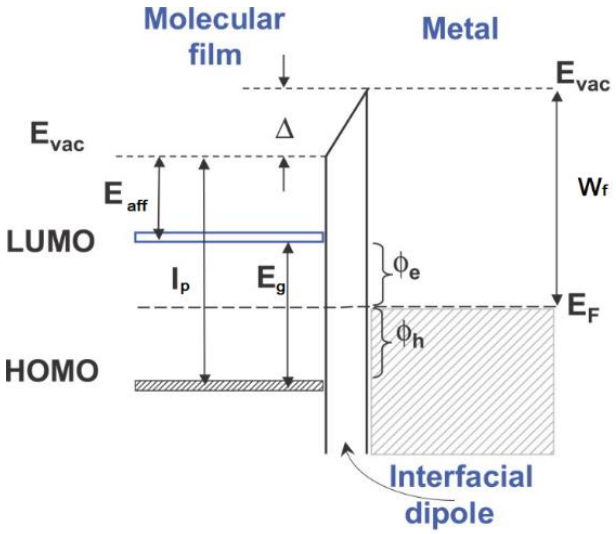

Figure 2.10 Energy diagram of an interface between a semiconductor and a metal electrode surface. The ionization potential I_p, electron affinity E_{aff}, and band gap E_g of the organic semiconductor are depicted. The electron and hole injection barriers φ_e and φ_h correspond to the energy difference between Fermi Energy E_F of the metal (work function W_f) and LUMO and HOMO, respectively. The effect of interfacial dipole layer with energy offset Δ is shown as well. Reported from Ref [49]

When a semiconductor is physisorbed on a metallic contact, different interactions occurs at the interface, which affect surface properties of both materials. *(i)* metal electrons wave-function tails becomes closer to the surface, modifying metal surface dipole, *(ii)* screening due to charge images reduces the transport gap in the semiconductor in the first 2 nm *(iii)* HOMO/LUMO levels are statistically distributed due to energetic disorder, (*iv*) different level alignments can cause charge transfer.[48] When Fermi level of the metal is close to the LUMO level (HOMO for p-type semiconductors) charge transfer to the LUMO (from the HOMO) take place. Direct consequence is the formation of a barrier (Schottky barrier φ_b). The height of the barrier depends of metal W_f , intensity of dipole momentum at the interfaces and ionization energy of semiconductor.[50] In **Figure 2.10** φ_e and φ_h represent barrier injection for electrons and hole respectively, while the barrier caused by the interfacial dipole is represented with Δ. Applying appropriate voltage will lower injection barrier by decreasing barrier thickness and shifting work function value. On the other hand barrier height cannot be modified due to pinning of energetic levels at interfaces.[49] Charge injections from the electrode to the semiconductor

due to particular triangular form of the barrier can happens by **thermionic emission or tunneling.**

$$J = J_0(e^{\left(\frac{qV_a}{KT}\right)} - 1) \qquad 2.6$$

Equation 2.6 represent current density J in a metal/semiconductor diode. V_a is applied potential, q elementary charge. J_0 is defined as

$$J_0 = AT^2 e^{(-\frac{q\vartheta_b}{KT})} \qquad 2.7$$

J_0 is dependent on the temperature T and on barrier height φ_b. A is Richardson constant and K Boltzmann constant. **Equation 2.6** with J_0 defined by **Equation 2.7** describes the thermionic emission and predict that charges are thermally activated over the injection barrier. On the other hand, if the applied external electric field V_a is large, Δ becomes thinner and thus tunneling of charges from the metal directly into semiconductor becomes preponderant. Also if some trap states are localized at the interfaces some charges can hop in those level and then tunnel form them in the semiconductor, lowering tunneling efficiency (**injection via gap states)**. [51]

2.3.3 Interface's functionalization

2.3.3.1 SAMs

The chemisorption of Self-assembled Monolayers (SAMs) is a common way to functionalize a metallic surface in order to change its properties. Thiolated SAMs have been widely used especially for organic electronics application.[52] The chemisorption is typically obtained by immersion of a cleaned Au surface (or AuNPs) in a solution containing the thiol substituted molecules. SAM formation starts with the molecular physisorption forming disordered and loosely packed layers on the substrate surface. They are in a shallow minimum of energy at a certain distance from the substrate.

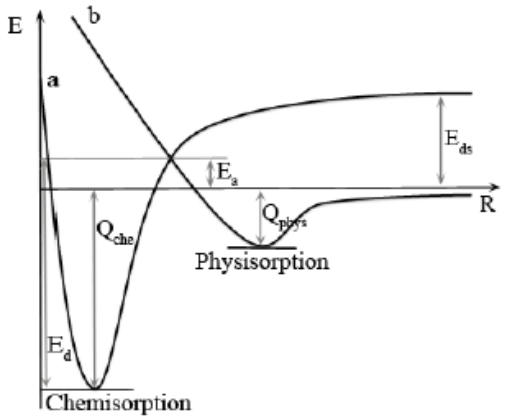

Figure 2.11 Potential description of the self-assembly process. *A* and *B* are respectively the potential energy curves associated to chemisorption and physisorption. Q is the heat of absorption associated to enthalpy. E_a is the activation energy for the intercrossing between the two curves, R is the reaction coordinate.

When they move closer, the sulphur forms a chemical bond with gold, and thus a new a deeper energy minimum is reached, which is closer to the gold surface (**Figure 2.11**)**.** When almost all the surface is covered by thiolated molecules laying down, a "nucleation" phase starts where molecules tilt-up, creating islands with a dense phase of upright molecules. The coverage can be homogenous in all across the surface or, especially if gold surface is defect-rich, formation of island with different orientation can be observed. [53]

The formation of SAM changes drastically interface between gold and a semiconductor for electronic devices. First effect is a change in wettability that foster or decrease affinity of the organic material on the electrode, this the capacity to form homogeneous layers. Second effect is a change in work function of the electrode, and third effect is the introduction of a not-conductive barrier. The experimental details for the preparation of all the SAMs employed within this thesis will be given in the respective materials and method section in Chapter 4, 5, 6 and 7.

2.3.3.2 Work function tuning with SAM

The work function is the energy necessary to extract an electron to the vacuum level. In a standard electrode-semiconductor junction, the introduction of an interlayer of molecules bonded to metallic surface has two effects: *(i)* the electrons need to overcame an additional potential created by the dipole moment between gold and molecule to be extracted to the vacuum level (ΔU_{vac}), *(ii)* the bond formation itself shifts the potential well of metal work function according to the intensity of bond dipole (BD).[54]

Overall work function shift can be described as (**Equation 2.8**)

$$\Delta W_f = \Delta U_{vac} + BD \qquad 2.8$$

The BD contribution strongly depends on the metal, and thus for a given metal, *e.g.* gold, the contribution of molecular dipole ΔU_{vac} dominates the overall work function shift.[54] This means that by carefully choosing thiolated moiety by proper design it is possible to increase or decrease work function of the electrode, reducing or increasing the energetic barrier to inject charges. In particular terminated methyl group decreases W_f, while halogen-terminated thiols increase it.[51]

2.3.3.3 Tunneling through a SAM

The adsorption of a SAM on a metallic electrode adds a barrier that charges must overcome to be injected in the semiconductor. In this case tunneling is the key physical process modulating charge injection. For a molecular layer tunneling resistance is defined by **Equation 2.9**

$$R_t = R_0 e^{-\beta L} \qquad 2.9$$

R_t is tunneling resistance, R_0 is effective contact resistance, β is the exponential prefactor that depends on the nature of bonding in the molecular back-bone and L is SAM thickness.[55]

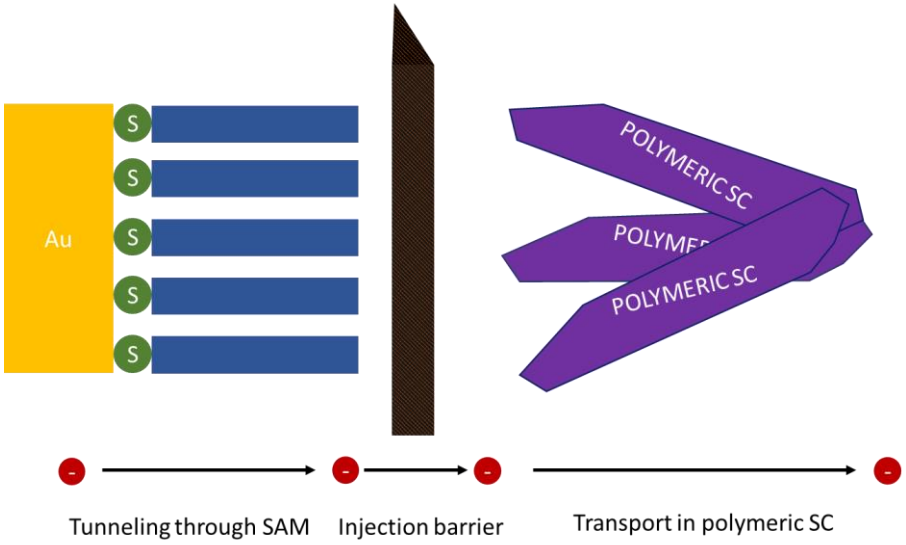

Figure 2.12 A schematic of the three steps of charge injection from the metal layer to organic semiconductor. First the charge tunnels through the SAM, then it is injected in the semiconductor. At this second step it needs to overcome the injection barrier (between the SAM and the semiconductor) by thermionic emission or tunneling... Inspired by Ref [51]

This means that two factors must be considered. One is that the longer the molecules forming the SAM is, the higher is tunneling resistance. The second is that molecular structure affects β. It depends from the packing of the SAM and as well from conjugation of self-assembled molecules. In particular molecules with more extended conjugation present a lower R_t.

As summarized in **Figure 2.12** after introduction of a SAM, a charge is injected in the semiconductor from the metal, first by tunneling through the SAM and then by overcoming (by tunneling or thermionic emission) the injection barrier that may exist between the SAM and the semiconductor.[51].

2.3.3.4 Gate Dielectric Functionalization

While source-drain electrodes are important to determine device behavior, another important interface plays a major role in organic transistors. The gate dielectric surface is typically composed of a layer of some hundreds nanometers of thermally grown silicon oxide on silicon. Surface of silicon oxide has then pending hydroxyl groups, which drastically impact wettability, charge trapping, polarization, morphology with regards of deposited semiconductor.[56] These groups are highly reactive towards water and other molecules and they can be used to functionalize this surface with appropriate molecules. Silane and silazane moieties can easily react with hydroxyl group and form a well packed and stable SAM.[57] Usually molecules with long or bulky group are used to functionalize gate dielectric surface to introduce dipole momentum, decrease surface energy, hydrophobicity *etc.* on the interface. Octadecyltrichlorosilane (OTS) is by far the most common choice since it forms a high

hydrophobic SAM, reduces interfacial trap states, increases deposited semiconductor crystallinity and it can also, in some cases, polarize the gate surface. The final result is an overall increases of performances of the devices.[58] The SAM formation complies with a mechanism which resembles that of thiols on gold.

A complete different method is to introduce nano-sized objects on the gate dielectric surface taking advantage of physisorption to add functionalization. In this regard, gold nanoparticles or conductive nanostructured objects can be evaporated or deposited on silicon oxide to introduce a charging element for flash memory device.[59]

Each of these functionalization are described in detail in materials and method of Chapter 4, 5 and 6.

2.4 PHOTOCROMIC MOLECULES

2.4.1 Introduction

A photochromic molecule is a chemical system that can change its state when it subjected to a light stimulus.[60] Photochromism, therefore, can be defined as a light-driven reversible transformation between two isomers which present different absorption spectra and different geometry and/or conjugation.[61] Among different options, spiropyrans, azobenzenes and diarylethenes are the most common class and appears to be adapt for applications in organic electronics.[62] We will focus mainly on (DAEs) which have been employed in this thesis as thiolated molecules and as well on azobenzenes (AZO).

2.4.2 Diarylethenes

Diarylethenes are a class of compounds in which two aromatic substituents are bonded at an olefinic bond discover in 1988 by M.Irie.[63] More specifically, typical employed diarylethene are bisthienylethenes. They have two thiophene group at both side of the double bond methyl substituted in position 2 and a 5 terms backbone connecting both carbons at the end of the double bond as shown in **Figure 2.13.**

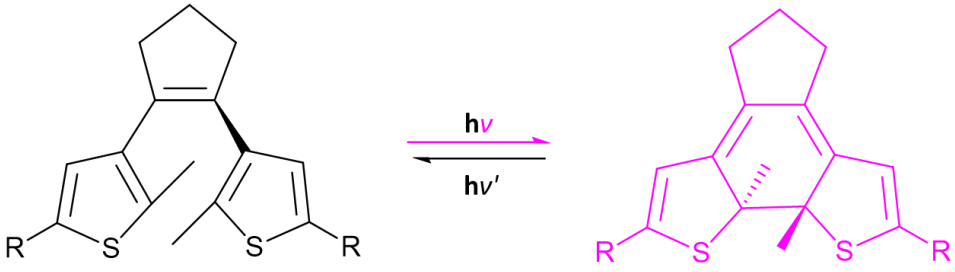

Figure 2.13 DAEs generic formula showing the two distinct addressable form, in correlation with irradiation at two different wavelength, between an open not conjugated form and a close conjugated form.

DAEs are photochemical photochromic molecules which means that the photo-generated isomer is thermally stable (half-time of thermal isomerization is usually about 400000 years), and that the only way to reverse the isomerization is by irradiation. From a chemical point of

view the open-isomer (o-DAE) is a hexatriene moieties and it is π-conjugated only on the thiophene unit. The closed-isomer (c-DAE) is a cyclohexadiene in which occurs a rearrangement of electrons in the structure, with the main effect of delocalizing the π-conjugation. Structural change occurring at the switching core is very small with a change of 1 Å in core length and 0.7 Å in height, with the closed structure more planar and the open slightly twisted.[61] This allows a large fatigue resistance and high cyclability of switching by irradiation. o-DAE are usually white-yellow and the c-DAE are violet, blue or green, as effect of more delocalized π-cloud that induces a red shift in the absorption spectrum. Substituents on the 5 member ring of the double bond or at the end of the double bond led to a wide range of colored molecules.

2.4.2.1 Electrical Properties of DAEs

Due to the drastic change in conjugation, many investigations have been carried out in the last decades on DAEs. The closed isomer has a smaller HOMO/LUMO gap with respect of the open form, with an energetic difference of about 1.5 eV due to more delocalized conjugation with respect to o-DAE. Single molecule conjugation has shown a difference of three order of magnitude between o-DAE and c-DAE [64] conductance. Also they have been used embedded in a AuNPs matrix, obtaining a 5 –fold increase of conductance when in the c-DAE form.[65] More recent work tried to use DAEs directly as active layer in an OFET. DAE molecules show some kind of semiconducting properties: while the measured currents were in the pico-ampere range in the o-DAE form, when switched to the closed state an increase of output current of two order of magnitude has been registered.[66]

2.4.2.2 SAM of thiolated DAEs: switching and electrical properties.

Self-assembled monolayers of thiolated DAEs (t-DAEs) is a viable approach to exploit the efficient switching characteristic of DAEs. The functionalization of a surface with a SAM, as we discussed in previous paragraph, allows to tune properties of interfaces, more specifically, charge injection and work function. This means that DAEs make possible to change these properties by irradiation in view of different conductance between the two isomers. The first issue to be address is the effect of a metallic Au surface on DAE's core when they are linked through a chemical bond and the concomitant packing effect on switching abilities. The packing can cause a decrease in switching performances because of the steric hindrance of neighboring molecules. The chemical bond is a more important factor. A DAE molecules coupled through an S-Au bond is not an isolated unit, but is an extended molecules composed by the first atoms of the surface and the molecules itself. This can lead to a drastically distress of switching mechanism up to complete quenching of isomerization properties. Lastly irradiation produce a formation of a dipole in the molecule that is mirrored in the metal, causing charge transfer which hinder any switching rearrangement. A way to circumvent this problem is to insert a layer of a non-conjugated molecule. In this way the switching core is decoupled from metal surface, but conductance in DAEs can be lowered of several orders of magnitude.[67]

On this regards different substituents have been investigated. Long alkyl chains are very effective in decoupling the core from the metal, but they increase both L and β parameters in **Equation 2.8** because they are not conjugated, therefore lowering conductance of 3 or 4 order of magnitude. Thiophene groups have also been studied as spacing parameter, since they are aromatic group. This groups allows the formation of SAM on gold or on AuNPs which can undergo isomerization from c-DAE to o-DAE, although reversible isomerization has been found to be not possible.[64] An explanation of this behavior can be found in the different HOMO alignment of open and closed isomer. For the former the HOMO level is strongly coupled with the gold, hence when irradiation promotes an electron to the LUMO the hole left in the HOMO is filled with an electron from the gold quenching the isomerization. For the latter this quenching mechanism in not as competitive.[68] On the other hand phenyl ring spacer does not suppress back-isomerization, and full switching behavior or t-DAE phenyl spaced SAM has been observed. The reason can be found in the fact that the phenyl ring is tilted with respect to the core switching symmetry plane, partially decoupling it from gold. The phenyl ring spacer is effective in avoiding quenching effects also for thiolated DAEs grafted on gold nanoparticles surface.[69]

Thiolated DAEs has been used in this work in Chapter 5 to study how changing conjugation of capping agent of AuNPs affects charge transfer in an AuNPs/polymer matrix and in Chapter 6 to functionalize source-drain electrodes in OFET in order to modulate charge injection with light.

2.4.3 Azobenzenes

Azobenzenes (AZO) are a class of diazene derivative with two phenyl rings substituted on the nitrogen atoms forming the double bond. They are photo-chromic systems that undergo isomerization between trans (E) and cis (Z) form. (**Figure 2.14**). Trans to cis isomerization occurs as a result of irradiation the deep blue-UV light. The cis isomer is metastable than the trans, hence cis to trans isomerization occurs spontaneously in the dark or with white light irradiation (450-600 nm).[70]

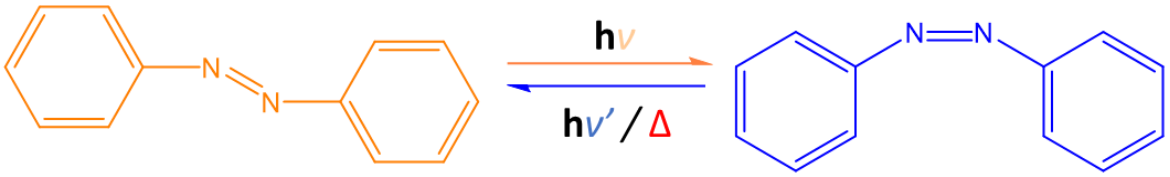

Figure 2.14 DAEs generic formula showing the two distinct addressable form, in correlation with irradiation or thermic relaxation, between cis and trans form

The optical absorption spectra of trans azobenzene presents a band at about 320-3670 nm (depending on substituent)[71] arising from π-π* symmetric allowed transition group and a much weaker absorption band at about 430-460 nm arising from n-π* forbidden transition.[72] Photo-isomerization mechanism can proceed through different pathways. The provided energy excites π-electrons of N double bond and thus allowing for rotational changes up to 180°.[73]

2.4.3.1 AZO-Polymers

One of the most studied AZO-compounds are AZO-polymers, especially the so called side-chain polymers in which chromophores are linked to the side chain of the backbone. In this position azobenzene are more free to undergo isomerization and thus to be optically activated to tune properties of the material by irradiation, like bi- birefringence, for creating gratings in optical memories application or inducing motion.[74] On this regards poly-methylmetacrilate (PMMA) polymers with side chain AZO group are promising materials for organic electronic. PMMA is a well-known dielectric layer and AZO-PMMA could be a useful tool to modulate by light morphological nanostructures

. We explored this possibility in Chapter 8.

2.5 GRAPHENE

2.5.1 Introduction

Carbon is one among the most popular chemical element and it is a fundamental constituent of organic molecules. Beyond them, other carbon-based materials are of great importance for electronics. In particular fully conjugated materials composed only by conjugated sp^2-hybridized carbon atoms are interesting because the charges can be delocalized over pretty large distances. This class of materials exists in different allotropes, all composed by a continuum of ideally fused together benzene hexagons. Graphene is the 2-D allotrope and consists of a planar sheet of benzene hexagons. 3-D fullerenes can be thought as wrapped-up graphene and carbon nanotubes as 1-D material obtained by rolling graphene in one direction.[75]

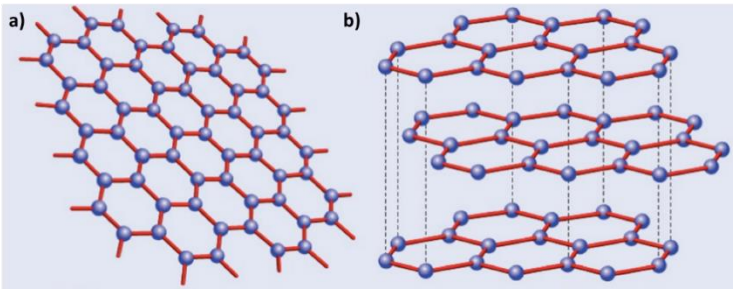

Figure 2.15 a) graphene single atom layer with its carbon honeycomb lattice. b) stacked layers of graphene with depicted van der walls force forming graphite. Reproduced from ref [75]

Graphene is directly derived from graphite, a material that entered everyday life in 1564 with the invention of the pencil and thus the name from ancient Greek Γραφειν (graphein), to write.[76] Graphene was first isolated in 2004 but is known since 1840.[77] Graphene (**Figure 2.15a**) can be described as a single atomic layer of graphite (F**igure 2.15b**).[78]

2.5.2 Electronic Properties

In 1947 Wallace predicted for a 2-D honeycomb carbon lattice an unusual semi-metallic behavior.[79] The unit cell of graphene is formed by two atoms (**Figure 2.16a**), and its electronic band structure has been calculated to have a valence band formed by π state and a conduction band formed by anti-bond state. While this picture presents no difference in principle with organic semiconductors, the form of these bands is unusual. They are bent and in six point they touch each other's, forming the so called Dirac-points. (**Figure 2.16b**).[80]

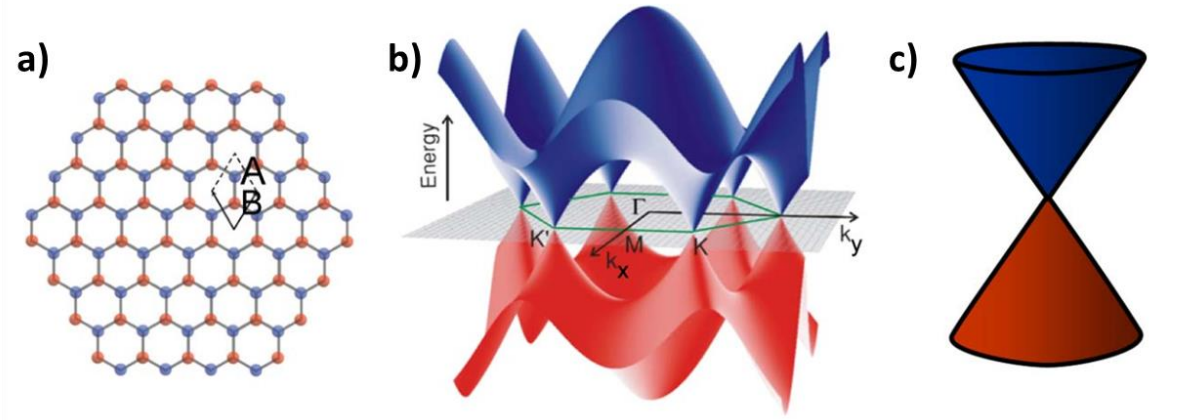

Figure 2.16 a) honeycomb structure of graphene, highlighting the two atoms forming the unit cell. b) Electronic band-structure in the Brillouin zone in red valence band and in blue the conduction band. , c) Dirac point at low energy. Adapted from Ref [80]

Because of this graphene is called a semimetal or zero band gap semiconductor. Symmetric considerations imply that we can describe these six points with two independent point K and K' that are at the limit of the Brillouin zone (the primitive cell in the reciprocal space).[80] At low energy, they are basically two cones mirrored touching their tips at the Dirac point and the symmetry of the band structure allows for conduction of both holes and electrons.[75]

The valence and conduction bands touch at the K and K' point. Because of this reason, the Hamiltonian that describes the band structures near the K(') points is a 2-D Dirac relativistic one. Graphene charge carriers are thus Dirac fermions that behave like massless particles.[81] This means that a very high carrier mobility should be expected and, indeed, a value of 10^5 $cm^2V^{-1}s^{-1}$ has been measured.[82]

This theory is valid for single infinite perfect sheet of graphene. Presence of multilayers, folding, defects and stacking, introduce scattering and increase or decrease overlap between bands, drastically changing transport regimes.[83]

2.5.3 Liquid Phase Exfoliated graphene

Graphene can be produced using different methods and each one presents advantages and disadvantages. Graphene was first isolated by abrupt detachment of graphene layer from graphite, in a process called mechanical exfoliation.[84] This method allows to obtain best quality graphene, in terms of defect, size, and purity. On the other hand is not suitable for mass scale

production.[84] Chemical vapor deposition is another strategy, which lead to high quality graphene, but transfer process to actual substrate in complex and lead to impurities to the final transfer sample.[85] On the other hand, liquid phase exfoliation produces high quantity of graphene. The so obtained graphene is not all single layer and its lateral size is difficulty over 1 µm. Anyhow it is an easily scalable method, with high yield and more important it produces solution of dispersed graphene that can be easily processed.[86] This method consists in dispersion of graphite in a solvent, exfoliation by ultra-sonication that produces cavitation of bubbles and thus acts as a force on bulk material to exfoliate it. Finally a purification step is carried out by centrifugation, to get rid of heavy multilayer not exfoliated chunks.[86] Surfactants can be used in order to enhance exfoliation yield and quality.[87]

2.5.4 Graphene based transistors

Very high carrier mobility has been measured for graphene transistor. A basic graphene transistor, with two contacts on a graphene mechanical exfoliated posed on a gate dielectric, has an ambipolar behavior as predicted by theory.[88] A gate bias shifts the Fermi level and thus electron transport or hole is enhanced if the voltage is positive or negative respectively. A typical curves representing resistivity dependence on gate voltage is reported in **Figure 2.17**

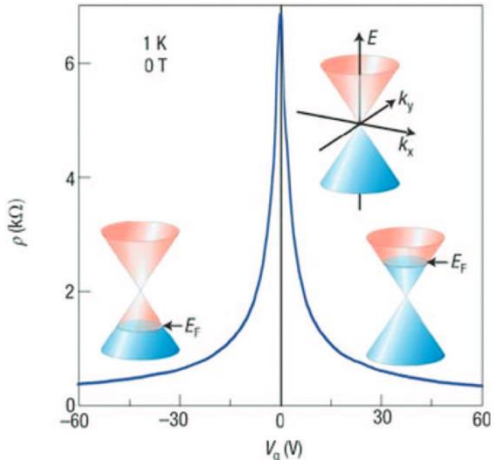

Figure 2.17 Diagram representing ideal ambipolar behavior due to field effect in graphene transistors. For each stage, i.e. p-type, Dirac point, n-type schematic representation of Fermi energy with respect to Dirac point. Proposed from Ref [89]

At 0 V gate bias resistivity is maximum, *i.e.* the registered current is the minimum and is called Dirac point. Dirac point position is affected by doping, size and interfaces with electrodes. At negative voltage Fermi level drops below Dirac point and a significant population of holes is introduced in the valence band increasing p-type conduction. At positive voltage Fermi level rise over the Dirac point promoting electrons to the conduction band and thus enhancing n-type conduction.[89] One major drawback is that graphene based transistor cannot be turned off and hence are not suitable for logic application. [90] Different solutions have been proposed as scaling the size of graphene to open a band gap[91] and reducing graphene oxide. We

propose in this work the option to introduce liquid phase exfoliated graphene (LPE-G) in polymeric semiconductor thin film transistors in order to tune and improve charge transport and at the same time obtaining well working OTFTs that can be turn off.

2.6 CONCLUSIONS

In this chapter, a background on organic supramolecular semiconductors charge transport properties has been presented. Gold nanoparticles have been introduced with their optical, chemical and optical properties, as suitable nano-objects for bi-component devices. Interface effects between a semiconductor and a metal have hence been described. It has been stressed how surface functionalization can mediate interactions occurring the interfaces, allowing to add and tune properties. On this regards photochromic thiolated molecules are presented as a tool for multifunctional device. Finally, LPE-G has been introduced as an easy processable materials, for electronic hybrid applications.

2.7 REFERENCES

1. Farges, J. P., *Organic Conductors: Fundamentals and Applications*. CRC Press: 1994.
2. Brooks, J. S., Organic crystals: properties, devices, functionalization and bridges to bio-molecules. *Chem. Soc. Rev.* **2010,** *39*, 2667-2694.
3. Shirakawa, H.; Louis, E. J.; MacDiarmid, A. G.; Chiang, C. K.; Heeger, A. J., Synthesis of electrically conducting organic polymers: halogen derivatives of polyacetylene, (CH). *J. Chem. Soc., Chem. Commun.* **1977**, 578-580.
4. Noriega, R.; Rivnay, J.; Vandewal, K.; Koch, F. P. V.; Stingelin, N.; Smith, P.; Toney, M. F.; Salleo, A., A general relationship between disorder, aggregation and charge transport in conjugated polymers. *Nat Mater* **2013,** *12*, 1038-1044.
5. Noriega, R.; Salleo, A., Charge Transport Theories in Organic Semiconductors. In *Organic Electronics II*, Wiley-VCH Verlag GmbH & Co. KGaA: 2012; pp 67-104.
6. Zvyagin, I., Charge Transport via Delocalized States in Disordered Materials. In *Charge Transport in Disordered Solids with Applications in Electronics*, John Wiley & Sons, Ltd: 2006; pp 1-47.
7. Vissenberg, M. C. J. M.; Matters, M., Theory of the field-effect mobility in amorphous organic transistors. *Physical Review B* **1998,** *57*, 12964-12967.
8. Vukmirović, N.; Wang, L.-W., Carrier hopping in disordered semiconducting polymers: How accurate is the Miller–Abrahams model? *Appl. Phys. Lett.* **2010,** *97*, 043305.
9. Coropceanu, V.; Cornil, J.; da Silva Filho, D. A.; Olivier, Y.; Silbey, R.; Brédas, J.-L., Charge Transport in Organic Semiconductors. *Chem. Rev.* **2007,** *107*, 926-952.
10. Troisi, A.; Orlandi, G., Dynamics of the Intermolecular Transfer Integral in Crystalline Organic Semiconductors. *J. Phys. Chem. A* **2006,** *110*, 4065-4070.
11. Rivnay, J.; Noriega, R.; Northrup, J. E.; Kline, R. J.; Toney, M. F.; Salleo, A., Structural origin of gap states in semicrystalline polymers and the implications for charge transport. *Physical Review B* **2011,** *83*, 121306.
12. Scharsich, C.; Lohwasser, R. H.; Sommer, M.; Asawapirom, U.; Scherf, U.; Thelakkat, M.; Neher, D.; Köhler, A., Control of aggregate formation in poly(3-hexylthiophene) by solvent, molecular weight, and synthetic method. *J. Polym. Sci., Part B: Polym. Phys.* **2012,** *50*, 442-453.
13. Zaumseil, J., P3HT and Other Polythiophene Field-Effect Transistors. In *P3HT Revisited – From Molecular Scale to Solar Cell Devices*, Ludwigs, S., Ed. Springer Berlin Heidelberg: 2014; Vol. 265, pp 107-137.
14. Olivier, Y.; Niedzialek, D.; Lemaur, V.; Pisula, W.; Müllen, K.; Koldemir, U.; Reynolds, J. R.; Lazzaroni, R.; Cornil, J.; Beljonne, D., 25th Anniversary Article: High-Mobility Hole and Electron Transport Conjugated Polymers: How Structure Defines Function. *Adv. Mater.* **2014,** *26*, 2119-2136.
15. Tremel, K.; Ludwigs, S., Morphology of P3HT in Thin Films in Relation to Optical and Electrical Properties. In *P3HT Revisited – From Molecular Scale to Solar Cell Devices*, Ludwigs, S., Ed. Springer Berlin Heidelberg: 2014; Vol. 265, pp 39-82.
16. Brown, P. J.; Thomas, D. S.; Köhler, A.; Wilson, J. S.; Kim, J.-S.; Ramsdale, C. M.; Sirringhaus, H.; Friend, R. H., Effect of interchain interactions on the absorption and emission of poly(3-hexylthiophene). *Physical Review B* **2003,** *67*, 064203.
17. Zen, A.; Saphiannikova, M.; Neher, D.; Grenzer, J.; Grigorian, S.; Pietsch, U.; Asawapirom, U.; Janietz, S.; Scherf, U.; Lieberwirth, I.; Wegner, G., Effect of Molecular Weight on the Structure and Crystallinity of Poly(3-hexylthiophene). *Macromolecules* **2006,** *39*, 2162-2171.
18. Kline, R. J.; McGehee, M. D.; Kadnikova, E. N.; Liu, J.; Fréchet, J. M. J., Controlling the Field-Effect Mobility of Regioregular Polythiophene by Changing the Molecular Weight. *Adv. Mater.* **2003,** *15*, 1519-1522.
19. Pearson, A. J.; Wang, T.; Dunbar, A. D. F.; Yi, H.; Watters, D. C.; Coles, D. M.; Staniec, P. A.; Iraqi, A.; Jones, R. A. L.; Lidzey, D. G., Morphology Development in Amorphous Polymer:Fullerene Photovoltaic Blend Films During Solution Casting. *Adv. Funct. Mater.* **2014,** *24*, 659-667.
20. Spano, F. C., Modeling disorder in polymer aggregates: The optical spectroscopy of regioregular poly(3-hexylthiophene) thin films. *J. Chem. Phys* **2005,** *122*, 234701.
21. Yan, H.; Chen, Z.; Zheng, Y.; Newman, C.; Quinn, J. R.; Dotz, F.; Kastler, M.; Facchetti, A., A high-mobility electron-transporting polymer for printed transistors. *Nature* **2009,** *457*, 679-686.

22. Luzio, A.; Criante, L.; D'Innocenzo, V.; Caironi, M., Control of charge transport in a semiconducting copolymer by solvent-induced long-range order. *Sci. Rep.* **2013,** *3*.
23. Rivnay, J.; Toney, M. F.; Zheng, Y.; Kauvar, I. V.; Chen, Z.; Wagner, V.; Facchetti, A.; Salleo, A., Unconventional Face-On Texture and Exceptional In-Plane Order of a High Mobility n-Type Polymer. *Adv. Mater.* **2010,** *22*, 4359-4363.
24. de Leeuw, D. M.; Simenon, M. M. J.; Brown, A. R.; Einerhand, R. E. F., Stability of n-type doped conducting polymers and consequences for polymeric microelectronic devices. *Synth. Met.* **1997,** *87*, 53-59.
25. Rivnay, J.; Steyrleuthner, R.; Jimison, L. H.; Casadei, A.; Chen, Z.; Toney, M. F.; Facchetti, A.; Neher, D.; Salleo, A., Drastic Control of Texture in a High Performance n-Type Polymeric Semiconductor and Implications for Charge Transport. *Macromolecules* **2011,** *44*, 5246-5255.
26. Wetzelaer, G.-J. A. H.; Kuik, M.; Olivier, Y.; Lemaur, V.; Cornil, J.; Fabiano, S.; Loi, M. A.; Blom, P. W. M., Asymmetric electron and hole transport in a high-mobility n-type conjugated polymer. *Physical Review B* **2012,** *86*, 165203.
27. Baeg, K.-J.; Khim, D.; Jung, S.-W.; Kang, M.; You, I.-K.; Kim, D.-Y.; Facchetti, A.; Noh, Y.-Y., Remarkable Enhancement of Hole Transport in Top-Gated N-Type Polymer Field-Effect Transistors by a High-k Dielectric for Ambipolar Electronic Circuits. *Adv. Mater.* **2012,** *24*, 5433-5439.
28. Lei, T., Ambipolar Polymer Field-Effect Transistors Based on Functionalized Isoindigo. In *Design, Synthesis, and Structure-Property Relationship Study of Polymer Field-Effect Transistors*, Springer Berlin Heidelberg: 2015; pp 59-79.
29. Lei, T.; Cao, Y.; Fan, Y.; Liu, C.-J.; Yuan, S.-C.; Pei, J., High-Performance Air-Stable Organic Field-Effect Transistors: Isoindigo-Based Conjugated Polymers. *J. Am. Chem. Soc.* **2011,** *133*, 6099-6101.
30. Lei, T., Side Chain Effects and Design of Isoindigo-Based Polymers. In *Design, Synthesis, and Structure-Property Relationship Study of Polymer Field-Effect Transistors*, Springer Berlin Heidelberg: 2015; pp 23-57.
31. Freestone, I.; Meeks, N.; Sax, M.; Higgitt, C., The Lycurgus Cup — A Roman nanotechnology. *Gold Bulletin* **2007,** *40*, 270-277.
32. Faraday, M., The Bakerian Lecture: Experimental Relations of Gold (and Other Metals) to Light. *Philos. Trans. R. Soc.* **1857,** *147*, 145-181.
33. Eustis, S.; El-Sayed, M. A., Why gold nanoparticles are more precious than pretty gold: Noble metal surface plasmon resonance and its enhancement of the radiative and nonradiative properties of nanocrystals of different shapes. *Chem. Soc. Rev.* **2006,** *35*, 209-217.
34. Kubo, R., Electronic Properties of Metallic Fine Particles. I. *J. Phys. Soc. Jpn.* **1962,** *17*, 975-986.
35. Edwards, P. P.; R. L, J.; Rao, C. N. R.; Tunstall, D. P.; Hensel, F., The metal–insulator transition: a perspective. *Phil. Trans. R. Soc. A* **1998,** *356*, 5-22.
36. Edwards, P. P.; Johnston, R. L.; Rao, C. N. R., On the Size-Induced Metal-Insulator Transition in Clusters and Small Particles. In *Metal Clusters in Chemistry*, Wiley-VCH Verlag GmbH: 2008; pp 1454-1481.
37. L.P. Gor'kov, G. M. E., Minute Metallic Particles in an Electromagnetic Field *J. Exp. Theor. Phys.* **1965,** *21*, 940-647.
38. Mie, G., A contribution to the optics of turbid media, especially colloidal metallic suspensions,. *Ann. Phys.* **1908,** *25*, 377-455.
39. Alex, S.; Tiwari, A., Functionalized Gold Nanoparticles: Synthesis, Properties and Applications—A Review. *J. Nanosci. Nanotechnol.* **2015,** *15*, 1869-1894.
40. Perenboom, J. A. A. J.; Wyder, P.; Meier, F., Electronic properties of small metallic particles. *Phys. Rep.* **1981,** *78*, 173-292.
41. Mosciatti, T.; Orgiu, E.; Raimondo, C.; Samori, P., The role of size and coating in Au nanoparticles incorporated into bi-component polymeric thin-film transistors. *Nanoscale* **2014,** *6*, 5075-5080.
42. Bigioni, T. P.; Whetten, R. L.; Dag, Ö., Near-Infrared Luminescence from Small Gold Nanocrystals. *J. Phys. Chem. B* **2000,** *104*, 6983-6986.
43. Bahrig, L.; Hickey, S. G.; Eychmuller, A., Mesocrystalline materials and the involvement of oriented attachment - a review. *Cryst. Eng. Comm* **2014,** *16*, 9408-9424.
44. Turkevich, J.; Stevenson, P. C.; Hillier, J., A study of the nucleation and growth processes in the synthesis of colloidal gold. *Farad. Discuss.* **1951,** *11*, 55-75.
45. Hakkinen, H., The gold-sulfur interface at the nanoscale. *Nat. Chem.* **2012,** *4*, 443-455.
46. Frenkel, A. I.; Nemzer, S.; Pister, I.; Soussan, L.; Harris, T.; Sun, Y.; Rafailovich, M. H., Size-controlled synthesis and characterization of thiol-stabilized gold nanoparticles. *J. Chem. Phys* **2005,** *123*, 184701.
47. Prasad, B. L. V.; Stoeva, S. I.; Sorensen, C. M.; Klabunde, K. J., Digestive Ripening of Thiolated Gold Nanoparticles: The Effect of Alkyl Chain Length. *Langmuir* **2002,** *18*, 7515-7520.
48. Natali, D.; Caironi, M., Charge Injection in Solution-Processed Organic Field-Effect Transistors: Physics, Models and Characterization Methods. *Adv. Mater.* **2012,** *24*, 1357-1387.
49. Cahen, D.; Kahn, A.; Umbach, E., Energetics of molecular interfaces. *Mater. Today* **2005,** *8*, 32-41.
50. Vitaly, P., Charge Carrier Transport in Single-Crystal Organic Field-Effect Transistors. In *Organic Field-Effect Transistors*, CRC Press: 2007; pp 27-72.
51. Liu, C.; Xu, Y.; Noh, Y.-Y., Contact engineering in organic field-effect transistors. *Mater. Today* **2015,** *18*, 79-96.
52. Love, J. C.; Estroff, L. A.; Kriebel, J. K.; Nuzzo, R. G.; Whitesides, G. M., Self-Assembled Monolayers of Thiolates on Metals as a Form of Nanotechnology. *Chem. Rev.* **2005,** *105*, 1103-1170.
53. Vericat, C.; Vela, M. E.; Benitez, G.; Carro, P.; Salvarezza, R. C., Self-assembled monolayers of thiols and dithiols on gold: new challenges for a well-known system. *Chem. Soc. Rev.* **2010,** *39*, 1805-1834.
54. Heimel, G.; Romaner, L.; Zojer, E.; Bredas, J.-L., The Interface Energetics of Self-Assembled Monolayers on Metals. *Acc. Chem. Res.* **2008,** *41*, 721-729.
55. Ho Choi, S.; Kim, B.; Frisbie, C. D., Electrical Resistance of Long Conjugated Molecular Wires. *Science* **2008,** *320*, 1482-1486.
56. Chua, L.-L.; Zaumseil, J.; Chang, J.-F.; Ou, E. C. W.; Ho, P. K. H.; Sirringhaus, H.; Friend, R. H., General observation of n-type field-effect behaviour in organic semiconductors. *Nature* **2005,** *434*, 194-199.
57. Kobayashi, S.; Nishikawa, T.; Takenobu, T.; Mori, S.; Shimoda, T.; Mitani, T.; Shimotani, H.; Yoshimoto, N.; Ogawa, S.; Iwasa, Y., Control of carrier density by self-assembled monolayers in organic field-effect transistors. *Nat Mater* **2004,** *3*, 317-322.
58. Virkar, A., Organic Semiconductor Growth and Transistor Performance as a Function of the Density of the Octadecylsilane Dielectric Modification Layer. In *Investigating the Nucleation, Growth, and Energy Levels of Organic Semiconductors for High Performance Plastic Electronics*, Virkar, A., Ed. Springer: 2012; pp 51-67.
59. Tseng, C.-W.; Huang, D.-C.; Tao, Y.-T., Azobenzene-Functionalized Gold Nanoparticles as Hybrid Double-Floating-Gate in Pentacene Thin-Film Transistors/Memories with Enhanced Response, Retention, and Memory Windows. *ACS Appl. Mater. Interfaces* **2013,** *5*, 9528-9536.
60. Li, J.; Speyer, G.; Sankey, O. F., Conduction Switching of Photochromic Molecules. *Phys. Rev. Lett.* **2004,** *93*, 248302.
61. Irie, M.; Fukaminato, T.; Matsuda, K.; Kobatake, S., Photochromism of Diarylethene Molecules and Crystals: Memories, Switches, and Actuators. *Chem. Rev.* **2014,** *114*, 12174-12277.
62. Orgiu, E.; Samorì, P., 25th Anniversary Article: Organic Electronics Marries Photochromism: Generation of Multifunctional Interfaces, Materials, and Devices. *Adv. Mater.* **2014,** *26*, 1827-1845.

63. Irie, M.; Mohri, M., Thermally irreversible photochromic systems. Reversible photocyclization of diarylethene derivatives. *J. Org. Chem.* **1988,** *53*, 803-808.
64. Dulić, D.; van der Molen, S. J.; Kudernac, T.; Jonkman, H. T.; de Jong, J. J. D.; Bowden, T. N.; van Esch, J.; Feringa, B. L.; van Wees, B. J., One-Way Optoelectronic Switching of Photochromic Molecules on Gold. *Phys. Rev. Lett.* **2003,** *91*, 207402.
65. Ikeda, M.; Tanifuji, N.; Yamaguchi, H.; Irie, M.; Matsuda, K., Photoswitching of conductance of diarylethene-Au nanoparticle network. *Chem. Commun.* **2007**, 1355-1357.
66. Hayakawa, R.; Higashiguchi, K.; Matsuda, K.; Chikyow, T.; Wakayama, Y., Optically and Electrically Driven Organic Thin Film Transistors with Diarylethene Photochromic Channel Layers. *ACS Appl. Mater. Interfaces* **2013,** *5*, 3625-3630.
67. van der Molen, S. J.; Liljeroth, P., Conductance Properties of Switchable Molecules. In *Molecular Switches*, Wiley-VCH Verlag GmbH & Co. KGaA: 2011; pp 719-777.
68. Perrier, A.; Maurel, F.; Aubard, J., Theoretical Study of the Electronic and Optical Properties of Photochromic Dithienylethene Derivatives Connected to Small Gold Clusters. *J. Phys. Chem. A* **2007,** *111*, 9688-9698.
69. Kudernac, T.; van der Molen, S. J.; van Wees, B. J.; Feringa, B. L., Uni- and bi-directional light-induced switching of diarylethenes on gold nanoparticles. *Chem. Commun.* **2006**, 3597-3599.
70. Bandara, H. M. D.; Burdette, S. C., Photoisomerization in different classes of azobenzene. *Chem. Soc. Rev.* **2012,** *41*, 1809-1825.
71. Forber, C. L.; Kelusky, E. C.; Bunce, N. J.; Zerner, M. C., Electronic spectra of cis- and trans-azobenzenes: consequences of ortho substitution. *J. Am. Chem. Soc.* **1985,** *107*, 5884-5890.
72. Howard, E. Z., Di-π-Methane Rearrangement. In *CRC Handbook of Organic Photochemistry and Photobiology, Third Edition - Two Volume Set*, CRC Press: 2012; pp 511-525.
73. Fujino, T.; Arzhantsev, S. Y.; Tahara, T., Femtosecond Time-Resolved Fluorescence Study of Photoisomerization of trans-Azobenzene. *J. Phys. Chem. A* **2001,** *105*, 8123-8129.
74. Natansohn, A.; Rochon, P., Photoinduced Motions in Azo-Containing Polymers. *Chem. Rev.* **2002,** *102*, 4139-4176.
75. Castro Neto, A. H.; Guinea, F.; Peres, N. M. R.; Novoselov, K. S.; Geim, A. K., The electronic properties of graphene. *Reviews of Modern Physics* **2009,** *81*, 109-162.
76. Petroski, H., *The Pencil: A History of Design and Circumstance*. Knopf: New York, 1989.
77. Schafhaeutl, C., Ueber die Verbindungen des Kohlenstoffes mit Silicium, Eisen und andern Metallen, welche die verschiedenen Arten von Gusseisen, Stahl und Schmiedeeisen bilden. *J. Prakt. Chem.* **1840,** *19*, 159-174.
78. Geim, A. K.; Novoselov, K. S., The rise of graphene. *Nat Mater* **2007,** *6*, 183-191.
79. Wallace, P. R., The Band Theory of Graphite. *Physical Review* **1947,** *71*, 622-634.
80. Yanqing, W.; Farmer, D. B.; Fengnian, X.; Avouris, P., Graphene Electronics: Materials, Devices, and Circuits. *Proc. IEEE* **2013,** *101*, 1620-1637.
81. Geim, A. K., Graphene: Status and Prospects. *Science* **2009,** *324*, 1530-1534.
82. Bolotin, K. I.; Sikes, K. J.; Jiang, Z.; Klima, M.; Fudenberg, G.; Hone, J.; Kim, P.; Stormer, H. L., Ultrahigh electron mobility in suspended graphene. *Solid State Commun.* **2008,** *146*, 351-355.
83. Terrones, M.; Botello-Méndez, A. R.; Campos-Delgado, J.; López-Urías, F.; Vega-Cantú, Y. I.; Rodríguez-Macías, F. J.; Elías, A. L.; Muñoz-Sandoval, E.; Cano-Márquez, A. G.; Charlier, J.-C.; Terrones, H., Graphene and graphite nanoribbons: Morphology, properties, synthesis, defects and applications. *Nano Today* **2010,** *5*, 351-372.
84. Novoselov, K. S.; Jiang, D.; Schedin, F.; Booth, T. J.; Khotkevich, V. V.; Morozov, S. V.; Geim, A. K., Two-dimensional atomic crystals. *Proc. Natl. Acad. Sci.* **2005,** *102*, 10451-10453.
85. Kim, K. S.; Zhao, Y.; Jang, H.; Lee, S. Y.; Kim, J. M.; Kim, K. S.; Ahn, J.-H.; Kim, P.; Choi, J.-Y.; Hong, B. H., Large-scale pattern growth of graphene films for stretchable transparent electrodes. *Nature* **2009,** *457*, 706-710.
86. Ciesielski, A.; Samori, P., Graphene via sonication assisted liquid-phase exfoliation. *Chem. Soc. Rev.* **2014,** *43*, 381-398.
87. Ciesielski, A.; Haar, S.; El Gemayel, M.; Yang, H.; Clough, J.; Melinte, G.; Gobbi, M.; Orgiu, E.; Nardi, M. V.; Ligorio, G.; Palermo, V.; Koch, N.; Ersen, O.; Casiraghi, C.; Samorì, P., Harnessing the Liquid-Phase Exfoliation of Graphene Using Aliphatic Compounds: A Supramolecular Approach. *Angew. Chem. Int. Ed.* **2014,** *53*, 10355-10361.
88. Novoselov, K. S.; Geim, A. K.; Morozov, S. V.; Jiang, D.; Zhang, Y.; Dubonos, S. V.; Grigorieva, I. V.; Firsov, A. A., Electric Field Effect in Atomically Thin Carbon Films. *Science* **2004,** *306*, 666-669.
89. Allen, M. J.; Tung, V. C.; Kaner, R. B., Honeycomb Carbon: A Review of Graphene. *Chem. Rev.* **2010,** *110*, 132-145.
90. Schwierz, F., Graphene transistors. *Nat Nano* **2010,** *5*, 487-496.
91. Chen, Y.-C.; de Oteyza, D. G.; Pedramrazi, Z.; Chen, C.; Fischer, F. R.; Crommie, M. F., Tuning the Band Gap of Graphene Nanoribbons Synthesized from Molecular Precursors. *ACS Nano* **2013,** *7*, 6123-6128.

3. Methods and experimental techniques

The main objective of this work is to design and study nanostructured systems for supramolecular electronics applications. Organic film transistor (OTFT) is the main tool used for gaining insight into the electrical characteristics of multicomponent nanostructured materials via controlling their order at the supramolecular level and their interfaces with metallic electrodes and dielectric surfaces. The key OTFT parameters such as mobility and threshold voltage, will be evaluated and their dependence on the bulk and interfaces properties explored. The integration of stimuli-responsive molecules as one of the components (either within a blend or as interface functionalization) will offer the possibility of modulate these parameters with an additional external input like light. In this framework, the main objective of this thesis work is the realization of efficient multifunctional devices. A key factor for optimizing nano-structured supramolecular functionalized systems is to understand different energetic interactions between the employed components. Towards this end, ambient photoelectron spectroscopy and Kelvin Probe will be used gaining a quantification on work function and ionization energy. For casting light onto the order at the supramolecular level and interaction between the different components, both UV-Vis spectroscopy and atomic force microscopy have been used.

3.1 ORGANIC THIN FILM TRANSISTORS

3.1.1 OTFT introduction

Organic Thin Film Transistors (OTFTs) are a powerful tool to study bulk semiconductor when interfaced with metallic electrodes and dielectric surfaces. They are three-terminal devices were the output parameter, called the drain current, can be tuned by applying two different voltages, *i.e*. the drain and the gate voltages (transistor effect). The gate electrode makes it possible to directly and precisely control the charge density in the channel as induced by electrostatic coupling. The drain-source voltage generates an electric field that allows drifting of the charges towards the electrodes which collect (drain) or inject (source) the current. The gate electrode is separated from the active channel by a dielectric layer and this allows charge accumulation within the channel according to a different physical principle as seen in inorganic (silicon) devices where a population inversion has to be induced. OTFT operate in

the so-called accumulation regime where a charge of opposite sign with respect to the gate potential is capacitively induced within the device channel. The active layer is composed by a semiconductor deposited by vacuum sublimation or solution casting and is in direct contact with two ohmic electrodes. With respect to source-drain contacts geometry, two parameter are defined: the width (W) and their distance that is named channel length (L). OTFT typical scheme is reported in **Figure 3.1.**

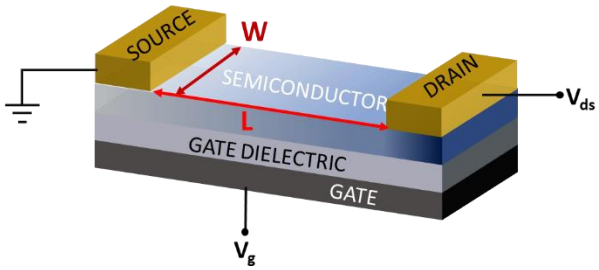

Figure 3.1 Structure of an OTFT. W is channel width and L is channel length. V_{ds} and V_g are applied drain and gate biases respectively.

Gate dielectric is an insulating layer completely covering the gate electrode. It is generally composed by SiO_2 or a polymer dielectric such as PMMA, PVA, PVP, PS. A dielectric material must withstand electric fields of at least 2 $MVcm^{-1}$withoht breaking, having good insulating property and low surface roughness.[1] The gate electrode is made by highly doped conductive silicon whilst other metals such as Al, Au, Ag, Pd, Cu, Ni or conductive polymers such as PANI or PEDOT:PSS can be employed for the same purpose and in different geometries. As seen for the gate electrode, the source and drain electrodes are made of noble metals like gold or silver or conducting polymers like PEDOT-PSS. In order to have flexible substrate usually a support of plastic is used, and dielectric is made by an organic insulating polymer like PET and PEN. Different geometries exist for OTFT.

3.1.2 OTFT Geometries

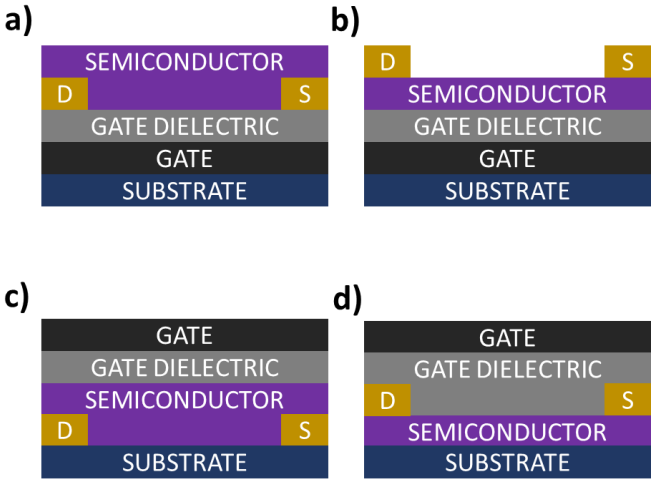

Figure 3.2 Typical OTFT geometries. a) bottom-gate/bottom-contact, b) bottom-gate/top-contact, c) bottom-contact/top-gate and d) top-contact/top-gate

Figure 3.2 portrays the four possible OTFT geometries. Bottom-contact, bottom-gate is the typical choice for studying semiconductor properties since they are the easiest to prepare. The semiconductor is usually deposited on pre-deposited (*via* evaporation or with lithography) source-drain electrodes on a high quality dielectric surface. Top-contact bottom-gate geometry is most useful when gate surface is decorated with nanostructures and in order to reduce contact resistance, since evaporated top electrode form a better physical contact. Finally top gate geometry with top or bottom electrodes reduces contact resistance and it can be built on top of a transparent substrate. Also it allows to easily deposit a chosen dielectric on top of the semiconductor and automatically encapsulating it.[2] Geometry has a big influence in contact resistance. As discussed in Chapter 2, contact resistance arises from the formation of a Schottky barrier at the metal/semiconductor interface. The bottom-contact geometry presents a higher contact resistance with respect to top-contact one. This is mainly due to the different contact area involved in charge injection. In bottom-contact devices injection area is reduced at just the first nm close to the gate dielectric while in top-contact devices all the electrodic area is involved in the process of injection of charges.[3]

Albeit it has an effect on contact resistance, the transistor's geometry does not change the general working principle of the OTFT. Charges are generated at the semiconductor/dielectric interfaces when a bias is applied to the gate voltage. When a voltage bias is applied between the source and the drain the charges move towards appropriate electrode, generating a current.

A semiconductive polymer can be chosen being p- or n-type. This means that it transport mainly holes or electrons, respectively. In the p-type the applied gate bias must be negative to generate appropriates charge carriers, and negative for the n-type polymer. When in the opposite situation (positive for p-type and negative for n-type) they are in the off-state. Since OTFTs work in accumulation regime, if the polymeric semiconductor is ambipolar, and it will behave like an n-type semiconductor under a positive gate bias and p-type under a negative one.

3.1.3 OTFT working principles

OTFT core (gate electrode and the gate dielectric) can be considered a plane capacitor. As previously described, when a bias is applied to the gate, carriers of opposite sign are generated at the dielectric/semiconductor interface. The amount of charges generated is proportional to the dielectric capacitance and to the applied gate voltage. A conductive channel is hence formed. By applying a bias between source-drain electrodes charges are induced to move and a current is measured.[4] It must be considered that organic semiconductors contains a not-negligible number of traps in the channel. They arise both from the interface between the polymer and the gate dielectric surface and from the intrinsic defective structural nature of the semiconducting material as discussed in Chapter 2. Because of this, a part of charges generated by applying a gate bias have the role of filling traps at the interface and a current is registered when gate voltage (V_g) is higher than the so-called threshold voltage (V_{th}), which is the voltage

value beyond which the conducting channel is formed.[5] When a bias is applied to the source-drain (V_{ds}) a current start flowing. If V_{ds} is lower than V_g-V_{th} the dependence of the current I_d is linear to V_g and $V_{ds.}$, as reported in **Equation 3.1.**[4]

$$I_{ds} = \frac{W}{L} C_i \mu \left(V_g - V_{th} - \frac{V_{ds}}{2}\right) V_d \qquad 3.1$$

C_i is dielectric capacitance (per area unit) and μ is the field-effect mobility.

When V_{ds}=V_g-V_{th} a point is reached in which the channel is "pinched off". An area depleted by charges is hence formed, called depletion region. At this point I_{ds} becomes independent from the gate bias. This is called saturation regime and I_{ds} is given by **Equation 3.2.**[4]

$$I_{ds} = \frac{W}{2L} C_i \mu \left(V_g - V_{th}\right)^2 \qquad 3.2$$

3.1.4 Characterization and parameter extraction

Two different types of measurements of (drain) current - voltage are possible when working with three-terminal field-effect devices. I_{ds} *vs.* V_{ds} called output curve and I_{ds} *vs.* V_g called transfer curve. Output curves are recorded upon sweeping V_{ds} and applying various constant bias to V_g at each trace. The first part of the plot exhibits a linear regime and then saturation regime is observed as depicted in **Figure 3.3a.**

Transfer curve is traced by sweeping the V_g at various constant V_{ds} bias as depicted in **Figure 3.3b.**

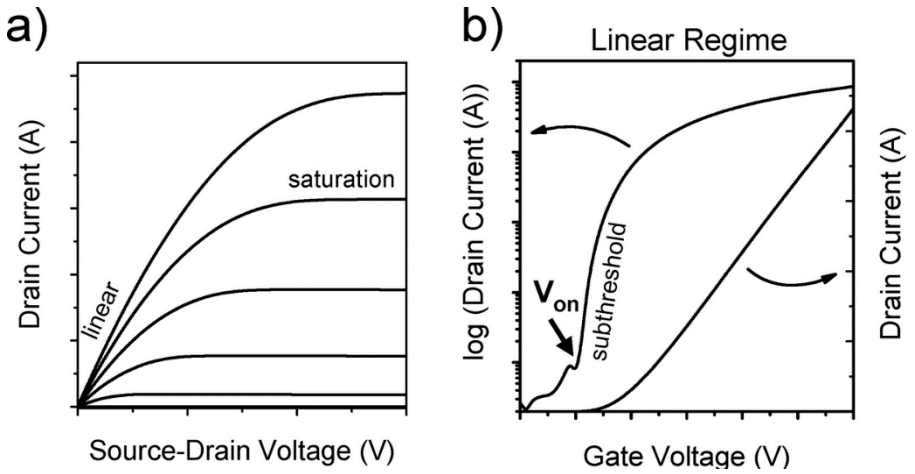

Figure 3.3 Typical a) output curve and b) transfer curve for OTFT. b) is reported on linear and log scale. Adapted from Ref[4]

From these curves it is possible to extract several important parameters such mobility, threshold voltage and I_{on}/I_{off} ratio which are presented in detail in the following sections.

3.1.4.1 Mobility

Charge carriers mobility is defined as the average drift velocity of a charge under an applied electric field (**Equation 3.3**).[6]

$$\mu = \frac{v_d}{\boldsymbol{E}} \qquad 3.3$$

Hence mobility unit is $cm^2V^{-1}s^{-1}$.From **Equations 3.1** and **3.2** is possible to extrapolate mobility for linear and saturation regime respectively as showed in **Equations 3.4** and **3.5.**

$$\mu_{lin} = \left(\frac{\partial I_{ds}}{\partial V_g}\right)\left(\frac{L}{W}\right)\left(\frac{1}{C_{insulator}}\right)\left(\frac{1}{|V_{ds}|}\right) \quad 3.4$$

$$\mu_{sat} = \frac{2L}{WC_{insulator}}\left(\frac{\partial\sqrt{|I_{ds}|}^2}{\partial V_g}\right) \quad 3.5$$

Mobility is strictly correlated to semiconductor properties. While it is an intrinsic properties for a given semiconductor, the measured mobility in a device can be affected by the deposition techniques , the semiconductor morphology, [7,8] eventual interface functionalization (e.g. SAM), and contact resistance[9]

3.1.4.2 Threshold voltage

As mentioned above, the voltage beyond which a conductive channel starts to be formed is called threshold voltage (V_{th}). It discriminates the regime of operation, being in *on* or *off* state. It can be extracted by linear regression of the I_{ds} current for liner regime and from the linear regression of the square root of saturation current for saturation regime. In an ideal system V_{th} should be 0. Shifts form this value can be ascribed to the presence of traps at the semiconductor/dielectric interface[10]. It is therefore a powerful parameter to estimate the presence of traps that stem from both the semiconductor bulk and the dielectric/semiconductor interfaces.[6] V_{th} value is directly related to the number of traps by the **Equation 3.6**

$$V_{th} \approx \frac{eN_{trap}}{C_{insulator}} \quad 3.6$$

The fundamental charge is indicated as *e*, N_{trap} is the number of traps and $C_{insulator}$ is the capacitance of the dielectric. This means that the number of traps presented in the channel are directly proportional with V_{th} and more important to estimate this number it is not needed a detailed knowledge of trap distribution or nature.

3.1.4.3 Ion/Ioff

The I_{on}/I_{off} ratio is defined as the ratio between the I_{ds} registered in the *on* state and I_{ds} flowing in *off* state at a given V_g. Indeed, a high I_{on}/I_{off} ratio is a very looked-for parameter in OTFTs. It can be measured both from transfer and output curves. It depends mainly of device mobility, but can be also influenced by the dielectric capacitance and the semiconductor thickness.[5]

3.2 OTFT PREPARATION AND CHARACTERIZATION

3.2.1 Solution processed depositions

A major advantage of organic semiconductor is the possibility to deposit them by solution casting. Solution casting can be done quickly in ambient pressure. This is one of the major differences from vacuum deposition, the latter requiring long time to achieve deposition. Usually a solution of the chosen polymer is deposited on the substrate. Key factors for a controlled solution casting include: *(i)* polymer properties like molecular weight, backbone, side chains, and regio-regularity. *(ii)* Solvent properties like boiling point and solubility of the polymers. *(iii)* Processing and post-processing conditions like the environment the deposition is carried out and post-annealing substrate treatments etc. All these parameters are key factors determining the degree of crystallinity within the material. [6]

The most basic solution processing method is **drop-casting**, which consists of dropping a polymer solution onto the substrate. The evaporation of the solvent occurs spontaneously or in case of low-volatile solvents it can be assisted by thermal annealing. The main advantage of drop-casting is that the whole amount of material deposited remains on the substrate surface. However, the main disadvantage is that the control over the film thickness, orientation and uniformity is limited. Among various reasons, hydrodynamic forces can lead to the formation of coffee rings during solvent evaporation, in which a capillary flow from the center to the edge is induced to replenish liquid evaporating. This results in the accumulation of material at the perimeter.[11] Coffee rings are suppressed if the solute is fully soluble or if the solute is anisotropic.[11]

The most used method is **spin-casting**, known also as **spin-coating**. In this method the substrate is hold by vacuum or magnetic forces on a spin-coater. A solution is applied to the substrate surface and the latter is spinned with a speed that varies from few hundreds of rounds (rpm) to several thousand turns per minute. Most of the solution is swept off from the surface. This method allow to have a good control over the film thickness, which depends on the concentration of employed solution and spin-coating speed. The major advantage of this technique is the possibility of generating homogenously coated films obtained on areas of several cm^2, at the expenses of losing the greatest part of the solution.[12] Thermal annealing of the film can be carried out to ensure complete solvent evaporation; it can also have a beneficial effect on improving the long-range order within the film.[13] All the spin-coating depositions performed in this work has been performed in nitrogen atmosphere, except in Chapter 8.

3.3 Devices fabrication and characterization

3.3.1 Pre-patterned OTFT

In the work presented in chapter 4-5 we have used pre-patterned gold electrodes supported on silicon oxide surface, on which a polymer and polymer/AuNPs solution have been spin-cast. These substrates are composed by 230 nm thick silicon oxide ($C=1.5\cdot10^{-8}$ Fcm^{-2}) thermally grown on a n++ doped conductive silicon, which is the gate electrode. The electrodes are 30 nm thick gold layer on 10 nm ITO adhesion layer. They are interdigitated, with the same channel width W= 1 cm and with four channel lengths: L = (20, 10, 5, 2.5) μm. For each channel length there are 4 transistors. After cleaning by sonication these substrates are used as support for spincasting. Complete details are given in the chapters.

3.3.2 Employed bottom-contact/top gate and top –contact OTFT

Interdigitated gold electrodes have been evaporated in high vacuum on quartz using a mask. Each mask has 4 channel lengths (120, 100, 80, 60 μm) with two devices per each length and W= 1 cm for each device. On this substrates first the semiconductor, then Cytop (C_r = 2.1) have been spincasted. An aluminum electrode has been evaporated on the top using an appropriate mask. Conversely, top-contact devices were prepared by evaporating gold electrodes on the top of a semiconducting film deposited on a silicon oxide layer thermally grown on n++ doped silicon electrode.

3.3.3 Electrodes evaporation

Both top-contact/bottom-gate and top-gate electrodes employed in this work have been evaporated under vacuum. Source-drain electrodes were made by evaporating gold. A chromium adhesion layer has been evaporated between gold and the substrate in bottom-contact device to improve gold/quartz grip. Aluminum has been used as top-gate electrode, since it does not diffuse into the dielectric polymer layer as gold. All evaporation procedures followed the same steps. The metal is placed at the bottom of the evaporator in a crucible. The substrate is put face-down at the top with appropriate mask on top. Vacuum is achieved with a system consisting in a primary pump and a secondary turbo molecular pump. When the pressure is below 10^{-6} mbar, the crucible is heated and metal evaporates, ideally in straight line up to the sample. The thickness of the evaporated layer is followed using a quartz microbalance.

3.3.4 Electrical Characterization

OTFT characterization was performed in nitrogen environment. A probe station (Cascade Microtech M150) has been used. The central plate was connected the gate electrode in bottom-gate devices. Two fingers Suss probes were used to connect the source-drain contacts. A Keithley 2636A was used to apply and measure voltage and current. Top-gate device irradiated from the bottom were placed on a free standing 3-D printed support, on which samples were

clicked and thus irradiation from the bottom side was possible. In this case a 3rd finger was used to contact the top gate.

3.4 ELECTRICAL CHARACTERIZATION OF SAM AND INSULATING NANOMETRIC FILMS

3.4.1 E-GaIn soft junction

Vertical junctions are usually facile architectures to explore at the lab scale the electrical conductance athwart an organic film integrated between two electrodes. While the bottom electrode can be a solid metallic film, the non-invasive deposition of a top contact on the top of an organic layer is not easy. A wise solution has been proposed which relies on the use of a liquid compliant fluid metal as top electrode.[14] Among the various liquid metals we have focused out attention on a eutectic of Gallium and Indium 75-25 in weight with a melting point of 15.5 °C (E-GaIn). E-GaIn has a high surface tension (624 mN/m) which is the result of the thin layer of external oxide which is formed in air (0.7 nm thick), guaranteeing the formation of flat contacts. The formation of the oxide layer is very important, because it helps the eutectic to retain its form and prevents it to diffuse through the organic film. It presents many advantage, which are the possibility of forming multiple junctions on a sample, to not diffuse in the measured layer, reducing shorts, and to achieve reproducible high-throughput, non-destructive current density–voltage (J–V) measurements.[15]

The employed setup consisted of a syringe (Hamilton) filled with the eutectic. Substrates were put on a support stage, controlled in the Z direction, by an electric actuator (Z8-Thorlabs). A camera placed behind the contact zone recorded in real time the micro manipulation. A metallic probe was placed at the stage with a screw in order to contact the metallic electrode placed under the measured organic layer. This electrode and the syringe needle were connected to a Keithley 2635. The liquid exiting the syringe needle formed a drop which could be approached to the sample surface forming a contact (**Figure 3.4**). A small tip is essential to contact a small area and thus reducing drastically shorts. Average contact areas obtained in this work were about 0.05 mm^2

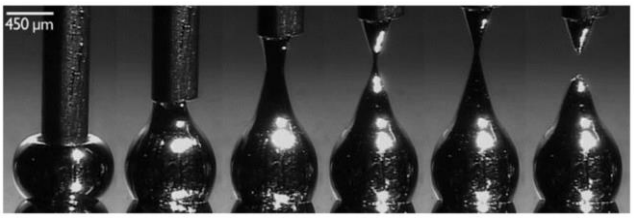

Figure 3.4 Series of photographs showing how the conical tip used for junctions is produced, by pressing the E-GaIn drop on the sample and quickly retracting the needle. Reproduced from Ref [14]

This tip was then gently contacted to the sample and voltage was swept from negative to positive V (usually -0.2 to 0.2V). This bias was applied in continuous cycles of 20 measures,

in order to test the junction robustness.[14] The recorded current was then divided by the contact area, measured with a reference made by a pre-patterned 20 μm channel device, and current density was extracted. Typically the J is averaged on at least 500 independent measurements. Such E-GaIn junction is employed in Chapter 6 to evaluate difference in conductance between a SAM of DAE in the open and closed form once chemisorbed on planar gold electrodes, and in Chapter 8 to measure difference in conductance in AZO-PMA dielectric layer.

3.5 WF AND IE MEASUREMENTS TECHNIQUES

3.5.1 Ambient photoelectron spectroscopy

The ionization energy of the employed materials, semiconductors, metal surfaces modified by SAM have been measured with an Ambient Photoelectron Spectroscope RIKEN AC-2. This tool is a ultra-violet photoelectron spectroscope that operates in air. This apparatus measures oxygen ions generated by the extracted photoelectrons. With respect to the standard ultra-high-vacuum UPS, it performs a scanning at different energies, it does not measure directly the kinetic energy of the extracted photoelectrons, and its reference is the vacuum level and not the Fermi Level.

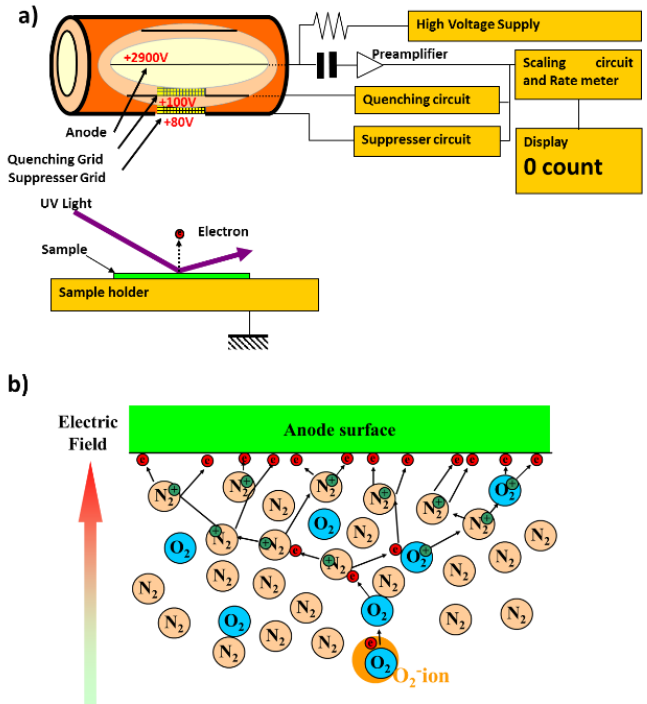

Figure 3.5 a) Schematic illustration of the ambient photoelectron spectrometer. The light source is not depicted. b) Mechanism of ion avalanches generation nearby the anode.

Figure 3.5a depicts a cartoon of the working principle. The sample is placed on the grounded holder and it is irradiated with light at different wavelength (usually between 3.4 to 6.2 eV, *i.e.* 364 nm to 200 nm) using a deuterium lamp passing through a monochromator. When the irradiation energy is enough, a photoelectron is extracted. The presence of air does not allow a

direct detection of emitted photoelectrons, but instead the extracted electrons are collected by oxygen molecules present in air forming O_2^- ions. The ions drift towards the detectors which is positively charged. When the ions arrives nearby the anode which is kept at +2900 V, the electron is detached from it and it is accelerated towards the anode. This causes an avalanches of electrons, that produces many ions, positive or negative, collected from the anode as showed in **Figure 3.5b**. An electric pulse is then generated and recorded. This pulse is associated to 1 count.

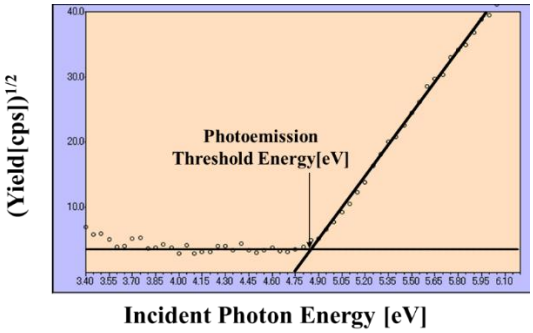

Figure 3.6 Typical square root of photoelectron count vs energy from which IP is extracted

Figure 3.6 shows a typical photoelectron yield *vs*. energy plot. The threshold energy is the ionization potential of the material and it is obtained by linear regression after having set the baseline. For a metal it corresponds to work function and for a semiconductor to its HOMO. The sensitivity of the instrument is 50 meV.

3.5.2 Single point macroscopic Kelvin probe

The kelvin probe (KP) is a noninvasive technique employing a vibrating tip to measure changes in surface potential on a surface. It is based on the method invented by Lord Kelvin in 1898, which consists of an electrical link connecting both faces of a capacitor made by two conductors.[16]

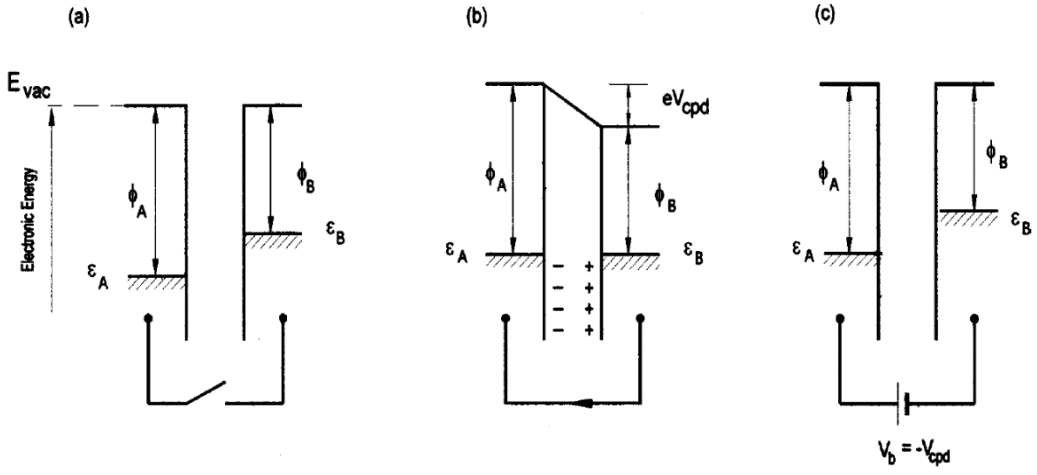

Figure 3.7 Energetic diagram of KP principle. a) Two metals with different work function (indicated with Φa and Φb) are brought close together. b) an electrical contact is made and electron flows produce a difference in potential. C) an external voltage Vb is applied to compensate induced voltage Vcpd. Reproduced from Ref [17]

Two metals with different work function are close to enough to be considered a plane capacitor (**Figure 3.7a**). When they are electrically contacted an equilibrium is established, with electrons flowing from the metal with smallest work function to the other one, producing a potential gradient $\mathbf{V_{cpd}}$ between the plates (**Figure 3.7b**). If one of the two plates vibrates, for a KP is the tip of the instrument, capacitance is varied and a current starts to flow back and forth. If the other electrode is potentially biased when provided voltage $\mathbf{V_b}$ equalizes potential difference induced by electrical contact the electrical field between the armors vanish as reported in **Figure 3.7c**. Hence the work function difference corresponds to the potential needed to nullify the output signal. [17]

This working mechanism allows for a cheap instrument setup, and more important with appropriate isolation of the system, usually achieved with a Faraday cage, a KP measure has an accuracy of a few meV. KP is an ideal instrument to measure differences in work function, especially if related to photo-switchable molecules. The biggest drawback is that KP does not measure absolute work function, and calibration is needed using a sample with a known work function. Despite this, absolute work function values that can be obtained with calibration are just an approximation. Reference surfaces are never completely clean and they get easily contaminated by impurities coming from air which as well can induce formation of thin layers of metal oxide. Because of this reason, the maximum precision that can be achieved in the estimation of the work function amounts to 200meV.[17]

The KP employed in this thesis is a single point macroscopic ambient Kelvin probe system developed by KP Technology Ltd. This means that the vibrating tip is fixed and does not scan the surface along the X-Y axes. The tip size, thus the area sampled on a single measurements corresponds to 1 mm^2.

3.6 OPTICAL PROPERTIES: UV-VIS SPECTROSCOPY

3.6.1 Introduction

Light is defined by Maxwell equations as a radiating energy propagating in the space as a sinusoidal wave. At the same time light is a stream of photons, quanta with energy depending on light wavelength. Electromagnetic radiation and matter can interact in various way, which depend basically from energy of involved photons. UV-VIS spectroscopy is related to photons with enough energy to promote an electron of a molecule to an orbital of higher energy. In other word, a molecule, by light irradiation is brought from a fundamental state to an excited state. [18]

Molecular orbital structure can be calculated by assuming that electrons move faster than the nuclei (Born-Hoppenheimer approximation). For each nuclei coordinate a set of electronic wave-function is the solutions of Schrodinger equation. At each quantum number correspond

different set of energies related to different nuclei geometry. Those adiabatic potential energy surfaces represent different geometric configurations of the molecule as showed in **Figure 3.8**. An electron in fundamental state can be promoted to excited state if energy of the incident photon is exactly equal to the energetic gap between the final state and the initial state. Those energies are of about 10^{-19} J, hence wavelength between 800 and 180 nm are needed to induce these transitions.[18]

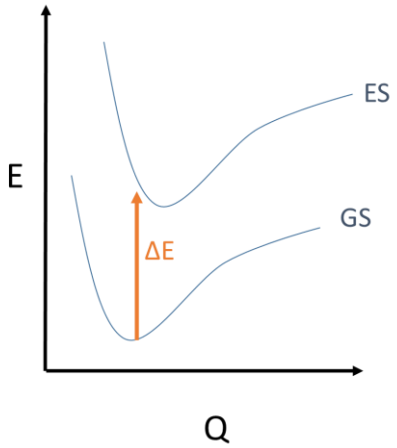

Figure 3.8 Simplified scheme of electronic potential energy surfaces. Difference in energy between ground state (GS) and excited state (ES) is represented as ΔE. Vibrational and rotational energy levels are not depicted.

3.6.2 UV-VIS absorbance spectroscopy

As depicted **in Figure 3.7** the ground state (GS) and excited state (ES) are broad since for each level there are many rotational and vibrational states. When irradiated with white light, photons with energy corresponding to ΔE are absorbed. Transmitted light is recorded and the ratio incident light, transmitted light is called transmittance T. Absorbance is directly obtained from it by **Equation 3.7**

$$A = \mathrm{Log}(T) = -\varepsilon dc \qquad 3.7$$

The absorbance band is not a sharp peak in reason of electronic potential energy surface shape and vibrational levels, as previously discussed. If absorbance spectroscopy is performed in solution, absorbance depends on ε which is the molar absorption coefficient depending on the solvent, d the distance travelled by light through the sample and c is concentration.[19]

The recorded spectra presented in this thesis were recorded with a JASCO V670 spectrophotometer which has been used for studying both solution and film samples.

3.6.3 UV-VIS spectroscopy: a tool to gain information on semiconductors

UV-VIS absorbance spectra are a very useful to study both solutions and thin films. Each absorption band can be related to a specific transition. If we consider a typical semiconducting

film spectrum, many features are present. Of particular interest is the lowest energetic transition, because is the one between the HOMO and the LUMO, and in first approximation it corresponds to the longest wavelength absorption band recorded.[20] This is a straightforward method to calculate the optical band gap of a semiconductor.

An absorption spectra also contains precious information on the supramolecular structure within the film.

On these regard, P3HT has been deeply studied by Spano which developed a model to analyze film morphology from its absorption spectra. [21]

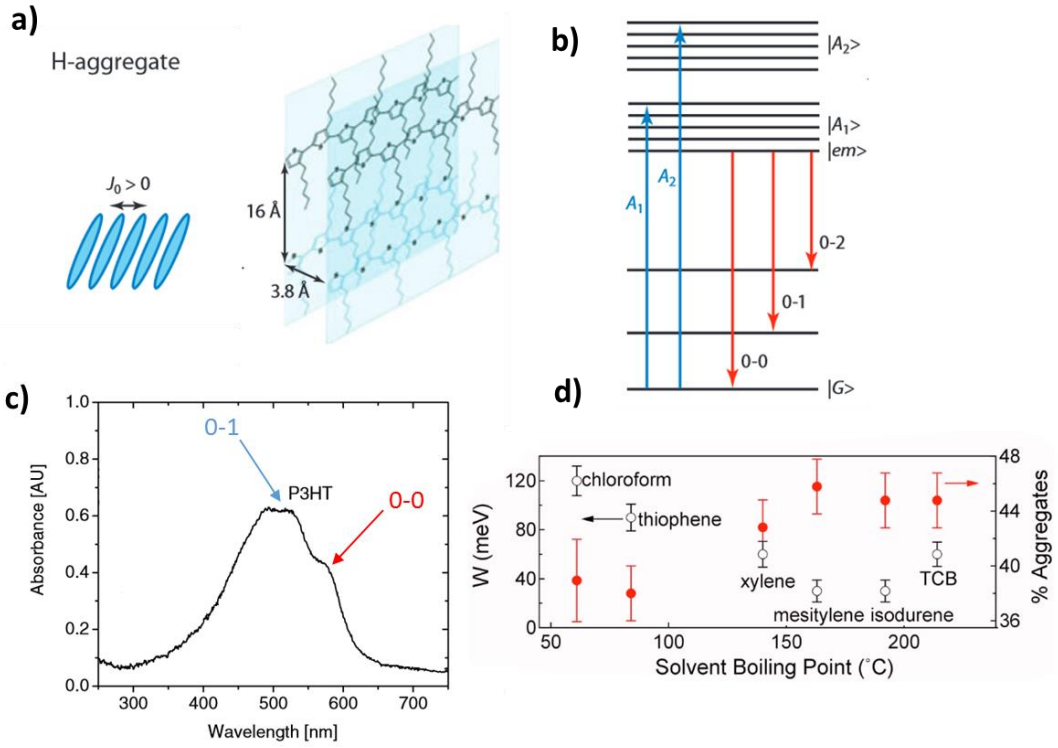

Figure 3.9 a) Molecular orientation in H-aggregates and π-stacking in P3HT film. b) Jablonski diagram corresponding to the weakly coupled H-aggregate model. C) Typical P3HT thin film absorption spectrum with highlighted the features arising from 0-0 (in red) and 0-1) transitions. d) Excitons bandwidth *W* (open black circles), left axis, and percentage of film made up of aggregates (full red circle), right axis, for film spun from different solvents Composed from Ref [22](a and b), Ref [23] (c) and Ref [24].

Two bands of P3HT thin film spectrum are used in the framework of Spano[25] model to gain insight into the crystallinity within a deposited film. P3HT films form a crystalline structure composed by weakly coupled H-aggregates. H-aggregates are aggregates formed by π-stacking, in which the nearest neighbor chromophore is oriented in a side-by-side fashion as showed in **Figure 3.9a**. This orientation allows optically produced excitons on the top of the excitons band. [22]The main effect is that the 0-exciton band is optically accessible from the ground state (0-0 A_1 transition, **Figure 3.9b**) while 0-1 is permitted just in disordered part of the film.[25]

Spano model successfully describes absorption band of P3HT thin film. The spectrum is always composed by two typical for P3HT absorption band, a lower-energy from the film region forming H-aggregates and a higher-energy part arising from intrachain states of

disordered chains (**Figure 3.9c**).[24] The ratio between the intensity of those two peaks is directly related to the nearest-neighbor interchain coupling via the free-excitons bandwidth of the aggregates. From **Equation 3.8**

$$\frac{A_{0-0}}{A_{0-1}} \approx \left(\frac{1-0.24W/E_p}{1+0.073W/E_p}\right)^2 \qquad 3.8$$

Where *W* is the excitons bandwidth and E_p is the intramolecular vibration with the electronic transition. W is henceforth directly related to the average molecular conformation of P3HT films. An increase in order and crystallite conjugation length lead to a decrease of *W*. Those findings have been demonstrated by combining AFM analysis and UV-VIS spectroscopy. The percentage of crystallite aggregates can be estimated from **Figure 3.9d**, where different values of *W* calculated for different films spun from different solvents correlate with the aggregates percentage.[24]

3.7 Morphological analysis: Atomic Force Microscope

Among Scanning Probe Microscopy techniques, Atomic force microscopy (AFM) can generates true topographical maps of a surface with a nanoscale spatial resolution. A tip interacts with sample surface while it is raster scanning on its top. The point-by-point quantification of such forces enables the generation of an array of data point which is the image. Tips are micro-fabricated on a flexible cantilever and possess a conical tip with a radius of curvature < 10 nm. AFM can reach lateral resolution of 0.1 nm and vertical resolution < 0.01 nm.

AFM can be operated in different modes. The most classical mode is the contact mode in which the tip touches the sample surface while it is scanning. Due to the proximity between the sample surface and the tip it allows to reach high spatial resolution. However, such a mode can be invasive when soft (e.g. organic) films are explored. To circumvent this problem non-contact modes and intermitting-contact modes have been introduced in the early 90's.

In intermittent-contact mode, during a scan a piezoelectric crystal forces the tip to oscillate in such a way that it touches intermittently the surface. This mode is also called tapping mode. The forces involved in the tip-sample interaction affect probe oscillations. These interferences are sensed by a laser which is shone on the rear side of the cantilever. The laser beam is then reflected on quadrant photodiode. The oscillation amplitude is maintained constant during the scanning and it adjusted by a feedback loop compensating the changes in oscillation by modifying the distance between the tip and the surface. The final result is a topographical image in which at each X and Y point a Z value is provided. [26]

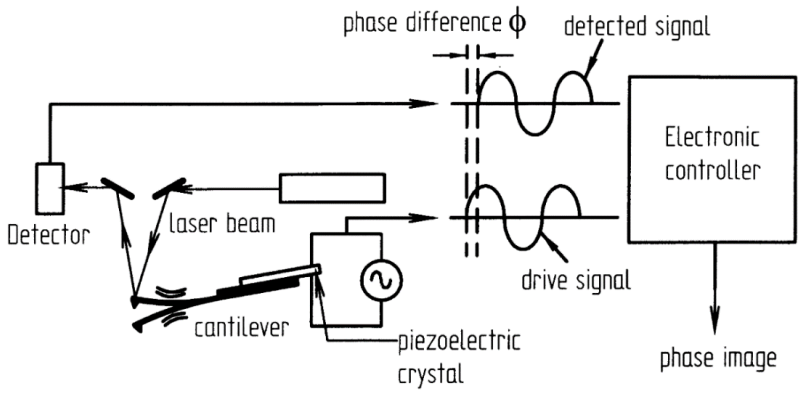

Figure 3.10 Schematic working principle of a tapping AFM mode, with a focus on contrast phase detection. Reproduced from Ref[27]

As highlighted in **Figure 3.10** also a phase contrast image can be produced by an AFM in tapping mode using a laser detector. The instrument monitors the phase of cantilever oscillation and compare it with the detected signal, recording a phase contrast image. Differences between the two phases arise from surface dissimilarity, and different contrast is produced by different friction and adhesion between the tip and the surface. It also can be due to compositional variation, like grain boundaries.[27] Therefore it is possible to use phase images to explore the composition and inter-component interactions in a multicomponent film like that of a polymeric thin film interacting with underlying graphene nano-flakes. (Chapter 7).

A Nanoscope Veeco Multimode V Bruker microscope operating in tapping mode was used in this work.

3.8 ELECTRONIC MICROSCOPY: SEM AND TEM

3.8.1 Scanning electron microscope (SEM)

Scanning electron microscopy (SEM) is a useful tool to gain important information on external morphology and chemical composition of a material.

A high energetic electron beam is produced at the top of the column of the microscope. They are accelerated towards the sample by a combination of lenses while slits are used in order to focus the beam on the (grounded) substrate. Both the sample and the column are kept in high vacuum (10^{-8} bar).The finals lens is used to deflect the beam and move it in XY directions.

Electron beam impacting the sample produces typical pear-shaped interaction areas from which arise a series of emission, due to energy dissipations (**Figure 3.11**)

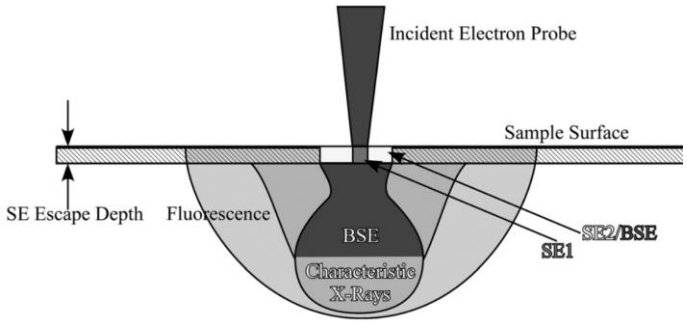

Figure 3.11 Schematic representation of the pear shape interaction volume for an electronic beam and the substrate and from which are each extracted particles come from. Reproduced from Ref [28]

Electrons emitted are divided in secondary electrons (SE < 50meV) and backscattered electrons (BSE > 50 meV), while photons are emitted at different wavelength from visible to X-rays. SE emerge from the first nm of the pear, and they are outer-shell electrons directly excited by the beam and thus able to escape. BSE are high energy electrons emerging from the inner-shells due to elastic or inelastic scattering with electron beam. X-rays are emitted from the sample and they are useful for chemical analysis. Each different emission has its own detector in the chamber. [28]

In Chapter 7 SEM images were used to estimate coverture of deposited LPE-G on the sample and to evaluate morphology of deposited flakes. All SEM images have been taken with a Quanta FEG microscope with a SE detector and 5kV acceleration. Spot size was used to be 3.5.

3.8.2 Transmission electron microscope (TEM)

Transmission electron microscope (TEM) share with the SEM the same working principle. An electron beam in vacuum is focused by lenses on the sample. The main difference with respect to the SEM is that the detector is placed below the sample, and thus what is recorded are electrons which passed through the specimen. The main advantage is that is possible to achieve a spatial resolution of 0.1 nm, but the sample must be very thin and must allow the electron beam to pass through it. In chapters 4-5 we have used a Jeol 2100 microscope with a LaB6 filament as electron source, operating at 200kV with resolution of 0.1 nm. The use of TEM was necessary to image AuNPs of diameter of 3 nm or smaller, employed in the study.

3.9 REFERENCES

1. Li, F.; Nathan, A.; Wu, Y.; Ong, B. S., *Organic Thin Film Transistor Integration: A Hybrid Approach*. Wiley: 2011.
2. Lee, W.; Park, Y., Organic Semiconductor/Insulator Polymer Blends for High-Performance Organic Transistors. *Polymers* **2014,** *6*, 1057-1073.
3. Cosseddu, P.; Bonfiglio, A., A comparison between bottom contact and top contact all organic field effect transistors assembled by soft lithography. *Thin Solid Films* **2007,** *515*, 7551-7555.
4. Zaumseil, J.; Sirringhaus, H., Electron and Ambipolar Transport in Organic Field-Effect Transistors. *Chem. Rev.* **2007,** *107*, 1296-1323.
5. Horowitz, G., Organic Field-Effect Transistors. *Adv. Mater.* **1998,** *10*, 365-377.

6. Z. Bao, J. L., *Organic Field-Effect Transistors*. CRC Press: New york, 2007.
7. Jurchescu, O. D.; Hamadani, B. H.; Xiong, H. D.; Park, S. K.; Subramanian, S.; Zimmerman, N. M.; Anthony, J. E.; Jackson, T. N.; Gundlach, D. J., Correlation between microstructure, electronic properties and flicker noise in organic thin film transistors. *Appl. Phys. Lett.* **2008,** *92*, 132103.
8. DeLongchamp, D. M.; Sambasivan, S.; Fischer, D. A.; Lin, E. K.; Chang, P.; Murphy, A. R.; Fréchet, J. M. J.; Subramanian, V., Direct Correlation of Organic Semiconductor Film Structure to Field-Effect Mobility. *Adv. Mater.* **2005,** *17*, 2340-2344.
9. Masashi, T.; Naoya, K.; Shingo, I.; Takashi, N.; Takashi, K.; Hiroyoshi, N., Effect of contact resistance on mobility determination by impedance spectroscopy. *Jpn. J. Appl. Phys.* **2014,** *53*, 02BE02.
10. Wang, A.; Kymissis, I.; Bulović, V.; Akinwande, A. I., Tunable threshold voltage and flatband voltage in pentacene field effect transistors. *Appl. Phys. Lett.* **2006,** *89*, 112109.
11. Pengzhan, S.; Renzhi, M.; Kunlin, W.; Minlin, Z.; Jinquan, W.; Dehai, W.; Takayoshi, S.; Hongwei, Z., Suppression of the coffee-ring effect by self-assembling graphene oxide and monolayer titania. *Nanotechnology* **2013,** *24*, 075601.
12. Spin Coating Guide. Ossila, Ed. Ossila: 2014.
13. Rivnay, J.; Steyrleuthner, R.; Jimison, L. H.; Casadei, A.; Chen, Z.; Toney, M. F.; Facchetti, A.; Neher, D.; Salleo, A., Drastic Control of Texture in a High Performance n-Type Polymeric Semiconductor and Implications for Charge Transport. *Macromolecules* **2011,** *44*, 5246-5255.
14. Chiechi, R. C.; Weiss, E. A.; Dickey, M. D.; Whitesides, G. M., Eutectic Gallium–Indium (EGaIn): A Moldable Liquid Metal for Electrical Characterization of Self-Assembled Monolayers. *Angew. Chem. Int. Ed.* **2008,** *47*, 142-144.
15. Lilly, G. D.; Whalley, A. C.; Grunder, S.; Valente, C.; Frederick, M. T.; Stoddart, J. F.; Weiss, E. A., Switchable photoconductivity of quantum dot films using cross-linking ligands with light-sensitive structures. *J. Mater. Chem.* **2011,** *21*, 11492-11497.
16. Baikie, I. D.; Smith, P. J. S.; Porterfield, D. M.; Estrup, P. J., Multitip scanning bio-Kelvin probe. *Rev. Sci. Instrum.* **1999,** *70*, 1842-1850.
17. Baikie, I. D.; Estrup, P. J., Low cost PC based scanning Kelvin probe. *Rev. Sci. Instrum.* **1998,** *69*, 3902-3907.
18. Ceroni, P.; Balzani, V., Excited-State Properties. In *The Exploration of Supramolecular Systems and Nanostructures by Photochemical Techniques*, Ceroni, P., Ed. Springer Netherlands: 2012; Vol. 78, pp 1-20.
19. Zaccheroni, N., Spectrophotometry, Measurements in Solution. In *The Exploration of Supramolecular Systems and Nanostructures by Photochemical Techniques*, Ceroni, P., Ed. Springer Netherlands: 2012; Vol. 78, pp 39-66.
20. Ceroni, P.; Balzani, V., Photoinduced Energy and Electron Transfer Processes. In *The Exploration of Supramolecular Systems and Nanostructures by Photochemical Techniques*, Ceroni, P., Ed. Springer Netherlands: 2012; Vol. 78, pp 21-38.
21. Spano, F. C., Modeling disorder in polymer aggregates: The optical spectroscopy of regioregular poly(3-hexylthiophene) thin films. *The Journal of Chemical Physics* **2005,** *122*, 234701.
22. Spano, F. C.; Silva, C., H- and J-Aggregate Behavior in Polymeric Semiconductors. *Annu. Rev. Phys. Chem.* **2014,** *65*, 477-500.
23. Shrotriya, V.; Ouyang, J.; Tseng, R. J.; Li, G.; Yang, Y., Absorption spectra modification in poly(3-hexylthiophene):methanofullerene blend thin films. *Chem. Phys. Lett.* **2005,** *411*, 138-143.
24. Clark, J.; Chang, J.-F.; Spano, F. C.; Friend, R. H.; Silva, C., Determining exciton bandwidth and film microstructure in polythiophene films using linear absorption spectroscopy. *Appl. Phys. Lett.* **2009,** *94*, 163306.
25. Clark, J.; Silva, C.; Friend, R. H.; Spano, F. C., Role of Intermolecular Coupling in the Photophysics of Disordered Organic Semiconductors: Aggregate Emission in Regioregular Polythiophene. *Phys. Rev. Lett.* **2007,** *98*, 206406.
26. Haugstad, G., Overview of AFM. In *Atomic Force Microscopy*, John Wiley & Sons, Inc.: 2012; pp 1-32.
27. Pang, G. K. H.; Baba-Kishi, K. Z.; Patel, A., Topographic and phase-contrast imaging in atomic force microscopy. *Ultramicroscopy* **2000,** *81*, 35-40.
28. Scheu, C.; Kaplan, W. D., Introduction to Scanning Electron Microscopy. In *In-Situ Electron Microscopy*, Wiley-VCH Verlag GmbH & Co. KGaA: 2012; pp 1-37.

4. The role of size and coating in Au nanoparticles incorporated in organic thin-film transistors

4.1 INTRODUCTION

Solution-processed thin film transistors (OTFTs) garnered great attention in the last decade because they hold a huge potential as key components for large-area electronics and logic circuits.[1-6] Nowadays, one among the greatest challenges in such a field of research relies on the increase of the structural and functional complexity of the devices by tailoring and exploiting multicomponent, hybrid films and more generally sophisticated nanocomposites[7], paving the way towards multifunctional devices[8,9]. Among various organic and polymeric semiconductors, poly(3-hexylthiophene) (P3HT) is a reference component because of its easy processability in numerous solvents and large field-effect mobility in thin film[10]. Organic/inorganic hybrid materials are gaining much attention because of the possibility of varying the properties of different individual components enables the optimization of the characteristics of the overall material. Metallic nanoclusters, like gold nanoparticles (AuNPs), are space-confined objects holding unique properties determined by their nanoscale size, and by their stabilizing coating layer.[11,12] However, the effect on charge transport of different sized AuNPs exposing various coating layers has never been analyzed in-depth. It is known that a transition from semiconductor to insulator occurs in AuNPs with a diameter below 1.5 nm[13]. While a bulk metallic material exhibits a continuous spectrum of states, when the very same material possesses a finite size, like a nanoparticle, the states are rather discrete. This stems from the proportionality between the density-of-states (DOS) and the number of atoms in the ensemble, leading to the formation of a band gap even in metal aggregates[14]. While bulk gold exhibits metallic behavior, with the decreasing size of gold aggregates the DOS smoothly scales up to the formation of a band gap between energy levels (Kubo gap)[15]. The coating layer of AuNPs can consist of chemisorbed Self-Assembled Monolayers (SAMs) of a specific molecule that imparts additional functions including a specific surface energy[16], optoelectronic properties[17] and capacity to penetrate cell-membranes[18]. These features can be optimized by

achieving control over the packing of the molecules forming SAMs on the NPs. When NPs are integrated in a device they can act as charge storage sites enabling the system to operate as a memory. Thin-film transistors incorporating blends of an organic semiconductor and AuNPs as active layer have already been studied. Previous research endeavor was focused on the effect of different sizes AuNPs or decorated with different coating layers in OTFT[19-21] as well as floating gates[22], memristors [23-25] and inverters[26,27].

Among thiol-functionalized molecules capable of chemisorbing on Au nanostructures, oligophenyl-thiols (OPTs) not only exhibit interesting electronic properties[28,29] but can also form ordered SAMs on Au surfaces[30]. Because of these reasons OPTs have been used to coat the planar Au electrodes of an OTFT in order to modulate the charge injection at the metal-semiconductor interface [31]. Although the optical properties of AuNPs were found to be modified via chemisorption of OPTs on their surface[32], it is unknown how this functionalization influences their electrical characteristics.

4.2 MATERIALS AND METHODS

AuNPs Synthesis. All materials have been purchased from Aldrich and used without further purification: auric acid ($HAuCl_4 \cdot 3H_2O$), sodium borohydride ($NaBH_4$), tetraoctylammonium bromide ($C_{32}H_{68}BrN$ - TOAB), octadecylamine ($CH_3(CH_2)_{17}NH_2$ - ODA), thiophenol (PhSH – MPT), biphenyl-4-thiol (Ph_2SH – BPT), 1,1′,4′,1″-terphenyl-4-thiol (Ph_3SH – TPT).

The nanoparticles were synthetized with a modified procedure derived from Leff & Co.[33], and with some difference used in previous work performed in our lab[21].

49 mg of Au $HAuCl_4$ was solubilized in 20 ml of MilliQ water. A solution of 200 mg of TOAB in 40 ml of toluene was prepared and added to the water solution. After 45 minutes of vigorous stirring the organic phase turned orange and water becomes transparent. Water phase was then discarded. 1 gr of ODA was dissolved in 40 ml of toluene, and afterwards added to the previous solution while it was vigorous stirred. A fresh solution of 35 mg of sodium borohydride in 4 ml of MilliQ water was added to the gold solution, which quickly turned dark brown. After 10 h the water phase was discarded. This stock solution was then divided in aliquots of 10 ml. For obtaining AuNPs-3.0 nm coated with the three different thiols we used a Ligand Exchange Reaction[34]. To obtain the three different coatings are added to the aliquots: 10 µl of a solution of MPT prepared with 60 µl of MPT diluted in 10 ml of toluene; 1.2 mg of BPT; 0.85 mg of TPT. Every solution was let stirring 18 hours. Obtained crude was purified with multiple precipitations by centrifugation adding ethanol and subsequently removing the surfactant.

AuNPs – 1.3 nm were prepared by digestive using molecular ratio already present in previous work[35] . We followed a procedure that we briefly describe: aliquots of 20 ml of AuNPs – ODA of stock solution were dried under vacuum and then dispersed in 5 ml of toluene with 30-second

sonication. 100 µl of MPT were added to one aliquot, 110 mg of BPT to another, 75 mg of TPT to the last one. Solutions turned transparent after 1 hour and were stirred vigorously for 48 hour (TPT solution did not became transparent, because TPT solubility in toluene or chlorobenzene in not enough). The crude was purified with multiple precipitations by centrifugation adding ethanol and subsequently removing the surfactant.

Blends and Device preparation. Every solution was dried under reduced pressure, the obtained solid was weighted and then chlorobenzene was added in proportion to obtain 50% weight/weight ratio (Au/solvent) solution. Under nitrogen atmosphere solution of P3HT and AuNPs/P3HT were prepared: each solution had a ratio P3HT/solvent w/w of 100%, for 3.0 nm-AuNPs 5%, 10%, 20% (n, 2n, 4n) and for 1.3 nm-AuNPs 0.25%, 0.5%, 1% (n, 2n, 4n) to obtain solution with approximately the same number of AuNPs.

Solution were stirred at 50° for 30 minutes to ensure complete miscibility of the components. OTFTs were prepared spincoating cold solutions on n^{++}-Si/SiO_2 substrates pre-patterned interdigitated gold source and drain electrode (IPMS Fraunhofer) for 60 sec at 1500 rpm (100 µl drop) and then annealed for 2h at 75 °C.

4.3 RESULTS AND DISCUSSION

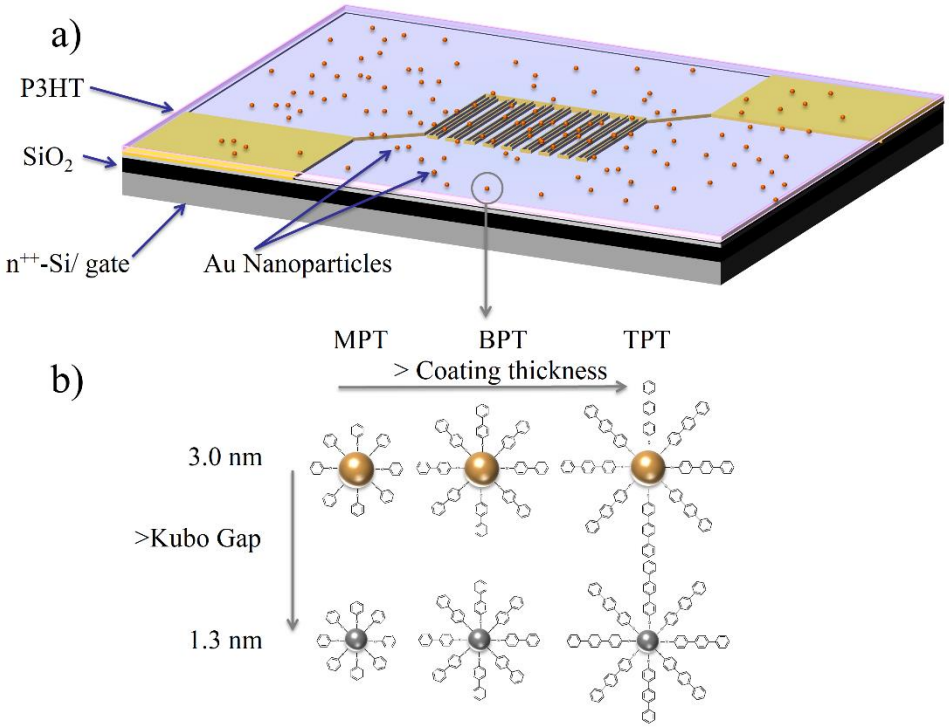

Figure 4.1 (a) Scheme of the bottom-contact/bottom-gate thin-film transistor using a bi-component P3HT-AuNPs blend as the active layer. (b) Schematic summary of the system: the three different oligophenyl-thiols used as the coating for the AuNPs (MPT, BPT, TPT) with increasing molecular length and the AuNPs encompassed in this study, semiconducting (3.0 nm) and insulating (1.3 nm), respectively

Here we show that the presence of different sized AuNPs coated with SAMs of oligophenyl-thiols (OPTs) with increasing contour length can modify structural and electrical properties of

P3HT films. This includes its crystalline nature and field-effect mobility as well as bias-stress response when it acts as the active layer in bottom-contact bottom-gate TFT. We have used three linear oligophenyl-thiol derivative, i.e. (mono) phenylthiol (MPT), biphenyl-4-thiol (BPT) and 1,1′,4′,1″-terphenyl-4-thiol (TPT). The device scheme is portrayed in **Figure 4.1a** while the different coating molecules are shown in **Figure 4.1b**. We have focused our attention on AuNPs with a diameter of either 3.0 nm or 1.3 nm which, according to the Kubo rule, possess an energy gap of 6.4 meV and 80 meV, respectively, therefore being over 3 times larger or smaller than kT.[13]

4.3.1 AuNPs design and synthesis

Complete chemisorption of the OPTs on the two sized AuNPs has been accomplished starting from a solution of $HAuCl_4$ in toluene which has been reduced to metallic gold in presence of an amine followed by a ligand exchange reaction with the chosen thiolated molecule (see ESI for experimental details). The coated AuNPs have been characterized by UV-Vis absorption and TEM (see ESI). Up to six different samples types were prepared and tested in OTFTs: pristine P3HT, P3HT/AuNPs-3.0 nm coated with MPT, BPT and TPT blends, and P3HT/AuNPs-1.3 nm coated with MPT and BPT. Unfortunately 1.3 nm AuNPs coated with TPT could not be studied because their synthesis turned out to be extremely difficult due to low solubility of TPT in all the attempted solvents (toluene, tetrahydrofuran, acetone, chloroform, dichloromethane, chlorobenzene, dichlorobenzene). For the sake of comparison we also prepared 3.0 nm-AuNPs coated with a saturated SAM of octadecylamine (ODA) to get greater insight into the role of the coating layer.

4.3.2 AuNPs optical Characterization

AuNPs were characterized by UV-VIS spectroscopy. Absorption spectra of prepared solution were recorded with a JASCO V-650 UV-Vis Spectrophotometer and quartz cuvettes (HELLMA ANALYTICS). AS reported in **Figure 4.2** peaks around λ=510 nm are obtained for 3.0 nm AuNPs related to the surface plasmon resonance. A blue shift is present after LER with thiols. For 1.3 nm AuNPs no peaks are present, and the solution appears transparent as expected

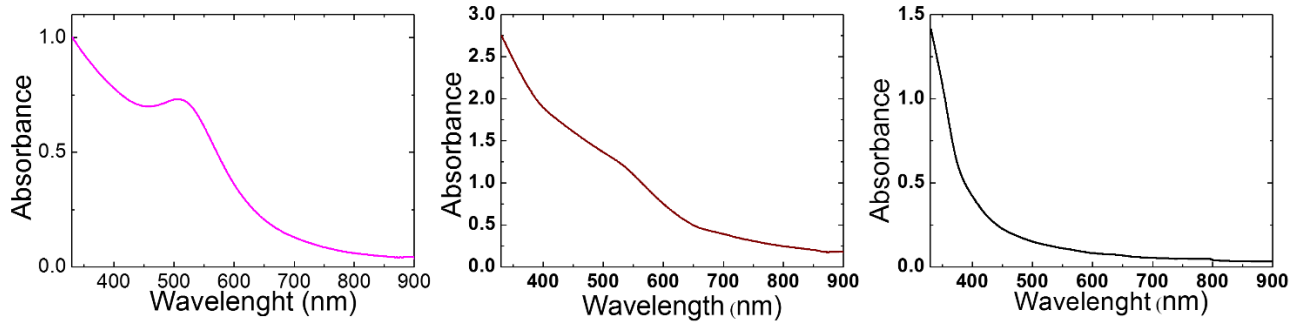

Figure 4.2. Absorption spectra normalized of (a) 3.0 nm AuNPs/ODA without purification, (b) 3.0 nm AuNPs/BPT after purification, (c) 1.3 nm AuNPs/BPT after purification.

4.3.3 AuNPs size and aggregation analysis.

A fundamental part in this study is AuNPs size. In order to control that the 2 different sizes designed has been achieved by synthesis, and to get a confirmation of UV-VIS measurements TEM has been employed. The Transmission Electron Microscopy (TEM) experiments have been carried out on a Jeol 2100 microscope with a LaB6 filament as electron source, operating at 200kV. The TEM micrographs have been acquired on an Orius camera. The microscope is equipped with an EDX JED 2300T detector and BF and DF detectors for operation under the scanning TEM (STEM) mode. The microscope resolution is 0.1 nm in the TEM mode and 1 nm in STEM.

Prior to analysis, the specimens have been diluted in Toluene solution for AuNPs specimen and a chlorobenzene solution for the blend P3HT/AuNPs with samples with a concentration of 1 mg/ml for the former and a concentration of 1 mg/ml of P3HT with 0.1 mg/ml AuNPs. For the TEM experiments, 1 to 3 drops of solution have been deposited on a holey carbon film deposited on a 300 mesh copper grid. Afterwards, the samples have been left to dry in air at the room temperature, for at least 30 minutes.

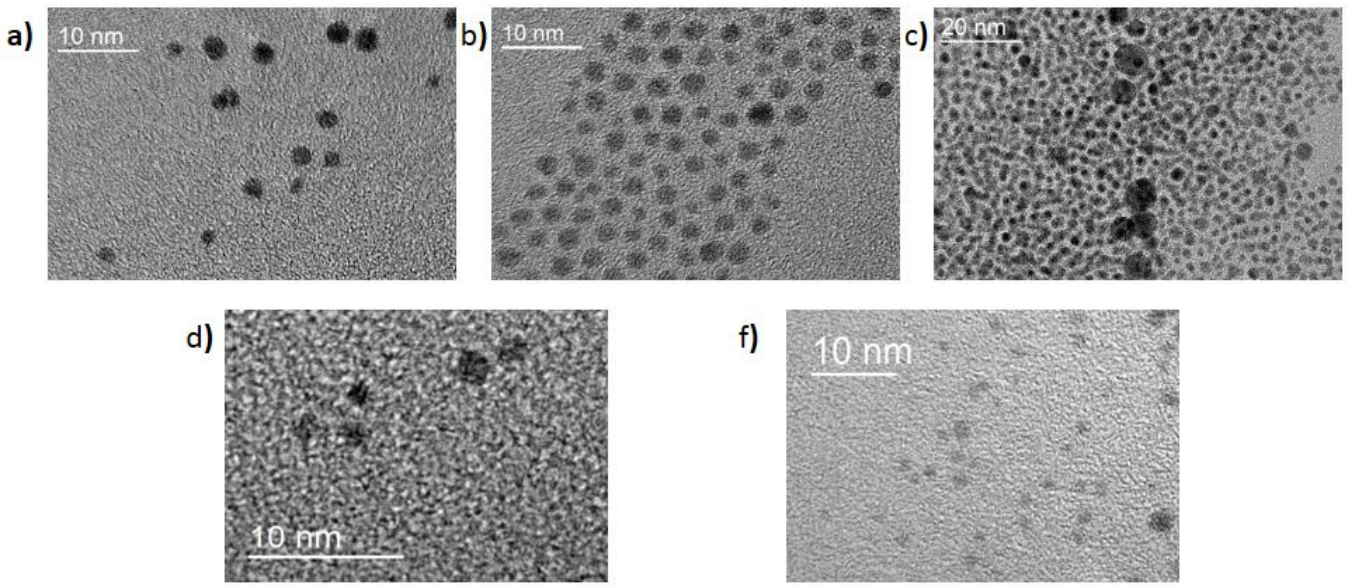

Figure 4.3. TEM images of the synthesized coated AuNPs drop-cast on carbon-coated, gold-plated copper microscope grids. (a) 3.0 nm AuNPs/MPT, (b) 3.0 nm AuNPs/BPT, (c) 3.0 nm AuNPs/TPT, (d) 1.3 nm AuNPs/MPT, (e) 1.3 nm AuNPs/BPT.

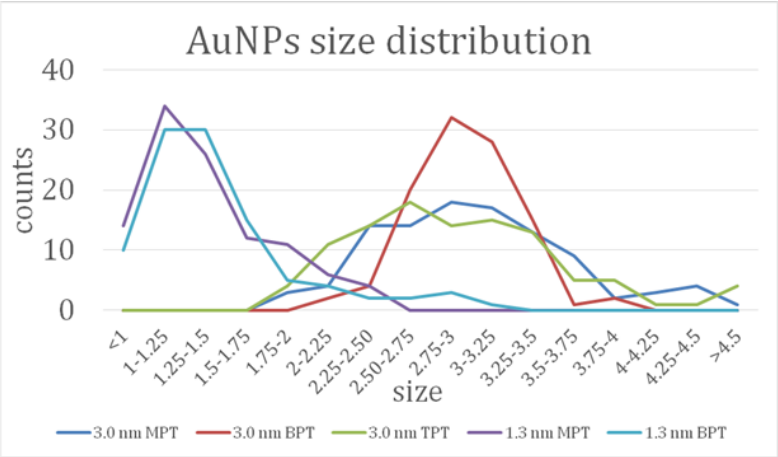

Figure 4.4. Size diagram distribution for the different NPs studied, as determined on TEM images. The mean diameter and the standard deviation of the population of particles are expressed in table 4.1. The values represent a statistic analysis of more than 100 particles for each sample.

Table 4.1 Average sizes

	Avg. Size (nm)
3nm NPs/MPT	3.0 ±0.6
3nm NPs/BPT	3.0 ±0.3
3nm NPs/TPT	3.0 ±0.9
1.3nm NPs/MPT	1.3 ±0.4
1.3nm NPs/BPT	1.3 ±0.4

As reported by **Table 4.1** and **Figure 4.3** we achieve a very good control on AuNPs size, with a narrow size monodispersion for all different coatings. As highlighted by **Figure 4.4** size distribution between AuNPs labelled 1.3 and 3.0 is evident, with the latter centered on 3 nm and the former around 1.3 nm.

Also aggregation of all AuNPs employed when embedded in P3HT matrix has been studied

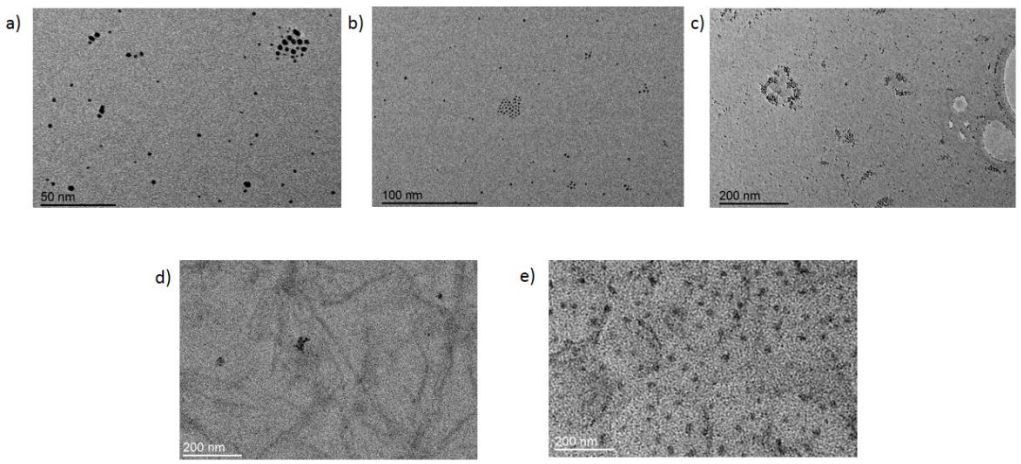

Figure 4.5. TEM images a blend of P3HT/AuNPs drop-cast on carbon-coated, gold-plated copper microscope grids. (a) 3.0 nm AuNPs/MPT, (b) 3.0 nm AuNPs/BPT, (c) 3nm AuNPs/TPT, (d) 1.3 nm AuNPs/MPT, (e) 1.3 nm AuNPs/BPT.

In P3HT (**Figure 4.5**) all AuNPs tend to aggregate a bit in cluster, of different size. This effect on OTFTs performances will be discussed later in this chapter.

4.3.4 AuNPs/P3HT OTFTs: mobility and threshold voltage shift.

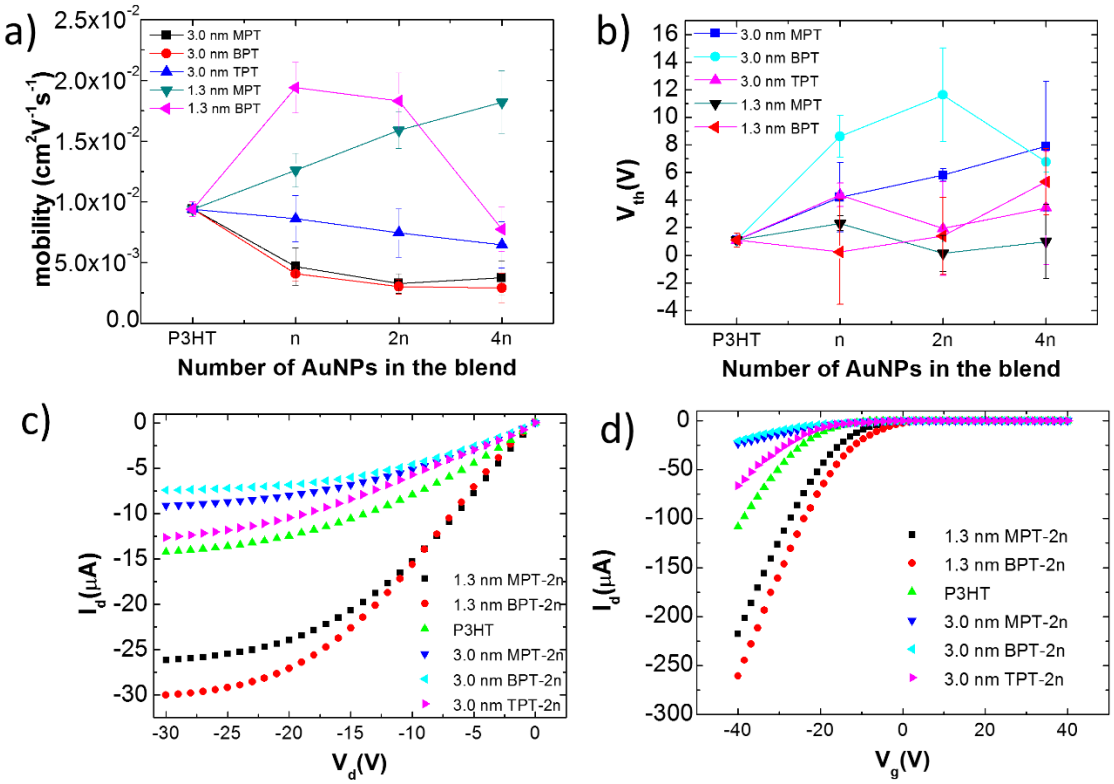

Figure 4.6. Comparative plots of (a) field-effect mobility vs. blend composition. (b) Threshold voltage devices for all the different blends for channel length 10 μm. (c) Output and (d) transfer characteristics for OTFTs and 2n-blends with AuNPs ((c) with V_g = -20 V) for channel lengths of 10 μm.

We have chosen to compare blends of P3HT with 1.3 nm and 3 nm AuNPs incorporating the same number of AuNPs. For this purpose $1.8 \cdot 10^{14}$ (n), $3.6 \cdot 10^{14}$ (2n), $7.2 \cdot 10^{14}$ (4n) AuNPs of the two sizes have been added to P3HT maintaining the weight-to-weight ratio of P3HT with the solvent always at 1 mg/ml. These values of AuNPs correspond to percentages in weight of AuNPs with respect to P3HT of 5%, 10%, 20% for AuNPs-3.0 nm and 0.25%, 0.5%, 1% for AuNPs-1.3 nm. The devices have been prepared by spincoating of the blends on bottom-contact bottom-gate TFTs followed by thermal annealing at 75 °C for 2 hours, as detailed in Materials and Method section. Results on the electrical characteristics, performed in N_2 atmosphere, relied on a statistics of over 30 devices for every different combination of AuNPs size/coating type.

Table 4.2 Average mobility values extracted from the saturation regime

Semi conductive Active layers	Mobility of n blends ($cm^2 \cdot V^{-1} \cdot s^{-1}$)	Mobility of 2n blends ($cm^2 \cdot V^{-1} \cdot s^{-1}$)	Mobility of 4n blends ($cm^2 \cdot V^{-1} \cdot s^{-1}$)
P3HT	$(9.4\pm0.6)\times10^{-3}$	/	/
P3HT/AuNPs – 3.0 nm MPT	$(4.7\pm1.5)\times10^{-3}$	$(3.3\pm0.8)\times10^{-3}$	$(3.7\pm1.4)\times10^{-3}$
P3HT/AuNPs – 3.0 nm BPT	$(4.1\pm0.6)\times10^{-3}$	$(3.0\pm0.6)\times10^{-3}$	$(2.9\pm1.2)\times10^{-3}$
P3HT/AuNPs – 3.0 nm TPT	$(8.6\pm1.9)\times10^{-3}$	$(7.4\pm2.0)\times10^{-3}$	$(6.5\pm1.9)\times10^{-3}$
P3HT/AuNPs – 1.3 nm MPT	$(1.30\pm0.14)\times10^{-2}$	$(1.60\pm0.15)\times10^{-2}$	$(1.8\pm0.3)\times10^{-2}$
P3HT/AuNPs – 1.3 nm BPT	$(1.9\pm0.2)\times10^{-2}$	$(1.8\pm0.2)\times10^{-2}$	$(7.7\pm1.8)\times10^{-3}$

All devices exhibited a very good p-type behavior, responding with an almost ideal spacing between curves at different gate voltages as presented in **Figure 4.7**. The extracted mobility's (μ) from saturation regime are reported in **Table 4.2** and are plotted in **Figure 4.6**a. They reveal that the use of 3.0 nm AuNPs induces a universal three-fold decrease in mobility for n-NPs blends when compared to pristine P3HT and differently coated AuNPs exhibited a similar electrical behavior, with the field-effect mobility which decreases with the increasing quantity of AuNPs in the blend. The type of coating seems not to influence notably the mobility: MPT and BPT blends exhibit the same trend and values, whereas TPT blends show the same trend with slightly higher μ values which is likely due to the greatest tendency of this type of AuNPs to aggregate, ultimately reducing the occurrence of scattering centers within the film. Conversely, AuNPs-1.3 nm devices present an increase of mobility.

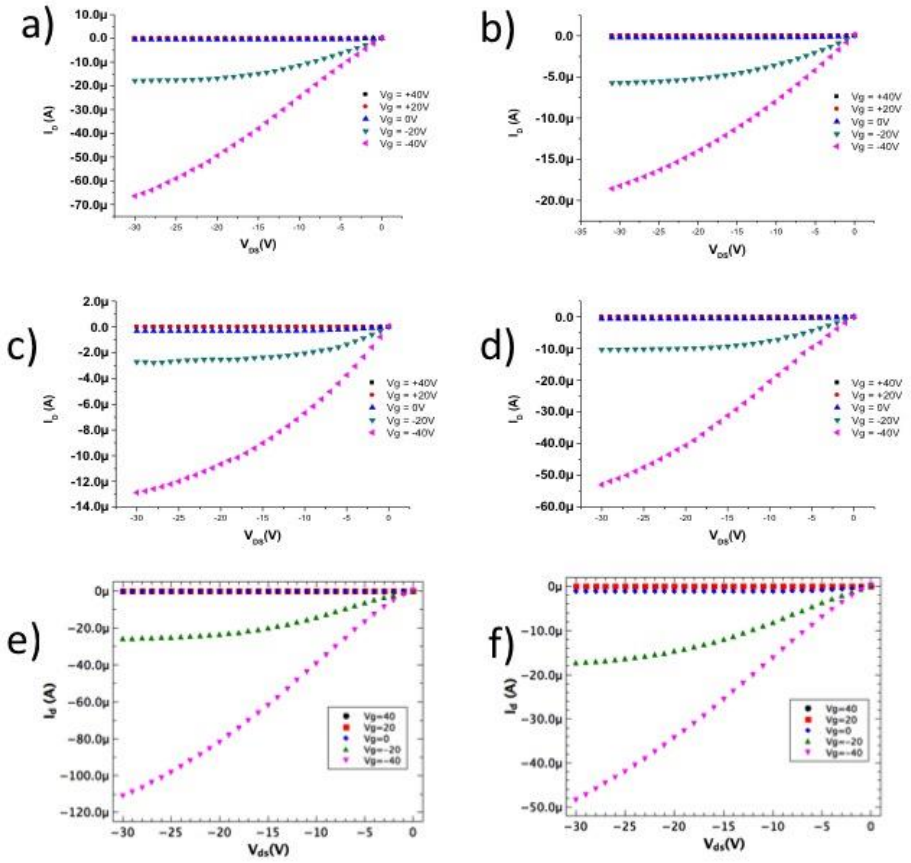

Figure 4.7. Transfer characteristics for (a) P3HT based OTFT. (b) P3HT/AuNPs-3.0 nm MPT. (c) P3HT/AuNPs-3.0 nm BPT. (d) P3HT/AuNPs-3.0 nm TPT. (e) P3HT/AuNPs-1.3 nm MPT. (f) P3HT/AuNPs-1.3 nm BPT.

Significantly, MPT blends reveal a linear enhancement in mobility up to 100% with the increasing number of AuNPs in the blend. For BPT there is a two-fold enhancement in mobility already for n-blends while for 4n-blends the μ drops down to a value slightly lower than pristine P3HT devices. OTFT devices based on P3HT blends with 1.3 nm AuNPs coated with as much as MPT 2.25% in weight (10n) revealed $\mu = (8.7 \pm 1.4) \times 10^{-3}$ $cm^2 \cdot V^{-1} \cdot s^{-1}$. Such a result demonstrates that with the increasing quantity of 1.3 nm sized AuNPs in the blend, after an initial increase in μ, a decrease is observed. The latter finding can be likely ascribed to inter-particle aggregation when large quantities of AuNPs in the blend material are used, as discussed in the next paragraphs. The increase in mobility in P3HT/AuNPs based OTFTs was already reported[20], and a strong dependence on the concentration if AuNPs in the blend was found. However, here we demonstrate how the contribution of size and type of coating of the AuNPs are two entangled parameters. In order to provide a comparative picture of the different electrical properties of the different blends, **Figure 4.6c,d** displays the output and transfer characteristic of 2n-blend of AuNPs compared to pure P3HT based devices. It shows a higher

mobility and a maximum current reached for 1.3 nm AuNPs/P3HT active layers, both parameters decreasing in 3.0 nm AuNPs/P3HT blends.

Threshold voltage (V_{th}) have also have been extracted from the transfer curves in the saturation regime. V_{th} values were larger and positive at small channel lengths for all the different blends, which is a marked short-channel effect coming from the bare semiconductor as observable in the pristine P3HT values. In **Figure 4.6b** are reported the values of V_{th} for 2n-blends with different coating and size. There is a general shift toward more positive values for P3HT/AuNPs devices, but increasing the number of AuNPs does not lead to a clear trend though they would all be comprised in the 0 - 10 V range which makes it appealing for low-power dissipation applications. It is interesting to take into account other studies on similar system for V_{th} shift in AuNPs/P3HT OTFTs showing tunable values of the V_{th} with AuNPs concentration [27]. We believe that a major role is played by the coating type as evidenced by the dependence of the V_{th} on the chemisorbed SAM and the amount of coated AuNPs in the film, although a general trend on V_{th} vs. the concentration of AuNPs in P3HT is not evident. Moreover, it is worth noting the error bars associated with V_{th} that can be ascribed to the poor homogeneous dispersion of AuNPs in the blend films prepared by spincoating, indicative of locally randomly distributed NPs aggregates.

To shine more light onto the role of the coating layer we have extended our studies to devices incorporating 3.0 nm AuNPs in a number of 4n coated with the saturated ODA monolayer. ODA is a well-known reducing agent[33], but is not possible to obtain AuNPs smaller than 3 nm because amines are weak ligands for AuNPs[36]. The devices exhibited a mobility of $(6.6\pm5.2)\times10^{-4}$ $cm^{2}\cdot V^{-1}\cdot s^{-1}$, being one order of magnitude lower when compared to pristine P3HT and 50-folds lower compared to the worst performing P3HT/AuNPs-3.0 nm 4n devices. Also it displayed a shift of V_{th} towards more negative values up to 14 V for L = 20 μm, revealing overall poor device characteristics if compared to the others blend combination. This effect can be ascribed to three factors: (i) a more modest purification which is achieved with ODA-AuNPs, because they tend to aggregate after 5 cycles of centrifugation, (ii) the electrically insulating character of the octadecyl chain acting as an electrical barrier, and (iii) the weak physical interaction between the amino group and gold which could be perturbed by the presence of the sulfur atom of P3HT[37].

4.3.5 AuNPs effect on P3HT morphology

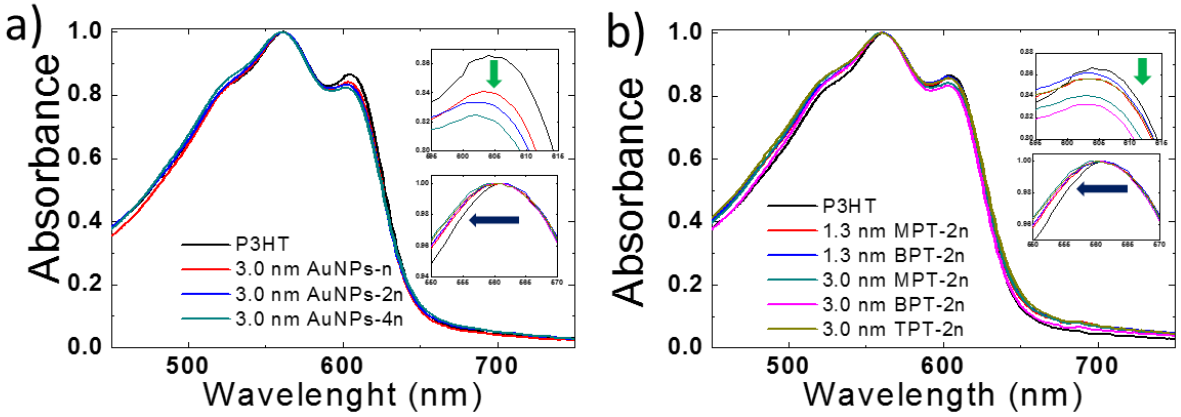

Figure 4.8. (a) Absorption spectra of P3HT/AuNPs-3.0 nm BPT with different load of AuNPs (n, 2n, 4n) compared to pristine P3HT. Spectra are normalized to the maximum at λ=560 nm to better show the variation of the peak related to the 0-0 transition. (b) Normalized absorption spectra of all the P3HT/AuNPs-2n blends compared to pristine P3HT.

To gain insight into the effect of AuNPs on the morphology of P3HT films we carried out UV-Vis measurements. The P3HT film exhibits two transitions in the UV-Vis spectral range, i.e. the 0-0 and the 0-1 transition. These transitions can be explained in the framework of the H-aggregate model[38]. The 0-0 transition arises from the weak π-π interaction between crystalline parts forming H-aggregates while the 0-1 is due to inter-chain states of disordered chains. The relative intensity of such bands is determined by the free exciton bandwidth (W) of aggregates which is inversely proportional to the percentage of crystalline aggregates in the film.[39] The value obtained for W is ca. 20 meV for all the different blends, as reported in **Table 4.3,** which is indicative of a high percentage of crystalline aggregates within the film. [39]

Table 4.3 Calculated W for all P3HT/AuNPs employed blends

	0-0/0-1 ratio	W (meV) (free exciton bandwidth)
P3HT	0.955 ±0.005	0.013±0.001
1.3 nm MPT	0.934 ±0.002	0.020±0.001
1.3 nm BPT	0.934 ±0.004	0.020±0.001
3.0 nm MPT	0.925 ±0.004	0.022±0.001
3.0 nm BPT	0.921 ±0.002	0.023±0.001
3.0 nm TPT	0.929 ±0.001	0.021±0.001

However, **Figure 4.8**a reveals that the increase in AuNPs content is accompanied by a decrease in the relative intensity of the 0-0 peaks as well as a peak broadening, indicating a lower π-π interaction between P3HT chains thus a decrease in the general order of the polymer in the film. The addition of further more AuNPs causes a larger decrease of the intensity of the 0-0 peak providing evidence for an increased disorder, the latter being responsible for the decreased mobility in the devices. **Figure 4.8b** compares the difference in absorbance for all 2n blends. AuNPs-3.0 nm TPT exhibits a lower decrease at λ=602 nm, indicating weaker

perturbation of the P3HT crystalline structure when compared the other two coatings. It is worth noting that pristine AuNPs and blend P3HT/AuNPs exhibit different aggregation propensities and morphologies as monitored by TEM (**Figure 4.3** and **Figure 4.5**). For 3.0 nm AuNPs the coating plays a major role, in fact AuNPs-3.0 nm TPT strongly aggregate while, an ordered honeycomb arrangement was found for AuNPs-3.0 nm BPT. If dispersed in P3HT (**Figure 4.5**) the NPs are much less aggregated, with TPT coated nanoparticles presenting still some tendency to form clusters. This result can be attributed to the presence of a longer oligophenylene chain in TPT causing stronger π-π interactions between TPT-TPT and TPT-P3HT. This finding is reflected in the relatively greater mobility measured in AuNPs coated TPT based devices with respect to MPT and BPT. On the other hand, 1.3 nm sized AuNPs are well dispersed on the TEM grid but in a P3HT matrix they tend to aggregate more, forming small clusters of NPs. However, a very mild decrease in the absorption 0-0 peak for 2n blends is observed, due to the smaller perturbation of the P3HT crystalline structure induced by the smaller AuNPs size.

4.3.6 AuNPs/P3HT energetic interactions

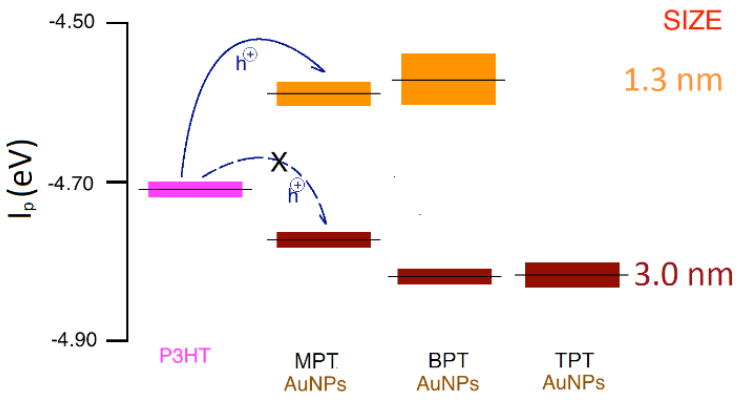

Figure 4.9. Ionization potential of the employed components.

To gain a greater understanding, we have performed ambient photoelectron spectroscopy measurements to quantify the ionization potential (I_p) of bare P3HT films and AuNPs with different sizes and coatings (**Figure 4.9**). P3HT thin film spun from solution in chlorobenzene exhibited a I_p = 4.68 eV, in agreement with previous reports.[40] AuNPs have been drop casted in 35 nm thick films on gold and then measured: 3.0 nm-AuNPs exhibit an Ip which lies about 100 meV below that of P3HT, hence out of the band gap of P3HT. This means that no favorable hole interaction is possible between P3HT and AuNPs, which can only act as a scattering centers for charges. 1.3 nm-AuNPs possess an I_p of ca. 80 meV above that of P3HT, i.e. its I_p is sitting inside the band gap of the active polymeric semiconductor.

Table 4.4 Extracted Ip values for all the components employed in this study

Materials	I_p (eV)
P3HT	4.69±0.02

AuNPs-3nm-MPT	4.73±0.02
AuNPs-3nm-BPT	4.78±0.02
AuNPs-3nm-TPT	4.79±0.02
AuNPs-1.3 nm-MPT	4.61±0.03
AuNPs -1.3 nm-BPT	4.60±0.06

This favorable energetics will allow the 1.3 nm-AuNPs to interact with charge carriers transported in the P3HT matrix at the HOMO level. Interestingly, these results are in contrast with the Kubo gap theory for the sole NPs that predicts a bigger band gap for smaller nanoparticles, *i.e.* the HOMO levels of AuNPs-1.3 nm should be placed outside the band gap while should be the opposite for 3.0 nm AuNPs. However, we believe that the mismatch can arise from the effect of a different number of sulphur-gold dipoles which is directly proportional to the number of gold atoms in the two types of NPs, i.e. 1.3 nm and 3.0 nm. The less are the atoms present in a cluster the more the energetic level are affected of the sulfur-gold bond enthalpy which is more exothermic in NPs with respect to gold in flat surfaces[41]. In our case the different contribution to the dipole from oligophenyl thiols is negligible because they possess a very similar structure, thus the energy level shift should depend mainly on the different number of gold atoms in different size NPs, being ca. 900 and 50 atoms for the 3.0 nm and 1.3 nm AuNPs, respectively.

4.3.7 AuNPs effect on traps and bias stress

To better understand the meaning and the consequences of the I_p measurements, we performed Space-Charge-Limited Current (SCLC) measurements to calculate the number of surface traps present in the active layers with different blends[42].

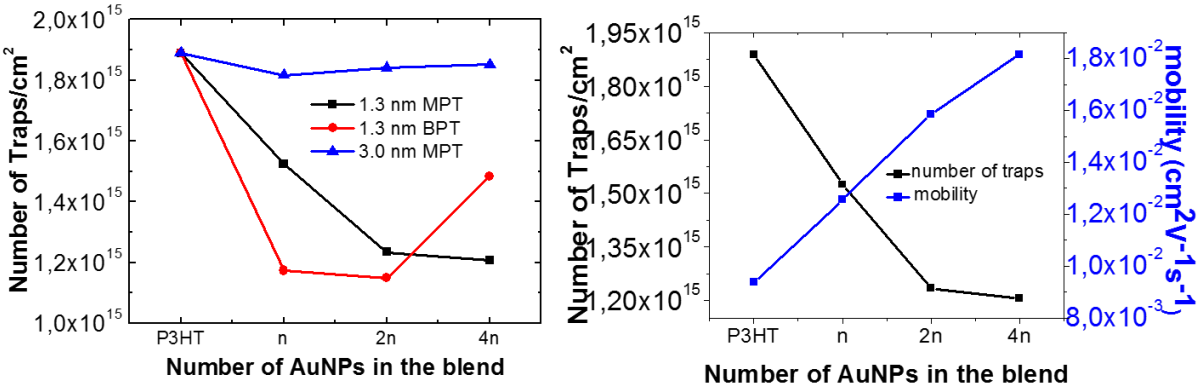

Figure 4.10. (a) Plot of the number of traps/cm^2 vs. different blends percentage of AuNPs for AuNPs-1.3 nm MPT and BPT, and AuNPs-3.0 nm MPT as a comparison. The first point is referred to P3HT. (b) Comparison of number of traps/cm^2 vs. mobility for AuNPs-1.3 nm MPT.

The SCLC model is based on the analysis of three different current regimes: a first regime which follows Ohm's law, a second regime which is governed by Child's law for solids and a

third one, entered once all the trap levels are filled up. In particular, a characteristic threshold voltage called trap-filled limit voltage (V_{TFL}) has to be overcome in order to enter the trap-filled regime. According to the SCLC theory, the number of electrical traps in a semiconducting material is directly proportional to the trap-filled limited voltage (V_{TFL}) and its electrical permittivity, thereby making it possible to extract the density of traps from the I-V curve, using the **Equation 4.1.**[43]

$$N_t = \frac{\varepsilon V_{TFL}}{eL^2} \qquad 4.1$$

Where L is the inter-electrodes distance, ε is the dielectric permittivity of the semiconductor and e is the elementary charge. The values, obtained from these measurements with a statistic of 16 samples for each blend are plotted in **Figure 4.10a** The value we used for the calculation of relative electrical permittivity of P3HT is 3.3[44]. Pristine semiconductor devices present a number of traps of the order of magnitude of 10^{15} and all AuNPs-3.0 nm blends present about the same number of traps of P3HT with no variation regarding the percentage or the coating layer. Conversely, devices incorporating 1.3 nm sized AuNPs revealed a more modest amount of traps, with values up to 25% lower respect to P3HT pristine devices. For small NPs a higher percentage present less traps for MPT coating, while for BPT coating there is a decrease of traps at small percentage and then an increase for 4n-blends. In these two system the mobility values follow an opposite trend (as shown for AuNPs-1.3 nm MPT devices in **Figure 4.10b**): they become bigger when adding NPs-MPT coated, while for NPs-BPT coated it decreases at 4n-blend. This mirroring behavior between mobility and number of traps confirm the fact that 1.3 nm AuNPs electronically interact with P3HT and that their presence fill traps in the P3HT electronic structure, leading to higher mobility. On the other hand, 3.0 nm AuNPs do not affect charge transport in P3HT based OTFT.

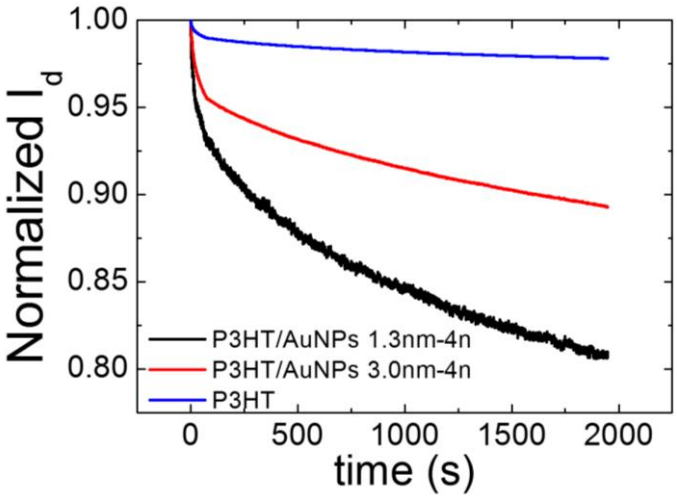

Figure 4.11. Normalized current with respect to the initial current vs. time for P3HT devices, and AuNPs blends (4n-BPT) of the different sizes.

To further address the effect of the presence of AuNPs, we have studied the behavior of transistor under a constant bias-stress voltage applied to the drain. It is well know that P3HT based OTFT show a decrease of current until a plateau is reached,[45] as determined by charge trapping inside deep energy states of P3HT[46]. We measured the drain current in function of time, for 10% blend of AuNPs-BPT coated devices, by applying a constant bias stress at the drain V_{ds} =-5 V and a gate voltage V_g calculated from the threshold voltage of the device extracted from the saturation regime with V_g-V_{th}=-5 V for a time of 30 minutes. The drain current decreases in the first minutes and reaches a plateau at different time depending of the sample (see **Figure 4.11** with a normalized current with respect to the initial current on the Y-axis). A statistic over 8 devices with variable percentage variation revealed that pristine devices exhibit the smallest time decay, with a minor fatigue, reaching a well stable plateau. AuNPs blends displayed a larger fatigue and decay time of two orders of magnitude lower with respect to pristine P3HT. 1.3 nm-AuNPs devices do not reach the plateau after the end of the measurement; they have the biggest decrease of current and bigger time decay which is indicative of a better electronic interaction with the active layer. Conversely, 3.0 nm-AuNPs devices exhibited a reduced current decay if compared to the former ones. This can be seen as an undesired presence of defects in the film which lowers the possibility for the charges to percolate. By decreasing the nanoparticle size, 1.3 nm-AuNPs electronically interact with P3HT by acting as doping agent, thereby increasing mobility of a factor up to two. However, an excess of 1.3 nm-AuNPs in the blend led to a decrease of performance. On the other hand, the effect of the coating layer is subtle but not less important. It influences very much the aggregation tendency of NPs, thus influencing the mobility and while giving subtle variation on the V_{th} .

4.4 CONCLUSIONS

We have shown that the size of AuNPs markedly affects the charge transport mechanism in OTFTs based on P3HT blended with AuNPs coated with OPTs. In particular, OPT coated AuNPs with a 1.3 nm diameter were observed to electronically interact with P3HT, increasing the OTFT device performances without significantly disrupting the crystalline nature of the P3HT film. On the other hand, bigger AuNPs, i.e. with a 3 nm diameter, were found not to interact electronically with P3HT, and just act as scattering centers for charges, while slightly altering the P3HT crystalline aggregates. AuNPs coated with different chemisorbed SAMs exhibited different behaviors, in particular determined by the different tendency of the AuNPs to aggregate, indirectly influencing the field-effect mobility. Overall, we have showed that the use of AuNPs in bi-component hybrid TFTs is a simple yet powerful method for modifying the physical and chemical properties of a polymeric semiconductor. Being based on thiol-based chemisorption, this approach combines a simple synthesis route with an easy processability and a high reproducibility. Noteworthy, the possibility of tuning different characteristics, *i.e.* size and coating, can lead to an enhancement of the electronic properties in OTFTs. Therefore, the

use of AuNPs has a double advantage: it enables the improvement of the performance of OTFTs and the integration of multiple functions in a single device, towards smart logic solutions.

4.5 REFERENCES

1. Arias, A. C.; MacKenzie, J. D.; McCulloch, I.; Rivnay, J.; Salleo, A., Materials and Applications for Large Area Electronics: Solution-Based Approaches. Chem. Rev. 2010, 110, 3-24.
2. Dodabalapur, A., Organic and polymer transistors for electronics. Mater. Today 2006, 9, 24-30.
3. Forrest, S. R., The path to ubiquitous and low-cost organic electronic appliances on plastic. Nature 2004, 428, 911-918.
4. Gelinck, G. H.; Huitema, H. E. A.; van Veenendaal, E.; Cantatore, E.; Schrijnemakers, L.; van der Putten, J. B. P. H.; Geuns, T. C. T.; Beenhakkers, M.; Giesbers, J. B.; Huisman, B.-H.; Meijer, E. J.; Benito, E. M.; Touwslager, F. J.; Marsman, A. W.; van Rens, B. J. E.; de Leeuw, D. M., Flexible active-matrix displays and shift registers based on solution-processed organic transistors. Nat. Mater. 2004, 3, 106-110.
5. Sirringhaus, H., Reliability of Organic Field-Effect Transistors. Adv. Mater. 2009, 21, 3859-3873.
6. Smits, E. C. P.; Mathijssen, S. G. J.; van Hal, P. A.; Setayesh, S.; Geuns, T. C. T.; Mutsaers, K. A. H. A.; Cantatore, E.; Wondergem, H. J.; Werzer, O.; Resel, R.; Kemerink, M.; Kirchmeyer, S.; Muzafarov, A. M.; Ponomarenko, S. A.; de Boer, B.; Blom, P. W. M.; de Leeuw, D. M., Bottom-up organic integrated circuits. Nature 2008, 455, 956-959.
7. Caironi, M.; Anthopoulos, T. D.; Noh, Y.-Y.; Zaumseil, J., Organic and Hybrid Materials for Flexible Electronics. Adv. Mater. 2013, 25, 4208-4209.
8. Guo, Y.; Yu, G.; Liu, Y., Organic FETs: Functional Organic Field-Effect Transistors (Adv. Mater. 40/2010). Adv. Mater. 2010, 22, 4427-4447.
9. Crivillers, N.; Orgiu, E.; Reinders, F.; Mayor, M.; Samorì, P., Optical Modulation of the Charge Injection in an Organic Field-Effect Transistor Based on Photochromic Self-Assembled-Monolayer-Functionalized Electrodes. Adv. Mater. 2011, 23, 1447-1452.
10. Sirringhaus, H.; Brown, P. J.; Friend, R. H.; Nielsen, M. M.; Bechgaard, K.; Langeveld-Voss, B. M. W.; Spiering, A. J. H.; Janssen, R. A. J.; Meijer, E. W.; Herwig, P.; de Leeuw, D. M., Two-dimensional charge transport in self-organized, high-mobility conjugated polymers. Nature 1999, 401, 685-688.
11. Klajn, R.; Stoddart, J. F.; Grzybowski, B. A., Nanoparticles functionalised with reversible molecular and supramolecular switches. Chem. Soc. Rev. 2010, 39, 2203-2237.
12. Otsuka, H.; Nagasaki, Y.; Kataoka, K., PEGylated nanoparticles for biological and pharmaceutical applications. Adv. Drug Delivery Rev. 2003, 55, 403-419.
13. Kubo, R.; Kawabata, A.; Kobayashi, S., Electronic Properties of Small Particles. Annu. Rev. Mat. Sci. 1984, 14, 49-66.
14. Kubo, R., Electronic Properties of Metallic Fine Particles. I. J. Phys. Soc. Jpn. 17, 975.
15. Roduner, E., Size matters: why nanomaterials are different. Chem. Soc. Rev. 2006, 35, 583-592.
16. Karakoti, A. S.; Das, S.; Thevuthasan, S.; Seal, S., PEGylated Inorganic Nanoparticles. Angew. Chem. Int. Ed. 2011, 50, 1980-1994.
17. Seker, F.; Malenfant, P. R. L.; Larsen, M.; Alizadeh, A.; Conway, K.; Kulkarni, A. M.; Goddard, G.; Garaas, R., On-Demand Control of Optoelectronic Coupling in Gold Nanoparticle Arrays. Adv. Mater. 2005, 17, 1941-1945.
18. Verma, A.; Uzun, O.; Hu, Y.; Hu, Y.; Han, H.-S.; Watson, N.; Chen, S.; Irvine, D. J.; Stellacci, F., Surface-structure-regulated cell-membrane penetration by monolayer-protected nanoparticles. Nat. Mater. 2008, 7, 588-595.
19. Wong, M.-C.; Yeh, S.-C.; Chiu, L.-K.; Chen, Y.-H.; Ho, J.-R.; Tsiang, R. C.-C., Enhanced Performance of Au/P3HT/(Bilayer Dielectrics)/Si Thin-Film-Transistor Having Gold Nanoparticles Chemically Bonded to P3HT. J. Nanosci. Nanotechnol. 2012, 12, 2292-2299.
20. Han, S.-T.; Zhou, Y.; Yang, Q.-D.; Lee, C.-S.; Roy, V. A. L., Poly(3-hexylthiophene)/Gold Nanoparticle Hybrid System with an Enhanced Photoresponse for Light-Controlled Electronic Devices. Particle & Particle Systems Characterization 2013, 30, 599-605.
21. Raimondo, C.; Crivillers, N.; Reinders, F.; Sander, F.; Mayor, M.; Samorì, P., Optically switchable organic field-effect transistors based on photoresponsive gold nanoparticles blended with poly(3-hexylthiophene). Proc. Natl. Acad. Sci. 2012, 109, 12375-12380.
22. Tseng, C.-W.; Huang, D.-C.; Tao, Y.-T., Azobenzene-Functionalized Gold Nanoparticles as Hybrid Double-Floating-Gate in Pentacene Thin-Film Transistors/Memories with Enhanced Response, Retention, and Memory Windows. ACS Appl. Mater. Interfaces 2013, 5, 9528-9536.
23. Alibart, F.; Pleutin, S.; Bichler, O.; Gamrat, C.; Serrano-Gotarredona, T.; Linares-Barranco, B.; Vuillaume, D., A Memristive Nanoparticle/Organic Hybrid Synapstor for Neuroinspired Computing. Adv. Funct. Mater. 2012, 22, 609-616.
24. Novembre, C.; Guerin, D.; Lmimouni, K.; Gamrat, C.; Vuillaume, D., Gold nanoparticle-pentacene memory transistors. Appl. Phys. Lett. 2008, 92, 103314.
25. Prakash, A.; Ouyang, J.; Lin, J.-L.; Yang, Y., Polymer memory device based on conjugated polymer and gold nanoparticles. J. Appl. Phys. 2006, 100, 054309-054309-054305.
26. Zhou, Y.; Han, S.-T.; Huang, L.-B.; Huang, J.; Yan, Y.; Zhou, L.; Roy, V. A. L., A low voltage programmable unipolar inverter with a gold nanoparticle monolayer on plastic. Nanotechnology 2013, 24, 205202.

27. Han, S.-T.; Zhou, Y.; Xu, Z.-X.; Roy, V. A. L., Controllable threshold voltage shifts of polymer transistors and inverters by utilizing gold nanoparticles. Appl. Phys. Lett. 2012, 101, 033306-033305.

28. Masillamani, A. M.; Crivillers, N.; Orgiu, E.; Rotzler, J.; Bossert, D.; Thippeswamy, R.; Zharnikov, M.; Mayor, M.; Samorì, P., Multiscale Charge Injection and Transport Properties in Self-Assembled Monolayers of Biphenyl Thiols with Varying Torsion Angles. Chem.–Eur. J. 2012, 18, 10335-10347.

29. Bürkle, M.; Viljas, J. K.; Vonlanthen, D.; Mishchenko, A.; Schön, G.; Mayor, M.; Wandlowski, T.; Pauly, F., Conduction mechanisms in biphenyl dithiol single-molecule junctions. Physical Review B 2012, 85, 075417.

30. Azzam, W.; Wehner, B. I.; Fischer, R. A.; Terfort, A.; Wöll, C., Bonding and Orientation in Self-Assembled Monolayers of Oligophenyldithiols on Au Substrates. Langmuir 2002, 18, 7766-7769.

31. Orgiu, E.; Crivillers, N.; Rotzler, J.; Mayor, M.; Samori, P., Tuning the charge injection of P3HT-based organic thin-film transistors through electrode functionalization with oligophenylene SAMs. J. Mater. Chem. 2010, 20, 10798-10800.

32. Busby, M.; Chiorboli, C.; Scandola, F., Relaxation Dynamics and Transient Behavior of Small Arenethiol Passivated Gold Nanoparticles. The Journal of Physical Chemistry B 2006, 110, 6020-6026.

33. Leff, D. V.; Brandt, L.; Heath, J. R., Synthesis and Characterization of Hydrophobic, Organically-Soluble Gold Nanocrystals Functionalized with Primary Amines. Langmuir 1996, 12, 4723-4730.

34. Woehrle, G. H.; Brown, L. O.; Hutchison, J. E., Thiol-Functionalized, 1.5-nm Gold Nanoparticles through Ligand Exchange Reactions: Scope and Mechanism of Ligand Exchange. J. Am. Chem. Soc. 2005, 127, 2172-2183.

35. Prasad, B. L. V.; Stoeva, S. I.; Sorensen, C. M.; Klabunde, K. J., Digestive Ripening of Thiolated Gold Nanoparticles: The Effect of Alkyl Chain Length. Langmuir 2002, 18, 7515-7520.

36. Sidhaye, D. S.; Prasad, B. L. V., Many manifestations of digestive ripening: monodispersity, superlattices and nanomachining. New J. Chem. 2011, 35, 755-763.

37. Zhai, L.; McCullough, R. D., Regioregular polythiophene/gold nanoparticle hybrid materials. J. Mater. Chem. 2004, 14, 141-143.

38. Spano, F. C., Modeling disorder in polymer aggregates: The optical spectroscopy of regioregular poly(3-hexylthiophene) thin films. The Journal of Chemical Physics 2005, 122, -.

39. Clark, J.; Chang, J.-F.; Spano, F. C.; Friend, R. H.; Silva, C., Determining exciton bandwidth and film microstructure in polythiophene films using linear absorption spectroscopy. Appl. Phys. Lett. 2009, 94, 163306-163311.

40. Orgiu, E.; Crivillers, N.; Herder, M.; Grubert, L.; Pätzel, M.; Frisch, J.; Pavlica, E.; Duong, D. T.; Bratina, G.; Salleo, A.; Koch, N.; Hecht, S.; Samorì, P., Optically switchable transistor via energy-level phototuning in a bicomponent organic semiconductor. Nat Chem 2012, 4, 675-679.

41. Reimers, J. R.; Wang, Y.; Cankurtaran, B. O.; Ford, M. J., Chemical Analysis of the Superatom Model for Sulfur-Stabilized Gold Nanoparticles. J. Am. Chem. Soc. 2010, 132, 8378-8384.

42. Lampert, M. A.; Mark, P., Current Injection in Solid. Academic Press: 1970.

43. Lampert, M. A.; Rose, A.; Smith, R. W., Space-charge-limited currents as a technique for the study of imperfections in pure crystals. J. Phys. Chem. Solids 1959, 8, 464-466.

44. Müller, K.; Richter, M.; Philip, S.; Kunst, M.; Schmeißer, D., Excited States in P3HT and P3HT/PCBM Blends. BioNanoScience 2012, 2, 42-51.

45. Estrada, M.; Mejía, I.; Cerdeira, A.; Pallares, J.; Marsal, L. F.; Iñiguez, B., Stability of PMMA on P3HT PTFTs under stress. Solid-State Electron. 2009, 53, 1063-1066.

46. Liu, Y. R.; Liao, R.; Lai, P. T.; Yao, R. H., Bias-Stress-Induced Instability of Polymer Thin-Film Transistor Based on Poly(3-Hexylthiophene). Device and Materials Reliability, IEEE Transactions on 2012, 12, 58-62.

5. Photo-chromic AuNPs/polymeric bi-component n-type OTFT.

5.1 INTRODUCTION

Gold Nanoparticles (AuNPs), when suitably decorated with ad-hoc moieties, can be used as functional components in organic thin film transistor (OTFTs).[1-3] When introduced and embedded in a semiconductive polymeric matrix they generate a great interfacial area,[4,5] that can expose well defined functions which are coating AuNPs.[6,7] In this way one can confer new functions to a multicomponent material[8], as imparting a memory behavior,[9-11] tune electrical properties[10,12] and enhance light response[13]. At the same time AuNPs size plays a key role in determining how these nanoclusters will electronically interact with the OTFTs semiconducting layer since they can drastically affect energetic alignment of the blend, aggregation and electrical response.[14]

In this framework, AuNPs decorated with photochromic molecules, covalently grafted through their thiolated termini, are nanometric objects which allow to confer or tune the light response of a certain material[15] for different applications.[1,16] With regard to organic electronics, different approaches have been explored. AuNPs decorated with azobenzene have been successfully employed to tune aggregation in solution[17,18] and the drain current in a transistor,[18] as well as to functionalize the gate electrode for memory elements.[9] A further step has already been studied by using diarylethenes (DAEs) as coating layers. DAEs are a class of molecules capable of undergoing isomerization between two (meta)stable forms by light irradiation at well-defined wavelengths; importantly, both forms are thermodynamically stable and the light triggered isomerization is highly efficient.[19] In particular, the open form (o-DAE), *i.e.* not conjugated, undergoes isomerization under UV light to a closed form (c-DAE) form, which is conjugated and undergoes isomerization to open upon illumination with visible light (typically $\lambda > 400$ nm). The isomerization in DAEs is accompanied by a change in the conjugation whereas the conformational/geometrical change is rather minor, decreasing drastically fatigue effect of light isomerization.[20] Because of these interesting properties we considered diarylethenes thiols suitable for self-assembled monolayer formation on Au with a di-tert-butyl

groups in the ω-position, in order to hinder the aggregation of AuNPs by steric hindrance. AuNPs with DAE coating have been widely studied with a particular focus on their optical properties and their switching efficiency.[21,22] In addition, gold clustered tailored with DAEs have been used as active layer for various electronic applications[20] and in particular in two terminal devices where light was able to induce a drastic change in conductance.[23 24]

In this work we focused on embedding for the first time DAE/AuNPs in a n-type polymer P(NDI2OD-T2), and we explored the effect of the isomerization between open and closed form of DAE/AuNPs on the charge transport in OTFTs. We used two different DAE moieties (**Figure 5.12)**, one with the thiol group in *para* position (p-DAE) and one with the thiol group in *meta* position (m-DAE) to investigate specifically how coupling of switching core with metallic clusters affects AuNPs/semiconductor interactions.

5.2 MATERIALS AND METHODS

DAE capped AuNPs synthesis: DAEs were synthetized by Prof. Hecht group**.** All the other materials have been purchased from Aldrich and used without further purification: auric acid ($HAuCl_4 \bullet 3H_2O$), sodium borohydride ($NaBH_4$), tetraoctylammonium bromide ($C_{32}H_{68}BrN$ - TOAB), dodecanthiol ($CH_3(CH_2)_{10}CH_2SH$-DDT). Protected DAE were synthesized by Stefan Hecht and co-workers using the procedure described in Ref. [21] with the only difference that 3,5-ditert-butylphenol was employed instead of bromobenzene in step 1. AuNPs synthetic procedure is reported in **Figure 5.1**

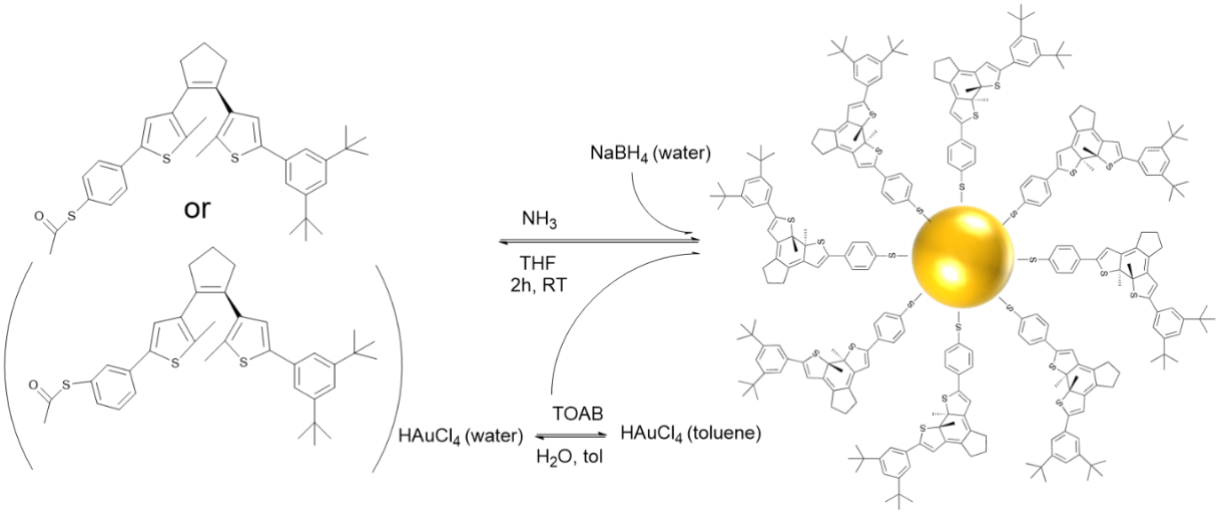

Figure 5.1 Synthetic procedure of DAE/AuNPs. Between brackets is reported the *meta* derivative. Deprotected DAEs were added to a toluene gold solution and then the reducing agent was added to obtain the final product.

Nanoparticles were produced using Leff synthesis method[25] derived from Kudernac *et al*. 15 mg of protected DAE were solubilized in 2 ml of THF. 100 µl of a 30% water solution of ammonia were quickly added under stirring. Solution was degased 10 times and left stirring for 5 hours in dark and then dried under reduced pressure. The obtained white powder was

redispersed in 2 ml of toluene. In the meanwhile 10 mg of $HAuCl_4$ were solubilized in 2.6 ml of MilliQ water. A solution of 27.5 mg of TOAB in 7 ml of toluene was prepared and added to the water solution. After 45 minutes of vigorous stirring the organic phase turned orange and water becomeed transparent. The water phase was then discarded. The deprotected DAE solution in toluene was added to the gold solution in toluene under stirring. A freshly prepared solution of 9.5 mg of sodium borohydride in 2.6 ml of MilliQ water was quickly added to the gold solution, which turned dark brown after few seconds. Solution was left under stirring in dark for 10 h, after which the water phase was discarded. The crude was purified with multiple precipitations by centrifugation adding ethanol and subsequently removing the surfactant. Finally solution of 1 mg/ml of DAE/AuNPs in toluene were prepared. In this way both *para* and *meta*/AuNPs were synthetized.

DDT capped AuNPs syhnthesis: 38.9 mg of $HAuCl_4$ were solubilized in 10 ml of MilliQ water. A solution of 197 mg of TOAB in 28 ml of toluene was prepared and added to the water solution. After 45 minutes of vigorous stirring the organic phase turned orange and water becomes transparent. Water phase was then discarded. 24µl of dodecane thiol were added to the solution. A fresh prepared solution 37 mg of sodium borohydride in 4 ml of MilliQ water was added to the gold solution, which quickly turned dark brown. The crude was purified with multiple precipitations by centrifugation adding ethanol and subsequently removing the surfactant.

TEM images of AuNPs: The Transmission Electron Microscopy (TEM) experiments have been carried out on a Jeol 2100 microscope with a LaB6 filament as electron source, operating at 200kV. The TEM micrographs have been acquired on an Orius camera. The microscope is equipped with an EDX JED 2300T detector and BF and DF detectors for operation under the scanning TEM (STEM) mode. The microscope resolution is 0.1 nm in the TEM mode and 1 nm in STEM. For the TEM experiments, 1 to 3 drops of solution have been deposited on a holey carbon film deposited on a 300 mesh copper grid. Afterwards, the samples have been left to dry in air at room temperature, for 5 minutes. Images were taken by Dr. Simona Moldovan at IPCMS, Université de Strasbourg.

Devices pre*para*tion: Solutions of poly[N,N-9-bis(2-octyldodecyl)-naphthalene-1,4,5,8-bis (dicarboximide)-2,6-diyl]-alt-5,59-(2,29-bithiophene)]), namely **P**(NDI2OD-T2), in toluene (5 mg/ml) with 0%, 5%, 10% and 20% of AuNPs (p-DAE, m-DAE, DDT/AuNPs) were prepared and left stirred overnight to ensure complete solubilisation. In a cylindrical weighing bottle 38 µl of octadecyltrichlorosilane – OTS (purchased from Sigma Aldrich, purity > 90%, used with no further purification) were added to 10 ml of anhydrous toluene in nitrogen atmosphere. Ozone cleaned substrates n^{++}-Si/SiO_2 substrates pre-patterned interdigitated gold source and drain electrode (IPMS Fraunhofer) were immersed in the solution which was then warmed for 30 min at 60 °C. Then the solution with the dipped samples was left reacting for 12 h. Samples were then rinsed with copious amount of toluene to ensure a complete cleaning, and then baked at 60°C for 2 h. 150 µl of each solution were spin-casted at 1000rpm for 60 seconds. Samples

were then annealed two hours at 70°C. Each sample had 16 devices on it with channel length of 20, 10, 5, 2.5 µm and W = 10000 µm.

Irradiation cycles: Irradiation were performed with an optical fiber at 0.5 cm vertical distance from the samples. The Optical fiber was connected to a Polychrome V (Till Photonics) tunable light source providing a monochromatic beam of ± 15 nm. Wavelengths used were 313 and 540 nm with irradiance levels of 0.5 and 50 mW/cm^2 respectively.

5.3 RESULTS AND DISCUSSIONS

5.3.1 AuNPs optical Characterization in solution and in thin film.

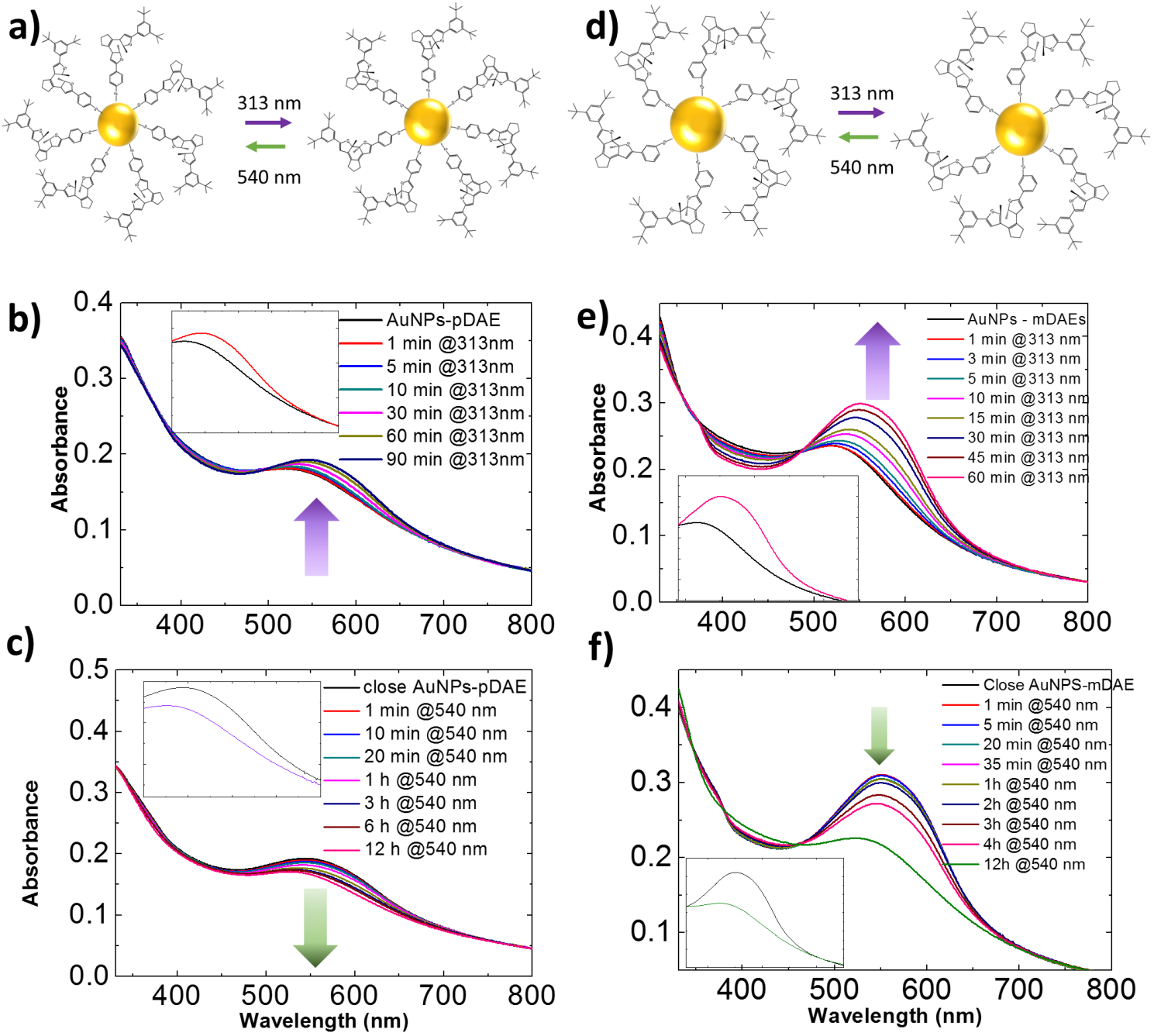

Figure 5.2 Scheme of a) p-DAE/AuNPs and d) m-DAE/AuNPs switching scheme. c) p-DAE/AuNPs absorption spectra from open to closed form under irradiation at 313 nm, in the inset are reported the first and last spectra of the main figure to highlight the growth of 550 nm band addressed to closed form. d) p-DAE/AuNPs absorption spectra from closed to open under irradiation at 540 nm, in the inset are reported the first and last spectra of the main figure to highlight the decreases of 550 nm band. e) m-DAE/AuNPs absorption spectra from open to closed form under irradiation at 313 nm, in the inset are reported the first and last spectra of the main figure to highlight the growth of 550 nm band addressed to closed form. d) p-DAE/AuNPs absorption spectra from closed to open under irradiation at 540 nm, in the inset are reported the first and last spectra of the main figure to highlight the decreases of 550 nm band rm.

In **Figure 5.2a** is reported the isomerization scheme of p-DAE decorated AuNPs. Their absorption spectra (**Figure 5.2b**) is composed by a band at 510 nm addressed to the surface plasmon resonance of AuNPs in toluene,[14] typical of 2.5-3 nm particles size, and a broad band of the open DAE shell. After irradiation with 313 nm, a band at 547 nm increased, typical of the closed form of capping DAE. Irradiation with a green LED (540 nm) allows the DAE to back isomerize to the open form (**Figure 5.2c).** *Meta*-capped AuNPs isomerization is reported in **Figure 5.2d**. The absorption spectra presented the same features of the *para* isomer, and irradiation with 313 nm increased an absorption band at 560 nm (**Figure 5.2e)**. In this case the increase is more pronounced with respect to the *para*. This could be explained with the fact that the *meta* position of the sulphur-gold bond is more effective in decoupling the switching core from NPs plasmon resonance.[20] As showed in **Figure 5.2f** irradiation with 540 nm LED triggered the back isomerization to the open isomer with the decrease of the associated band.

We also tested optical switching of AuNPs within a polymer P(NDI2OD-T2) matrix in thin films. A blend of 10% in weight of AuNPs and P(NDI2OD-T2) in toluene was prepared and spincoated on a clean quartz slide. The obtained film was 40 nm thick (measured with a profilometer). The absorption spectra of the film was recorded and effect of irradiation were studied (see **Figure 5.3**).

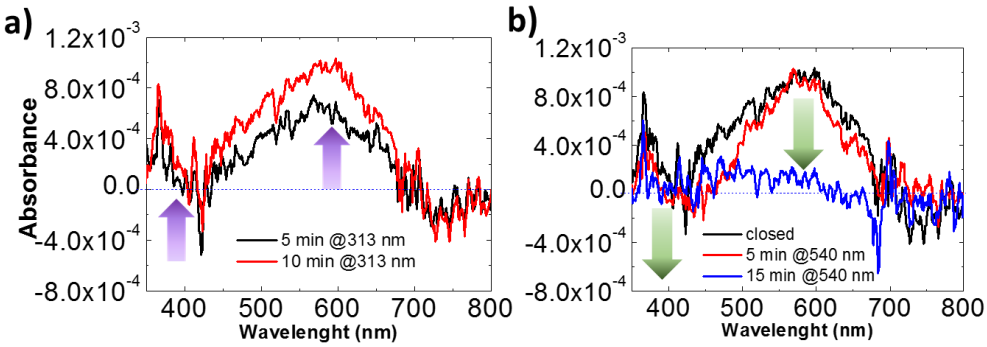

Figure 5.3 a) interconversion of AuNPs capped with open DAE to closed DAE embedded in a P(NDI2OD-T2) thin film as determined by UV–VIS absorption spectroscopy by subtraction of subsequent spectra with different irradiation time at 313 nm. b) interconversion of AuNPs capped with closed DAE (black curve) to open DAE (blue curves) embedded in a P(NDI2OD-T2) thin film as determined by UV–VIS absorption spectroscopy by subtraction of subsequent spectra with different irradiation time at 540 nm

After recording initial spectrum of the film DAE-AuNPs/ P(NDI2OD-T2), irradiation for 5 and 10 minutes was performed under a 313-nm LED light with previously reported irradiation

powers. The recorded spectra after irradiation were subtracted from the initial recorded absorbance, in order to remove the contribution of the polymer absorption bands and surface plasmon resonance band (SPR) of NPs. In **Figure 5.3a** is shown how subsequently subtraction is possible to observe the increase of a band centered at around 560 nm and as well the increase of a band at 365 nm, both typical of closed form of a diarylethenes molecule after 313 nm irradiation Likewise, the back isomerization was observed upon irradiation at 540 nm for 15 minutes and by subtracting the recorded spectra from the initial one (**Figure 5.3b**); the obtained absorbance is zero, proving a complete back isomerization to the open form. This result is fundamental for integration in devices.

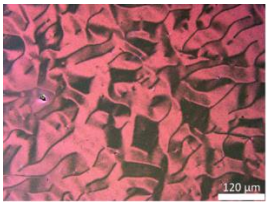

Figure 5.4 Polarized light optical image of spincoated P(NDI2OD-T2) films from toluene

Finally, we proved that P(NDI2OD-T2) films cast from toluene exhibit visible crystallite structures under polarized light due to low solubility of the polymer in toluene (**Figure 5.4**). It has been reported that this method improves crystalline nature in the film in order to achieve better performances.[26] While this process has already been used in top gate device,[26] we decided to test it in bottom-gate transistors which generally have lower mobility than the former ones.

5.3.2 AuNPs size characterization and aggregation analysis.

We imagined with TEM the following samples: p-DAE/AuNPs, m-DAE AuNPs and DDT/AuNPs.

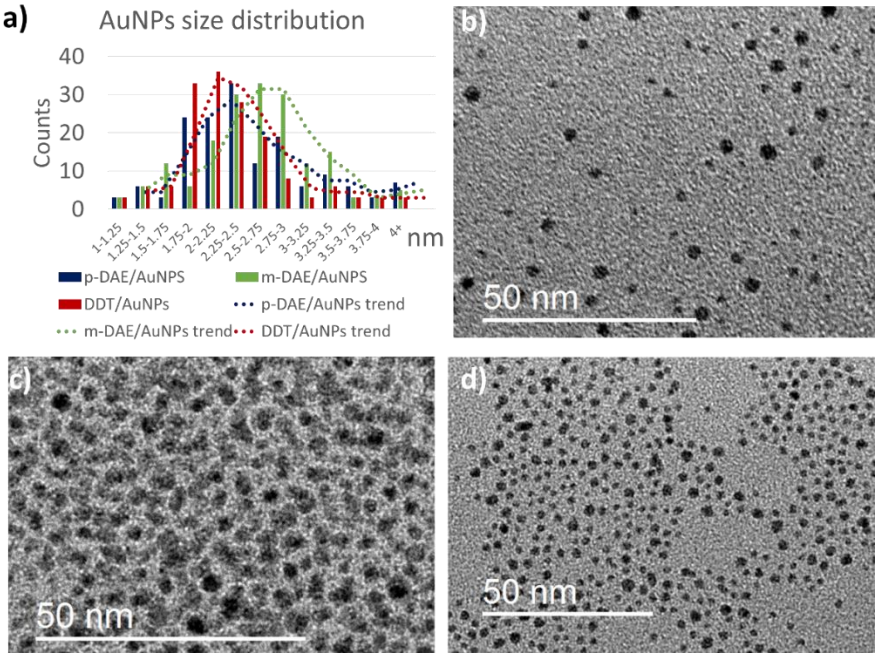

Figure 5.5 a) Size diagram distribution for the different NPs studied, as determined on TEM images. The mean diameter and the standard deviation of the population of particles are expressed in **Table 5.1.** The values represent a statistic analysis of more than 150 particles for each sample. TEM images of the synthesized coated AuNPs drop-cast on carbon-coated, gold-plated copper microscope grids: b) p-DAE/AuNPs, c) m-DAE/AuNPs and d) DDT/AuNPs

Table 5.1 AuNPs average size and standard deviation

	Avg. Size (nm)
p-DAE/AuNPs	2.5 ± 0.8
m-DAE/AuNPs	2.7 ±0.8
DDT/AuNPs	2.2 ±0.5

AuNPs have a size of around 2.5 nm, with DDT/AuNPs the smallest (2.2nm) and the most mono-dispersed. DAE/AuNPs are slightly bigger and with a wider size distribution (**Figure 5.5a**). These size differences are anyhow negligible from an energetic point of view, since over 2 nm diameter AuNPs are not supposed to feature a Kubo gap.[27] It is more interesting to notice the different aggregation of NPs. In **Figure 5.5b, c** are reported representative TEM images of p-DAE/AuNPs and m-DAE/AuNPs respectively. It is evident how *meta* decorated NPs are drastically more aggregated together with respect to *para* moieties.

5.3.3 Bi-component DAE/AuNPs OTFT based on P(NDI2OD-T2)

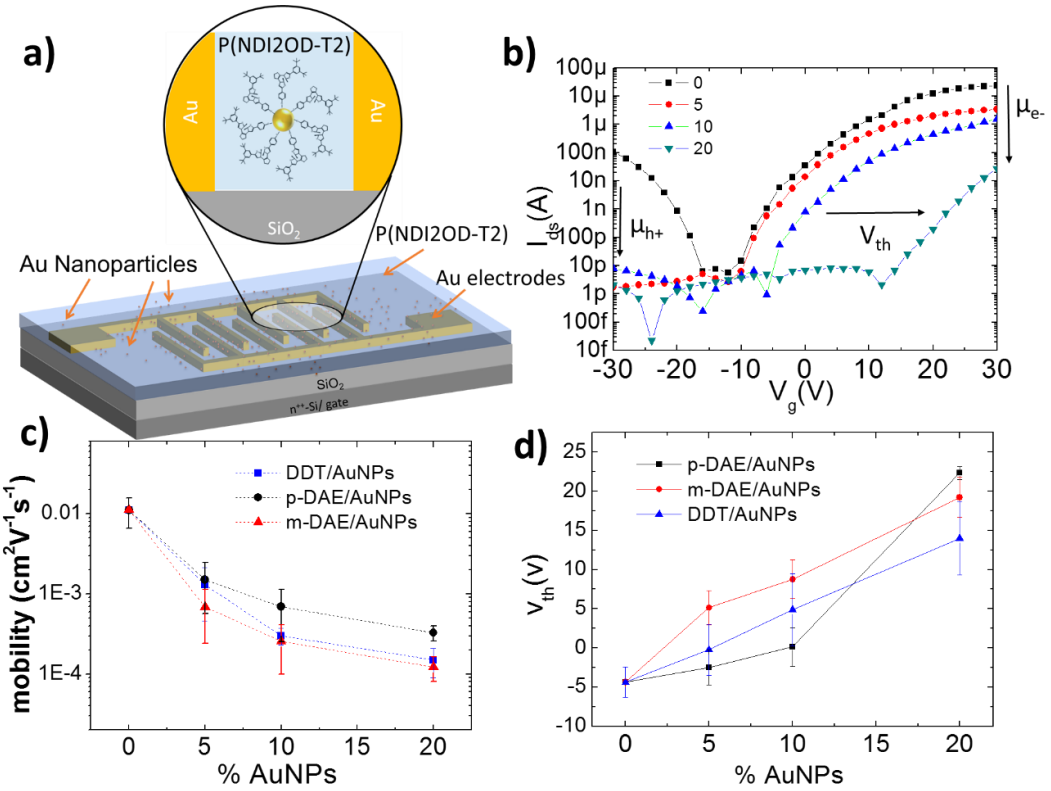

Figure 5.6a) General scheme of the employed system: a bottom-gate/ bottom contact system with a bi-component active layer of P(NDI2OD-T2) and photochromic capped AuNPs blend. b) Transfer characteristics for typical pristine (in black) and p-DAE/AuNPs blends with different percentage in weight (5, 10, 20%). Shift of V_{th}, and changes in electron (μ_{e-}) and holes mobilities (μ_{h+}) are indicated by arrows. Channel length 20µm, V_{ds}=40 V,

W= 10000 µm. c) Average electron mobility values and their standard deviation for pristine and bi-component based OTFTs for all the three capping agent employed at (5, 10, 20) % blends. d) Average V_{th} values and their standard deviation for 20 µm channel length OTFTs for pristine and bi-component based OTFTs for all the three capping agent employed at (5,10,20) % blend percentage.

P(NDI2OD-T2)/AuNPs solutions were spincoated on OTS functionalized substrates with pre-patterned gold electrodes. They were 5 mg/ml in toluene and (5, 10, 20)% in weight of AuNPs. The samples were prepared with the three differently coated NPs, *i.e.* p-DAE, m-DAE and dodecanethiol (DDT). DDT was chosen as a non-light-responsive molecule since it has a com*para*ble molecule length with the employed DAEs. A pristine sample of just P(NDI2OD-T2) for each deposition was prepared as reference. A schematic representation of the system is given in **Figure 5.6a**. All devices prepared showed a very good n-type behavior. The results here presented are an average of 32 different OTFTs from two different batches for pristine, p-DAE and m-DAE devices. DDT results are an average of 16 devices. Pristine devices present an electron saturation mobility of 0.01 $cm^2V^{-1}s^{-1}$ in line with other reported values for bottom-gate devices.[28] The introduction of AuNPs, independently of their capping agent, in the channel had the main effect of a universal decrease of performances, notability a reduction of electron mobility and maximum recorded drain-source current, as reported in **Figure 5.6c.** This is an accordance with our previous findings, in which the main effect of introducing AuNPs is to disturb polymer packing and thus performances. Also the similar effect on electrical output for all the three coating moieties was expected, because employed AuNPs had the same size and size is a more important factor in affecting electrical properties of bi-component OTFTs as we discussed in the previous chapter. Devices with already 5% of AuNPs exhibited a reduction of almost 1 order of magnitude of electron mobility. In general p-DAE/AuNPs OTFTs showed the better performance with respect the other two systems for all different percentages, with m-DAE decorated NPs systems recording the lowest values. This can be addressed to the different aggregation tendency as showed by TEM. *Meta*-DAE capped AuNPs have the strongest propensity to aggregate and this is a detrimental factor for electrical characteristics.[14] . Moreover, AuNPs OTFTs all showed more positive values of threshold voltage. Adding more AuNPs shifted the threshold voltage (V_{th}) to more positive values. This is an indication of charge trapping occurring because of the introduction of nano-objects in the active layer.[11] In **Figure 5.6d** V_{th} values are reported for different amount of NPs in the active layer for the all three systems employed. Reported data are for 20 µm channel length OTFTs. The shift was of 2-5 V for 5% blends and more than 20 V for all 20% blends and as a general trend the shift is increasing with the amount of AuNPs. This behavior is linked to the formation of traps due to introduced disorder and as well to energetic levels of AuNPs as it will be discussed in next paragraph. In **Figure 5.6b** are reported transfer characteristic at source drain voltage (V_{ds} = 40V – saturation regime) for different amount of p-DAE/AuNPs polymer blend. It is evident how increasing the percentage of gold clusters in the device shifted the threshold voltage and as well decreased maximum drain-source current (I_{ds}) which lead to minor mobility. Since P(NDI2OD-

T2) has a partial ambipolar behavior,[29] it is interesting to observe how p-type transport in P(NDI2OD-T2) based OTFET is strongly inhibited by the presence of p-DAE/AuNPs. The same behavior was observed for m-DAE and DDT/AuNPs. In **Table 5.2** are reported just discussed electron (μ_{e^-}) and hole mobility (μ_{h^+}) in saturation regime values for the three systems employed and as well V_{th} values for 20 µm channel length OTFTs.

Table 5.2 Electron and hole mobility and V_{th} for all the studied blends

System		μ_{e^-} ($cm^2V^{-1}s^{-1}$)	μ_{h^+} ($cm^2V^{-1}s^{-1}$)	V_{th} (V)
P(NDI2OD-T2)		$(1.12\pm0.4)\times10^{-2}$	$(8.1\pm0.6)\times10^{-4}$	(-4.4±1.9)
p-DAE/AuNPs	5%	$(1.5\pm0.9)\times10^{-3}$	$(6.0\pm0.4)\times10^{-5}$	(-2.5±2.2)
	10%	$(6.9\pm2.2)\times10^{-4}$	$(2.1\pm0.2)\times10^{-6}$	(0.1±2.5)
	20%	$(3.3\pm0.6)\times10^{-4}$	$(1.9\pm0.5)\times10^{-7}$	(22.3±2.4)
m-DAE/AuNPs	5%	$(6.8\pm4.4)\times10^{-4}$	$(3.2\pm1.4)\times10^{-5}$	(5.1±2.2)
	10%	$(2.5\pm1.5)\times10^{-4}$	$(1.0\pm0.5)\times10^{-6}$	(8.7±2.5)
	20%	$(1.2\pm0.4)\times10^{-4}$	$(0.9\pm0.9)\times10^{-7}$	(19.2±2.5)
DDT/AuNPs	5%	$(1.3\pm0.8)\times10^{-3}$	$(4.2\pm1.2)\times10^{-5}$	(-0.2±3.2)
	10%	$(3.0\pm0.7)\times10^{-4}$	$(0.9\pm1.0)\times10^{-6}$	(4.8±4.5)
	20%	$(1.5\pm0.6)\times10^{-4}$	$(1.5\pm0.7)\times10^{-7}$	(13.9±4.8)

5.3.4 Light Modulation of charge transport and trapping

Photochromic OTFTs systems were irradiated with 313 nm light in order to induce isomerization of capping agents to closed form and then with 540 nm light to achieve back isomerization to open form.

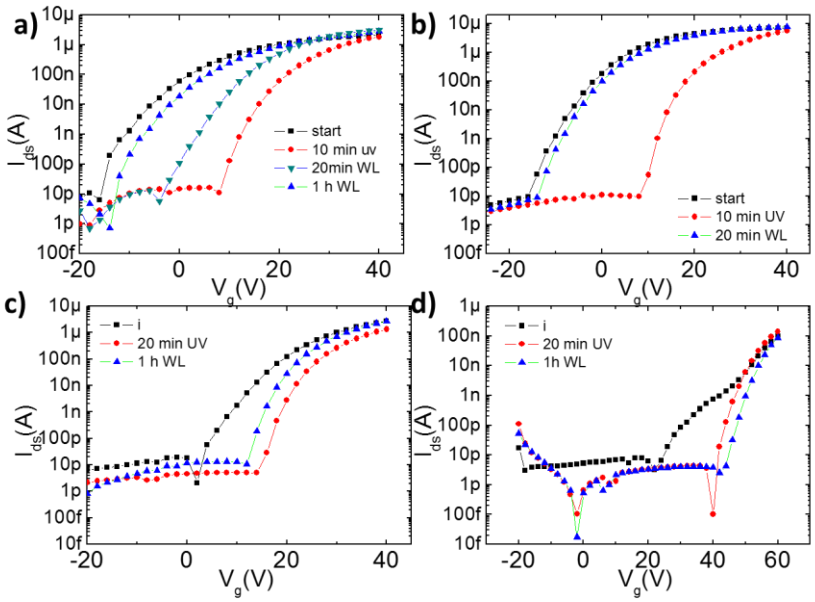

Figure 5.7 a) transfer characteristic of m-DAE/AuNPs - P(NDI2OD-T2) 5% blend device after 313 nm irradiation (UV in red) and after subsequently 540 nm light irradiation (WL in cyan and blue showing not complete recovery. b) transfer characteristic of p-DAE/AuNPs - P(NDI2OD-T2) 5% blend device after 313 nm irradiation (UV in red) and after subsequently 540 nm light irradiation (WL in and blue to bring it back to the original state (in blue).c) transfer characteristic of p-DAE/AuNPs - P(NDI2OD-T2) 10% blend and d) 20% devices after 313 nm irradiation (UV in red) and after subsequently 540 nm light irradiation (WL in and blue) showing not complete recovery. V_{ds}= 40V, channel length L= 20 µm, 10000 µm

In Figure **5.7a** are reported transfer characteristics for m-DAE/AuNPs - P(NDI2OD-T2) 5% blend OTFTs. Top irradiation with 313 nm light (called UV for shortness in the Figure) for 10 minutes caused a shift of V_{th} of 15 V to more positive values, and at the same time and 4-fold increase of mobility. Irradiation with 540 nm light (called white light (WL) in the Figure) caused a backshift towards more negative values of V_{th}, and also to mobility values, but after 1 hour irradiation no complete recovery was observed. Blends with 10% and 20 % did not exhibit any shift. On the other hand, p-DAE/AuNPs - P(NDI2OD-T2) 5% blend OTFTs performed better, as reported in **Figure 5.7b**. After 10 minutes of UV irradiation a shift of +20 V was measured together with a 3-fold increase of mobility. Further irradiation did not lead to further changes. In this case, irradiating for 20 minutes at 540 nm was enough to recover the initial mobility and V_{th}. In addition, blends with a higher amount of coated AuNPs were tested. In **Figure 5.7c** it is reported the effect of irradiation on a 10% p-DAE blend. UV irradiation triggered a smaller shift of V_{th} with respect to 5% blend, and mobility increased as previously discussed, but 1 hour irradiation at 540 nm light was not enough to bring back original values of both *para*meters. The same was observed in a 20% blend (**Figure 5.7d**) were it was necessary to apply a gate voltage up to +60 V to observe the switch, since the starting V_{th} value was already close to 30 V and no switch back was observed after 1 hour irradiation.

The reason for the different light response of the two system could be ascribed partially to AuNPs aggregation as reported by TEM images. When they are more concentrated, AuNPs tend to stack together, and by steric hindrance photo-isomerization can be inhibited.[30] In particular has already been demonstrated that a polymeric matrix favors aggregation among AuNPs.[14] It is remarkable that m-DAE/AuNPs - P(NDI2OD-T2) showed not only the slower light isomerization even at 5% blends, but also the lower performances for all blends with respect to the *para* capped NPs. This can be attributed to the stronger tendency to aggregate together for m-DAE coated NPs as showed by TEM image **Figure 5.5c,** which reveals a very high aggregation of *meta* capped NPs. This tendency to stack together is way less marked in p-DAE/AuNPs (**Figure 5.5b**). The reason for this big difference in aggregation between the *meta* and *para* capped AuNPs is not clear. A possible explanation could be that the less linear form of the *meta* DAE results in lower density of thiols on AuNPs surface, leaving more gold surface naked, therefor increasing aggregation tendency. We decided to explore further the 5% p-DAE/AunPs - P(NDI2OD-T2) blend isomerization performances as shown in **Figure 5.8**. OTFT 5% based p-DAE/AuNPs - P(NDI2OD-T2), 20 µm channel length OTFTs was studied by performing irradiation cycles: 10 min exposure time at 313 nm and 20 min at 540 nm

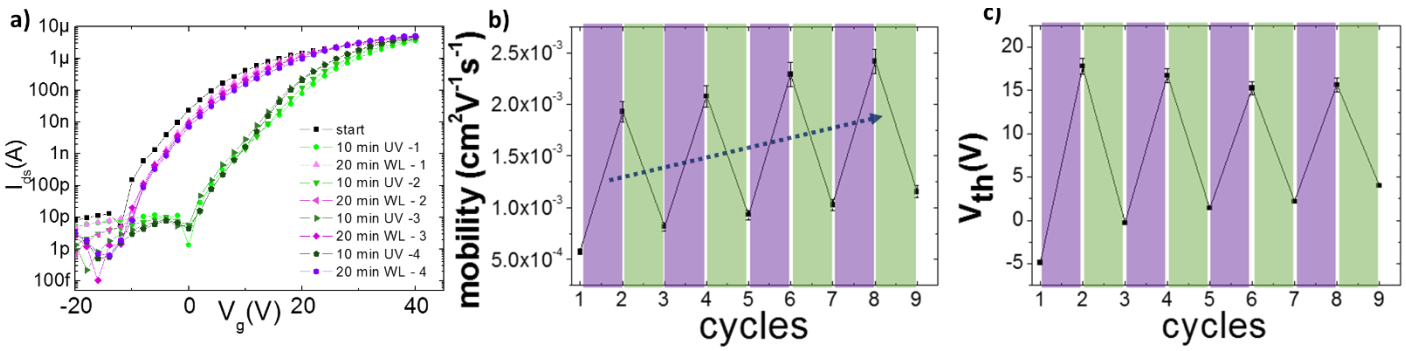

.

Figure 5.8 a) saturation transfer characteristic behavior under irradiation cycles. Starting curve is reported in black, closed p-DAE/AuNPs transfers curves in violet tones and back switched open p-DAE/AuNPs curves in green tones. V_g = +40V.b) Mobility b) and c) V_{th} values extracted from a) transfer curves for subsequently irradiation cycles performed. Arrow in b) indicates mobility trend due to irradiation cycles. Reported error bars represents fitting error.

In **Figure 5.8a** transfer characteristics recorded at V_{ds} = 30V are portrayed. The starting curve is depicted in black: a mobility of 0.5 x 10^{-3} $cm^2V^{-1}s^{-1}$ has been extracted and as well a V_{th} value of -4.9 V. The curve traced after 10 min UV irradiation is reported in red. A shift of 22.8 V of V_{th} was found but the I_{ds} measured at V_g = +40V had almost the same value of the initial one. A mobility value of 2 x 10^{-3} $cm^2V^{-1}s^{-1}$ with a 4-fold increase was found. The irradiation at 540 nm for 20 minutes shifted back both mobility and V_{th} close to the initial value. Further irradiation did not lead to any significant change. As reported in **Figure 5.8a** and highlighted in **Figure 5.8b**, the same behavior was recorded in the following performed irradiation cycles. It is noteworthy that mobility presented a general rising trend after each cycle. On the opposite irradiation effect on threshold voltage (**Figure 5.8c**) caused a lesser shift at each cycle performed, with a starting shift of a 22.8 V and a shift of 12 V after 9 cycles of UV/WL.

5.3.5 Characterization of the energy levels and hysteresis analysis.

In order to better understand energetic interactions and charge transport mechanism in the system ambient photoelectron spectroscopy (ambient-PS) were performed on film casted on silicon oxide with previously described procedure. Pristine P(NDI2OD-T2) film had a measured ionization energy (I_p) = 5.7 eV, being slightly deeper of literature reported values[29], which can be explained in view of the a different orientation of the polymer molecules due to the casting from toluene.[31] This allowed us to calculate a LUMO level at 4.1 eV adding the optical bandgap (1.55 eV) [32] of P(NDI2OD-T2) to the HOMO value. Blends (20%) of AuNPs/ P(NDI2OD-T2) exhibited the same value as for the pristine one, with variation lower than the instrument sensibility. Since A-PS extracts electron just from the first 5 nm of the sample, this measurement is an indirect proof that AuNPs were more concentrated at the bottom of the film. In order to evaluate the contribution on AuNPs we deposited AuNPs on top on polymer thin film, by cooling the sample at (-78°C) with dry ice, and then spin-coating 200 µl of AuNPs solution 1 mg/ml on it. The so obtained film had an I_e = 5.15eV. Irradiation with 313 nm at for

1 h caused a shift in I_e to 5.42 eV, for a difference of 270 meV as presented in **Figure 5.9a**. Both values sit in the band gap of the semiconductor, meaning that they can act as a trap for charges. In the case of electrons, c-DAE value implies a deeper trap state with respect to o-DAE. Similar values were found for m-DAE AuNPs as reported in **Table 5.**

Table 5.3 Determined ionization potential of different employed systems

System		Ionization Energy (eV)
P(NDI2OD-T2)		5.70±0.05
OPEN p-DAE/AuNPs - P(NDI2OD-T2)	Blend	5.63±0.05
	On top	5.15±0.05
CLOSED p-DAE/AuNPs - P(NDI2OD-T2)	Blend	5.64±0.05
	On top	5.42±0.05
OPEN m-DAE/AuNPs - P(NDI2OD-T2)	Blend	5.68±0.05
	On top	5.11±0.05
CLOSED m-DAE/AuNPs - P(NDI2OD-T2)	Blend	5.63±0.05
	On top	5.30±0.05

In view of its ionization energy, AuNPs can trap electrons, and this is the reason, together with induced defects in crystalline structure due to NPs volume, of decreased performances of devices integrating the AuNPs blend. On the same time they act also as holes traps, and thus hole-conduction is suppressed by their presence. While in theory no difference between *para* and *meta* capped NPs system should be found, the stronger tendency of undergoing aggregation of the latter hinder their switching capabilities.

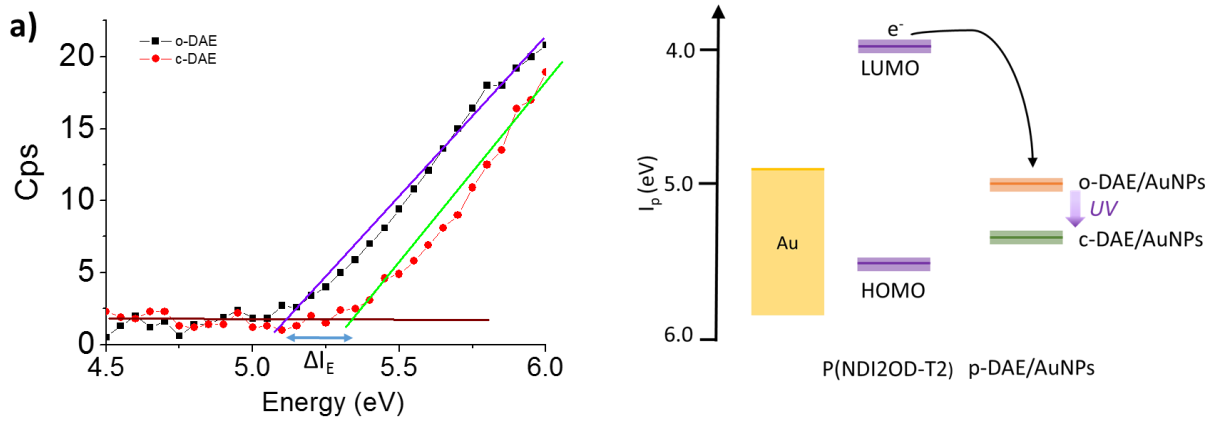

Figure 5.9 a) Square roots of photoelectron yield *vs.* energy spectra of p-DAE/AuNPs deposited on top of P(NDI2OD-T2) in open form (black) and p-DAE/AuNPs deposited on top of P(NDI2OD-T2 (red)in closed form. Reported lines in the figure are just a guide for eyes and not real linear regression of points collected. b) Schematic representation of the ionization energy of employed components.

Electrons are injected from gold electrodes (W_f=4.8eV) to the LUMO of P(NDI2OD-T2) which sits at 4.1 eV. An energetically favorable transition for an electron would be towards the nanoparticle, whose I_e is at 5.15eV as depicted in **Figure5.9b**. However, the electron will have to overcome the tunneling barrier of the capping DAE, which is particularly high for the open form.[23] Henceforward irradiation has two effect on the system on two effect: the first is to increase ionization potential and thus AuNPs act as more effective traps for electrons when

DAEs are closed. The second is related to the more conjugation of c-DAE form, which lowers the tunneling barriers that carriers have to overcome to travel inside NP core.[30] The combination of the two effects accounts for the dramatic shift of threshold voltage observed before and after UV irradiation. With respect to Baeg *et al.* [11] we achieved the same V_{th} window with 10 minutes irradiation instead of applying a 90 V voltage pulse. The transfer characteristics of the photochromic system demonstrated that, when in open form some traps are available and thus a small positive shift of threshold voltage is measured with respect to pristine OTFTs. On the other hand, when DAE on AuNPs are in the closed form, trap states generated by NPs are more effective because of their higher ionization energy. At the same time the lower tunneling barrier due to increased conjugation of DAE facilitate charge interactions between the NPs and the semiconductive matrix. This is reflected in the higher voltage needed to turn on the transistor embedding c-DAE capped AuNPs. At low gate voltage charges are efficiently collected by AuNPs and when it reaches V_{th}, charge carriers start to be de-trapped with the effect of increasing apparent device mobility. In fact mobility is an intrinsic properties of a semiconductor, and hence, registered increased value can be ascribed to release electrons after V_{th} is reached. This means that isomerization to closed form has the effect of facilitating charge trapping before V_{th}, when charges are trapped by energetically favorable traps states of NPs, and also to facilitate charge releasing mechanism after V_{th} is reached, since the decrease in tunneling resistance favors de-trapping of electrons.at higher bias voltages.

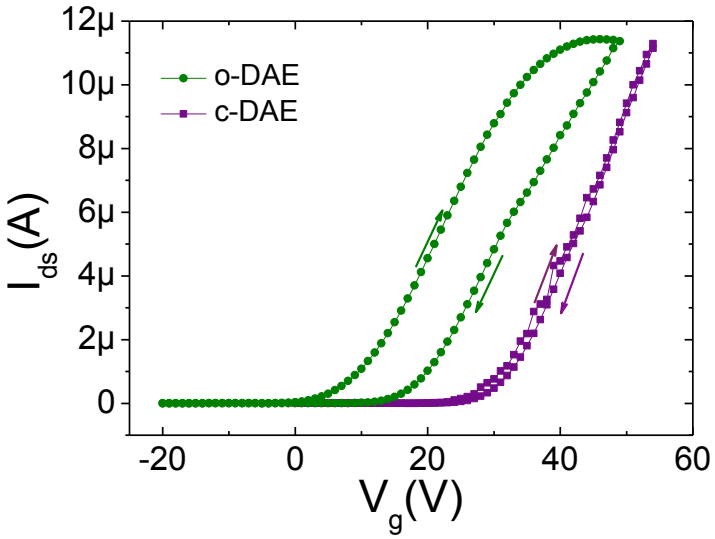

Figure 5.10 Hysteresis in open p-DAE/AuNPs 5% blend in P(NDI2OD-T2) in green and hysteresis in closed p-DAE/AuNPs 5% blend in P(NDI2OD-T2) of the very same sample traced after 10 min 313 nm irradiation. Curves has been traced starting from 20V before V_{th}, in order to have the same conditions. V_{ds}= 40V reported in magenta. Channel length L= 20 µm, 10000 µm.

Anyhow this process is not completely effective and some charges remain trapped as proved by increasing measured device mobility after each irradiation together with the decrease of V_{th} shift between subsequently irradiations. Hysteresis measurements, *i.e.* a continuous sweep from

negative to positive voltage and thus again to negative voltage were performed to explore this effect.

In open-DAE/AuNPs system, hysteresis was recorded with a threshold voltage window of about 10.5 V (**Figure 5.10**), with the backwards curves displaying a lower current. This result confirmed that charges were trapped in NPs and not easily released, thus a lower current is recorded in backward transfer curve. Conversely, when the DAE are in their closed form, a shift of about 22 V towards more positive value of the initial traced transfer curve was measured, yet backwards sweep showed almost no hysteresis (less than 4 V), indicating an higher number of charged trapped and at the same time an efficient release after V_{th} is reached, as a result of decreased tunneling barrier of the closed DAE. Pristine devices presented a negligible hysteresis, as previously proved for P(NDI2OD-T2) based OTFTs.

5.3.6 Blank experiment – DDT/AuNPs blends with P(NDI2OD-T2)

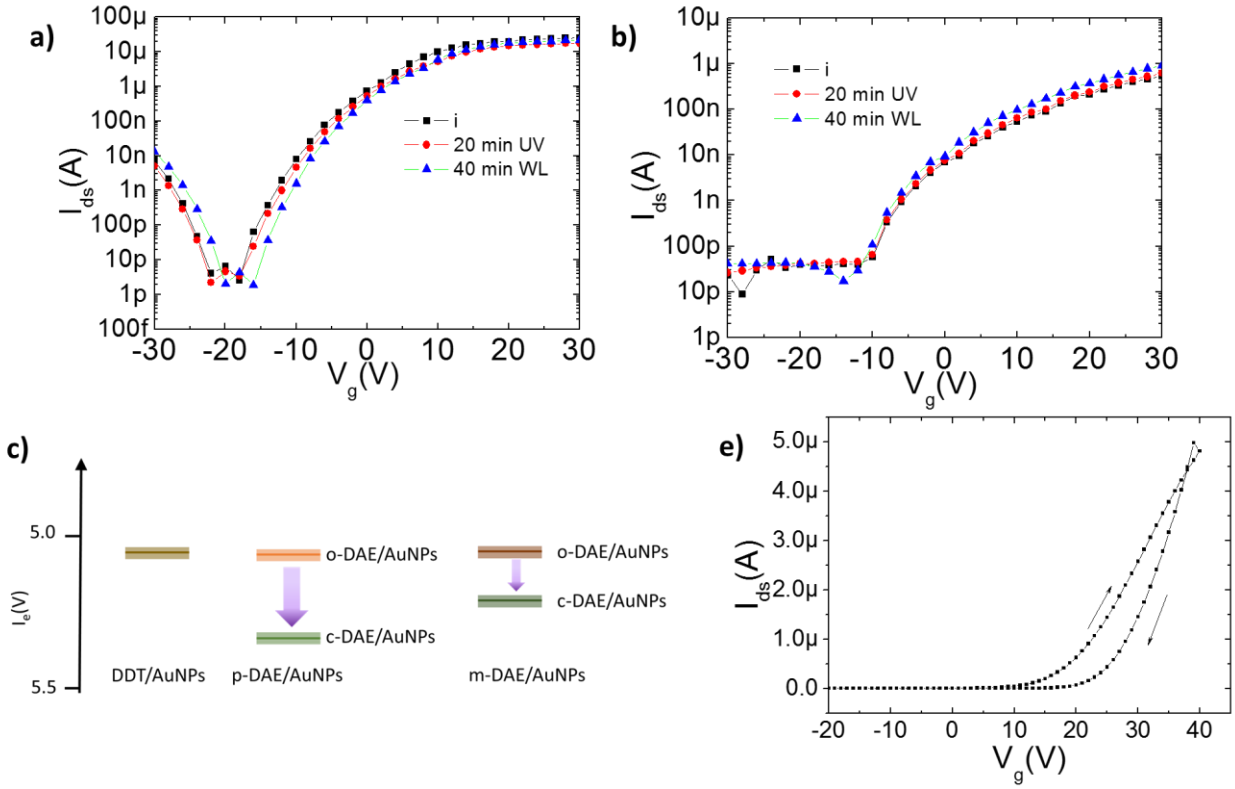

Figure 5.11 a) transfer characteristic of pristine P(NDI2OD-T2) traced before and after irradiation at 313 nm (UV) and 540 nm (WL). b) transfer characteristic of DDT/AuNPs P(NDI2OD-T2) 5% blend traced before and after irradiation at 313 nm (UV) and 540 nm (WL). c) Energy levels diagram of all the three different decorated AuNPs employed in the system d) Hysteresis in DDT/AuNPs 5% blend in P(NDI2OD-T2) transfer characteristics. V_{ds}= 30 V Channel length L= 20 µm, 10000 µm.

In order to prove that observed changes really arise from AuNPs in the active layer, we performed the same irradiation cycles on pristine device. We irradiated 20 min at 313 nm and then 40 min at 540 nm. As showed in **Figure 5.11a** after irradiation no differences in traced

transfer curves were observed. Also to make sure that current modulation by light arises form NPs decorated with DAE we performed the same cycles on DDT/AuNPs - P(NDI2OD-T2) based OTFTs (5% blend). As revealed in **Figure 5.11b** no changes were observed. In **Figure 5.11c** the ionization potential of all three differently decorated AuNPs are showed as measured by Ambient-PS. DDT/AuNPs - P(NDI2OD-T2) had a I_e of 5.11 eV the same value of DAEs decorated AuNPs on P(NDI2OD-T2). This confirm our previously results that capping agent has little influence on AuNPs I_p especially if they are similar, [14] not conjugated in this case. On the other hand the change in conjugation is effective on shifting the value up to 250 meV. Finally we tested hysteresis in DDT/AuNPs - P(NDI2OD-T2) based OTFTs. Figure **45.11d** shows that this system behaves similarly to p-DAE/AuNPs in open form, with a hysteresis window of about 8V due to partial charge trapping of AuNPs, a behavior consistent with o-DAE system.

5.4 CONCLUSIONS

In conclusion, we have studied the effect of the photomodulable conjugation of the AuNPs coating layer on the charge transport of n-type polymer bi-component OTFTs. Taking advantage of optical responsive nature of DAE we were able to modulate conjugation in the very same system employing light and charge transfer between AuNPs core and the semiconductor is mediated by the coating layer. The measures here reported are consistent with charge trapping due to AuNPs enhanced by conjugated capping agents. Memory window shift can exceed 20 V, and be reversely modulated by light multiple times, despite complete recovery was not possible. The reason of such a marked outcome could be addressed to the combined effect of increased trapping efficiency of open-DAE capped NPs and their lower tunneling barrier. Anyhow the presence of AuNPs in the active layer led to a decrease in general OTFTs performance. We also proved how AuNPs aggregation is fundamental to achieve good cyclability and their amount in the blend is a crucial factor in enhancing this kind of system. Overall the easy synthetic route and processability make this system a suitable candidate for efficient memory opto-electronic devices, charge storage, light sensing and finally by combining AuNPs light responsive nature with photochromic molecules is a promising system for more efficient light harvesting solar cells.

5.5 REFERENCES

1. Klajn, R.; Stoddart, J. F.; Grzybowski, B. A., Nanoparticles functionalised with reversible molecular and supramolecular switches. Chem. Soc. Rev. 2010, 39, 2203-2237.

2. Aleshin, A. N., Light-emitting transistor structures based on semiconducting polymers and inorganic nanoparticles. POLYM SCI SER C+ 2014, 56, 47-58.

3. Scott, J. C.; Bozano, L. D., Nonvolatile Memory Elements Based on Organic Materials. Adv. Mater. 2007, 19, 1452-1463.

4. Edwards, E. W.; Chanana, M.; Wang, D., Capping Gold Nanoparticles with Stimuli-responsive Polymers to Cross Water−Oil Interfaces: In-Depth Insight to the Trans-Interfacial Activity of Nanoparticles. J. Phys. Chem. C 2008, 112, 15207-15219.

5. Milano, G.; Santangelo, G.; Ragone, F.; Cavallo, L.; Di Matteo, A., Gold Nanoparticle/Polymer Interfaces: All Atom Structures from Molecular Dynamics Simulations. J. Phys. Chem. C 2011, 115, 15154-15163.

6. Walter, M.; Akola, J.; Lopez-Acevedo, O.; Jadzinsky, P. D.; Calero, G.; Ackerson, C. J.; Whetten, R. L.; Gronbeck, H.; Hakkinen, H., A unified view of ligand-protected gold clusters as superatom complexes. Proc. Natl. Acad. Sci. U. S. A. 2008, 105, 9157-9162.

7. Rao, C. N. R.; Kulkarni, G. U.; Thomas, P. J.; Edwards, P. P., Metal nanoparticles and their assemblies. Chem. Soc. Rev. 2000, 29, 27-35.

8. Tseng, C.-W.; Tao, Y.-T., Electric Bistability in Pentacene Film-Based Transistor Embedding Gold Nanoparticles. J. Am. Chem. Soc. 2009, 131, 12441-12450.

9. Tseng, C.-W.; Huang, D.-C.; Tao, Y.-T., Azobenzene-Functionalized Gold Nanoparticles as Hybrid Double-Floating-Gate in Pentacene Thin-Film Transistors/Memories with Enhanced Response, Retention, and Memory Windows. ACS Appl. Mater. Interfaces 2013, 5, 9528-9536.

10. Zhou, Y.; Han, S.-T.; Xu, Z.-X.; Roy, V. A. L., Controlled Ambipolar Charge Transport Through a Self-Assembled Gold Nanoparticle Monolayer. Adv. Mater. 2012, 24, 1247-1251.

11. Baeg, K.-J.; Noh, Y.-Y.; Sirringhaus, H.; Kim, D.-Y., Controllable Shifts in Threshold Voltage of Top-Gate Polymer Field-Effect Transistors for Applications in Organic Nano Floating Gate Memory. Adv. Funct. Mater. 2010, 20, 224-230.

12. Han, S.-T.; Zhou, Y.; Xu, Z.-X.; Roy, V. A. L., Controllable threshold voltage shifts of polymer transistors and inverters by utilizing gold nanoparticles. Appl. Phys. Lett. 2012, 101, 033306.

13. Han, S.-T.; Zhou, Y.; Yang, Q.-D.; Lee, C.-S.; Roy, V. A. L., Poly(3-hexylthiophene)/Gold Nanoparticle Hybrid System with an Enhanced Photoresponse for Light-Controlled Electronic Devices. Part. Part. Syst. Charact. 2013, 30, 599-605.

14. Mosciatti, T.; Orgiu, E.; Raimondo, C.; Samori, P., The role of size and coating in Au nanoparticles incorporated into bi-component polymeric thin-film transistors. Nanoscale 2014, 6, 5075-5080.

15. Zhang, J. J.; Zou, Q.; Tian, H., Photochromic Materials: More Than Meets The Eye. Adv. Mater. 2013, 25, 378-399.

16. Zhu, M. Q.; Zhu, L. Y.; Han, J. J.; Wu, W. W.; Hurst, J. K.; Li, A. D. Q., Spiropyran-based photochromic polymer nanoparticles with optically switchable luminescence. J. Am. Chem. Soc. 2006, 128, 4303-4309.

17. Raimondo, C.; Reinders, F.; Soydaner, U.; Mayor, M.; Samori, P., Light-responsive reversible solvation and precipitation of gold nanoparticles. Chem. Commun. 2010, 46, 1147-1149.

18. Raimondo, C.; Crivillers, N.; Reinders, F.; Sander, F.; Mayor, M.; Samorì, P., Optically switchable organic field-effect transistors based on photoresponsive gold nanoparticles blended with poly(3-hexylthiophene). Proc. Natl. Acad. Sci. 2012, 109, 12375-12380.

19. Matsuda, K.; Irie, M., Diarylethene as a photoswitching unit. J. Photochem. Photobiol. C: Photochem. Rev. 2004, 5, 169-182.

20. Tsujioka, T.; Irie, M., Electrical functions of photochromic molecules. J. Photochem. Photobiol. C: Photochem. Rev. 2010, 11, 1-14.

21. Kudernac, T.; van der Molen, S. J.; van Wees, B. J.; Feringa, B. L., Uni- and bi-directional light-induced switching of diarylethenes on gold nanoparticles. Chem. Commun. 2006, 3597-3599.

22. Perrier, A.; Tesson, S.; Jacquemin, D.; Maurel, F., On the photochromic properties of dithienylethenes grafted on gold clusters. Computational and Theoretical Chemistry 2012, 990, 167-176.

23. van der Molen, S. J.; Liao, J.; Kudernac, T.; Agustsson, J. S.; Bernard, L.; Calame, M.; van Wees, B. J.; Feringa, B. L.; Schönenberger, C., Light-Controlled Conductance Switching of Ordered Metal−Molecule−Metal Devices. Nano Lett. 2009, 9, 76-80.

24. Matsuda, K.; Yamaguchi, H.; Sakano, T.; Ikeda, M.; Tanifuji, N.; Irie, M., Conductance Photoswitching of Diarylethene−Gold Nanoparticle Network Induced by Photochromic Reaction. J. Phys. Chem. C 2008, 112, 17005-17010.

25. Leff, D. V.; Ohara, P. C.; Heath, J. R.; Gelbart, W. M., Thermodynamic Control of Gold Nanocrystal Size: Experiment and Theory. J. Phys. Chem. 1995, 99, 7036-7041.

26. Luzio, A.; Criante, L.; D'Innocenzo, V.; Caironi, M., Control of charge transport in a semiconducting copolymer by solvent-induced long-range order. Sci. Rep. 2013, 3.

27. Roduner, E., Size matters: why nanomaterials are different. Chem. Soc. Rev. 2006, 35, 583-592.

28. Mosciatti, T.; Haar, S.; Liscio, F.; Ciesielski, A.; Orgiu, E.; Samorì, P., A Multifunctional Polymer-Graphene Thin-Film Transistor with Tunable Transport Regimes. ACS Nano 2015, 9, 2357-2367.

29. Yan, H.; Chen, Z.; Zheng, Y.; Newman, C.; Quinn, J. R.; Dotz, F.; Kastler, M.; Facchetti, A., A high-mobility electron-transporting polymer for printed transistors. Nature 2009, 457, 679-686.

30. Kronemeijer, A. J.; Akkerman, H. B.; Kudernac, T.; van Wees, B. J.; Feringa, B. L.; Blom, P. W. M.; de Boer, B., Reversible Conductance Switching in Molecular Devices. Adv. Mater. 2008, 20, 1467-1473.

31. Rivnay, J.; Steyrleuthner, R.; Jimison, L. H.; Casadei, A.; Chen, Z.; Toney, M. F.; Facchetti, A.; Neher, D.; Salleo, A., Drastic Control of Texture in a High Performance n-Type Polymeric Semiconductor and Implications for Charge Transport. Macromolecules 2011, 44, 5246-5255.

32. Mori, D.; Benten, H.; Okada, I.; Ohkita, H.; Ito, S., Highly efficient charge-carrier generation and collection in polymer/polymer blend solar cells with a power conversion efficiency of 5.7%. Energy Environ. Sci. 2014, 7, 2939-2943.

6. Tunable charge injection in high performance polymeric thin-film transistors

6.1 INTRODUCTION

The fabrication and optimization of organic and polymeric optoelectronic devices have been the focus an active research endeavor during the last few years.[1,2] The use of multiple components in a single device opens naturally the door to multifunctional devices.[3] Such challenge can be targeted by considering as a prototypical device type an Organic Thin-Film Transistor (OTFT), and designing a device architecture where all interfaces could be decorated with functional molecular systems. This includes the interface between different components blended as electroactive (i.e. semiconducting) material and the interface between the electroactive material with either the gate electrode or the source and drain electrodes.[4] The main advantage of such an approach is to be able to use independent stimuli to address the individual component by changing their state, thereby attaining a control over the operation of the current passing in the transistor channel. Beside the electrical control via application of a given voltage to the gate electrode, another stimuli that can be easily tunable and leaves no side product is light.[5] In this framework, photochromic molecules are light-responsive elements which can be integrated in organic electronics devices towards logic solutions.[6,7] The ultimate goal is to develop approaches and devices that combine easy processability,[8] flexibility[9] and most important, imprinting of simple but not trivial multifunctional character.[4] Three are the most relevant photochromic molecules that can be used towards this end: azobenzenes (AZOs), diarylethenes (DAEs) and spiropyrans/-oxazines.[10] All these systems are able to undergo isomerization under irradiation with appropriate wavelength between isomers holding different properties.[11]

Among many possible approaches,[4] direct use of photochromic molecules as active layer is certainly a feasible choice. Nevertheless it presents a trade-off between very high switching

ratio in output current and very low carrier mobility devices.[12] A way to overcome this issue is to take advantage of both photochromic molecules and semiconducting organic materials, by blending to generate a bi-component electro- and photoactive layer, while another strategy relies on the use of photochromic molecules to functionalize electrodes and therefore tuning the charge injection at the interface with a semiconductor. For the first method a previous study performed by our group demonstrated that by design is possible to carefully tuning HOMO/LUMO levels of DAEs to integrate them in a polymeric matrix for modulating charge transport by irradiation.[13] Also this method is very general and by employing small semiconducting n- or p-type molecules, high performance devices can be obtained.[14,15] A different way is to take advantage of thiol-functionalized photochromic molecules that can be chemisorbed as self-assembled monolayers (SAMs) on gold electrodes, and thus used to modulate change injection by varying the tunneling barrier[16] or the work function simply using light irradiation at defined wavelengths.[17] These seminal studies were based on azobenzene SAMs integrated in a bottom-contact bottom-gate device. The mayor limitation of that approaches is the fact that *(i)* the use of bottom gate configuration determines a pretty limited current change as a result of the optical stimuli, *(ii)* the cis isomer is not thermodynamically stably thereby impeding the generation of a truly bi-stable device., (iii) azobenzene switching mechanism is fatigue-prone due to molecular geometry rearrangement.

In this framework we decided to bring this approach to a further level in terms of magnitude of output current modulation, electrical performances and stability. We employed a top-gate/bottom contact device geometry in order to have contribution from all the electrode surface to charge injection. With regard to the chemical species, we used thiolated DAEs [18] specifically designed for this scope. With respects to previously employed thiolated AZOs,[16] they present many advantages. The *first* is that both DAEs form are thermally stable with a high efficient isomerization[19], while AZO *cis* form thermally recover to *trans* more energetically favorable form.[20] The *second* advantage, is that for DAEs isomerization concern the molecular core conjugation and not molecular geometry. Low geometrical stress is hence expected in isomerization cycles improving fatigue resistance.[21] Conversely AZOs isomerization needs to physical move the interface[22] to occur, with subsequent molecular semiconductor rearrangement, causing a decrease of isomerization yield as function of time.[16] The *third* aspect is that DAEs induced light change is related to a chemical bond formation that drives to an extended conjugation. This is reflected on lowered band gap which is reflected in an increased conductance of at least two order magnitude,[23] while AZOs switch modulates tunneling distance with lower modulation output.[16] In order to maximize the just described benefits we designed diarylethenes moieties exposing a thiolated functional group (t-DAE) in the α-position, and a di-tert-butyl groups in the ω-position. The former enables efficient molecular chemisorption on metallic surfaces forming Self Assembled Monolayers (SAMs),[24] the latter makes possible to impart a hydrophobic nature to a surface [25] Our molecules have an absorption band at 313 nm when in open form, and two absorption band at 365 and 540 nm when in closed

form. Irradiating at these wavelengths it is possible to activate the switching between the two isomeric forms. Isomeric forms are: so called open-DAE (o-DAE), *i.e.* not conjugated, and a closed-DAE (c-DAE) form, which is conjugated. Molecular formula for open isomer (o-DAE) is reported on top **Figure 6.1a** and for closed form (c-DAE) on top **Figure 6.1b.** Different issues have been addressed in literature with regard to the properties of DAEs SAM on gold. The main aspect is the effect of gold-sulphur bond and its influence on the DAE core switching ability.[26,27] It has been demonstrated that a phenyl ring between the sulphur and the switching core is fundamental to achieve isomerization from both isomers.[28] Most important differences in conductance between the two forms have been deeply explored. Theoretically it has been calculated a decrease in HOMO/LUMO gap due to extended conjugation[26] and practical experiment found difference in conductance among two isomers exceeding two orders of magnitude.[23] We carefully studied optical, electrical and energetic properties of Au functionalized with t-DAE SAM and then we functionalized electrodes of OTFTs. In particular we aimed top-gate devices to maximize effective active electrodes' area involved in charge injection and minimize contact resistance, as previously discussed. In this regard, P(NDI2OD-T2)-based OTFTs were employed in order to have high performance devices. P(NDI2OD-T2) is an n-type semiconductor that reach device mobility > 1 $cm^2 V^{-1}s^{-1}$ in top-gate geometry .[29]

6.2 MATERIALS AND METHODS

SAM growth on gold: 2.5 mg of t-DAE were dissolved in 5 ml of EtOH (1 mM). Solution was left stirred 30 minutes to ensure complete solubilisation. For preparing c-DAE samples, solution was irradiated at 313 nm for 1h while stirred. Gold sample freshly cleaned with ozone (5-min ozone irradiation and 25-min incubation) were then dipped in it and left for 72h. Samples were then rinsed with 10 ml of warm EtOH, 15 ml of chloroform and then dried under a gently blow of nitrogen. MPT (mono-phenyl thiol) samples were prepared with the same procedure, the only difference was solution concentration of 5mM and dipping time of 12h.

UV-Vis experiments: Semitransparent substrates were prepared for UV-Vis absorption experiments evaporating 3nm of chromium followed by 15 nm of gold on quartz slides previously cleaned by sonication in acetone, isopropanol and UV-ozone treatment. UV-Vis absorbance spectra were recorded with a UV-Vis Jasco V-650 spectrophotometer. The spectra concerning the switching of the self-assembled monolayers were recorded in nitrogen atmosphere irradiating the sample in-situ.

Irradiation was performed using the following light sources.

- LED with wavelength 310 ± 5 nm (UVTOP310 by Roithner Laser Technik Gmbh)
- UV lamp with centered wavelength 312 ± 15 nm (HeroLab).
- Fiber coupled LED with wavelengths 540 ± 5 nm (ThorLabs).

XPS analysis: XPS analyses were carried out on a Thermo Scientific K-Alpha X-ray photoelectron spectrometer with a basic chamber pressure of about 10^{-8} mbar and an Al anode as the X-ray source (x-ray radiation of 1486 eV). Spot sizes between 30 µm and 400 µm were

used. Survey spectra are an average of 10 scans with a pass energy of 200.00 eV and a step size of 1 eV. High-resolution spectra are an average of 10 scans (or even 50 or 100 when needed) with a pass energy of 50.00 eV and a step size of 0.1 or 0.05 eV.

Device Preparation: High quality quartz slides were purchased from SCIENCE SERVICES GmbH and were cleaned blowing them with nitrogen. P(NDI2OD-T2) poly[N,N-9-bis(2-octyldodecyl)-naphthalene-1,4,5,8-bis (dicarboximide)-2,6-diyl]-alt-5,59-(2,29-bithiophene)] was purchased from Polyera and used as received. Cytop and its solvent were purchased from Ashai Glass Japan. Interdigitated electrodes were evaporated on quartz slides by using evaporation masks. 3 nm of chromium were followed by evaporation of 15 nm of gold. Samples were ozone-cleaned and immersed in t-DAE solution (this step was not used for pristine P(NDI2OD-T2) samples.) After cleaning, 520µl of a solution 5mg/ml of P(NDI2OD-T2) in chloroform were spincast and annealed at 70° for 2h. The resulting film was 60 nm thick. Samples were cooled down to room temperature. Then 1020 µl of Cytop/Cytop-solvent solution 9/1 were deposited on top and samples were annealed 4 h at 70°C. All this procedure were performed in nitrogen environment. Resulting dielectric film thickness was about 750 nm. Finally 100 nm of aluminum were deposited on top as gate electrode. Each sample had 8 devices on it with channel length of 120, 100, 80, 60 µm and W=10000 µm.

Device Irradiation: top-gate OTFTs were put on specific designed and 3D-printed support in order to irradiate them from the bottom. Irradiation was performed with an optical fiber at 0.5 cm distance from the quartz slide. The Optical fiber was connected to a Polychrome V (Till Photonics) tunable light source providing a monochromatic beam of ± 15 nm. Wavelength used were 313 and 540 nm with irradiance levels of 0.5 and 50 mW/cm^2 respectively.

6.3 RESULTS AND DISCUSSION

6.3.1 DAE UV-Vis characterization in solution and as a SAM on gold

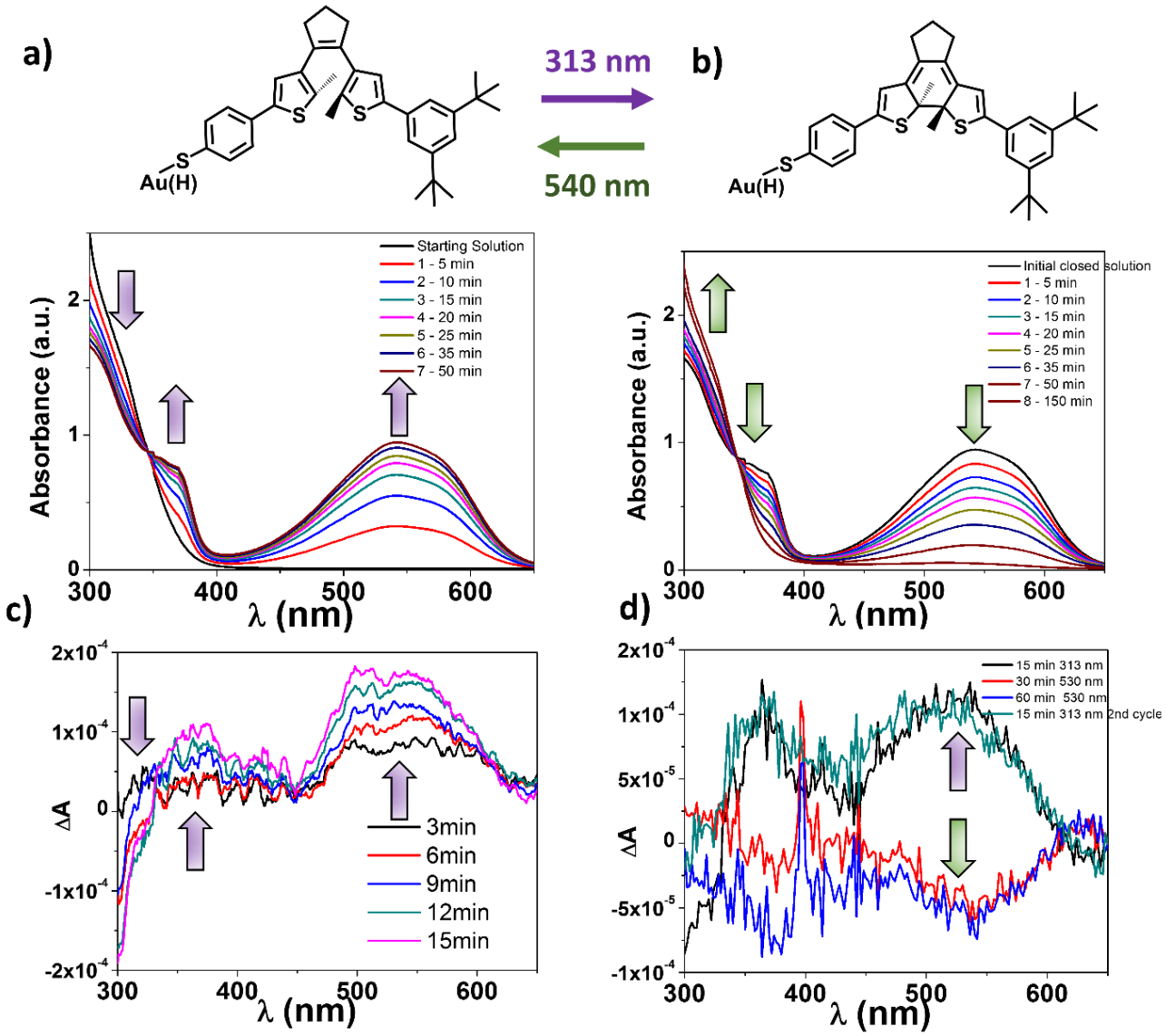

Figure 6.1 a) chemical formula of o-DAE (between brackets when in solution) and its absorption spectrum in black. Changes in absorption are reported after irradiation with 313 nm light up to c-DAE. b) Chemical formula of c-DAE (between brackets when in solution) and its absorption spectrum in black. Changes in absorption are reported after irradiation with 540 nm light up to o-DAE. c) Interconversion of isomers o-DAE to c-DAE on a thin transparent gold electrode as determined by UV–Vis absorption spectroscopy by subtraction of subsequent spectra with different irradiation time at 313 nm. d) Interconversion of isomers c-DAE (black curve) to o-DAE (red and blue curves) and then to c-DAE again (green curve) on a thin transparent gold electrode as determined by UV–vis absorption by subtraction of subsequent spectra with different irradiation time at 540 nm and 313 nm respectively.

We report the absorption spectra of a 0.01 mM solution of o-DAE in chloroform in **Figure 6.1a** and how the initial spectrum changes under irradiation at 313 nm (0.14 mW/cm^2), with an increase of a broad band centered at 541 nm and another narrower band at 365 nm. These features are characteristic of the c-DAE form. At the same time absorption band at 313 nm

decreases. Opposite isomerization from c-DAE was achieved by irradiation at 540 nm - 0.42 mW/cm^2 - (**Figure 6.1b**) and the same bands previously mentioned performed in the opposite direction up to full recovery.

SAM of t-DAE on gold has been growth, by immersing in a 1 mM solution of t-DAE in ethanol a freshly ozone cleaned flat gold substrate for 72 h. Gold thickness was 15 nm and was evaporated on top of a quartz slide preceded with 3 nm of chromium in order to enhance quartz/gold adhesion. This allowed us to have a transparent layer of gold on top of high-quality high-transparent quartz slides. Optical spectroscopy has then been performed on so prepared samples with a SAM of t-DAE. After recording initial absorption spectrum, irradiation at 313 nm was performed. The switching is not clearly visible directly in the UV-Vis spectra due to the strong absorption of gold surface plasmon resonance and just by subtraction of consecutive spectra it is possible to observe characteristic peaks.

As showed in **Figure 6.1c** we were able not only to register the increase of 540 nm absorption band, belonging to the c-DAE, but for the first time with this technique, also the increase of the one at 365 nm and the decrease in intensity of 313 nm band. As reported 12 min irradiation power 0.14 mW/cm^2 was enough to achieve the maximum switching from o-DAE to c-DAE. This short irradiation time and this experiment confirm that if the switching core is not decoupled from gold and isomerization is not inhibited[30] despite theoretical calculations.[31]

More difficult was to record the switching back isomerization irradiating at 530 nm (irradiance 0.42 mW/cm^2) due to the fact that the process is very slow and the baseline of the spectrophotometer is not stable for long time. Anyhow a switch back of the molecule was monitored already upon half hour of irradiation as shown in **Figure 6.1d.**

Finally another irradiation at 313 nm was performed. We were able to observe the increase up to previous intensity of 365 and 540 nm absorption band indicating formation of c-DAE after isomerization. The measurements proves that when t-DAE are growth as SAM on gold they can isomerize by proper wavelength irradiation from both configuration. Since our aim is integration of a functionalized gold electrode in a top gate OTFTs in order to maximize switching efficiency we explored further properties of t-DAE SAM on gold. Three major factors play a role in charge injection for this kind of system: *(i)* conductance of SAM molecule, *(ii)* work function shift induced by photochromism, and *(iii)* wettability.

6.3.2 XPS analysis

XPS survey spectra were recorded in different samples of DAE SAM on gold (both [111] and polycrystalline) revealing always the presence of four main elements: Carbon, sulphur and oxygen elements constituting the diarylethene molecules employed in this study, and gold, whose signal comes from the substrate. XPS analysis shows that, despite the unsuccessful detection of SAM by STM the molecules are present and from the S2p XPS spectrum we can confirm that the molecules are bounded to gold.

In **Figure 6.2** a typical S2p XPS spectrum recorded for the tDAE SAM can be deconvoluted in three doublets, which correspond to different chemical species of sulphur. The S2p peak in general can be decomposed in different contributions, each one being described by a doublet whose peaks, $S2p_{1/2}$ and $S2p_{3/2}$, have intensity ratio 2:1 and a spin orbit split of ca. 1.2 eV. The doublet with the main peak around 162 eV corresponds to thiolated sulphur chemisorbed on gold while the one with main peak at 163.5 eV is characteristic of the sulphur belonging to the thiophene moiety. [32]

The peak at 161 eV can appear sometimes in self-assembled monolayer spectra. The origin of this feature is still under investigation but the most accredited hypothesis attribute this peak to atomic sulfur formed by the C-S bond cleavage[33] or to isolated sulphur in sp configuration.[34]

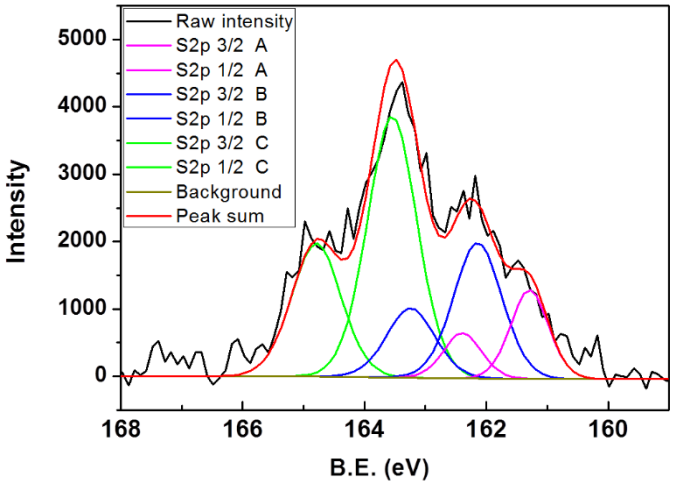

Figure 6.2: S2p XPS spectra recorded for DAE SAM. The black line represents the raw data as recorded. The peak has been de-convoluted in three doublets: doublet A (pink) corresponds to isolated sulfur or C-S cleaved sulfur; doublet B (blue) corresponds to thiolated sulphur chemisorbed on gold; doublet C is assigned to S belonging to thiophene moiety. The red line is the global fitting obtained by the sum of the three doublets.

As it is possible to see from **Table 5.1** the ratio between peaks C (thiophene sulphur) and peak B (thiol sulphur) is close to 2, as expected since in one molecule there are two thiophene units and just one thiol.

Table 5.1: summary of the peaks resulting from the deconvolution of the S2p peak of DAE SAM. For each peak, binding energy, FWMH, area and percentage are reported. For each doublet the assignment to a specific sulphur bond is reported.

Name		Peak BE (eV)	FWHM (eV)	Area (P) CPS.eV	Atomic %
S2p3/2 Scan A	-S-C broken bond -sulfur with sp configuration	161.29	0.73	1048.43	7.37
S2p1/2 Scan A		162.39	0.73	535.55	7.38
S2p3/2 Scan B	S-Au	162.14	0.93	2040.43	14.36
S2p1/2 Scan B		163.24	0.93	1042.27	14.37
S2p3/2 Scan C	thiophene	163.55	0.96	4011.51	28.25
S2p1/2 Scan C		164.79	0.96	2049.12	28.27

6.3.3 t-DAE SAM on gold: conductance changes upon irradiation

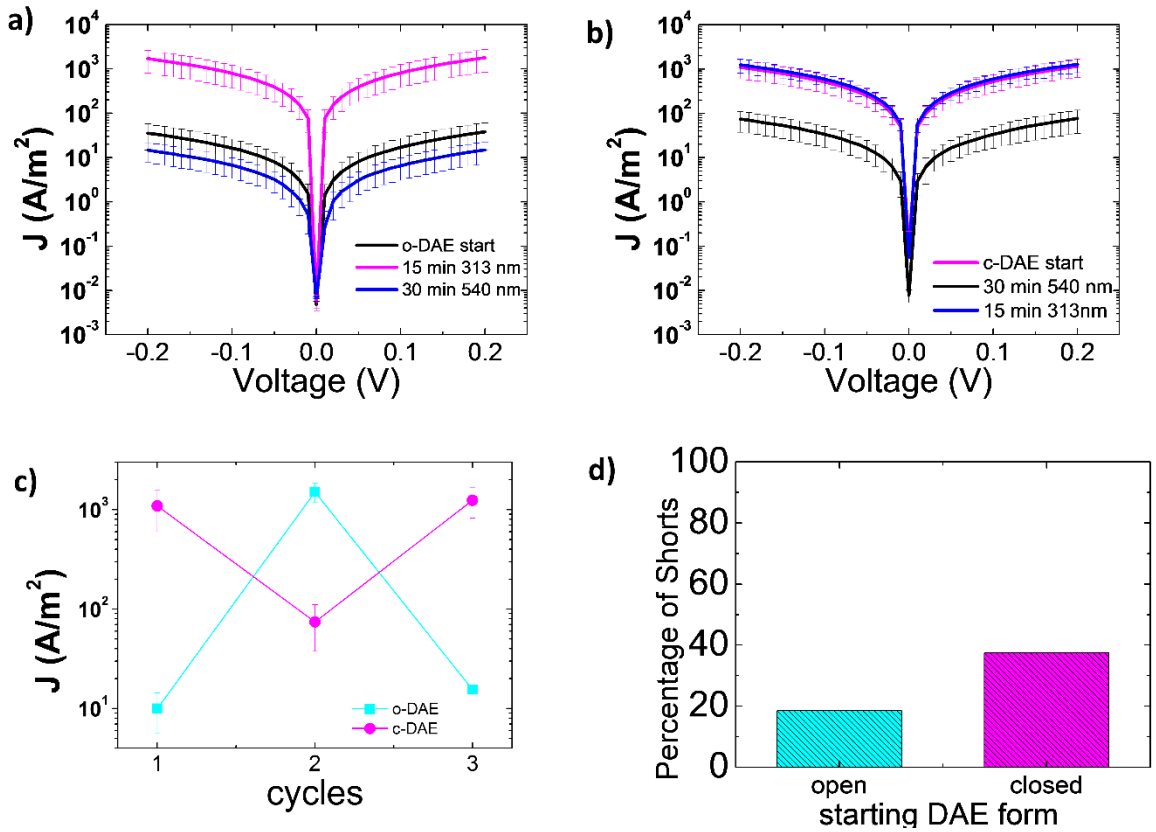

Figure 6.3. Characteristics of mean log current density as a function of junction bias of E-GaIn electrode on t-DAE SAM on gold. a) Starting from open form initial current density is reported in black. After 15 min irradiation at 310 nm higher current density recorded addressed to c-DAEs reported in violet. Curves obtained after 30 min at 540 nm irradiation are reported in blue. In b) the same scheme is reported for the DAE starting from closed form. c) Plot of maximum current density at 0.2 V for o-DAE (cyan) and c-DAE (violet) and successively irradiation cycles. d) Percentage of shunts starting from open and from close recorded over all the samples.

Differences in conductance among DAEs isomers are well known and have been widely studied by STM, [28,35,36] AFM [37] and molecular junctions.[23] In order to better understand and to prove different electrical contribution between the two forms of employed DAE when growth as a SAM on gold, we performed current density measurements through the SAM with a vertical junction made with a liquid compliant Gallium/Indium (E-GaIn) top electrode. E-GaIn electrode has already been proved to be an ideal way to explore tunneling resistance in SAM [38] since a small oxide layer is formed on the edge that helps to retain its form and preventing diffusion in the SAM without influencing the measurement.[39-41] It has been demonstrated that this technique allows for reproducible, non-destructive, high throughput current density–voltage (J–V) measurements.[42] A SAM of DAE was grown as previously described, starting both from a not-irradiated solution, o-DAE, and from an UV irradiated solution (313 nm), *i.e.* with DAE in closed form, c-DAE. The samples were contacted with a pear-shaped drop of E-GaIn connected to a syringe needle, while the gold on the bottom has been used as second

electrode as discussed in Chapter 3.31 - **Figure3.4**. Irradiation has always been performed from the top at the previous described powers, with the E-GaIn junction not in contact. A differential of potential was applied between the two electrodes and by extracting the contact area of the soft electrode, current density characteristics (J) has been calculated. Each of these measurements were programmed in order to sweep 20 times in a row to test electrical robustness by counting the number of shorts recorded. Two samples with o-DAE and two samples with c-DAE were tested, prepared from different bath, and at least 4 points *per* conformation have been recorded on each sample with at least 4 cycles of 20 sweep recorded for a total of at least 640 measurements *per* configuration. As shown in **Figure 6.3a**, for o-DAE sample initial curve is reported in black. After 15 min 313 nm irradiation current density increases of more than two order of magnitude. This result is coherent both with theory[36] and literature[23,43], where a same shift value in conductance has been reported for a similar vertical junction.[23] The closed form has an extended π- conjugation with respect to the o-DAE, hence the tunneling of charges across the molecule backbone is more difficult.[44] After 30 min irradiation with 540 nm light, current density is lowered again at the initial values, as highlighted in **Figure 6.3c** in cyan, where values at 0.2 V are reported for the three different DAE states: initial o-DAE, closed after 313 nm irradiation and back to open after 540 nm irradiation. The same measurements were performed for c-DAE samples as reported in **Figure 6.3b**. Upon irradiation with a light source centered at 540 nm, a lower conductance was recorded, in accordance with previous measurements, but the shift obtained after 540 nm irradiation was minor (**Figure 6.3c**) with respect to o-DAE starting case. Anyhow it was possible to go back to c-DAE isomer after 15 min irradiation at 313 nm as demonstrated by the increase in J. The electrical robustness, *i.e.* the ability of the system of maintaining its electrical characteristics when external condition changes,[45] is reported in **Figure 6.3d**. The number of time a short circuits has been registered during the voltage bias cycles is a good estimation of how often a SAM survives measurements.[39] It is evident how o-DAE starting conformation is forming SAMs which are more electrically stable with less than 20% of shorts recorded against a value > 40% recorded for the c-DAE isomer based SAMs. We can address lower switching ratio and robustness to more tight packing of c-DAE SAM with respect to o-DAE as previously reported.[23] Accordingly, decrease in conformational freedom can partially hinder isomerization and consequently the SAM is more rigid and fragile. In light of these findings, *i.e.* lower electrical robustness and lower switching ratio with respect to o-DAE, c-DAE has not been investigated further electrically, and all transistors prepared and tested in this work present o-DAE as starting conformation.

6.3.4 t-DAE SAM on gold: WF modification by irradiation.

Another aspect to take into account is the shift in work function (WF) due to Au functionalization of SAM.[46] Introduction of a SAM on gold surface convey an intrinsic electric dipole moment at the interface, lowering or raising work function of the metal.[47] This is one of

the most known and employed effect in which SAM on Au electrodes are fruitful employed in OTFT in order to effectively align energetic level between electrode and semiconductors.[48,49] By growing a SAM of specifically designed photochromic thiols it is also possible to change electrode's work function with light.[50] To quantify whether the work function of gold is modified upon formation of t-DAE SAM we employed Ambient Photoelectron Spectroscopy (Ambient-PS). This technique is very well-known, but a couple of remarks have to be made before discussing results. Basically a scan at different energies (4.0 eV to 5.5 eV corresponding to 309 to 225 nm) of the incident beam is performed on the sample in order to extract electrons from it, starting from low energy to higher energy, *i.e.* deep UV. This means that when employed on a sample presenting t-DAE on the surface, the monolayer will be irradiated at wavelength that could generates photo-isomerization between open and closed form. To avoid any kind of deviation between real and experimental values we decided to proceed in two ways. The first is to set parameters scan in order to affect the less possible the sample. We already proved that photo isomerization occurs with irradiation at 313 nm at 0.14 mW/cm^2 for 15 minutes. We fixed scan parameter starting from 4.0 eV corresponding to 310 nm at 50 nW irradiating for 10 seconds. In this way virtually no photo-isomerization should occurs in light of 2 order of magnitude less powerful irradiation for a 90 times lower time. The second is to repeat measurements using macroscopic kelvin probe to double check WF shift due to isomerization. To prove our assumption we performed 3 measurements in a row. No observable work function shift has been recorded, indicating no effect of the low intensity and time irradiation on a SAM of o-DAE.

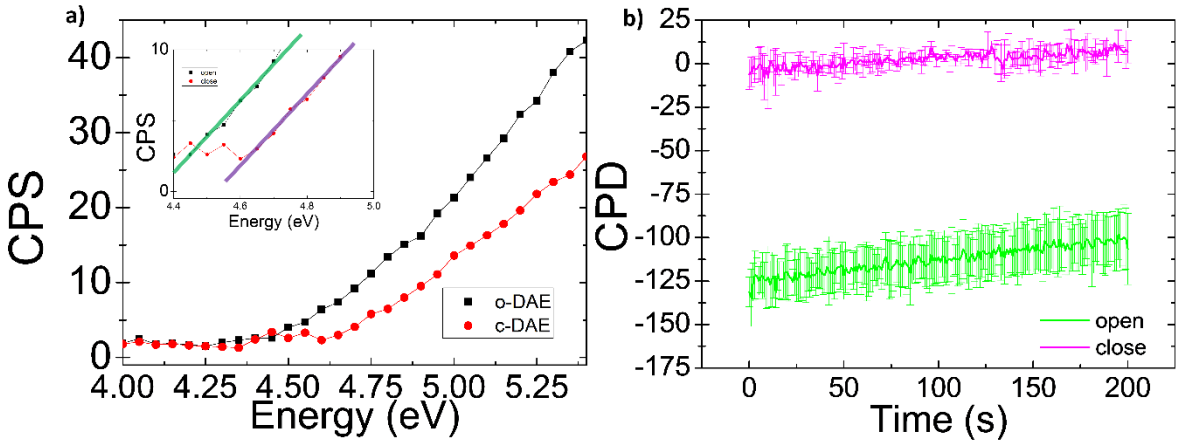

Figure 6.4 a) Square roots of photoelectron yield vs. energy spectra of o-DAE (black) and c-DAE (red) from which values have been extracted. Work function shift is highlighted in the inset b) Kelvin probe 200 sec measurements of o-DAE (violet) and c-DAE (green) reporting average and standard deviation of all measurements performed for both SAM.

As reported in **Figure 6.4a,** the WF recorded on o-DAE functionalized gold is (4.5 ±0.05) eV, while for the c-DAE is (4.62 ±0.05) eV (average and standard deviation on 6 measurements from two different sample each). The shift is of just 120±50 meV as highlighted by the inset of **Figure 6.4a**. The Au/o-DAE system features a higher work function, which translates into an

easier electron injection with respect to the Au/c-DAE system into the LUMO of P(NDI2OD-T2), which lies at 4.0 eV. Also both WF levels lie within the P(NDI2OD-T2)[51] band-gap indicating that a minor contribution should be expected in OFET when functionalized DAE are switched from WF shift.

The very same samples tested through Ambient-PS was tested with macroscopic kelvin probe. Each sample has been tested in at least six different points and a measurement of 200 seconds was carried on in order to verify no charging of the sample as shown in **Figure 6.4b**. The difference in mV found between o-DAE SAM on gold and c-DAE SAM on gold is (125 ± 24) mV (6 point each sample, 2 samples. 12 measurements *per* configuration), with the c-DAE sample presenting the higher work function, a value in perfect accordance with the obtained with Ambient PS, and a further prove of no effect on work function of the acting of measurements itself carried out with Ambient PS.

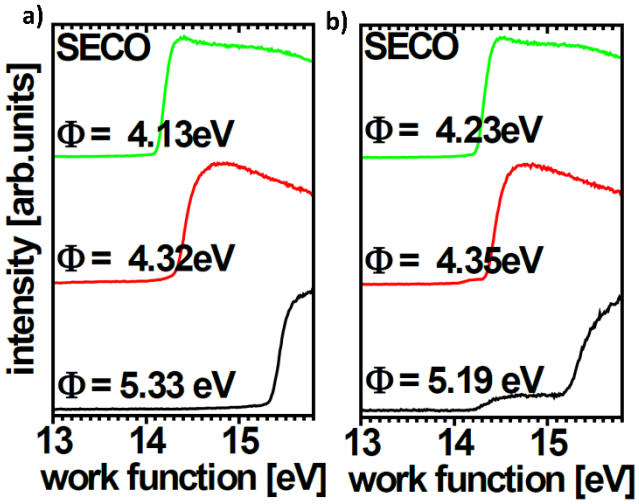

Figure 6.5 Secondary electron cutoff (SECO) region spectra. Is reported bare gold in black, t-DAE as SAM on gold in red and a thin film of P(NDI2OD-T2) deposited on t-DAE SAM on gold in green for a) o-DAE and b) c-DAE. Extracted work functions values are reported over the respective curves.

To further explore this aspect in collaboration with Prof. Koch of the Humboldt University Berlin ultraviolet photoelectron spectroscopy has been performed on o-DAE and c-DAE SAM on gold. In this case the samples have never got in contact with air. We obtained a value of work function for o-DAE/Au of (4.32 ± 5**)** eV and for c-DAE/Au of (4.35 ± 5) eV as reported by red line in **Figure 6.5a,b** respectively. The difference in WF between the two forms is lower than the experimental error bar of 50 meV. Variance of work function values obtained from UPS and Ambient-PS can be explained with different cleaning procedure of gold (Ar-sputtering cycles for the former and ozone cleaning for the latter), considering also that a difference of 300 meV is usually found in measuring gold work function with the two methods.[52] It is worth noticing, as reported in **Figure 6.5a,b** with black line, that the work function values for the reference bare gold is different in the two cases. Taking into account this fact, we can calculate a shift of 1 eV due to o-DAE and 0.84 eV for c-DAE. This means that difference between the two forms is of (170±50) meV a value in perfect accordance with

previous measurements. On that sample a thin film of P(NDI2OD-T2) has been deposed to study interaction between Au/t-DAE/ semiconductor. Deposition of polymer decrease again the work function as shown in **Figure 6.5a,b** with green lines. The low work function of both DAE-SAMs brings the Fermi level very close to the conduction band of P(NDI2OD-T2).This could indicate a charge transfer of electrons directly in conduction band of the polymer, thus acting as very efficient traps for holes.

6.3.5 t-DAE SAM on gold: water contact angle measurements

Lastly water contact angle measurements have been performed on Au functionalized with o-DAE and c-DAE. This allowed to verify very good hydrophobic nature induced by the SAM, with values of (108±4) ° for o-DAE and (100±3) ° for c-DAE. While basically no change is observed in contact angle between the two isomers, values are way higher then bare gold which present a value of (53±4) °. In Table 5.2 are reported all the values extracted for WF and contact angle for all the system employed, included mono-phenylthiol (MPT) as SAM on gold. We decide to characterize MPT for the same parameters in order to have a comparison with a not-conjugated not-photochromic molecule growth as a SAM on electrodes to rule out any contribution of the SAM itself on current changes after irradiation.

Table 5.2. An overview of work function and contact angle of all gold functionalized surfaces employed in this study and bare gold itself.

Sample	Work Function by A-PS (eV)	Contact Angle (°)
Bare Au	5.0±0.05 eV	53±4
MPT	5.05±0.05	79 ± 2
o-DAE	4.5 ±0.05	108±4
c-DAE	4.62 ±0.05	100±3

The same measurements discussed above have been performed on MPT SAM. Values obtained both for WF and contact angle are in agreement with previous studies.[53] Gold surface functionalized with MPT is more hydrophobic with respect to bare gold, but is not as high as the t-DAEs functionalized surface because MPT molecules tend to lie down on the surface. [53]

6.3.6 OTFTs characterization

Finally we employed this system in OTFT. We designed it on a top-gate device, using quartz slides as a support for the structure and a very thin Au electrode of 15 nm as shown in **Figure 6.6a**. This choice has been dictated by two requirement. The first is to irradiate from the bottom and thus a very good transparency is required. The second is to maximize performances and the effect of t-DAE on charge injection. In fact with this geometry the whole electrode is involved in charge injection, while in bottom-gate configuration just a few nanometers near the gate are engaged. As mentioned P(NDI2OD-T2) has been chosen since it is has high performance which are maximized in top-gate configuration.[29] Briefly, on a high quality quartz slide interdigitates

electrodes of 3 nm of chromium and 15 nm of gold has been evaporated. After ozone cleaning, samples have been immersed in a t-DAE in open form solution for 72 h. Also samples with MPT on gold electrode have been prepared by immersion in 5mM solution in EtOH for 12 h. They have been tested as a reference of a OTFTs comprising electrodes functionalized with a not photochromic moiety. Subsequently proper cleaning, a thin film of 60 nm of P(NDI2OD-T2) has been deposited by spincoating and then a thick film of Cytop as dielectric of 750 nm has been deposited on top of it. Lastly, 100 nm of aluminum has been evaporated in order to contact the gate electrode. In the same way also pristine P(NDI2OD-T2) without any electrode functionalization have been prepared in order to have a blank reference

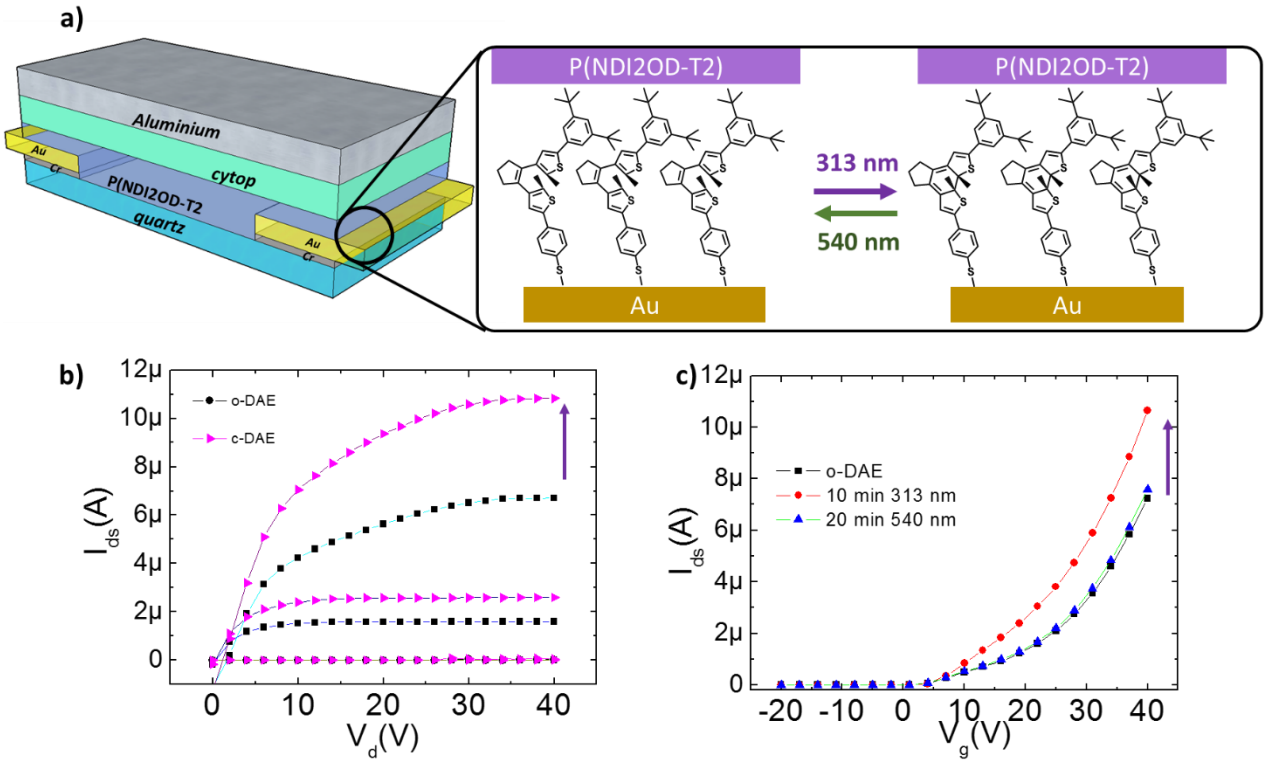

Figure 6.6 a) Schematic representation of top-gate employed OTFTs. It's highlighted the switching mechanism under irradiation at the interfaces of t-DAE on gold surface and the two stable state, open and closed. b) Output characteristic of t-DAE device before (black) and after (violet) UV irradiation. c) Transfer characteristic of t-DAE device after UV irradiation (in red) and after subsequently 540 nm light irradiation to bring it back to the original state (in blue).

Table 5.3 Extracted electrical parameters for all different functionalized of OTFTs employed in the study

Sample	Linear Mobility ($cm^2V^{-1}s^{-1}$)	V_{th} Linear (V)	Saturation Mobility($cm^2V^{-1}s^{-1}$)	V_{th} Saturation (V)	I_{on}/I_{off} (log 10)
P(NDI2OD-T2)	0.17-0.35	12.1±0.5	0.13-0.31	4.6±0.7	4-5
P(NDI2OD-T2) +MPT	0.08-0.25	19±5	0.07-0.13	8.3±1.8	4-5
P(NDI2OD-T2)+o-DAE	0.07-0.16	5.5±0.7	0.05-0.8	-3.1±0.9	5-6

Mobility has been calculated considering Cytop layer thickness of 750 nm and its dielectric constant of 2.1.[54] All devices were tested in nitrogen atmosphere and presented very good electrical characteristics and a very good reproducibility. They exhibited a very good n-type behavior, responding with an almost ideal spacing between curves at different gate voltages as presented in **Figure 6.7**. Pristine P(NDI2OD-T2) OTFTs presented mobilities values up to $0.35 \cdot cm^2V^{-1}s^{-1}$ slightly higher than what reported in the literature for Cytop top-gate devices,[51] a very constant threshold voltage and an I_{on}/I_{off} between 10^4-10^5. These very high mobility values stem from a face-on configuration that P(NDI2OD-T2) chains tend to assume at the surface[55], which is favorable for charge transport in top-gate OTFTs. A less pronounced p-type behavior has been observed as evidenced in **Figure 6.8a,d**. which is well known for this material.[51]

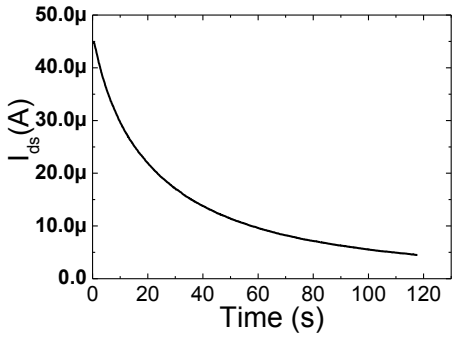

Figure 6.7 I_{ds} drain source current evolution over time under a constant applied V_g bias of 40V and V_{ds} bias of 10V. L=80 µm, W=10000 µm.

It is worth pointing out that our devices, in contrary to previous reports, exhibit always a slightly higher value of mobility when extracted from linear regime with respect to mobility extracted from saturation regime. This could be ascribed to the fact that P(NDI2OD-T2) is prone to bias stress and thus we are measuring electrical stress occurring in the material while tracing saturation curves. To prove our assumption we performed a bias-stress curve to evaluate how I_{ds} current change under an applied constant gate voltage of 40 V. As shown in **Figure 6.7** after 15 seconds current decrease of 100% with respect to initial value. Considering that an average transfer curve is recorded in 25 seconds we cannot rule out stress effect on saturation curves.

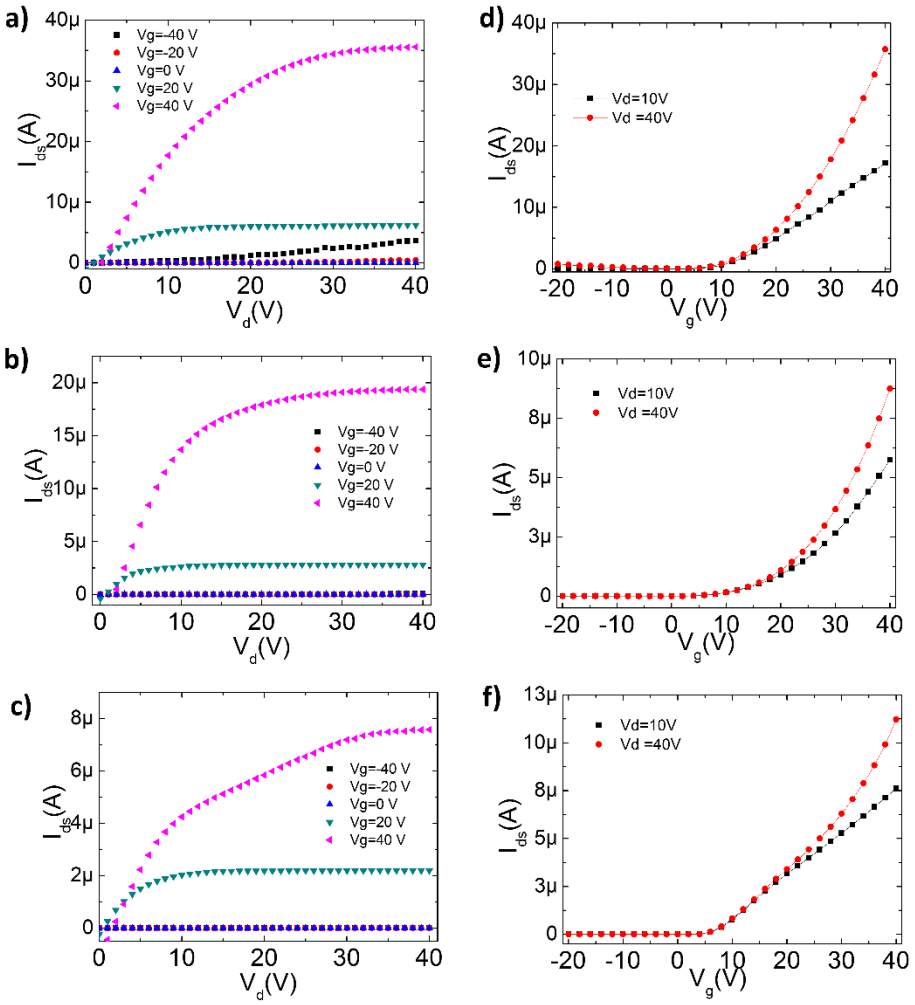

Figure 6.7 Output characteristics of top-gate devices based on a) pristine P(NDI2OD-T2), b) MPT functionalized electrodes, c) o-DAE functionalized electrodes together with their transfer characteristics reported respectively in d),e),f). Devices reported here have L=100 µm, and V_{ds} applied for transfer reported is 10 V and 40 V for linear and saturation regime.

Also MPT devices have been tested. It has been chosen to analyzed devices with MPT growth as a SAM on electrodes in light of a previous study which showed that their main effect on Au electrodes is to improve wettability.[53] Also their very short length should help minimize tunneling resistance introduced by their presence and finally the WF of an electrode MPT-functionalized is very close to the one of bare gold. Mobility values for MPT-OTFTs are somewhat lower with respect to pristine device. Decrease is of the order of 50% for saturation regime mobility and 20% for linear regime mobility. This small difference can be ascribed to the introduction of a tunneling barrier at the electrode surface, which is not compensated by the increase of wettability introduced by the SAM. This is confirmed by V_{th} shift towards more positive values, indicating that the introduced barrier at the Au/semiconductor interface is not compensate by increased wettability (**Figure 6.8b,e**).

Electrical characterization of o-DAE device showed again a very good reproducibility and very good performances. In this case mobility values have been found to be decreased in

average by just 50% in the linear regime and 60% on the saturation one, but with average value of 0.1 $cm^2V^{-1}s^{-1}$ and a maximum value of 0.16 $cm^2V^{-1}s^{-1}$. On the other hand an increase of a medium I_{on}/I_{off} ratio of 1 order of magnitude has been observed together with a shift towards more negative values of V_{th}. The increase in wettability and higher work function do not compensate enough the introduction of a barrier at the interface Au/semiconductor, but the interplay between the three factors allows to minimize performances loss. At the same time for o-DAE devices V_{th} is shifted negatively, which means that functionalized OTFTs turn on at lower voltage with respect to pristine one. In other words o-DAE electrodes at a given gate voltage can inject more charge with respect to not functionalized one. This findings is in perfect agreement with WF values reported before, where we have found that WF of o-DAE gold sits closer to P(NDI2OD-T2) LUMO level with respect to bare gold, hence the energetic barrier overcame by charges is decreased. At the same time holes injection is completely inhibited as can be seen in **Figure 6.8c,f** and as expected from previously discussed UPS measurements.

The devices have then been irradiated with UV light (313 nm) to achieve isomerization from o-DAE to c-DAE, and then tested. We found that 10 minutes are enough to record a marked change in electrical performances and that a further irradiation does not lead to further changes. The c-DAE devices present a maximum source-drain current increase both in output (**Figure 6.6b**) and transfer characteristics (**Figure 6.6c**). An irradiation at 540 nm for 20 minutes is enough to bring back electric characteristics to the original value, indicating a complete switch of molecules in o-DAE isomer.

6.3.7 Irradiation effect on electrical properties

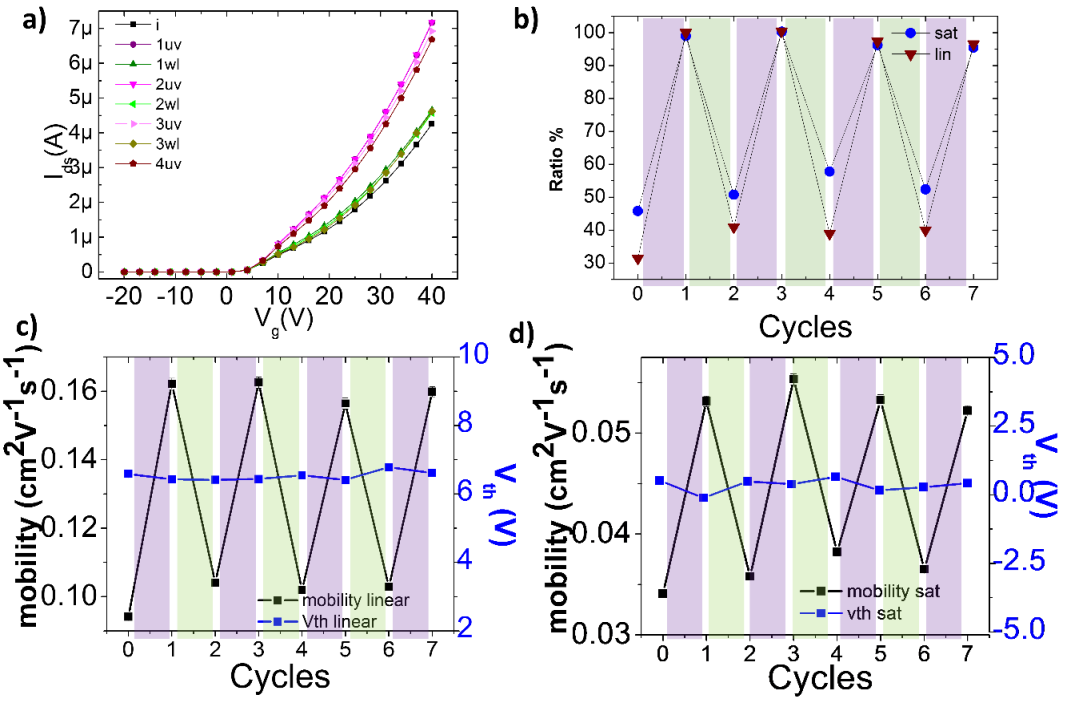

Figure 6.9a) linear transfer characteristic behavior under irradiation cycles. UV indicates 313 nm irradiation for 10 min and WL indicates 540 nm irradiation for 20 min. Curves were recorded in dark after irradiation. Starting

curve is reported in black, c-DAE curves in violet tones and back switched o-DAE transfers in green tone. V_g =+ 10 V. b) Normalized maximum drain-source current from the transfer characteristics at V_g= +10 V for linear (in brown) and V_g=+40V for saturation (in blue). Mobility and V_{th} values extracted from c) linear and d) saturation regime transfer curves for subsequently irradiation cycles performed.

After proving the possibility of controlling with light both isomerization of t-DAE, we explored further the possibility of modulation of electric characteristics by irradiation of o-DAE device. We performed multiple irradiation cycles to test reproducibility and fatigue effect. Each irradiation step was of 10 minutes irradiation at 313 nm to switch to c-DAE and 20 minutes irradiation at 540 nm for switching to o-DAE. As shown in **Figure 6.9a** for linear regime, it is possible to perform multiple cycles with no loss of performance and full recovery of electrical characteristic. Starting curve for o-DAE configuration is reported in black, c-DAE configuration obtained after irradiation at 313 nm (UV light) transfer curves are reported in violet tones. Successive transfer curves after irradiation at 540 nm (white light WL) are reported in green tones. It is evident how irradiation induces an increase of source-drain current, but not a shift of $V_{th,}$ In **Figure 6.9b** are plotted differences in current between o-DAE and c-DAE configurations for both the linear and the saturation regime normalized with respect to c-DAE drain–source current at V_g=+30 V for performed irradiation cycles. The increase in maximum source drain current is of about 50% for saturation regime and 65% for linear regime. The obtained values are the higher ever reported for OTFTs with a photochromic molecules growth as SAM on electrodes. Higher modulation is achieved in linear regime since contact effect that govern charge injection are more pronounced at low source drain applied voltage. Also a full recovery to original value is obtained after 540 nm irradiation for all cycles performed. A more detailed analysis has been carried out by extracting mobility and V_{th} values from reported curves. The values are reported in **Figure 6.9c,d** for linear and saturation regime, respectively. As previously mentioned, it is evident that V_{th} is not affected by irradiation, and is constant through the whole measurement. This proves that difference in WF between o-DAE and c-DAE is not important enough to play a role in this parameter, while on the other hand the difference in conductance has an overwhelming effect which is responsible for the increase in devices mobility. Since no shift in V_{th} was observed with an increase in maximum current, extracted mobility when in c-DAE state is higher with respect to o-DAE state. The increase in mobility, of about 70%, can be ascribed to the fact that the molecule switches from a not conjugated to a conjugated form, characterized by a lower tunneling resistance.[56] This is reflected in molecule conductance as we proved with E-GaIn measurements on the Au/t-DAE/GaIn junction. Increased conductance improves charge injection and thus the number of charges in the channel which lead to improved mobility. It is important to notice how no fatigue effect is visible after 5 cycles for both mobility and source drain current.

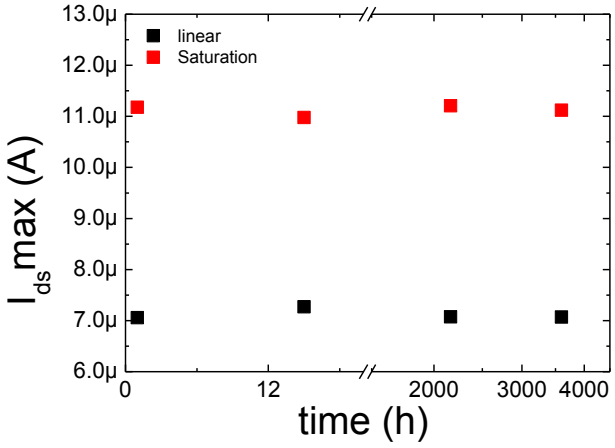

Figure 6.10 Maximum I_{ds} for c-DAE form vs. time for linear (black dots) and saturation regime (red dots).

Furthermore we proved how the system is perfectly stable in both configuration and no thermal relaxation is observed. After 313 nm irradiation we did not irradiated further the sample and we tested it after 14 hours, then after 90 days and then after 150 days, without exposing it to direct irradiation, but not in complete dark. As showed in **Figure5.10** no changes at all are observed in maximum source-drain current. This measurement proves not only that c-DAE is stable for very long time but also that direct irradiation with appropriate wavelength is needed for isomerization to occur.

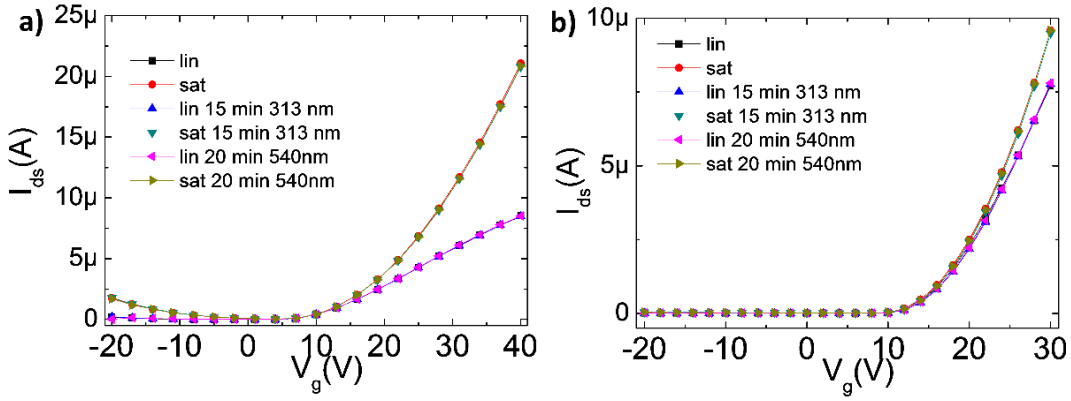

Figure 6.11 a) Pristine P(NDI2OD-T2) and b) MPT transfer curves in linear and saturation regime before and after irradiation cycles at 313 and 540 nm

In **Figure6.11a** a cycle performed on a pristine device sample with irradiation power and time used for o-DAE samples is shown. It is evident that no changes occurs, hence that the shift observed is due to presence of SAM on electrodes and their isomerization. To also rule out any effect due to chemisorption of a molecule with an aromatic group the very same irradiation cycle has been completed on MPT devices.

As reported in **Figure 6.11b** no changes at all happened to the sample. This allow us to conclude without doubt that the effect arising from irradiation is addressed to the presence of t-DAE SAM on gold and to their two isomers

6.4 .CONCLUSIONS

In conclusion, for the first time we designed and fabricated a top-gate bottom-contact OTFT employing t-DAE-functionalized gold source-drain electrodes where the charge injection can be reversibly photo-tuned. Introduction of t-DAEs SAM layer didn't disrupt significantly electrical characteristics, allowing to obtain high-performance transistors with mobility > 0.1 $cm^2 V^{-1}s^{-1}$. Moreover taking advantage of photochromic nature of t-DAEs, we bestowed multi-functionality to OTFTs. Light control of isomerization is directly reflected to charge injection modulation and thus in current output and device mobility. It is worth noticing that we obtained the maximum switching ratio ever performed for OTFTs with photochromic molecules functionalizing electrodes with no fatigue effect on the cycles performed. More importantly, both state, *i.e.* o-DAE and c-DAE, are stable for long time. All the improvements presented in this chapter have been achieved by a careful design of both fundamental factors, molecules structure and transistors geometry. Finally we proved how the main factor that allows these performances is the difference in conjugation of the two DAE isomers, and thus the difference in conductance is the main and fundamental factor that overcomes wettability issues and WF shift. Our findings bring the concept of electrode functionalization to a whole new level, demonstrating that high-performance, bi-stable, full light controlled transistor can be obtained. Therefore we bring the challenge directly to efficient integration of multifunctional devices in electronic circuit for real applications.

6.5 REFERENCES

1. Dong, H.; Zhu, H.; Meng, Q.; Gong, X.; Hu, W., Organic photoresponse materials and devices. *Chem. Soc. Rev.* **2012,** *41*, 1754-1808.
2. Shirota, Y., Organic materials for electronic and optoelectronic devices. *J. Mater. Chem.* **2000,** *10*, 1-25.
3. Di, C.-a.; Zhang, F.; Zhu, D., Multi-Functional Integration of Organic Field-Effect Transistors (OFETs): Advances and Perspectives. *Adv. Mater.* **2013,** *25*, 313-330.
4. Orgiu, E.; Samorì, P., 25th Anniversary Article: Organic Electronics Marries Photochromism: Generation of Multifunctional Interfaces, Materials, and Devices. *Adv. Mater.* **2014,** *26*, 1827-1845.
5. Raimondo, C.; Crivillers, N.; Reinders, F.; Sander, F.; Mayor, M.; Samorì, P., Optically switchable organic field-effect transistors based on photoresponsive gold nanoparticles blended with poly(3-hexylthiophene). *Proc. Natl. Acad. Sci.* **2012,** *109*, 12375-12380.
6. Shallcross, R. C.; Zacharias, P.; Köhnen, A.; Körner, P. O.; Maibach, E.; Meerholz, K., Photochromic Transduction Layers in Organic Memory Elements. *Adv. Mater.* **2013,** *25*, 469-476.
7. Pärs, M.; Hofmann, C. C.; Willinger, K.; Bauer, P.; Thelakkat, M.; Köhler, J., An Organic Optical Transistor Operated under Ambient Conditions. *Angew. Chem. Int. Ed.* **2011,** *50*, 11405-11408.
8. Zhang, H.; Guo, X.; Hui, J.; Hu, S.; Xu, W.; Zhu, D., Interface Engineering of Semiconductor/Dielectric Heterojunctions toward Functional Organic Thin-Film Transistors. *Nano Lett.* **2011,** *11*, 4939-4946.
9. Kim, D.; Jeong, H.; Lee, H.; Hwang, W.-T.; Wolf, J.; Scheer, E.; Huhn, T.; Jeong, H.; Lee, T., Flexible Molecular-Scale Electronic Devices Composed of Diarylethene Photoswitching Molecules. *Adv. Mater.* **2014,** *26*, 3968-3973.
10. Zhang, J.; Zou, Q.; Tian, H., Photochromic Materials: More Than Meets The Eye. *Adv. Mater.* **2013,** *25*, 378-399.
11. Pardo, R.; Zayat, M.; Levy, D., Photochromic organic-inorganic hybrid materials. *Chem. Soc. Rev.* **2011,** *40*, 672-687.
12. Hayakawa, R.; Higashiguchi, K.; Matsuda, K.; Chikyow, T.; Wakayama, Y., Optically and Electrically Driven Organic Thin Film Transistors with Diarylethene Photochromic Channel Layers. *ACS Appl. Mater. Interfaces* **2013,** *5*, 3625-3630.
13. Orgiu, E.; Crivillers, N.; Herder, M.; Grubert, L.; Pätzel, M.; Frisch, J.; Pavlica, E.; Duong, D. T.; Bratina, G.; Salleo, A.; Koch, N.; Hecht, S.; Samorì, P., Optically switchable transistor via energy-level phototuning in a bicomponent organic semiconductor. *Nature Chem.* **2012,** *4*, 675-679.
14. Gemayel, M. E.; Börjesson, K.; Herder, M.; Duong, D. T.; Hutchison, J. A.; Ruzié, C.; Schweicher, G.; Salleo, A.; Geerts, Y.; Hecht, S.; Orgiu, E.; Samorì, P., Optically switchable transistors by simple incorporation of photochromic systems into small-molecule semiconducting matrices. *Nat. Commun.* **2015,** *6*.

15. Borjesson, K.; Herder, M.; Grubert, L.; Duong, D. T.; Salleo, A.; Hecht, S.; Orgiu, E.; Samori, P., Optically switchable transistors comprising a hybrid photochromic molecule/n-type organic active layer. *J. Mater. Chem. C* **2015**.

16. Crivillers, N.; Orgiu, E.; Reinders, F.; Mayor, M.; Samorì, P., Optical Modulation of the Charge Injection in an Organic Field-Effect Transistor Based on Photochromic Self-Assembled-Monolayer-Functionalized Electrodes. *Adv. Mater.* **2011,** *23*, 1447-1452.

17. Crivillers, N.; Osella, S.; Van Dyck, C.; Lazzerini, G. M.; Cornil, D.; Liscio, A.; Di Stasio, F.; Mian, S.; Fenwick, O.; Reinders, F.; Neuburger, M.; Treossi, E.; Mayor, M.; Palermo, V.; Cacialli, F.; Cornil, J.; Samorì, P., Large Work Function Shift of Gold Induced by a Novel Perfluorinated Azobenzene-Based Self-Assembled Monolayer. *Adv. Mater.* **2013,** *25*, 432-436.

18. Irie, M., Diarylethenes for Memories and Switches. *Chem. Rev.* **2000,** *100*, 1685-1716.

19. Matsuda, K.; Irie, M., Diarylethene as a photoswitching unit. *J. Photochem. Photobiol. C: Photochem. Rev.* **2004,** *5*, 169-182.

20. Heinemann, N.; Grunau, J.; Leißner, T.; Andreyev, O.; Kuhn, S.; Jung, U.; Zargarani, D.; Herges, R.; Magnussen, O.; Bauer, M., Reversible switching in self-assembled monolayers of azobenzene thiolates on Au (111) probed by threshold photoemission. *Chem. Phys.* **2012,** *402*, 22-28.

21. Tsujioka, T.; Irie, M., Electrical functions of photochromic molecules. *J. Photochem. Photobiol. C: Photochem. Rev.* **2010,** *11*, 1-14.

22. Ferri, V.; Elbing, M.; Pace, G.; Dickey, M. D.; Zharnikov, M.; Samorì, P.; Mayor, M.; Rampi, M. A., Light-Powered Electrical Switch Based on Cargo-Lifting Azobenzene Monolayers. *Angew. Chem. Int. Ed.* **2008,** *47*, 3407-3409.

23. Kronemeijer, A. J.; Akkerman, H. B.; Kudernac, T.; van Wees, B. J.; Feringa, B. L.; Blom, P. W. M.; de Boer, B., Reversible Conductance Switching in Molecular Devices. *Adv. Mater.* **2008,** *20*, 1467-1473.

24. Love, J. C.; Estroff, L. A.; Kriebel, J. K.; Nuzzo, R. G.; Whitesides, G. M., Self-Assembled Monolayers of Thiolates on Metals as a Form of Nanotechnology. *Chem. Rev.* **2005,** *105*, 1103-1170.

25. Zhao, X.; Liu, P., Hydrophobic-Polymer-Grafted Graphene Oxide Nanosheets as an Easily Separable Adsorbent for the Removal of Tetrabromobisphenol A. *Langmuir* **2014,** *30*, 13699-13706.

26. Dulić, D.; van der Molen, S. J.; Kudernac, T.; Jonkman, H. T.; de Jong, J. J. D.; Bowden, T. N.; van Esch, J.; Feringa, B. L.; van Wees, B. J., One-Way Optoelectronic Switching of Photochromic Molecules on Gold. *Phys. Rev. Lett.* **2003,** *91*, 207402.

27. Arramel; Pijper, T. C.; Kudernac, T.; Katsonis, N.; van der Maas, M.; Feringa, B. L.; van Wees, B. J., Reversible light induced conductance switching of asymmetric diarylethenes on gold: surface and electronic studies. *Nanoscale* **2013,** *5*, 9277-9282.

28. Katsonis, N.; Kudernac, T.; Walko, M.; van der Molen, S. J.; van Wees, B. J.; Feringa, B. L., Reversible Conductance Switching of Single Diarylethenes on a Gold Surface. *Adv. Mater.* **2006,** *18*, 1397-1400.

29. Luzio, A.; Criante, L.; D'Innocenzo, V.; Caironi, M., Control of charge transport in a semiconducting copolymer by solvent-induced long-range order. *Sci. Rep.* **2013,** *3*, 3425.

30. Sense Jan van der, M.; Peter, L., Charge transport through molecular switches. *J. Phys.: Condens. Matter* **2010,** *22*, 133001.

31. Zhuang, M.; Ernzerhof, M., Reversibility and transport properties of dithienylethene photoswitches. *The Journal of Chemical Physics* **2009,** *130*, 114704.

32. Vericat, C.; Vela, M. E.; Benitez, G.; Carro, P.; Salvarezza, R. C., Self-assembled monolayers of thiols and dithiols on gold: new challenges for a well-known system. *Chem. Soc. Rev.* **2010,** *39*, 1805-1834.

33. Noh, J.; Jeong, Y.; Ito, E.; Hara, M., Formation and Domain Structure of Self-Assembled Monolayers by Adsorption of Tetrahydrothiophene on Au(111). *J. Phys. Chem. C* **2007,** *111*, 2691-2695.

34. Ishida, T.; Hara, M.; Kojima, I.; Tsuneda, S.; Nishida, N.; Sasabe, H.; Knoll, W., High resolution x-ray photoelectron spectroscopy measurements of octadecanethiol self-assembled monolayers on Au(111). *Langmuir* **1998,** *14*, 2092-2096.

35. Jin, H.; Fan, C.; Paul, A. L.; Joakim, A.; Stephen, D. S.; Devens, G.; Thomas, A. M.; Ana, L. M.; Jun, L.; Otto, F. S.; Stuart, M. L., Switching of a photochromic molecule on gold electrodes: single-molecule measurements. *Nanotechnology* **2005,** *16*, 695.

36. Kim, Y.; Hellmuth, T. J.; Sysoiev, D.; Pauly, F.; Pietsch, T.; Wolf, J.; Erbe, A.; Huhn, T.; Groth, U.; Steiner, U. E.; Scheer, E., Charge Transport Characteristics of Diarylethene Photoswitching Single-Molecule Junctions. *Nano Lett.* **2012,** *12*, 3736-3742.

37. Uchida, K.; Yamanoi, Y.; Yonezawa, T.; Nishihara, H., Reversible On/Off Conductance Switching of Single Diarylethene Immobilized on a Silicon Surface. *J. Am. Chem. Soc.* **2011,** *133*, 9239-9241.

38. Masillamani, A. M.; Crivillers, N.; Orgiu, E.; Rotzler, J.; Bossert, D.; Thippeswamy, R.; Zharnikov, M.; Mayor, M.; Samorì, P., Multiscale Charge Injection and Transport Properties in Self-Assembled Monolayers of Biphenyl Thiols with Varying Torsion Angles. *Chem.–Eur. J.* **2012,** *18*, 10335-10347.

39. Chiechi, R. C.; Weiss, E. A.; Dickey, M. D.; Whitesides, G. M., Eutectic Gallium–Indium (EGaIn): A Moldable Liquid Metal for Electrical Characterization of Self-Assembled Monolayers. *Angew. Chem. Int. Ed.* **2008,** *47*, 142-144.

40. Thuo, M. M.; Reus, W. F.; Nijhuis, C. A.; Barber, J. R.; Kim, C.; Schulz, M. D.; Whitesides, G. M., Odd−Even Effects in Charge Transport across Self-Assembled Monolayers. *J. Am. Chem. Soc.* **2011,** *133*, 2962-2975.

41. Simeone, F. C.; Yoon, H. J.; Thuo, M. M.; Barber, J. R.; Smith, B.; Whitesides, G. M., Defining the Value of Injection Current and Effective Electrical Contact Area for EGaIn-Based Molecular Tunneling Junctions. *J. Am. Chem. Soc.* **2013,** *135*, 18131-18144.

42. Lilly, G. D.; Whalley, A. C.; Grunder, S.; Valente, C.; Frederick, M. T.; Stoddart, J. F.; Weiss, E. A., Switchable photoconductivity of quantum dot films using cross-linking ligands with light-sensitive structures. *J. Mater. Chem.* **2011,** *21*, 11492-11497.

43. Tam, E. S.; Parks, J. J.; Shum, W. W.; Zhong, Y.-W.; Santiago-Berríos, M. E. B.; Zheng, X.; Yang, W.; Chan, G. K. L.; Abruña, H. D.; Ralph, D. C., Single-Molecule Conductance of Pyridine-Terminated Dithienylethene Switch Molecules. *ACS Nano* **2011,** *5*, 5115-5123.

44. Sun, L.; Diaz-Fernandez, Y. A.; Gschneidtner, T. A.; Westerlund, F.; Lara-Avila, S.; Moth-Poulsen, K., Single-molecule electronics: from chemical design to functional devices. *Chem. Soc. Rev.* **2014,** *43*, 7378-7411.

45. Carpinelli, G. D. P., C. ; Caramia, P. ; Varilone, Pietro ; Verde, P., Methods for Assessing the Robustness of Electrical Power Systems Against Voltage Dips. *IEEE Transactions* **2009,** *24*, 43-51.

46. Heimel, G.; Romaner, L.; Zojer, E.; Bredas, J.-L., The Interface Energetics of Self-Assembled Monolayers on Metals. *Acc. Chem. Res.* **2008,** *41*, 721-729.

47. Hamadani, B. H.; Corley, D. A.; Ciszek, J. W.; Tour, J. M.; Natelson, D., Controlling Charge Injection in Organic Field-Effect Transistors Using Self-Assembled Monolayers. *Nano Lett.* **2006,** *6*, 1303-1306.

48. Asadi, K.; Gholamrezaie, F.; Smits, E. C. P.; Blom, P. W. M.; Boer, B. d., Manipulation of charge carrier injection into organic field-effect transistors by self-assembled monolayers of alkanethiols. *J. Mater. Chem.* **2007,** *17*, 1947-1953.

49. Fenwick, O.; Van Dyck, C.; Murugavel, K.; Cornil, D.; Reinders, F.; Haar, S.; Mayor, M.; Cornil, J.; Samori, P., Modulating the charge injection in organic field-effect transistors: fluorinated oligophenyl self-assembled monolayers for high work function electrodes. *J. Mater. Chem. C* **2015**.

50. Masillamani, A. M.; Osella, S.; Liscio, A.; Fenwick, O.; Reinders, F.; Mayor, M.; Palermo, V.; Cornil, J.; Samori, P., Light-induced reversible modification of the work function of a new perfluorinated biphenyl azobenzene chemisorbed on Au (111). *Nanoscale* **2014,** *6*, 8969-8977.

51. Yan, H.; Chen, Z.; Zheng, Y.; Newman, C.; Quinn, J. R.; Dotz, F.; Kastler, M.; Facchetti, A., A high-mobility electron-transporting polymer for printed transistors. *Nature* **2009,** *457*, 679-686.

52. M.Uda, Open Counter for Low Energy Electron Detection. *Jpn. J. Appl. Phys.* **1985,** *24*, 284.

53. Orgiu, E.; Crivillers, N.; Rotzler, J.; Mayor, M.; Samori, P., Tuning the charge injection of P3HT-based organic thin-film transistors through electrode functionalization with oligophenylene SAMs. *J. Mater. Chem.* **2010,** *20*, 10798-10800.

54. Khodayari, M.; Crane, N. B.; Volinsky, A. A., Electrochemical explanation for asymmetric electrowetting response. *Thin Solid Films* **2013,** *548*, 632-635.

55. Rivnay, J.; Toney, M. F.; Zheng, Y.; Kauvar, I. V.; Chen, Z.; Wagner, V.; Facchetti, A.; Salleo, A., Unconventional Face-On Texture and Exceptional In-Plane Order of a High Mobility n-Type Polymer. *Adv. Mater.* **2010,** *22*, 4359-4363.

56. Liu, C.; Xu, Y.; Noh, Y.-Y., Contact engineering in organic field-effect transistors. *Mater. Today* **2015,** *18*, 79-96.

s

7. A multifunctional graphene/polymer memory device with tunable transport regimes.

7.1 INTRODUCTION

The modern electronics industry is continuously searching for novel materials and processing methods that could lead to devices based on new physical concepts, paving the way towards the exploitation of unprecedented properties. Among these novel materials, graphene has certainly garnered a great deal of attention. Graphene is constituted by a single layer of covalently tethered carbon atoms arranged in a honey-comb lattice; it is a zero band-gap semiconductor exhibiting extraordinary electronic properties.[1,2] To become a golden component for the electronic industry, two greatest challenges need to be addressed: (i) developing methods that can be up-scaled for mass production of high quality graphene, and (ii) opening a band gap to "switch off" graphene devices and thus make them suitable for logic application.[3,4]. On the one hand, liquid-phase exfoliation of graphite into graphene is emerging as a suitable up-scalable method for the production of high quality graphene.[5-9] On the other hand, different strategies have been proposed in order to open a band gap in graphene such as the production of reduced graphene oxide[10,11] or graphene nanoribbons.[12-16] A different way of employing graphene for electronics relies on the use of hybrid solutions that combine graphene with suitable molecules to enable reciprocal modification of the component properties, e.g. *via* tailoring of interfaces or blending. Graphene/inorganic devices were proposed for different ferroelectric and semiconductors applications[17] or as excellent option for radio frequency transistors that do not need high I_{on}/I_{off} ratio.[18] Liquid-phase exfoliated graphene (LPE-G) in

presence of suitable molecules was successfully used as a bi-component graphene/organic hybrid active layer for tuning the transport in thin-film transistors. [19,20] A well explored way to address this approach relies on the use of a blend of graphene and an organic or polymeric semiconductor, although blends exhibit mayor downsides like phase segregation,[19] graphene random aggregation,[21] crystallinity loss in the semiconductor matrix[22] and very poor control over graphene deposition.[23]

In this chapter we describe a novel strategy for fabricating a multifunctional polymeric-graphene thin-film transistor (PG-TFT) that relies on solution processing of semiconducting polymers on the top of solution processed graphene nanoscale patches having thermally tunable IE. This graphene's energy level engineering resulting in a broad range of IEs makes it possible to modulate the electronic interactions between the LPE-G and the semiconducting polymer. In this work, we focused our attention on two exemplary cases, i.e. LPE-G with an IE laying either inside or outside the band-gap of either a p- or an n-type polymer active layer. When the IE is outside the polymer band-gap one obtains tunable device's working regimes which depend on the surface coverage. In particular, it was possible to adjust the transport in the bi-component film from semiconducting to truly conductive, i.e. exhibiting no gate modulation. The control over the IE of deposited LPE-G interacting with the polymer makes it possible also to operate the three-terminal device as a memory element without the need of depositing a further dielectric interlayer as previously reported in literature.[24-26] Noteworthy, the approach has been tested with both n- and p-type polymer semiconductor demonstrating that this novel and general working mechanism is viable for both hole and electron transport.

7.2 MATERIALS AND METHODS

LPE-G exfoliation procedure: In a typical exfoliation process, N-methyl-2-pyrrolidone (NMP) was purchased from Sigma-Aldrich and used as solvent for the exfoliation. Graphite powder (p.n. 332461) was also acquired from Sigma-Aldrich and used without further treatment. Graphene was prepared by liquid phase exfoliation as reported elsewhere[5]. Briefly, graphene dispersion was prepared by adding 100 mg of graphite powder in 10 mL of N-methyl-2-pyrrolidinone (NMP) (1 wt%) followed by bath ultra-sonication (6 h) at 45 °C. Sonication of graphite powder led to grey liquid consisting of a homogeneous phase and large numbers of macroscopic aggregates, i.e. unexfoliated graphitic material. These aggregates were removed by centrifugation (Eppendorf 5804, rotor F-34-6-38, 45 min at 10,000 rpm), yielding to a homogeneous dark dispersion. To quantify the concentration of graphene after centrifugation, a mixture of graphene dispersion and chloroform ($CHCl_3$) was first heated up to 50 °C for 30 min and then passed through polytetra-fluoroethylene (PTFE) membrane filters (pore size 100 nm). The remaining solvent were washed several times with diethyl ether and $CHCl_3$. Careful measurements of the filtered mass were performed on a microbalance (Sartorius MSA2.75) to

give the concentration of graphene after centrifugation. By analyzing 15 independent experiments, concentrations of graphene were obtained amounting 86 ± 10 μg mL^{-1}. Also the average lateral size of the LPE-graphene sheets was estimated to be 224 ± 50 nm and the percentage of mono- and bi-layer thick flakes amounts to 16 ± 1 %.

LPE-G deposition on SiO_2: High quality thermally grown SiO_2 substrate ($n^{++}Si/SiO_2$) (IPMS Fraunhofer) were cleaned by sonication in acetone and then isopropanol. They were carefully dried under nitrogen gas flow. Freshly LPE-G in NMP obtained as described above, was drop-casted on newly ozone treated (5 min irradiation + 25 min incubation) $n^{++}Si/SiO_2$ substrates. Samples were stored in a perfectly plane by spirit-level hoven for 4 h at 50 °C and then at 65 °C for other 2 h to allow gradual, partial solvent evaporation, letting graphene flakes to stick on the surface. Subsequently samples was annealed in air or in nitrogen atmosphere for 14 h at 415 °C to ensure complete solvent evaporation and removal of possible solvent residues[27]. Different amount of dispersions were drop-casted on samples, nominally [2.5: 5: 10: 20] μl of LPE-G. LPE-G dispersion had a density of 86 μg/ml of graphene in NMP. To cover the whole surface ($1.5 \cdot 10^{-4}$ m^2 surface area) a minimum amount of 10 μl are necessary so for 2.5 and 5 μl we diluted the mother dispersion 4 and 2 times, respectively. Also blank samples was prepared with the same procedure, drop-casting 10 μl of pure NMP on samples and then providing thermal annealing at the same conditions of LPE-G samples, in order to have a reliable blank reference for TFTs electrical performance and behavior.

Device Preparation: LPE-G surface patterned $Si\text{-}n^{++}/SiO_2$ samples were used as a scaffold for OTFTs device. In a cylindrical weighing bottle 38 μl of octadecyltrichlorosilane – OTS (purchased from Sigma Aldrich, purity > 90%, used with no further purification) were added to 10 ml of anhydrous toluene in nitrogen atmosphere. Selected samples were immersed in the solution which was then warmed for 30 min at 60 °C. Then the solution with the dipped samples was left reacting for 12 h. Samples were then rinsed with copious amount of toluene to ensure a complete cleaning, and then baked at 60°C for 2 h. Solutions 5 mg/ml of poly[N,N-9-bis(2-octyldodecyl)-naphthalene-1,4,5,8-bis (dicarboximide)-2,6-diyl]-alt-5,59-(2,29-bithiophene)], *P(NDI2OD-T2)* (purchased from Polyera Corporation), and a *p*-type polymer, i.e. poly[1,1'-bis(4-decyltetradecyl)-6-methyl-6'-(5'-methyl-[2,2'-bithiophen]-5-yl)-[3,3'-biindolinylidene]-2,2'-dione] *IIDDT-C3* (purchased from 1-Materials Inc.) in chloroform were pre-pared and stirred overnight to ensure complete solubilisation of the two polymers. 150 μl of polymer solution were spin-coated on the samples with different amount of deposited graphene on the surface. Reference samples were prepared too. For each polymer at least two sets of [0, 2.5, 5, 10, 15, 20] μl of deposited LPE-G was prepared. After spin coating the samples were annealed at 70 °C for 2 h to remove any solvent residual. Casted films were 60 nm thick for both polymers. As last step, 40 nm of gold were evaporated over the polymeric film to finalize top-contact, bottom gate devices. Each sample had 8 devices on it with channel length of 120, 100, 80, 60 μm and W =10000 μm. P(NDI2OD-T2) OTFTs were then annealed for 14h at 120°C to avoid contact problem as reported in literature.[28]

7.3 RESULTS AND DISCUSSIONS

7.3.1 Deposition of LPE-G on SiO_2

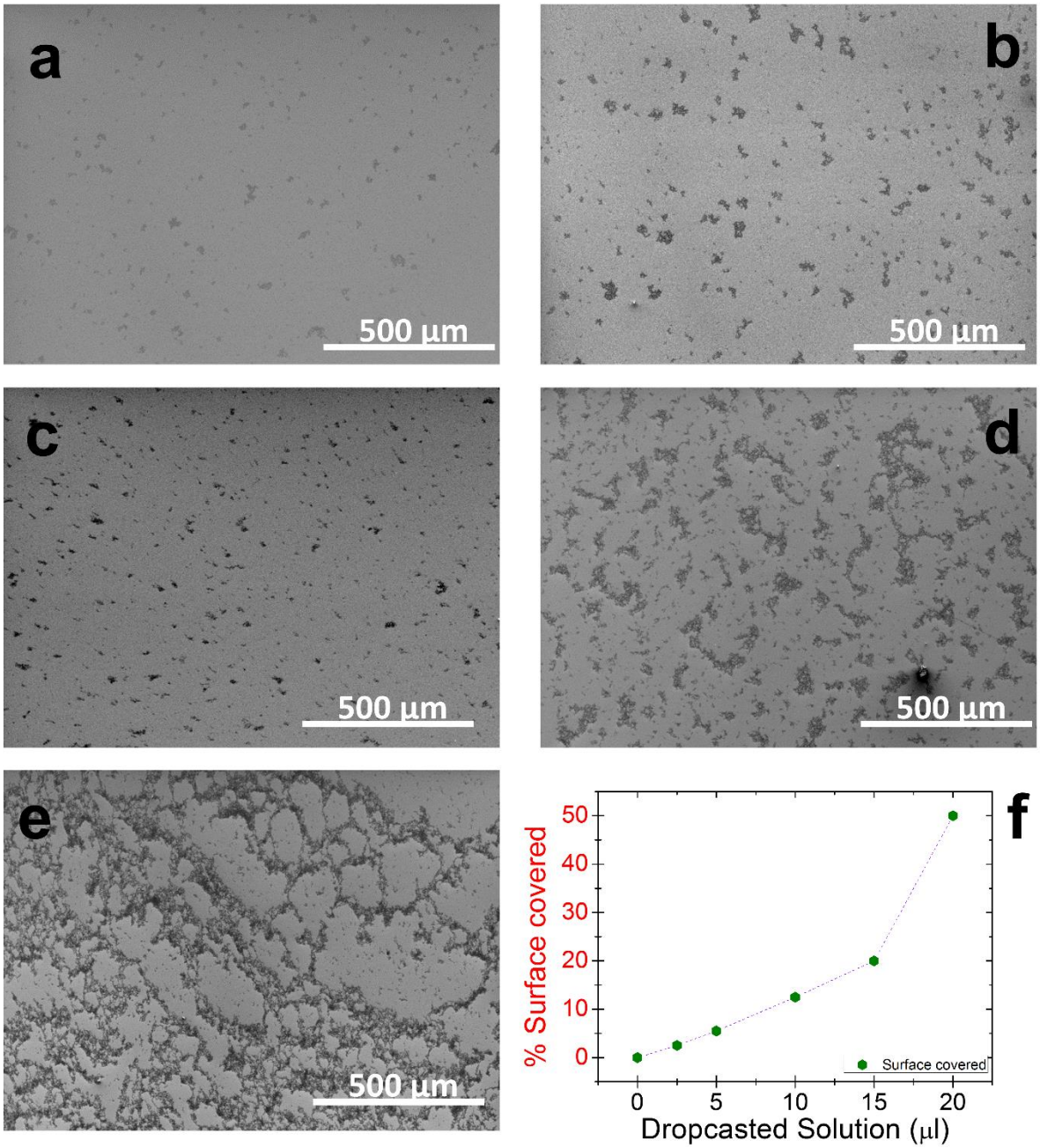

Figure 7.1: SEM images of LPE-G patterns on SiO_2 realized by using different dispersion volume in NMP: (a) 2.5 µl, (b) 5 µl, (c) 10 µl, (d) 15 µl, (e) 20 µl. (f) Correlation between area surface coverage of graphene and volume of drop-cast dispersion of LPE-G.

The device fabrication started with controlled deposition of LPE-G dispersion on SiO_2: The exfoliated graphene dispersion contains high-quality graphene with a concentration of mono

and bi-layer flakes exceeding 55%, as reported in our previous study.[5] A variable volume (nominally 2.5, 5, 10 or 20 µl) of LPE-G dispersion was drop-cast on the SiO_2 surface. The obtained samples were thermally annealed at 415 °C. The Scanning Electron Microscope (SEM) images in **Figure 7.1** display the morphology of films obtained by drop-casting an increasingly greater volume of LPE-G on the SiO_2 surface, followed by thermal annealing. It reveals an increase in surface coverage (amounting to 2.5, 5.5, 12.5, 20, and 50 % reported in **Figure 7.1f**) with isolated graphene nano-patches merging to form a continuous network. Importantly, for each specific volume employed, the coverage of the graphene pattern is homogeneous over the whole sample surface. Graphene nano-patches are also visible by optical microscope. **Figure 7.2** portrays representative images for each sample deposition nominally [2.5; 5; 10; 20] µl of LPE-G on the SiO_2 surface.

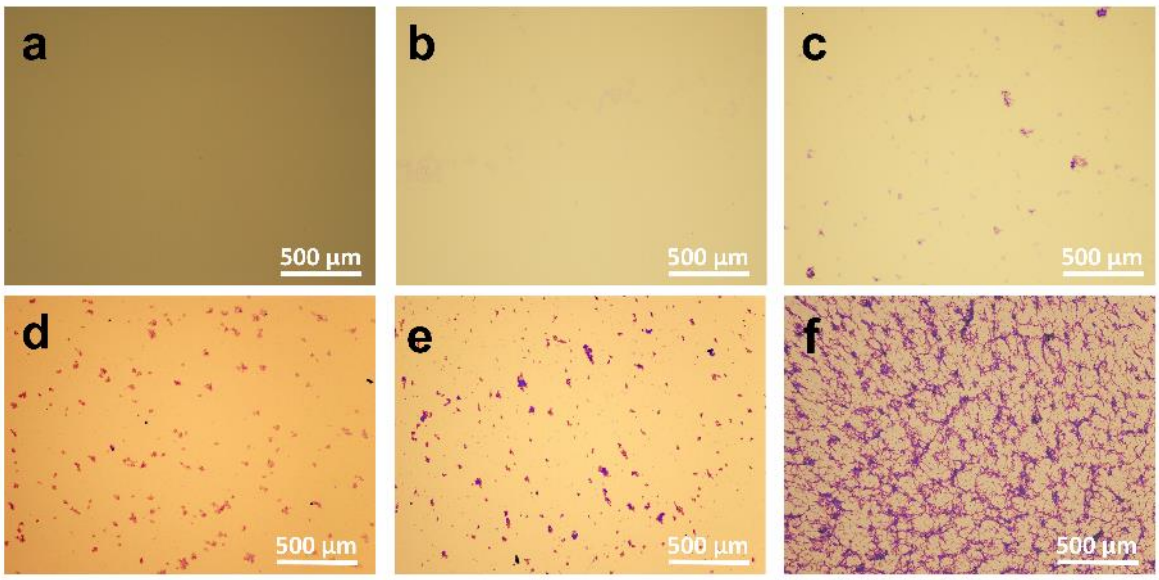

Figure 7.2: Optical images of graphene patches on SiO_2 realized by casting different dispersion volumes in NMP: (a) no graphene, (b) 2.5 µl, (c) 5 µl, (d) 10 µl, (e) 15 µl, (f) 20 µl.

Optical microscope images clearly show the increase in graphene patches with the increasing amount of LPE-G dispersion deposited on SiO_2, as also evident by SEM imaging Moreover, the contrast augments with the increasing number aggregates and thickness. AFM imaging in tapping mode has been used to further investigate the morphology of LPE-G films, and in particular to quantify the thickness of graphene islands adsorbed on the SiO_2 surface.

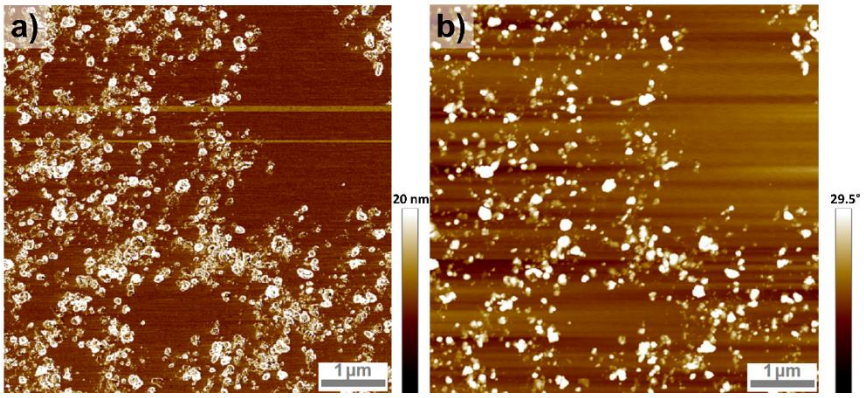

Figure 7.3: Tapping mode AFM images (a) height and (b) phase of 10 µl LPE-G deposited on SiO_2.

The AFM images in **Figure 7.3** provide direct evidence for the rough nature of the discontinuous films. It reveals also small aggregates being part of bigger graphene islands, resulting in a very high effective surface area. The graphene aggregates are of various lateral and vertical sizes as evident in the topographical profiles shown in **Figure 7.4**.

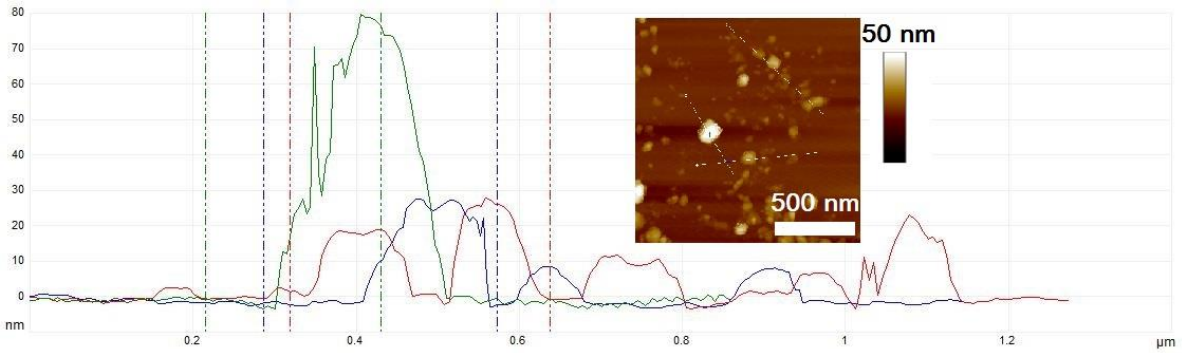

Figure 7.4: Topographical profiles traced along the lines shown in the AFM image in the inset. The sample was prepared by casting 15 µl of LPE-G on SiO_2 and annealed at 415 °C for 14 h.

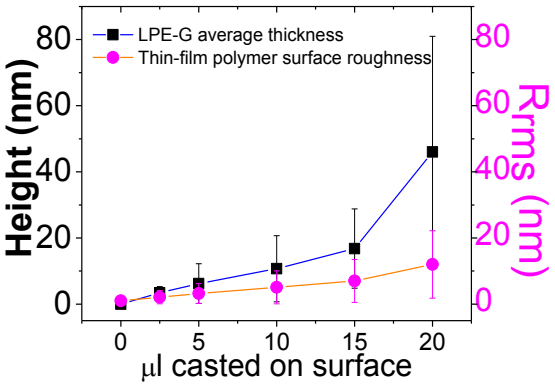

Figure 7.5: Average height of the LPE-G aggregates on SiO_2 as a function of the volume of LPE-G dispersion cast on SiO_2. This correlates well with the polymer film root mean square roughness (R_{rms}) on samples supported on the LPE-G treated SiO_2.

The height of the graphene aggregates varies from a few nm up to 80 nm. **Figure 7.5** displays the statistical analysis (based on > 100 individual measurements for each sample type) of the

average height determined for all the different amounts of LPE-G drop-cast on SiO_2. It reveals that the height of the graphene aggregates increases with the amount of dispersion drop-cast at surface. When a polymer is spin-coated on its top, the roughness is partially transferred to the thin film surface.

7.3.2 Thermal annealing effect on ionization energy of LPE-G and employed polymers

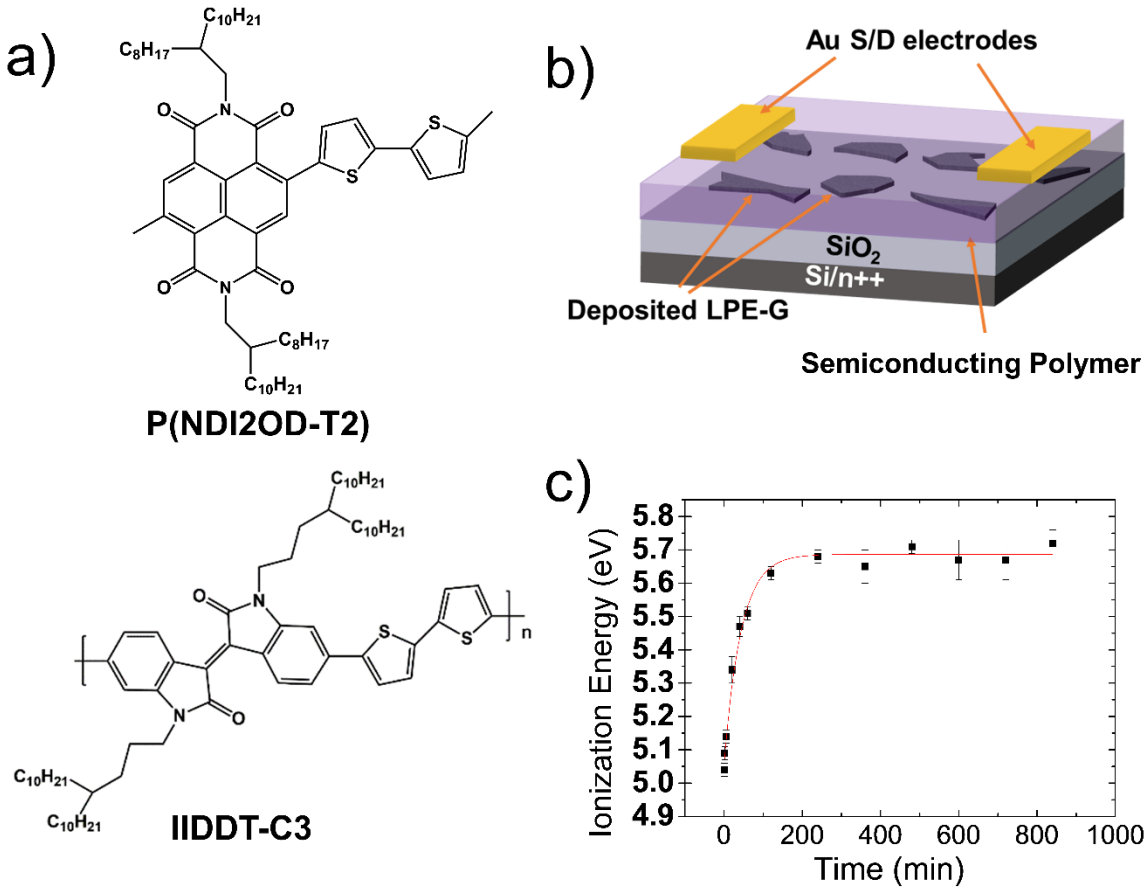

Figure 7.6: (a) Chemical formula of the two polymeric semiconductors encompassed in this study. (b): Scheme of the device geometry implemented, showing the deposition of LPE-G on the SiO_2 dielectric surface, the polymer thin film and the top gold electrodes. (c) Average measured ionization energy shift by ambient photoelectron spectroscopy at different annealing time with their standard deviation (at 415 °C in air environment) and the single exponential fitting thereof.

The thermal annealing treatments of the LPE-G dispersion drop-cast on the SiO_2 were carried out at 415 °C either in environmental conditions, i.e. at RT and RH = 20 % - 30 %, or in a nitrogen-filled atmosphere, i.e. with a few ppm of oxygen and water, in order to remove the N-

methylpyrrolidone (NMP) solvent left-over, including inter-flake residues as proved by X-ray Photoelectron Spectroscopy (XPS) as shown in next paragraph. Ambient photoelectron spectroscopy measurements were performed by sampling in each measurement an area of about 4 mm^2 (beam size) by using a Photoelectron Yield Spectrometer operating in air (PYSA), Model AC-2 from Riken Keike Co., Ltd. The LPE-G samples were prepared by drop-casting 1 ml of dispersion onto the sample holder, to ensure complete coverage of the surface by a deposition of 40 nm thick graphene material to avoid substrate contribution. The samples have been then thermally annealed for different periods at 415 °C in air or nitrogen. The work function of the so prepared samples has been measured by extrapolating the energy point (in eV) where the square root of the photoelectron yield begins to rise upon excitation from the ground state.

In the former case, the IE of graphene patches annealed in air was found to shift from 5.0 eV to 5.7 eV with an exponential trend reaching a plateau after 4 h as shown in figure **Figure 7.6c** where the average value (with standard deviation) obtained from two set of samples is reported for each different annealing time. In the latter case, when the LPE-G deposited on SiO_2 is annealed under N_2 atmosphere at 415 °C for 14 h the IE value was found to remain constant at 4.9 eV as shown in **Figure 7.7** where is also highlighted the difference of 0.9 eV between the LPE-G annealed in air (red dots) and in nitrogen (black dots) The possibility of modulating the IE made it possible to explore the electronic interaction between a polymeric semiconductor and the graphene with IE values at their two extremes, thereby placing the IE level either outside or inside the semiconductor band-gap.

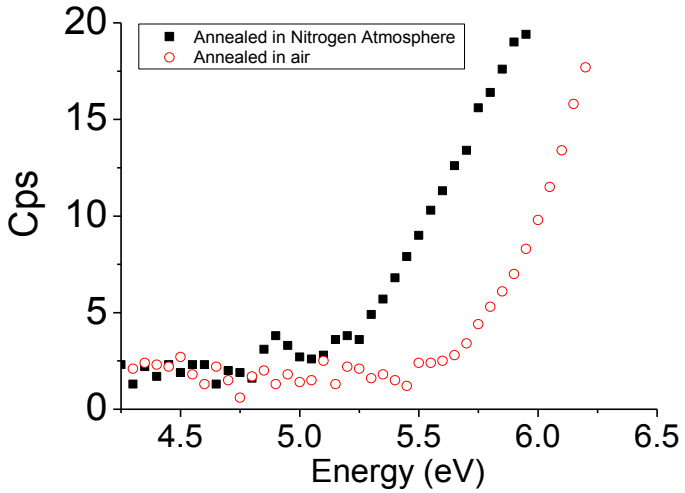

Figure 7.7: Square roots of photoelectron yield vs energy for annealed LPE-G in nitrogen (black dots) and for comparison the spectra reported in Figure S13 for LPE-G annealed in air (void red dots)

.

7.3.3 XPS analysis of annealed LPE-G

In order to evaluate the effect of annealing on LPE-G and NMP residual in the sample, X-ray photoelectron spectroscopy has been carried out on graphene deposited on SiO_2 and then annealed following the procedure described in the manuscript.

Table 6.1 annealed LPE-G on SiO_2 composition

Element	Peak BE	FWHM eV	Area (P) CPS.eV	Atomic %	Q
O1s	533.03	2.81	1593344.69	40.42	1
C1s	284.3	2.78	659267.36	40.41	1
Si2p	104.15	2.69	313737.24	19.17	1

The XPS analysis reveals the absence of nitrogen is in the sample, indicating a complete removal of NMP upon annealing. The amount of oxygen is twice the amount of Silicon indicating just a very small amount of oxygen signal arousing from Carbon-Oxygen bond.

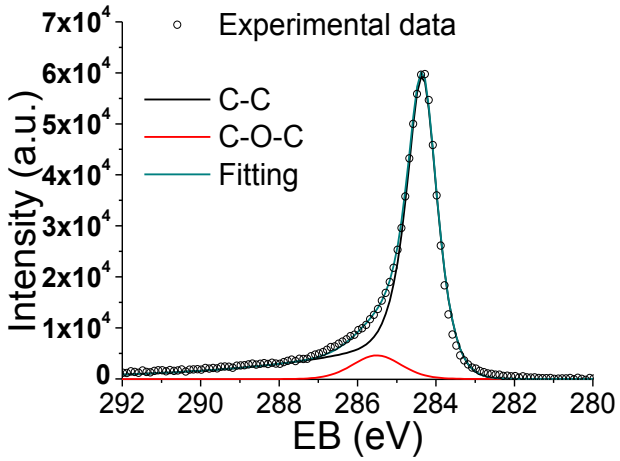

Figure 7.8 C1s spectra for annealed graphene. Experimental data are shown as black circles, the total fit curves as cyan line. C-C sp2 fit is in black and the C-O-C fit in red.

Carbon signal is reported in **Figure 7.8**. The peak at 284.3 eV reveals the presence of graphene with its the typical asymmetric Doniach – Sunjic profile[29]. Deconvolution proves the presence of a second peak at ~ 286 eV, indicating C-O-C bonds in a percentage of 7% based on area ratio.

7.3.4 PG-TFT design and preparation

By taking advantage of the insoluble nature of the thermally annealed LPE-G patches, prior to the deposition of the polymer layer a further functionalization from solution of the SiO_2 areas uncoated by the graphene with octadecyltrichlorosilane (OTS) were carried out in order to

render them more hydrophobic. In essence, such a treatment has the ultimate goal of promoting crystallization of the semiconducting polymer in thin continuous film as well as preventing the electron trapping coming from the silanol groups at the surface.[30] A 60 nm thick polymer semiconductor film (measured with a profilometer) was spin-coated onto the LPE-G pre-patterned on SiO_2. The fabrication of the OTFT was completed with the thermal evaporation of two gold top pads acting as the source and drain electrodes (**Figure 7.6b**). As polymer semiconductor we focused our attention on a *n*-type polymer, i.e. which were used as the active layers in the TFT devices **(Figure 7.6a**). Both polymers combine high charge carrier mobility, air-stability and HOMO/LUMO levels close in energy, as revealed by cyclic voltammetry.[31,32]

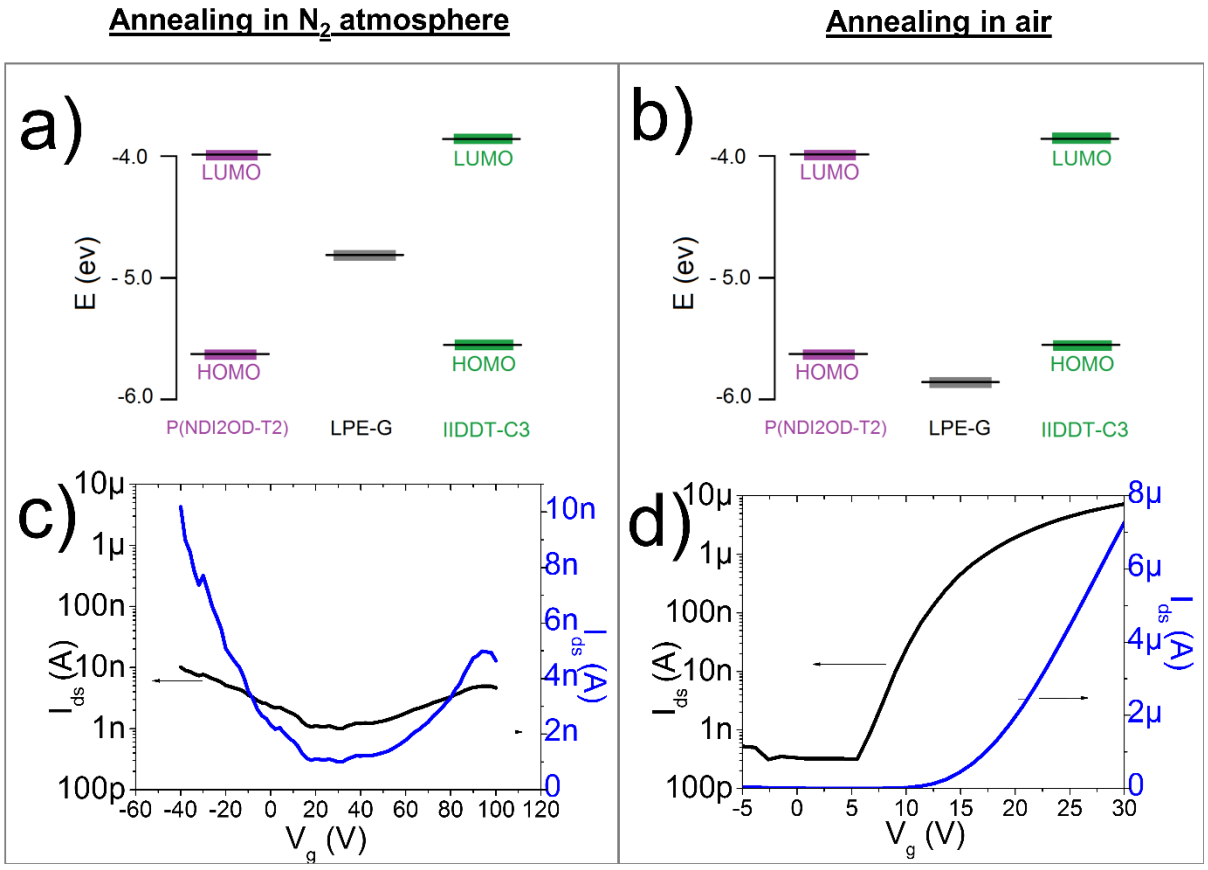

Figure 7.9: Energy scheme of LPE-G, with respect to the two polymeric semiconductors HOMO/LUMO levels as measured by ambient photoelectron spectroscopy annealed at 415 °C for 15 h (a) under nitrogen, and (b) in ambient conditions. (c) Transfer characteristic of a typical P(NDI2OD-T2) device with 10 µl of LPE-G deposited on the gate annealed under nitrogen. (d) Transfer characteristic of a typical P(NDI2OD-T2) device with 10 µl of LPE-G deposited on the gate annealed in ambient conditions. The current is reported in the same logarithmic scale (black) to underline the different conduction properties of the two systems.

Figure 7.9a,b display the energy diagrams which include the polymer's HOMO and LUMO levels as well as the respective IE of LPE-G annealed in a given environment.

For IIDDT-C3 the HOMO measured by Ambient PS amounted to (5.40 ± 0.05) eV, in good agreement with HOMO values reported in literature as determined by CV measurements[32]. For

P(NDI2OD-T2) the HOMO determined amounted to (5.55 ± 0.05) eV in perfect accordance with previous reports[31]. By considering an optical band gap of 1.55 eV as reported in literature,[33] it was possible to estimate the energy of the LUMO level of P(NDI2OD-T2) as (4.00 ± 0.05) eV.

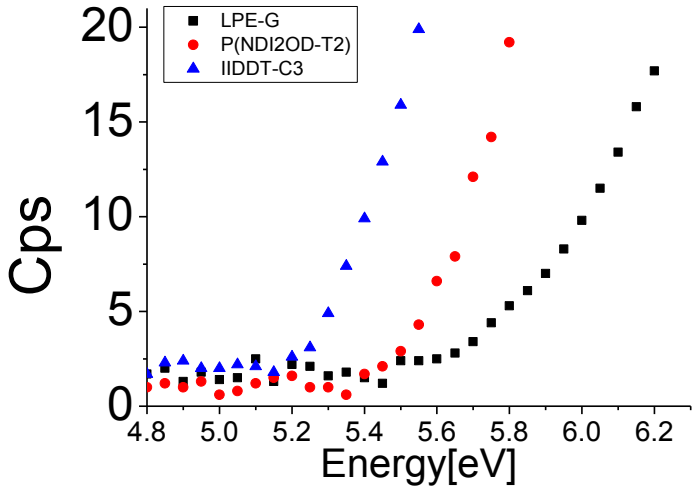

Figure 7.10: Square roots of photoelectron yield vs energy spectra for annealed LPE-G in air, P(NDI2OD-T2) and IIDDT-C3.

When LPE-G was annealed under N_2 atmosphere the IE amounts to 4.9 eV, which implies that this level lies inside the band-gap of both polymers, thereby allowing graphene to act as (deep) trap center in the channel. Thermal annealing of LPE-G at 415 °C for 4 h in air environment, lead to a drastic change in IE value which shifts to 5.7 eV. Such a value falls outside both polymers' band-gap, thus in such a case the LPE-G cannot act as an energy trap for charges. Overall, the IE of the deposited LPE-G can be modified by changing the duration of thermal annealing at 415 °C and the environment in which such an annealing is executed. **Figure 7.9c,d** portrays the transfer characteristics of device consisting of P(NDI2OD-T2) spin-coated on LPE-G that was previously drop-cast on SiO_2 (volume = 10 µl) and annealed at 415 °C for 15 h either under N_2 atmosphere or in air, respectively. **Figure 7.9c** reveals a drastic reduction in both the output current of the device and in the gate modulation effect. In particular, currents below 10 nA were measured together with very low gate modulation. On the other hand, when the ionization energy of LPE-G is higher in energy than the HOMO of both polymers (**Figure 7.9d**), the TFTs exhibit a very good behavior with current exceeding 10 µA and high mobility values In light of these findings we decided to perform an in-depth study of devices based on LPE-G drop-cast on SiO_2 followed by thermal annealing in air environment.

The LPE-G nano-patches on SiO_2 shown in **Figure 7.1**, exhibiting different coverages, were used as templates for the fabrication of hybrid graphene-polymer based TFTs. In particular, the effect of degree of coverage of graphene nano-patches on SiO_2 on the charge transport in the hybrid material was explored by fabricating bottom-gate top-contact TFTs using the two

semiconducting polymers described above. Smooth polymer films were prepared by spin-coating onto the previously patterned LPE-G samples (**Figure 7.6b**) followed by the evaporation of the gold top electrodes. These PG-TFTs were characterized in order to cast light onto the role of the graphene nano-patches annealed in air on the electrical properties of the hybrid active layer, by quantifying the relevant device parameters such as the field-effect mobility, threshold voltage and I_{on}/I_{off} ratio. We prepared two set of samples for each polymer. This allowed us to measure 16 devices for each different surface coverage for a total of 80 devices for each polymer.

Figure 7.11 and **6.12** display the typical output and transfer characteristics for the different coverages employed for both polymers.

7.3.5 P(NDI2OD-T2)/ PG-TFT

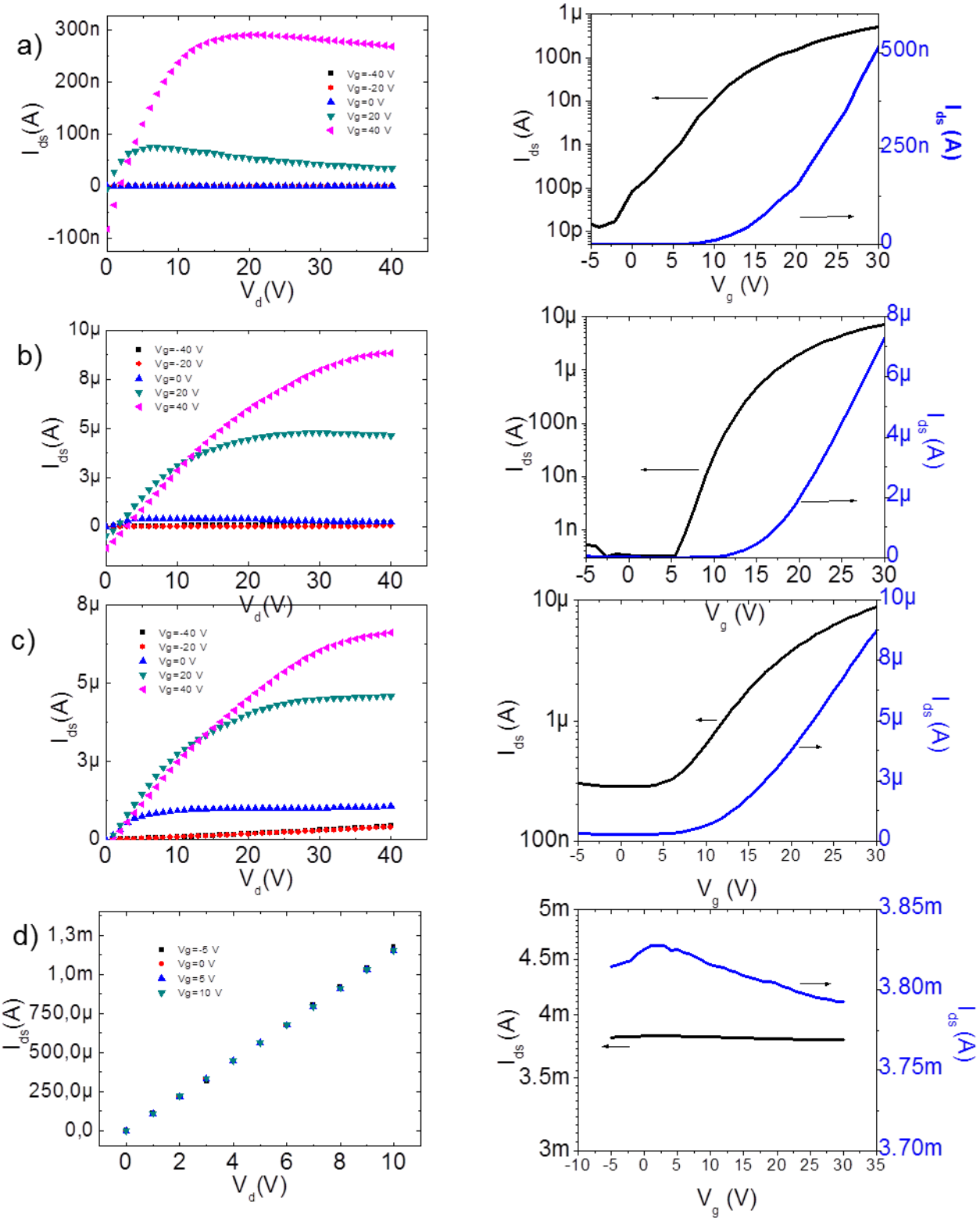

Figure 7.11 Output (left) and transfer (right) characteristics of 120 µm width channel OTFTs based P(NDI2OD-T2) for (a) pristine semiconducting behavior, (b) enhanced semiconducting behavior, (c) semiconducting/graphene hybrid behavior, (d) graphenic behavior. For transfer characteristics V_{ds} = 40 V.

7.3.6 IIDDT-C3/ PG-TFT

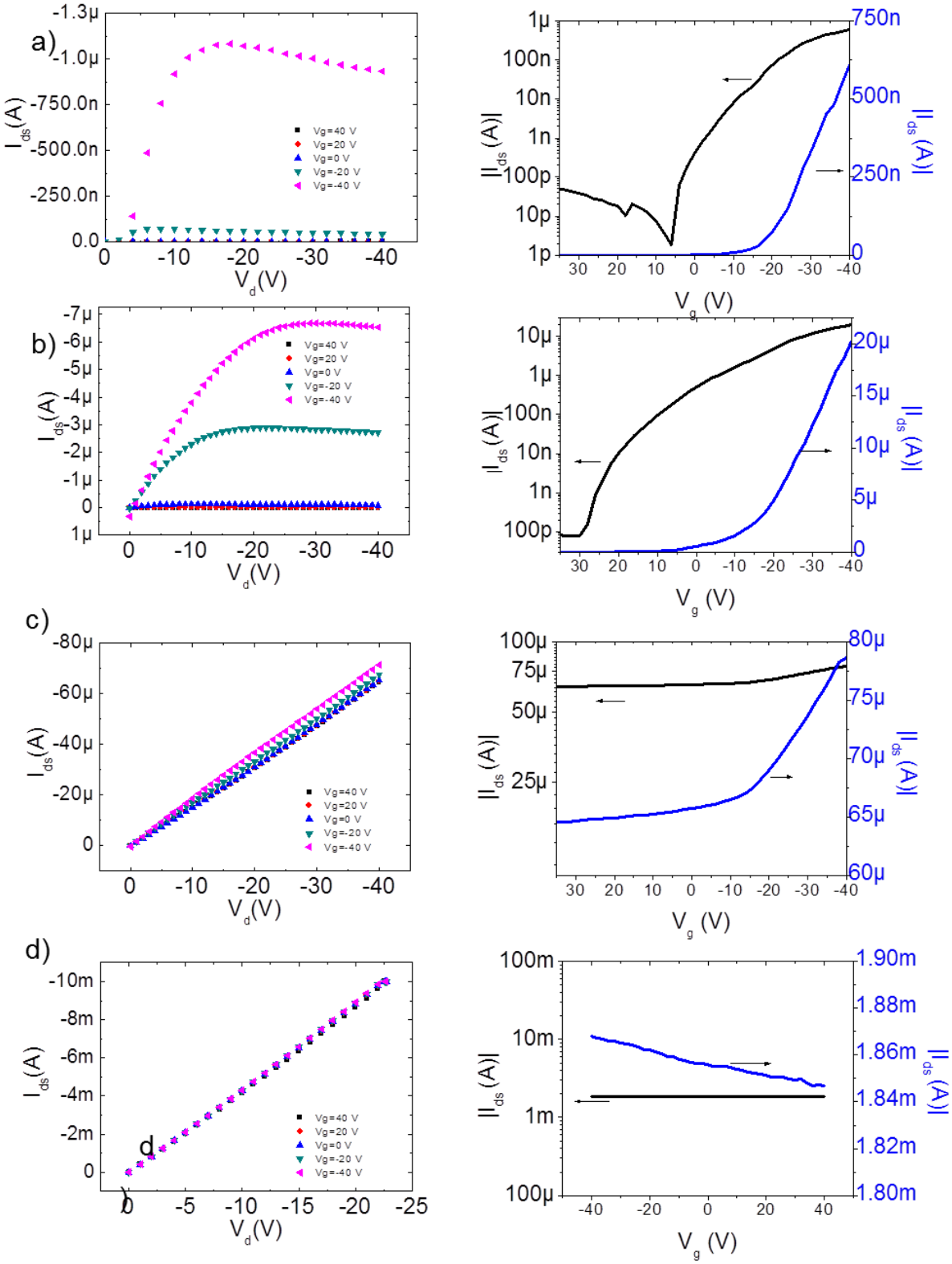

Figure 7.12 Output (left) and transfer (right) characteristics of 120 µm width channel OTFTs based IIDDT-C3 for (a) pristine semiconducting behavior, (b) enhanced semiconducting behavior, (c) semiconducting/graphene hybrid behavior, (d) graphenic behavior. For transfer characteristics V_{ds} = -40 V.

7.3.7 Discussion of Electrical measurements – tunable working regimes

Pristine semiconducting TFTs exhibit low mobility and high I_{on}/I_{off} ratio as shown in **Figure 7.11a** and **6.12a**. Increasing the amount of graphene on the SiO_2 surface, increases the gate surface area, leading to an increase of a performance and a small decrease of I_{on}/I_{off} ratio (**Figure 7.11b** and **6.12b**). When the graphene patches increases in density, percolation pathways are formed, leading first to a behavior that can be defined hybrid, in which there are combined the characteristic of a semiconductor, *i.e.* gate modulation and graphene one, *i.e.* no off current as shown **Figure 7.11c** and **6.12c**, and then to a full graphenic behavior with high currents, no gate modulation and I_{on}/I_{off} ratio around 1 (**Figure 7.11d** and **6.12d**).

A general view of the effect on the I_{on}/I_{off} ratio of LPE-G concentration on the gate surface is shown in **Figure 7.13.** It is interesting to note how the I_{on}/I_{off} ratio decrease is below one order of magnitude for enhanced semiconducting regime and that there is a defined quantity of graphene after which percolation pathways are always present.

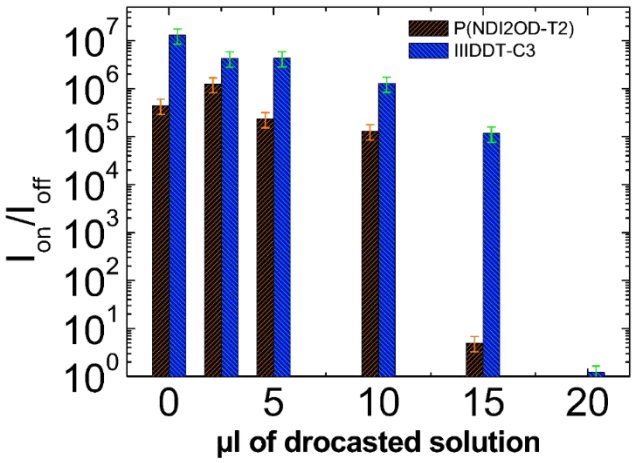

Figure 7.13*:* I_{on}/I_{off} ratio for the different OTFTs with different mesh densities at the surface (mesh density increases with the volume of the dispersion drop-cast on SiO_2).

Table 6.2 reports the values of field-effect mobility calculated for the two semiconducting polymer at the different amounts of LPE-G dispersion drop-cast on SiO_2.

Table 6.2 *extracted saturation mobility values and threshold voltage.*

µl of drop-cast LPE-G dispersion on the SiO_2 surface	P(NDI2OD-T2) – n type FE mobility ($cm^2 V^{-1} s^{-1}$)	P(NDI2OD-T2) – n type highest FE mobility ($cm^2 V^{-1} s^{-1}$)	P(NDI2OD-T2) V_{th} (V)	IIDDT – C3 – p type FE mobility ($cm^2 V^{-1} s^{-1}$)	IIDDT – C3 – p type highest FE mobility ($cm^2 V^{-1} s^{-1}$)	IIDDT – C3 V_{th} (V)
0 µl	0.002±0.001	0.0025	6.2±3.1	0.005±0.002	0.008	-8.3±3.5
2.5 µl	0.006±0.002	0.009	7.1±3.4	0.008±0.002	0.011	-11.2±4.2
5 µl	0.018±0.008	0.032	10.2±4.2	0.010±0.003	0.013	-6.5±4.1
10 µl	0.014±0.004	0.018	10 ±2.7	0.012±0.004	0.017	-7.2±3.8
15 µl	-	-	-	0.016±0.004	0.024	-7.9±3.1

The mobility increases with the increasing amount of graphene deposited on the surface, as shown in Figure 3a up to one order of magnitude for P(NDI2OD-T2) and up to a factor of three for IIDDT-C3. For P(NDI2OD-T2) these values of mobility are remarkably high when compared to bottom-gate device previously published for P(NDI2OD-T2)[34]. Conversely, for IIDT-C3 values are lower with respect to previously reported work[32], but different solvent and annealing process were performed. This leaves ample room for further improvements in the performances. On the other hand threshold voltage does not significantly shift with increasing graphene surface coverage for both polymer.

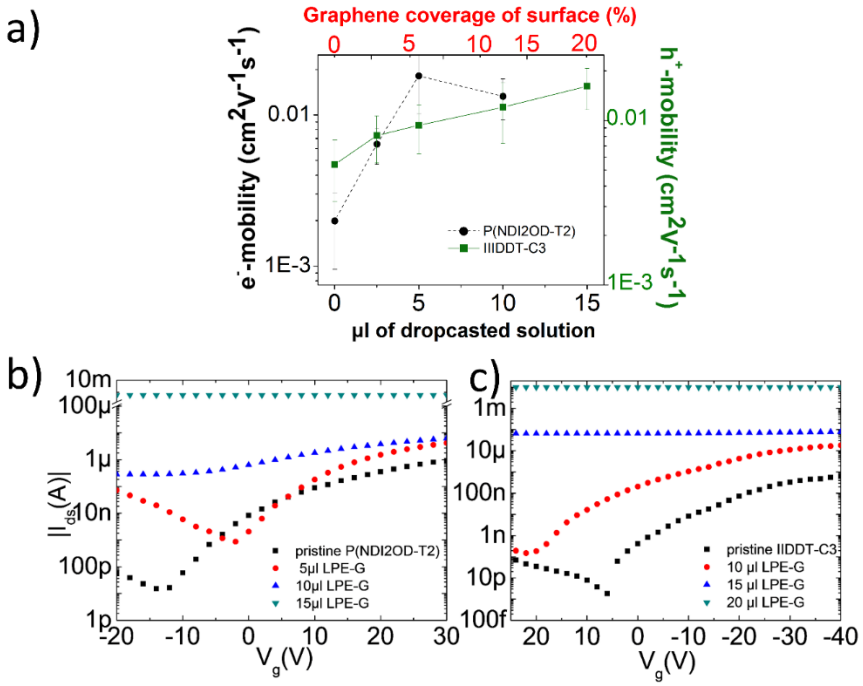

Figure 7.14: (a) Average field-effect mobility and corresponding standard deviation for P(NDI2OD-T2) and IIDDT-C3 films supported on pre-patterned LPE-G at increasing volume of LPE-G suspension deposited on SiO_2 surface (bottom axis) and respective LPE-G surface coverage (top axis). (b) Transfer characteristic of devices for different amounts of LPE-G deposited on the gate surface for P(NDI2OD-T2) and (c) IIDDT-C3 based devices. The curves displayed are representative of the 4 working, i.e. conductive, regimes found in the system. Channel length 100µm, width 10000 µm, V_{ds} = 40 V for P(NDI2OD-T2) and V_{ds} = -40 V for IIDDT-C3.

Since the large amount of data presented more deep discussion of the results is needed. As a general trend, the device output current increased with the degree of coverage of graphene on the surface, but such an enhancement is accompanied by different changes in electrical performances (**Figure 7.14a**). Four different types of device operation could be identified based on our data. *(I)* Semiconducting behavior ($I_{on}/I_{off} > 10^5$, strong gate field-effect); *(II)* enhanced semiconducting behavior (I_{on}/I_{off} ~10^5-10^4, strong gate field-effect, increase in mobility); *(III)* semiconducting/graphene hybrid behavior ($I_{on}/I_{off} < 10^3$, low gate field-effect, OFF currents > 10^{-7} A; *(IV)* graphene-like behavior (I_{on}/I_{off}<10, no gate field-effect, current > 10^{-4} A). When 0 - 5 µL of LPE-G were drop-cast on the dielectric surface, an increase in the recorded current

and field-effect mobility for both polymers was observed entering in regime *(II).* In particular, compared to the pristine devices *(I),* the graphene pre-patterned based TFT incorporating P(NDI2OD-T2) and IIDDT-C3 exhibited an over ten- and three-fold increase in field-effect mobility, respectively. This improved mobility is attained at the expenses of a subtle decrease of the I_{on}/I_{off} ratio (being below one order of magnitude), indicating a preponderant semiconducting working regime. Upon increasing the graphene deposited on the surface, by drop-casting 10-15 µl LPE-G on the SiO_2, hybrid *(III)* or graphenic *(IV)* devices were obtained. In hybrid devices gate modulation is still present, but the I_{on}/I_{off} ratio is reduced significantly with respect of regime *(II)* most likely indicating that LPE-G on the gate surface is enough interconnected to generate partial percolation pathways. This proves that the graphene effect on I_{on}/I_{off} ratio is related to gate voltage modulation, which decreases up its disappearance when a fully interconnected network of deposited graphene acts as a percolation pathways for charges. In this regime (*IV*), because of the high amount of graphene adsorbed on SiO_2, the devices display a drastic reduction of I_{on}/I_{off} ratio. In general, the I_{on}/I_{off} ratio decreases progressively upon increasing the graphene content in the device (**Figure 7.14b,c**). The graphene-like regime displays high current and no gate modulation in logarithmic scale, while a small but measurable gate effect is still evident in **Figure 7.11d** and **6.12d.** This aspect will be better exploited in next paragraph. As a result of the thermal treatment the deposited LPE-G on SiO_2 can electronically behave as graphene; in particular the presence of Dirac point and high current flowing, providing evidence for absence of a chemical oxidation of graphene induced despite thermal annealing treatment. Interestingly, the transition between semiconducting to fully graphenic transport regime is not abrupt but it can be finely tuned upon changing the degree of coverage of the graphene nano-patches pre-patterning the surface. The mobility increase is strongly correlated with the degree of coverage of the LPE-G pattern on the dielectric gate surface up to a point in which devices cannot be turned off, albeit preserving gate modulation. Those two intermediate regimes are particularly interesting from a scientific and engineering point of view. In fact, having a regime in which mobility is enhanced with an I_{on}/I_{off} ratio exceeding 10^5 and a regime in which we can have higher current flowing yet still gate effect modulation open future possibilities on the application of this method for fabricating tunable graphene/organic hybrid device.

To determine the reproducibility of our deposition method and the homogeneity of the device built on a single chip we report in **Table 6.3** for each amount of drop-cast graphene on the surface how many different working regime are present and in which percentage.

Table 6.3 Percentage of different working regime for each LPE-G deposition amount for both polymers based OTFTs.

µl of drop-cast LPE-G dispersion on	P(NDI2OD-T2) based OTFTs	IIDDT-C3 based OTFTs

the surface SiO_2								
20	Semiconducting	Enhanced Semiconducting	Hybrid	Graphenic	Semiconducting	Enhanced Semiconducting	Hybrid	Graphenic
0 µl	100%				100%			
2.5 µl	50%	50%			80%	20%		
5 µl		92%	8%		60%	40%		
10 µl		70%	18%	12%		94%	6%	
15 µl				100%		82%	6%	12%
20 µl				100%				100%

We considered as "enhanced device semiconductor" each device exhibiting a 5-fold increase in the mobility with respect pristine average values for P(NDI2OD-T2) and 2-fold increase with respect pristine average values for IIDDT-C3. 5 µl deposition are enough for P(NDI2OD-T2) to have very improved mobility with no percolation pathways, while the same is achieved with 10 µl deposition for the other polymer. This demonstrates the good homogeneity achieved with this deposition methods. However, hybrid graphene/semiconducting regime is the most difficult to accomplish and it is present in chips in which mostly enhanced semiconducting regime device are found. To obtain a complete chip with a complete hybrid regime a more careful controlled and complex deposition method is required.

7.3.8 Annealed LPE-G: electrical characteristic

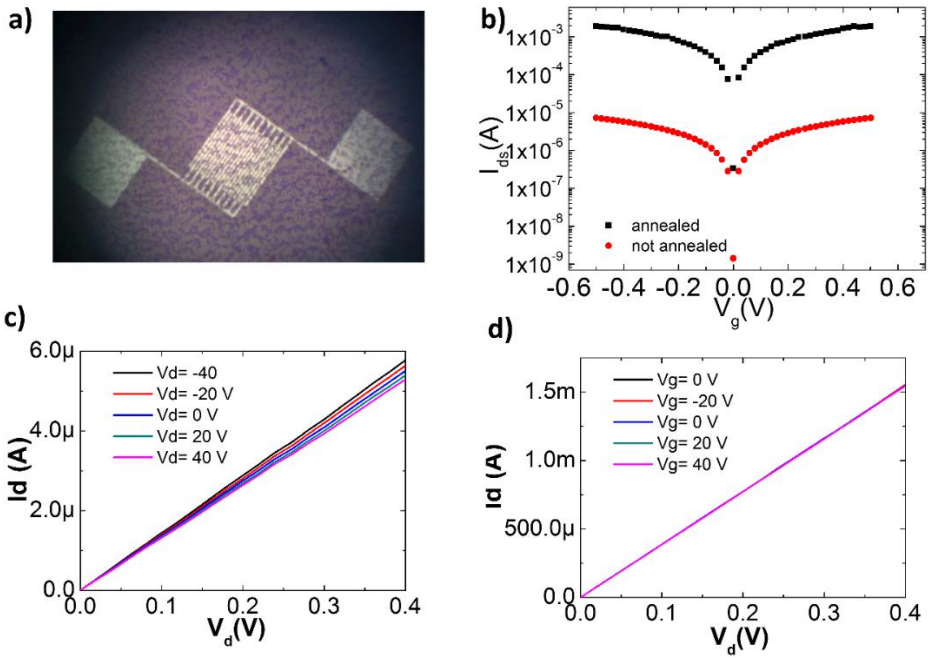

Figure 7.15 a) Optical image of LPE-G deposited on pre-patterned electrodes. b) Current -voltage (transfer) curves after (black) and before (red) annealing cycle at 415 on the same device reported in a). c) Transfer characteristic of LPE-G before annealing and d) after annealing

In order to better investigate electrical properties we deposited 50 µl of LPE-G on pre-patterned interdigitated gold electrodes on SiO_2 (bottom-contact bottom-gate geometry). First we dried our samples in oven at 40C ° under continuous vacuum at 10^{-2} mbar for 12 h. Ionization energy of deposited graphene processed in this way has been measured to be 5.1 eV. Since the deposition was uniform and deposited material was continuous enough, it was possible to test it. First, almost no gate modulation has been registered as reported in **Figure 7.15c**. Second, very low current has been registered for a conductive materials as deposited LPE-G should be.[35] This electrical behavior finds its explanation in the fact that NMP is still present between flakes, hence LPE-G are still partially solvated by an "insulating material" hindering the *inter*-flake charge hopping. The same samples have been then annealed for 14 h at 415 °C at ambient conditions with RH of about 25%. As shown in **Figure 7.15d** the sample loses completely the gate modulation, but at the same time current registered increases more than 100-fold as highlighted in **Figure 7.15 b**. These findings underline importance of annealing for enough time to achieve complete removal of solvent to any kind of effect in electrical properties.

From these measurements, we can estimate the difference in sheet resistance between annealed and not annealed LPE-G. In general, the sheet resistance for a given material is defined as the ratio between resistivity and thickness. Sheet resistance is commonly used to evaluate the transport properties of graphene-based materials, for which the thickness is negligible when compared to the other dimensions.

In our device, to compare the difference between the annealed and not annealed sample we can estimate sheet-resistance as reported in equation **6.1**

$$R_s = R_{tot}\frac{W_{eff}}{L}$$

R_{tot} is the total resistance as defined by the ratio between appl ıge and measured current, W_{eff} is the effective coverage of electrode by LPE-G and L is the channel length. Since the sample had the same W_{eff} and L, we can approximate a difference of sheet resistance of around two orders of magnitude between annealed and not annealed sample. Considering a coverage of 50% and L = 20 µm for the reported sample in **Figure 7.15** it is possible to estimate a sheet resistance of 2.5 MΩ for the device before and 25 KΩ after annealing, respectively. These values are in perfect agreement with what reported by our group for the same material measured in the same geometry,[5] anyhow both values are higher than the intrinsic graphene sheet resistance.[36] This can be explained by considering that we are measuring a fragmented conductive material and thus a flake to flake percolation pathways of charge is formed between electrodes - This introduce a resistance which is not present in the case of a continuous layer of carbon atoms with a few defects as CVD-graphene where charges do not hop from a flake to another

Furthermore, the electrode geometry is not ideal for measuring the sheet resistance of low-resistive materials. Interdigitates electrodes are normally employed to measure high resistive semiconductors in order to geometrically enhance the current. For the annealed LPE-g, the resistance of the material in the channel is very low, so that other contributions are picked up when the resistance is measured. In particular, the contribution of the contact resistance, gold/graphene in our case[37-39], becomes significant, also because bottom contact geometry maximizes it[40]. Therefore, our measurement overestimates the real sheet resistance of the annealed LPE-g, but still gives a valuable information on the phenomena taking place during the annealing. An accurate estimation of the sheet resistance would require microfabrication steps which are out of the scope of this thesis.

37-39

7.3.9 Morphological Investigation of LPE-G with a polymeric film deposited on top- GIXRD

To gain a greater understanding on the enhanced electrical characteristics in the enhanced semiconducting regime (*II*) and in general on the effect of the pre-patterning of the SiO_2 with graphene when a polymer is spin-coated on its top, we explored the structure and morphology of the graphene and graphene/polymer films. The crystallinity of the semiconductor films of P(NDI2OD-T2) and IIDDT-C3 was investigated by Grazing Incidence X-Ray Diffraction (GIXRD) measurements performed at the ELETTRA-XRD1 beam line at Trieste's synchrotron facility (Italy) using a monochromatic beam with a wavelength (λ) of 1 Å and a dimension of 0.2×0.2 (H×V) mm^2. The incident angle of the X-ray beam, α_i, was chosen slightly larger than the critical angle for total reflection of the organic film (~0.18°), in order to penetrate through the full film depth. The diffraction patterns were recorded under helium atmosphere to reduce the beam damage and air scattering using a 2D camera (Pilatus detector) placed normal to the incident beam direction at 200 mm and 470 mm from the sample. This latter was chosen to increase the resolution of the Bragg peak at small angle. Several images were collected translating the sample 0.5 mm in a direction perpendicular to the beam to probe the sample homogeneity. Background coming from the air/He scattering was estimated by collecting the scattering signal from the sample holder environment without film.

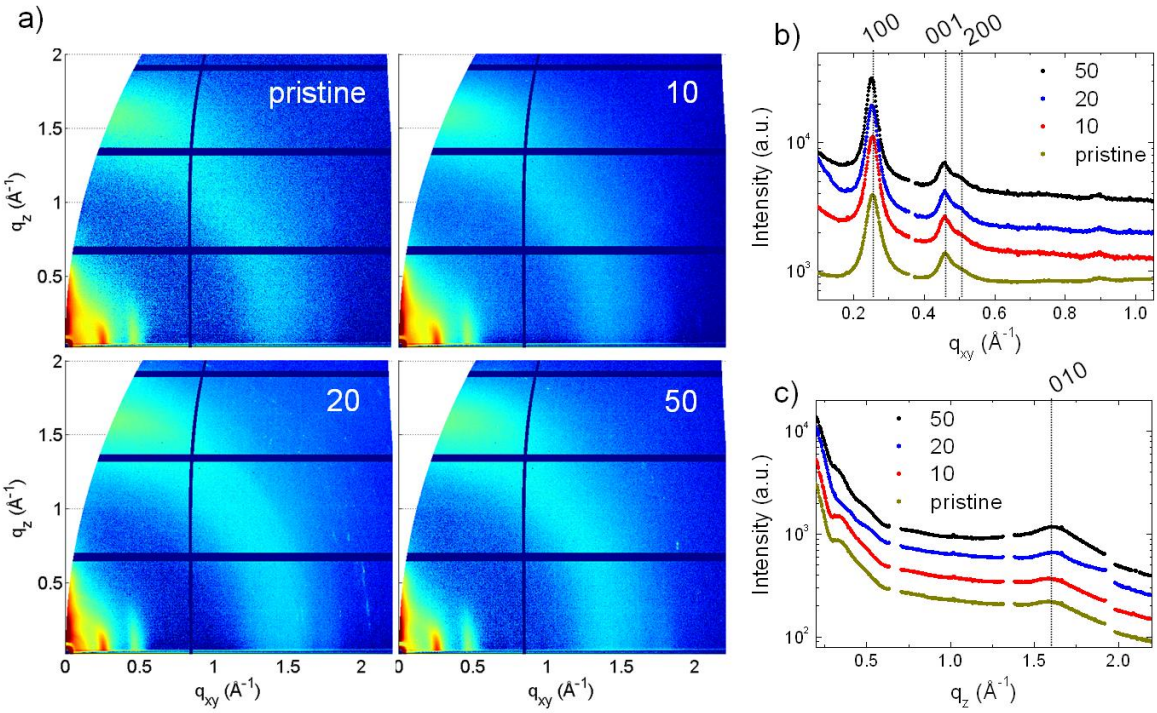

Figure 7.16: (a) 2D-GIXRD images of pristine P(NDI2OD-T2) and of P(NDI2OD-T2) film deposited on graphene in different concentrations. Scattering intensity integrated along (b) the Yoneda, and (c) the specular direction (q_{xy} ~ 0). Curves are shifted for clarity. The integration along Yoneda has been performed from the 2DGIXRD images collected at small angle to increase the resolution.

Figure 7.16 shows representative 2D-GIXRD maps of P(NDI2OD-T2) films deposited on SiO_2 bare (pristine) and on SiO_2 surface covered by graphene sheets at different concentrations (from 10 to 50 μL). All patterns exhibit the same features regardless the graphene concentration, as highlighted in **Figures 6.16b**,**c** where the scattering intensities along the in-plane and out-of-plane direction are displayed. Several weak rod-shape Bragg spots related to the lamellar stacking and to the chainbone repeat (001) are observed along the in-plane direction (q_z~ 0), whereas a wide π-stacking peak (010) is spread along the out-of-plane direction, indicating that the lamellar stacking adopts the face-on orientation.

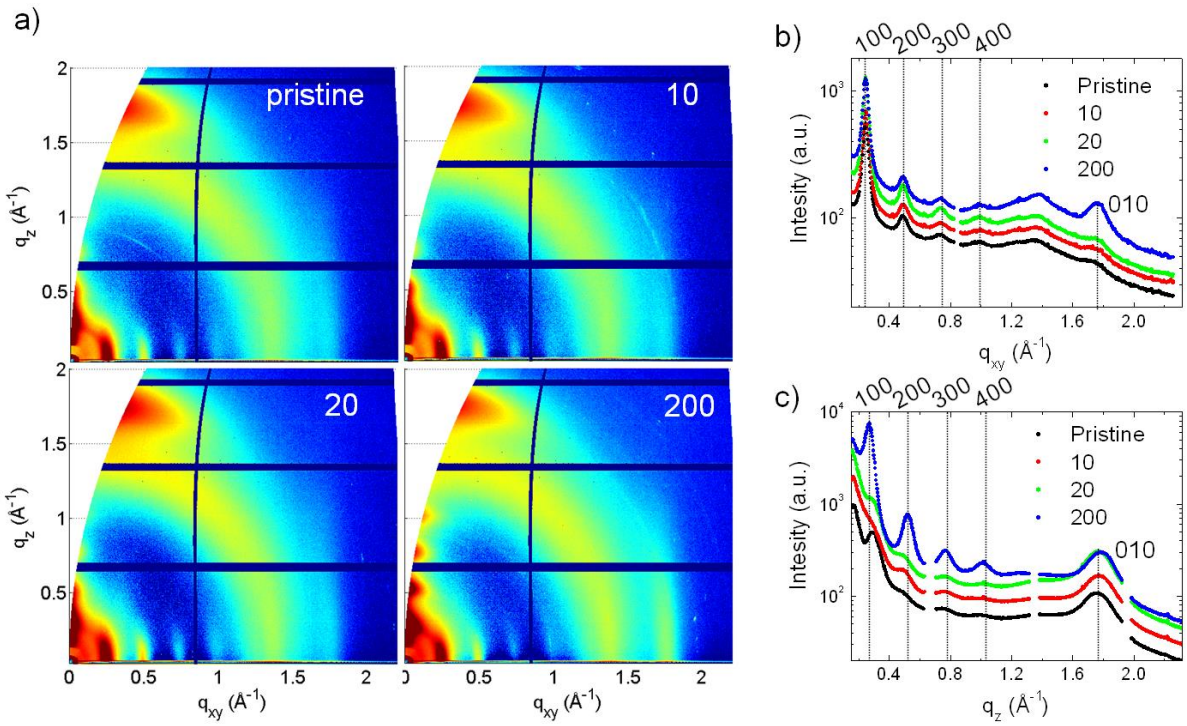

Figure 7.17: (a) 2D-GIXRD images of pristine IIDDT-C3 film and of IIDDT-C3 films deposited on graphene in different concentrations. Scattering intensity integrated along (b) the Yoneda, and (c) the specular direction (q_{xy} ~ 0). Curves are shifted for clarity.

The same molecular packing orientation has been found for IIDDT-C3 films. As shown by GIXRD patterns (**Figure 7.17**), for the majority of crystallites the lamellar stacking adopts the face-on orientation which is also observed when the polymer film was grown on a low amount of graphene sheets. At very high concentration lamellar and π-stacking peaks get stronger along the out-of-plane and in-plane direction, respectively, indicating the increasing of the crystallites amount with edge-on orientation. In this configuration the IIDDT-C3 structure is more compact as exemplified by an inter-lamellar distance of 23.4 Å, i.e. 1 Å shorter than that extracted from face-on crystallites.

By and large, 2D-GIXRD measurements executed on films with different combinations of polymer vs. LPE-G surface coverage provided evidence for the absence of significant structural differences in the polymer crystallinity upon increasing the content of LPE-G coating the SiO_2 surface.

7.3.10 Morphological Investigation of PG-TFT

Atomic force Microscopy (AFM) studies on the graphene nano-patches on SiO_2 and the bi-component graphene/polymer films revealed that the roughness of pre-patterned LPE-G nano-patches (**Figure 7.3**) is partially transferred to the top polymer film. While mono-component polymer films are very smooth, as evidenced by a root mean square roughness (R_{rms}) below 1 nm determined on a 25 μm^2 AFM image, the presence of underlying LPE-G generates 6 nm

thick ripples on the polymer film surfaces when 10 µl of LPE-G are deposited as reported in **Figure 7.5.**

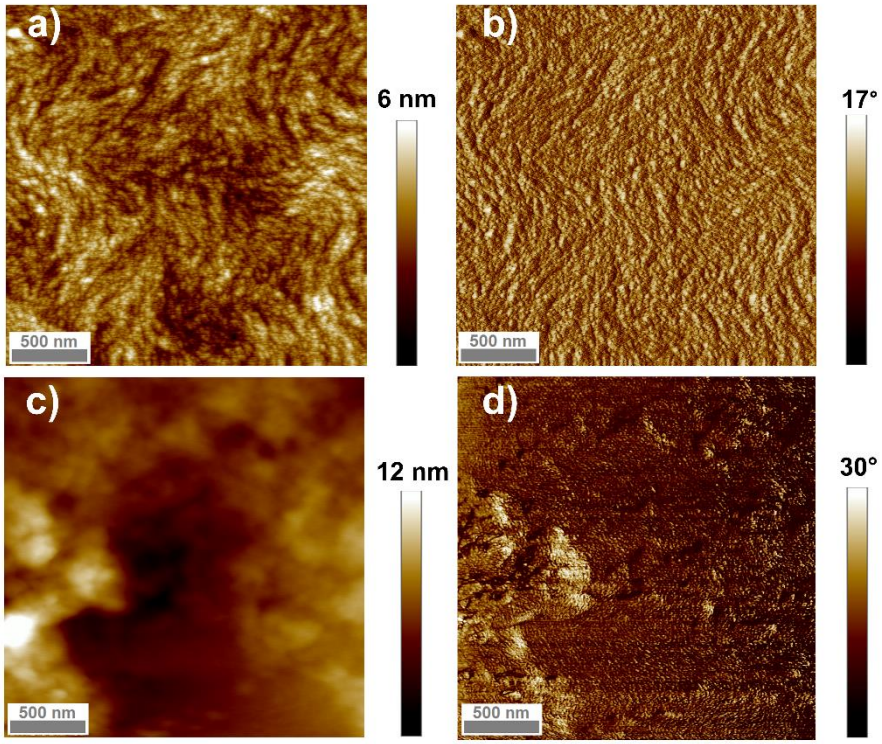

Figure S18: Tapping mode AFM images of a) height) and b) phase of P(NDI2OD-T2) on SiO_2, and c) height and d) phase of the polymer deposited on the LPE-G treated SiO_2.

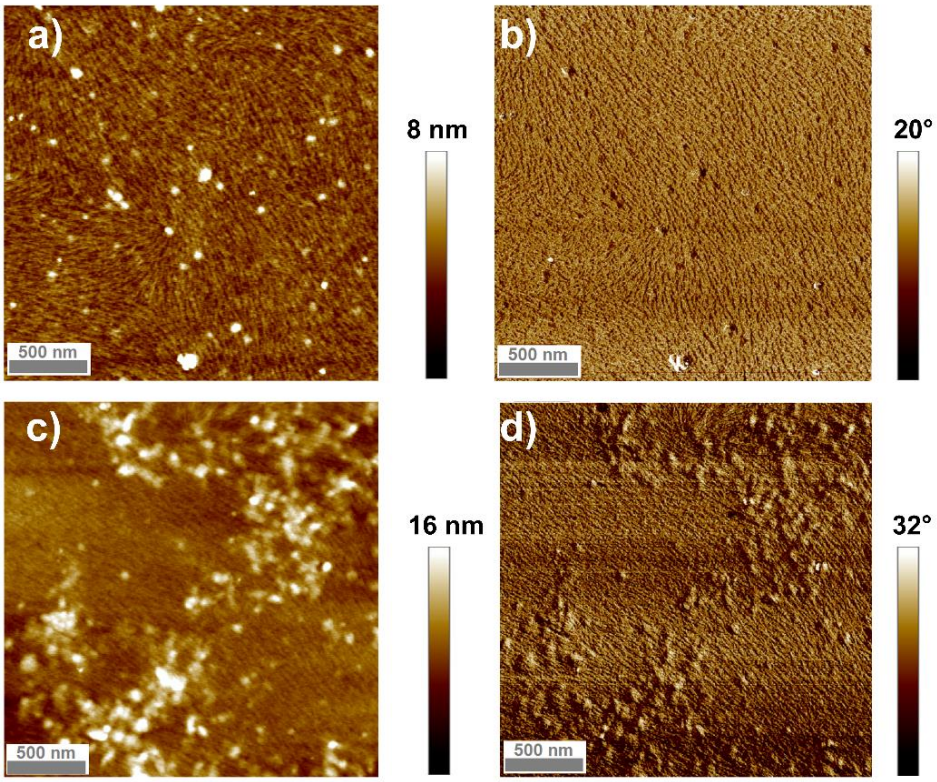

Figure 7.19: Tapping mode AFM images of a) height) and b) phase of IIDDT-C3 on SiO_2, and c) height and d) phase of the polymer deposited on the LPE-G treated SiO_2.

For both pristine polymers AFM images **Figure 7.18a,b** and **S19a,b** show the smooth film deposition and as well the crystallite structure. The presence of graphene underneath is shown in **Figure 7.18c,d** and **6.19c,d.** In this case roughness of the film is increased, but crystallite are still visible, meaning that LPE-G do not discompose the crystalline structure of polymers, as reported by XRD measures in section.

Those findings and a careful analysis of morphology of device are instrumental to correlate hybrid and graphenic regimes to graphene surface coverage on SiO_2. When spatially extended aggregates of deposited graphene are placed directly under evaporated source and drain gold electrodes they can form a continuous path through the channel, hence a graphenic device regime is obtained. For less continuous network of graphene the percolation path is interrupted, thus the charges are forced to travel through polymeric layer, allowing for partial yet evident gate modulation (hybrid regime).

7.3.11 Hysteresis Analysis in PG-TFT

In view of the unaltered crystallinity within the polymer film as observed by 2D-GIXRD, the enhancement in mobility in the devices can be ascribed to electronic/electrostatic interaction between graphene and polymer. Since we used LPE-G patches thermally annealed in air environment, thereby having an IE = 5.7 eV, the interactions between graphene and semiconductors can solely be of electrostatic nature. Our system with a layer (*i.e.* LPE-G) whose IE is sitting off the polymer band-gap can thus be related to works where graphene and reduced graphene oxide has been extensively studied as floating gate,[41] to build memories[42,43] and nano-memories.[44] Since continuous films (or aggregates forming continuous percolation pathways) of graphene nano-flakes behave as a semi-metallic material[35] our system can also be benchmarked to works where deposited metallic nanoparticles on a surface were proved to act as floating gate[25,45,46] and to be suitable for building memory device.[47] The above-mentioned approaches require the use of a dielectric layer between the nanoparticles and the active material, because direct contact between them would generate charge trapping and give raise to non-functioning devices.[48,49] This scenario is equivalent in our case when using LPE-G patches with an IE within the band gap, thereby generating states that act as traps or recombination centers for charges, which are extremely efficient in decreasing the overall device performance, as reported for system using metallic nanoparticles on the gate surface.[25] However, our ability to tune the IE of LPE-G enabled us to move the energetic level outside the band gap, as an alternative solution to introducing an additional dielectric interlayer. Our procedure permits to process from solution a conductive material that on the same time does not interact electronically with the active layer. This means that in a working regime where there are no percolation pathways across the LPE-G layer, the improved device performance must be attributed to the capacity of graphene to electrostatically charge upon the application of a gate

potential, similarly to the case observed with reduced graphene oxide[50]. Graphene nano-flakes are able of carrying charges of both signs as revealed by the measurements done both with *n*- and *p*-type polymers. The electrostatic charging of the LPE-G nano-patches induces a higher amount of carriers within the measurement scan time frame leading to an enhanced device mobility regime for both polymers. In particular, the increase of performance is due to higher number of carriers between source-drain electrodes generated by appropriate gate voltage.

To prove our assumption we performed hysteresis measurements at different sweep times. Electrical hysteresis measurements were performed in nitrogen atmosphere with a Keithley 2636A using a home-programmed software to command the operating machine to perform a double measurements sweep. Also the software allowed us to change the sweep time, *i.e.* the time between two consecutive measured points. Transfer characteristics were measured for four different sweep time (10^{-4}, 10^{-3}, 10^{-2}, 10^{-1}) s for each polymer. Since the aim of the measures was to find a physical explanation for the enhanced electrical performance we analyzed devices with an enhanced mobility regime and for the sake of comparison, pristine device.

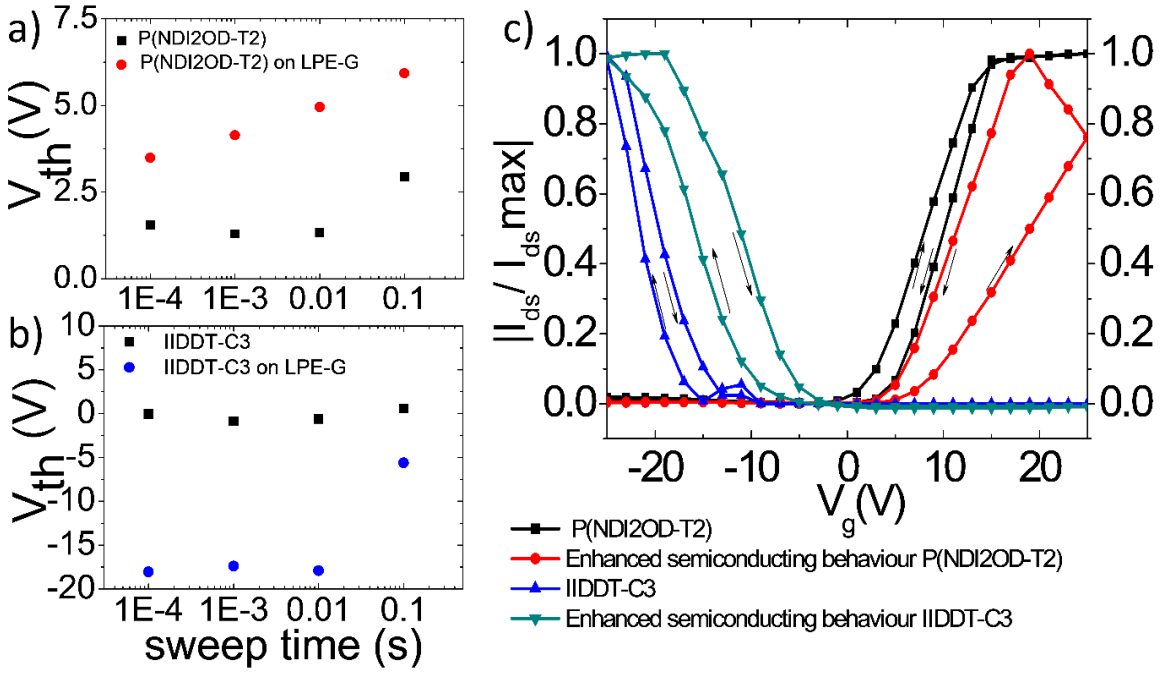

Figure 7.20. Threshold voltage (V_{th}) hysteresis shift between back and forth direction in different sweep time for (a) P(NDI2OD-T2) and (b) IIDDT-C3. (c) Hysteresis in the graphene patterned devices compared to pristine one for 0.1 s sweep time with respect to normalized I_{ds} current. Channel length 100 µm, width 10000 µm, V_{ds} = 20 V for P(NDI2OD-T2) and V_{ds} = -20 V for IIDDT-C3.

To better underline hysteresis behavior we normalized curves obtained as shown in **Figure 7.20c** with respect to the highest I_{ds} current registered in order to evidence the differences in hysteresis windows for 0.1 second, which is the time at which all previous measurements has been taken. At this sweep time pristine semiconductor mobility values show a discrepancy up to 15 % when double sweep measures were performed, while V_{th} hysteresis shift is no more

than 1 V for IIDDT-C3 and not more than 3 V for P(NDI2OD-T2). The shift is always in the opposite direction of the tracing curve. On the other hand, hysteresis behavior of devices with LPE-G on the SiO_2 surface is rather different. In the backwards curves, P(NDI2OD-T2) devices with LPE-G nano-patches at the surface show a mobility increase up to 75 % and V_{th} shift of at least 3.5 V (**Figure 7.20a**). Also IIDDT-C3/LPE-G based device show a marked hysteresis behavior: mobility is increased up to 60 % of the original value when extracted from the backward curves, whilst V_{th} hysteresis window exceeds 15 V (**Figure 7.20b**). The current increases when gate voltage is inverted, indicating an accumulation of a surplus of carriers towards the drain happened in the first branch of the measure. The shortest is the sweeping time, the more pronounced is the hysteresis effect, proving very low charging time for graphene. Our results are in accordance with previous reports on P(NDI2OD-T2) featuring a low hysteresis.[51] On the same time normalized hysteresis measured in devices employing LPE-G on the gate surface polymers is markedly increased with respect to reference sample, demonstrating that the presence of graphene increases the number of carriers in the channel.

7.3.12 PG-TFT as a flash memory device

The devices presenting enhanced semiconducting behavior (*II*) were tested as memory device. Charges are accumulated in the floating LPE-G nano-patches and can be released upon applying a potential of opposite sign. Memory devices with reduced graphene oxide were already reported from solution casting,[52] patterned floating gate,[41] embedded in polymeric matrix,[53] by doping with gold[54] and to achieve multilevel resistive memory devices.[55] As aforementioned, our system exhibits two major advantages when compared to previously reported architectures of floating gate based OTFTs memory devices. In our study, LPE-G was employed for the first time for memory applications and it acts as charging layer without the need of an additional dielectric layer. This greatly simplifies the device fabrication while maximizing the effect of the electrostatic charges, which scales with the dielectric thickness. In addition, the floating gate density that gives rise to different device functioning regimes can be finely tuned by choosing a proper volume of LPE-G. Both P(NDI2OD-T2)/LPE-G and IIDDT-C3/LPE-G enhanced devices were tested as memory device. When P(NDI2OD-T2)/LPE-G is used, a gate voltage of 60 V for 1 s was applied to write and a -60 V for 1 s to erase. When IIDDT-C3/LPE-G is employed, a gate voltage of -60 V for 1 s was applied to write and +100 V for 1 s to achieve the erase state. P(NDI2OD-T2) memory devices display a Vth shift towards more positive values when the information is written, which led to a decrease of maximum current. The memory window is of about 5 V (Figure 7.21c).

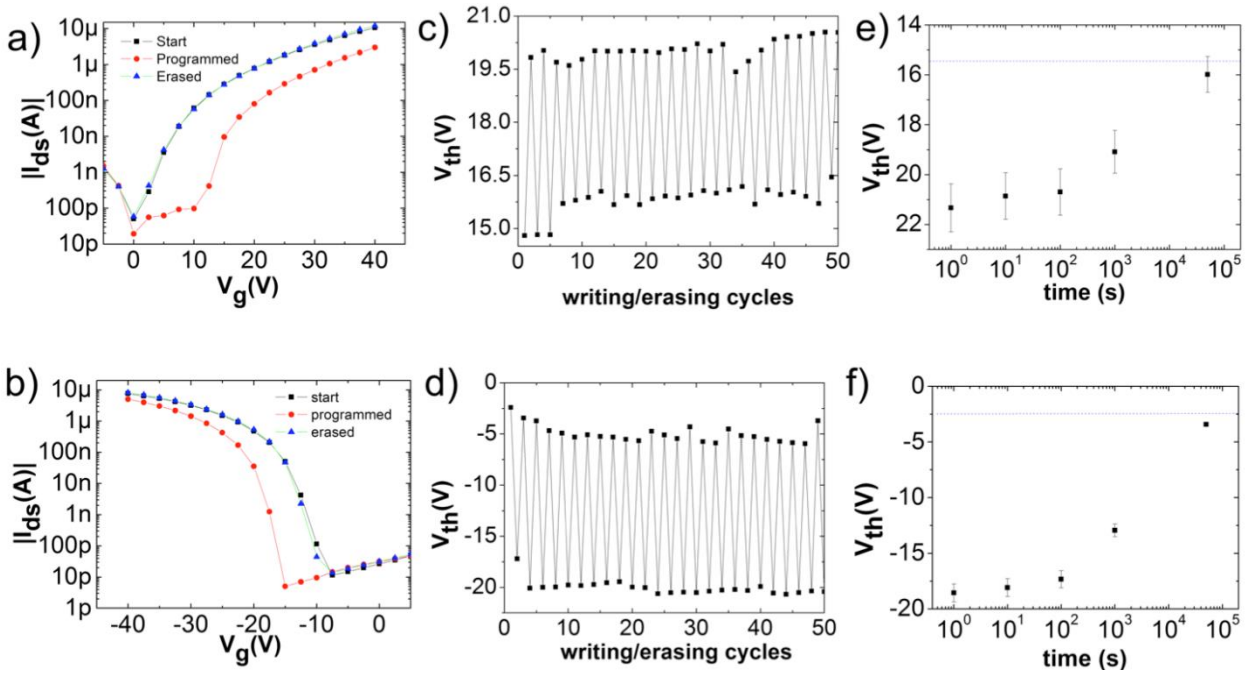

Figure 7.21. Transfer characteristic in log-scale of graphene enhanced devices in writing/erasing cycle for (a) P(NDI2OD-T2) and (b) IIDDT-C3. Writing was realized by applying a voltage pulse of -60 V to the gate electrode for 1 s for P(NDI2OD-T2) and 100 V for 1 s for IIDDT-C3. Erasing was achieved by applying a voltage pulse to the gate electrode for 1 s of 60 V P(NDI2OD-T2) and -60 V for 1 s for IIDDT-C3. V_{th} shift obtained by multiple of writing/erasing cycling for (c) P(NDI2OD-T2) and (d) IIDDT-C3. Retention time for programmed state of (e) P(NDI2OD-T2) and (f) IIDDT-C3. Initial V_{th} is reported by the dotted blue line. After applying a first appropriate voltage pulse, V_{th} was measured at different time up to when the value reached the initial one for both polymers. Retention time measures showed have been repeated three times. We report average values with standard deviation.

After applying a 1 s pulse with a gate voltage of opposite sign the transfer characteristic recorded moved back at the original position as shown in Figure 7.21a. All transfer characteristics were recorded at Vg = +40 V. Up to 50 writing/erasing cycles were performed in order to test the stability of the device as portrayed in Figure 7.21c. The hysteresis window remained constant all over the switching experiment with an initial small decrease. The retention time of the written state was also studied. The threshold voltage was found to be constant for the first 100 s; between 100 s and 1000 s there is a small negative shift, and after 104 seconds the value is back at the starting position, as indicated with a blue dot line in Figure 7.21e. On the other hand, IIDDT-C3 memory device displays a threshold voltage shift towards more negative values when the programmed state is performed with a memory window of about 17 V. This high value is in agreement with hysteresis measurements, in which IIDDT-C3 shows a bigger shift with respect to P(NDI2OD-T2) TFTs (**Figure 7.20a,b**). After applying an opposite pulse of 100 V the transfer characteristic recorded moved back at the original position as illustrated in **Figure 7.21b**. All transfer characteristics were recorded at V_g = -40 V. As for the other based polymer 50 writing/erasing cycles were performed (**Figure 7.21d**). The memory window remained constant, programmed V_{th} values were very stable in both programmed and erased states and a difference of more 15 V was recorded after 50 cycles. Interestingly, the

retention behavior is very similar to P(NDI2OD-T2). After applying the proper voltage to program a "writing" state the voltage shift was found being constant for the first 100 s, then a decrease was observed. Due to the higher memory window after 1000 s a shift value of over 10 V was still recorded. After this time a drastic positive shift towards the initial value was monitored (see **Figure 7.21f**). Overall, our results provide unambiguous confirmation of the electrostatic nature of the interaction between the two components. *Ad hoc* energetic alignment of the system under investigation enabled the LPE-G deposited and annealed to act as a floating gate; in other words, the graphene can be charged with an appropriate gate pulsed voltage. This led to the memory behavior, which exhibits interesting similarities with the hysteresis regime. In fact, as previously mentioned, the hysteresis windows is larger for IIDDT-C3 based TFTs with respect to P(NDI2OD-T2) and this is reflected by the larger V_{th} shift when a programmed cycles is performed on the former. From the memory windows values it was possible to roughly calculate the amount of charges stored in LPE-G using Equation (6.1)

$$\Delta V_{th} = \frac{Q}{C_i} \qquad (1)$$

where C_i is the total capacitance, Q the stored charge in graphene flakes, and ΔV_{th} is the shift in threshold voltage. For our system we obtain a maximum value of surface charge amounting to $1.6\,10^{12}$ cm^{-2} at $C_i = 15$ nF cm^{-2} when using IIDDT-C3, which is larger than the one previously reported (cfr. Ref. 25). Since the LPE-G surface coverage is ca. 12 % we can estimate also that the maximum number of accumulated charges would approach $1.3\,10^{13}$ cm^{-2} on the assumption that the whole surface of SiO_2 is covered (full coverage).

The retention time measurement quantifies how long an information can be stored, *i.e.* the device does not get discharged. The values of retention times which were obtained are slightly lower when compared to previous works where a dielectric layer between the floating gate and the semiconducting active channel is utilized.[41] The energy diagrams suggest that charges accumulated by electrostatic coupling (by the gate) on the LPE-G nano-flakes can be given to the semiconducting polymer. In addition, the fact that LPE-G at the gate dielectric surface enhances the charge transport suggests that pre-deposited LPE-G does not diffuse in the polymer matrix, a well-known effect[56] which is a major drawback for systems employing metallic nano-plates as floating gate.[25]

As a final experiment, a blank test on device without graphene has been carried out to prove that the memory effect arise from the presence of graphene.

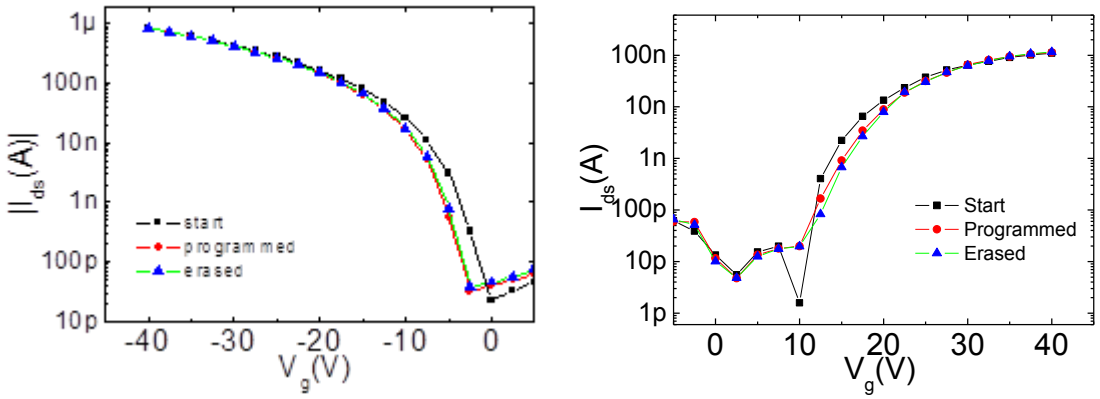

Figure S19 programmed/erased cycles as described in the main text on pristine (a) IIIDT-C3, and (b) P(NDI2OD-T2) based OTFTs.

Appropriate voltage pulses accordingly the previous mentioned parameters were applied to pristine device. As shown in **Figure S19a,b** for both polymers no observable V_{th} shift has been recorded both from the erased and programmed states after applying the gate pulses.

7.4 CONCLUSIONS

In summary, we devised a novel approach to fabricate a hybrid graphene-polymer thin-film transistor device whose electrical properties can be tuned for the first time *via* programming the ionization energy of one component upon highly reproducible thermal annealing treatments of the LPE-G pre-organized on SiO_2 by solution processing. The engineered position of the LPE-G ionization energy was exploited to modulate the physics of transport within established polymeric semiconductors. Our approach was found to be of general applicability as it is proven with both electron and hole polymer semiconductors.

By exploiting the different electronic interactions between LPE-G and a polymer it was possible to devise the multifunctional PG-TFT operating simultaneously as a three-terminal and as a memory element. The conception of this device with a hybrid active material is only possible thanks to a fine combination and control over the peculiar starting properties of each single component. Applying the same concept with different materials, like patterning an organic/polymeric semiconductor with a certain IE may be possible but the deposition of a second solution-processable semiconductor on its top would alter dramatically the properties of the first polymer layer due to potential occurrence of phase segregation or dissolution. The PG-TFT was therefore fabricated taking advantage that LPE-G strongly physisorbs on the SiO_2 after annealing and it does not get dissolved in organic solvents.

Interestingly, the electronic performances of the PG-TFTs with the IE of the LPE-G lying outside the polymer gap were tuned by modifying the amount of LPE-G deposited into nano-

flakes on the dielectric surface. Such a modulation made it possible not only to improve the mobility within the material, but also to confer unique properties to the devices, including changing the mechanism of charge transport.

Furthermore, the crystallinity of the semiconducting polymer employed as active layer is unperturbed by the presence of the LPE-G, which is of paramount importance for technological exploitation. The electrostatic nature of the interaction and unique LPE-G properties were further exploited for the realization of a (flash) memory device without the need of an additional dielectric layer to separate the active polymer layer from the floating part. A number of interesting future developments can be foreseen using this new PG-TFTs strategy: while the easy deposition method qualifies this approach as a suitable large scale process for hybrid graphene/polymer device, the special memory effect arising from a controlled engineering of the LPE-G ionization energy paves the way for novel and exciting routes in materials science, soft matter physics and chemistry.

7.5 REFERENCES

1. Novoselov, K. S.; Geim, A. K.; Morozov, S. V.; Jiang, D.; Zhang, Y.; Dubonos, S. V.; Grigorieva, I. V.; Firsov, A. A., Electric Field Effect in Atomically Thin Carbon Films. *Science* **2004,** *306*, 666-669.
2. Geim, A. K.; Novoselov, K. S., The Rise of Graphene. *Nat Mater* **2007,** *6*, 183-191.
3. Sire, C.; Ardiaca, F.; Lepilliet, S.; Seo, J.-W. T.; Hersam, M. C.; Dambrine, G.; Happy, H.; Derycke, V., Flexible Gigahertz Transistors Derived from Solution-Based Single-Layer Graphene. *Nano Lett.* **2012,** *12*, 1184-1188.
4. Schwierz, F., Graphene Transistors. *Nat Nano* **2010,** *5*, 487-496.
5. Ciesielski, A.; Haar, S.; El Gemayel, M.; Yang, H.; Clough, J.; Melinte, G.; Gobbi, M.; Orgiu, E.; Nardi, M. V.; Ligorio, G.; Palermo, V.; Koch, N.; Ersen, O.; Casiraghi, C.; Samorì, P., Harnessing the Liquid-Phase Exfoliation of Graphene Using Aliphatic Compounds: A Supramolecular Approach. *Angew. Chem. Int. Ed.* **2014,** *53*, 10355-10361.
6. Ciesielski, A.; Samori, P., Graphene via Sonication Assisted Liquid-Phase Exfoliation. *Chem. Soc. Rev.* **2014,** *43*, 381-398.
7. Coleman, J. N., Liquid Exfoliation of Defect-Free Graphene. *Acc. Chem. Res.* **2012,** *46*, 14-22.
8. Bonaccorso, F.; Lombardo, A.; Hasan, T.; Sun, Z.; Colombo, L.; Ferrari, A. C., Production and Processing of Graphene and 2d Crystals. *Mater. Today* **2012,** *15*, 564-589.
9. Kim, H.; Mattevi, C.; Kim, H. J.; Mittal, A.; Mkhoyan, K. A.; Riman, R. E.; Chhowalla, M., Optoelectronic Properties of Graphene Thin Films Deposited by a Langmuir-Blodgett Assembly. *Nanoscale* **2013,** *5*, 12365-12374.
10. He, Q.; Wu, S.; Gao, S.; Cao, X.; Yin, Z.; Li, H.; Chen, P.; Zhang, H., Transparent, Flexible, All-Reduced Graphene Oxide Thin Film Transistors. *ACS Nano* **2011,** *5*, 5038-5044.
11. Gómez-Navarro, C.; Weitz, R. T.; Bittner, A. M.; Scolari, M.; Mews, A.; Burghard, M.; Kern, K., Electronic Transport Properties of Individual Chemically Reduced Graphene Oxide Sheets. *Nano Lett.* **2007,** *7*, 3499-3503.
12. Wei, D.; Xie, L.; Lee, K. K.; Hu, Z.; Tan, S.; Chen, W.; Sow, C. H.; Chen, K.; Liu, Y.; Wee, A. T. S., Controllable Unzipping for Intramolecular Junctions of Graphene Nanoribbons and Single-Walled Carbon Nanotubes. *Nat Commun* **2013,** *4*, 1374.
13. Yan, Q.; Huang, B.; Yu, J.; Zheng, F.; Zang, J.; Wu, J.; Gu, B.-L.; Liu, F.; Duan, W., Intrinsic Current−Voltage Characteristics of Graphene Nanoribbon Transistors and Effect of Edge Doping. *Nano Lett.* **2007,** *7*, 1469-1473.
14. Wang, X.; Ouyang, Y.; Li, X.; Wang, H.; Guo, J.; Dai, H., Room-Temperature All-Semiconducting Sub-10-nm Graphene Nanoribbon Field-Effect Transistors. *Phys. Rev. Lett.* **2008,** *100*, 206803.
15. Li, X.; Wang, X.; Zhang, L.; Lee, S.; Dai, H., Chemically Derived, Ultrasmooth Graphene Nanoribbon Semiconductors. *Science* **2008,** *319*, 1229-1232.
16. Simmons, J. G., Generalized Formula for the Electric Tunnel Effect between Similar Electrodes Separated by a Thin Insulating Film. *J. Appl. Phys.* **1963,** *34*, 1793-1803.
17. Jie, W.; Hao, J., Graphene-Based Hybrid Structures Combined with Functional Materials of Ferroelectrics and Semiconductors. *Nanoscale* **2014,** *6*, 6346-6362.

18. Kim, K.; Choi, J.-Y.; Kim, T.; Cho, S.-H.; Chung, H.-J., A rRole for Graphene in Silicon-Based Semiconductor Devices. *Nature* **2011,** *479*, 338-344.

19. El Gemayel, M.; Haar, S.; Liscio, F.; Schlierf, A.; Melinte, G.; Milita, S.; Ersen, O.; Ciesielski, A.; Palermo, V.; Samorì, P., Leveraging the Ambipolar Transport in Polymeric Field-Effect Transistors via Blending with Liquid-Phase Exfoliated Graphene. *Adv. Mater.* **2014,** *26*, 4814–4819.

20. Yang, N.; Zhai, J.; Wang, D.; Chen, Y.; Jiang, L., Two-Dimensional Graphene Bridges Enhanced Photoinduced Charge Transport in Dye-Sensitized Solar Cells. *ACS Nano* **2010,** *4*, 887-894.

21. Sarbani, B.; Feri, A.; Yeong-Her, W., Blending Effect of 6,13-bis(triisopropylsilylethynyl) Pentacene–Graphene Composite Layers for Flexible Thin Film Transistors with a Polymer Gate Dielectric. *Nanotechnology* **2014,** *25*, 085201.

22. Huang, J.; Hines, D. R.; Jung, B. J.; Bronsgeest, M. S.; Tunnell, A.; Ballarotto, V.; Katz, H. E.; Fuhrer, M. S.; Williams, E. D.; Cumings, J., Polymeric semiconductor/graphene hybrid field-effect transistors. *Org. Electron.* **2011,** *12*, 1471-1476.

23. Kumari, A.; Singh, I.; Prasad, N.; Dixit, S. K.; Rao, P. K.; Bhatnagar, P. K.; Mathur, P. C.; Bhatia, C. S.; Nagpal, S., Improving the Efficiency of a Poly(3-hexylthiophene)-CuInS2 Photovoltaic Device by Incorporating Graphene Nanopowder. *Journal of Nanophotonics* **2014,** *8*, 083092-083092.

24. Sekitani, T.; Yokota, T.; Zschieschang, U.; Klauk, H.; Bauer, S.; Takeuchi, K.; Takamiya, M.; Sakurai, T.; Someya, T., Organic Nonvolatile Memory Transistors for Flexible Sensor Arrays. *Science* **2009,** *326*, 1516-1519.

25. Baeg, K.-J.; Noh, Y.-Y.; Sirringhaus, H.; Kim, D.-Y., Controllable Shifts in Threshold Voltage of Top-Gate Polymer Field-Effect Transistors for Applications in Organic Nano Floating Gate Memory. *Adv. Funct. Mater.* **2010,** *20*, 224-230.

26. Kim, S.-J.; Lee, J.-S., Flexible Organic Transistor Memory Devices. *Nano Lett.* **2010,** *10*, 2884-2890.

27. White, C. M.; Rohar, P. C.; Veloski, G. A.; Anderson, R. R., Practical Notes on the Use of N-Methyl-2-pyrrolidinone as a Solvent for Extraction of Coal and Coal-Related Materials. *Energy & Fuels* **1997,** *11*, 1105-1106.

28. Luzio, A.; Criante, L.; D'Innocenzo, V.; Caironi, M., Control of Charge Transport in a Semiconducting Copolymer by Solvent-Induced Long-Range Order. *Sci. Rep.* **2013,** *3*, 1-6.

29. Riedl, C.; Coletti, C.; Iwasaki, T.; Zakharov, A. A.; Starke, U., Quasi-Free-Standing Epitaxial Graphene on SiC Obtained by Hydrogen Intercalation. *Phys. Rev. Lett.* **2009,** *103*, 246804.

30. Chua, L.-L.; Zaumseil, J.; Chang, J.-F.; Ou, E. C. W.; Ho, P. K. H.; Sirringhaus, H.; Friend, R. H., General Observation of n-type Field-Effect Behaviour in Organic Semiconductors. *Nature* **2005,** *434*, 194-199.

31. Yan, H.; Chen, Z.; Zheng, Y.; Newman, C.; Quinn, J. R.; Dotz, F.; Kastler, M.; Facchetti, A., A High-mobility Electron-Transporting Polymer for Printed Transistors. *Nature* **2009,** *457*, 679-686.

32. Lei, T.; Dou, J.-H.; Pei, J., Influence of Alkyl Chain Branching Positions on the Hole Mobilities of Polymer Thin-Film Transistors. *Adv. Mater.* **2012,** *24*, 6457-6461.

33. Mori, D.; Benten, H.; Okada, I.; Ohkita, H.; Ito, S., Highly efficient charge-carrier generation and collection in polymer/polymer blend solar cells with a power conversion efficiency of 5.7%. *Energy & Environmental Science* **2014,** *7*, 2939-2943.

34. Szendrei, K.; Jarzab, D.; Chen, Z.; Facchetti, A.; Loi, M. A., Ambipolar all-polymer bulk heterojunction field-effect transistors. *J. Mater. Chem.* **2010,** *20*, 1317-1321.

35. De, S.; King, P. J.; Lotya, M.; O'Neill, A.; Doherty, E. M.; Hernandez, Y.; Duesberg, G. S.; Coleman, J. N., Flexible, Transparent, Conducting Films of Randomly Stacked Graphene from Surfactant-Stabilized, Oxide-Free Graphene Dispersions. *Small* **2010,** *6*, 458-464.

36. Zhang, J.; Hu, P.; Wang, X.; Wang, Z.; Liu, D.; Yang, B.; Cao, W., CVD growth of large area and uniform graphene on tilted copper foil for high performance flexible transparent conductive film. *J. Mater. Chem.* **2012,** *22*, 18283-18290.

37. Xia, F.; Perebeinos, V.; Lin, Y.-m.; Wu, Y.; Avouris, P., The origins and limits of metal-graphene junction resistance. *Nat Nano* **2011,** *6*, 179-184.

38. Russo, S.; Craciun, M. F.; Yamamoto, M.; Morpurgo, A. F.; Tarucha, S., Contact resistance in graphene-based devices. *Physica E: Low-dimensional Systems and Nanostructures* **2010,** *42*, 677-679.

39. Peng, S.-a.; Jin, Z.; Ma, P.; Zhang, D.-y.; Shi, J.-y.; Niu, J.-b.; Wang, X.-y.; Wang, S.-q.; Li, M.; Liu, X.-y.; Ye, T.-c.; Zhang, Y.-h.; Chen, Z.-y.; Yu, G.-h., The sheet resistance of graphene under contact and its effect on the derived specific contact resistivity. *Carbon* **2015,** *82*, 500-505.

40. Franklin, A. D.; Shu-Jen, H.; Bol, A. A.; Perebeinos, V., Double Contacts for Improved Performance of Graphene Transistors. *Electron Device Letters, IEEE* **2012,** *33*, 17-19.

41. Chung, D. S.; Lee, S. M.; Back, J. Y.; Kwon, S.-K.; Kim, Y.-H.; Chang, S. T., High Performance Organic Nonvolatile Flash Memory Transistors with High-Resolution Reduced Graphene Oxide Patterns as a Floating Gate. *ACS Applied Materials & Interfaces* **2014,** *6*, 9524-9529.

42. Gao, X.; She, X.-J.; Liu, C.-H.; Sun, Q.-J.; Liu, J.; Wang, S.-D., Organic field-effect transistor nonvolatile memories based on hybrid nano-floating-gate. *Appl. Phys. Lett.* **2013,** *102*, 023303-023304.

43. Hong, A. J.; Song, E. B.; Yu, H. S.; Allen, M. J.; Kim, J.; Fowler, J. D.; Wassei, J. K.; Park, Y.; Wang, Y.; Zou, J.; Kaner, R. B.; Weiller, B. H.; Wang, K. L., Graphene Flash Memory. *ACS Nano* **2011,** *5*, 7812-7817.

44. Yang, R.; Zhu, C.; Meng, J.; Huo, Z.; Cheng, M.; Liu, D.; Yang, W.; Shi, D.; Liu, M.; Zhang, G., Isolated Nanographene Crystals for Nano-Floating Gate in Charge Trapping Memory. *Sci. Rep.* **2013,** *3*, 1-7.

45. Ayesh, A. I.; Qadri, S.; Baboo, V. J.; Haik, M. Y.; Haik, Y., Nano-floating Gate Organic Memory Devices Utilizing Ag–Cu Nanoparticles Embedded in PVA-PAA-glycerol Polymer. *Synth. Met.* **2013,** *183*, 24-28.

46. Kang, M.; Baeg, K.-J.; Khim, D.; Noh, Y.-Y.; Kim, D.-Y., Printed, Flexible, Organic Nano-Floating-Gate Memory: Effects of Metal Nanoparticles and Blocking Dielectrics on Memory Characteristics. *Adv. Funct. Mater.* **2013,** *23*, 3503-3512.

47. Leong, W. L.; Mathews, N.; Tan, B.; Vaidyanathan, S.; Dotz, F.; Mhaisalkar, S., Solution Processed Non-volatile Top-Gate Polymer Field-Effect Transistors. *J. Mater. Chem.* **2011,** *21*, 8971-8974.

48. Kim, B. J.; Ko, Y.; Cho, J. H.; Cho, J., Organic Field-Effect Transistor Memory Devices Using Discrete Ferritin Nanoparticle-Based Gate Dielectrics. *Small* **2013,** *9*, 3784-3791.

49. Chaewon, K.; Ji-Min, S.; Jang-Sik, L.; Mi Jung, L., All-Solution-Processed Nonvolatile Flexible Nano-Floating Gate Memory Devices. *Nanotechnology* **2014,** *25*, 014016.

50. Shen, Y.; Zhang, X.; Wang, Y.; Zhou, X.; Hu, J.; Guo, S.; Zhang, Y., Charge Transfer Between Reduced Graphene Oxide Sheets on Insulating Substrates. *Appl. Phys. Lett.* **2013,** *103*, 053107-053104.

51. Caironi, M.; Newman, C.; Moore, J. R.; Natali, D.; Yan, H.; Facchetti, A.; Sirringhaus, H., Efficient Charge Injection From a High Work Function Metal in High Mobility n-type Polymer Field-Effect Transistors. *Appl. Phys. Lett.* **2010,** *96*, 183303-183303.

52. Rani, A.; Song, J.-M.; Jung Lee, M.; Lee, J.-S., Reduced Graphene Oxide Based Flexible Organic Charge Trap Memory Devices. *Appl. Phys. Lett.* **2012,** *101*, 233308-233305.

53. Kim, R. H.; Kim, H. J.; Bae, I.; Hwang, S. K.; Velusamy, D. B.; Cho, S. M.; Takaishi, K.; Muto, T.; Hashizume, D.; Uchiyama, M.; André, P.; Mathevet, F.; Heinrich, B.; Aoyama, T.; Kim, D.-E.; Lee, H.; Ribierre, J.-C.; Park, C., Non-volatile Organic Memory With Sub-Millimetre Bending Radius. *Nat Commun* **2014,** *5*, 1-12.

54. Han, S.-T.; Zhou, Y.; Yang, Q. D.; Zhou, L.; Huang, L.-B.; Yan, Y.; Lee, C.-S.; Roy, V. A. L., Energy-Band Engineering for Tunable Memory Characteristics through Controlled Doping of Reduced Graphene Oxide. *ACS Nano* **2014,** *8*, 1923-1931.

55. Khurana, G.; Misra, P.; Katiyar, R. S., Multilevel Resistive Memory Switching inGraphene Sandwiched Organic Polymer Heterostructure. *Carbon* **2014,** *76*, 341-347.

56. Cho, J. H.; Kim, D. H.; Jang, Y.; Lee, W. H.; Ihm, K.; Han, J.-H.; Chung, S.; Cho, K., Effects of Metal Penetration Into Organic Semiconductors on the Electrical Properties of Organic Thin Film Transistors. *Appl. Phys. Lett.* **2006,** *89*, 132101-132103

7.6 Appendix Chapter 6.

7.6.1 Hysteresis full data

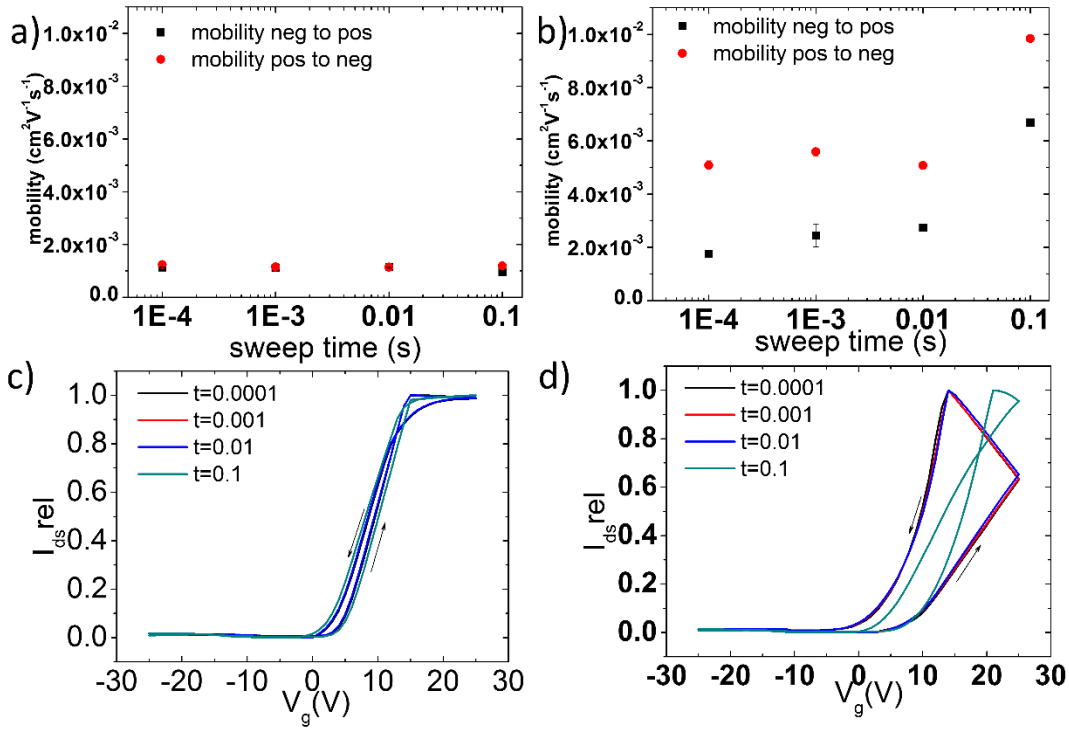

Figure A6.1: P(NDI2OD-T2) electrical hysteresis analysis: (a) mobility values extracted from negative to positive curves and positive to negative curves for pristine OTFTs, (b) mobility values extracted from negative to positive curves and positive to negative curves graphene enhanced P(NDI2OD-T2) based OTFTs, (c) hysteresis normalized curves at different sweep time for P(NDI2OD-T2) based OTFTs, and (d) for graphene enhanced P(NDI2OD-T2) based transistors.

Table A6.1 P(NDI2OD-T2) electrical hysteresis based OTFTs: mobility and V_{th} shift

Sweep time	P(NDI2OD-T2) mobility negative to positive sweep direction ($cm^2 V^{-1} s^{-1}$)	P(NDI2OD-T2) mobility positive to negative sweep direction ($cm^2 V^{-1} s^{-1}$)	Relative mobility variation	V_{th} value negative to positive sweep direction (V)	V_{th} value positive to negative sweep direction (V)	V_{th} Shift
0.0001	0.0011	0.0012	0.91	-0.25	1.28	1.5
0.001	0.001	0.0012	0.97	-0.55	0.73	1.3
0.01	0.0011	0.0011	0.99	-0.50	0.80	1.3
0.1	0.001	0.0011	0.86	-1.60	1.3	2.95

Table A6.2 Graphene enhanced P(NDI2OD-T2) based transistors electrical hysteresis: mobility and V_{th} shift

Sweep time	LPE-G/P(NDI2OD-T2) mobility negative to positive sweep direction ($cm^2 V^{-1} s^{-1}$)	LPE-G/P(NDI2OD-T2) mobility positive to negative sweep direction ($cm^2 V^{-1} s^{-1}$)	Relative mobility variation	V_{th} value negative to positive sweep direction (V)	V_{th} value positive to negative sweep direction (V)	V_{th} Shift
0.0001	0.0018	0.0051	0.34	1.35	-2.14	3.5
0.001	0.0024	0.0056	0.44	2.33	-1.81	4.15
0.01	0.0027	0.00508	0.54	2.47	-2.483	5
0.1	0.0067	0.0098	0.68	-0.96	4.98	5.9

Table A6.3 IIDDT-C3 based transistors electrical hysteresis: mobility and V_{th} shift

Sweep time	IIDDT-C3 mobility positive to negative sweep direction ($cm^2 V^{-1} s^{-1}$)	IIDDT-C3 mobility negative to positive sweep direction ($cm^2 V^{-1} s^{-1}$)	Relative mobility variation	V_{th} value positive to negative sweep direction (V)	V_{th} value negative to positive sweep direction (V)	V_{th} Shift
0.0001	0.0026	0.003	0.90	-10.8	-10.7	0.04
0.001	0.003	0.0035	0.82	12.2	-11.3	0.85
0.01	0.0026	0.003	0.87	-11.4	10.8	0.6
0.1	0.0027	0.0028	0.97	-11	11.6	0.58

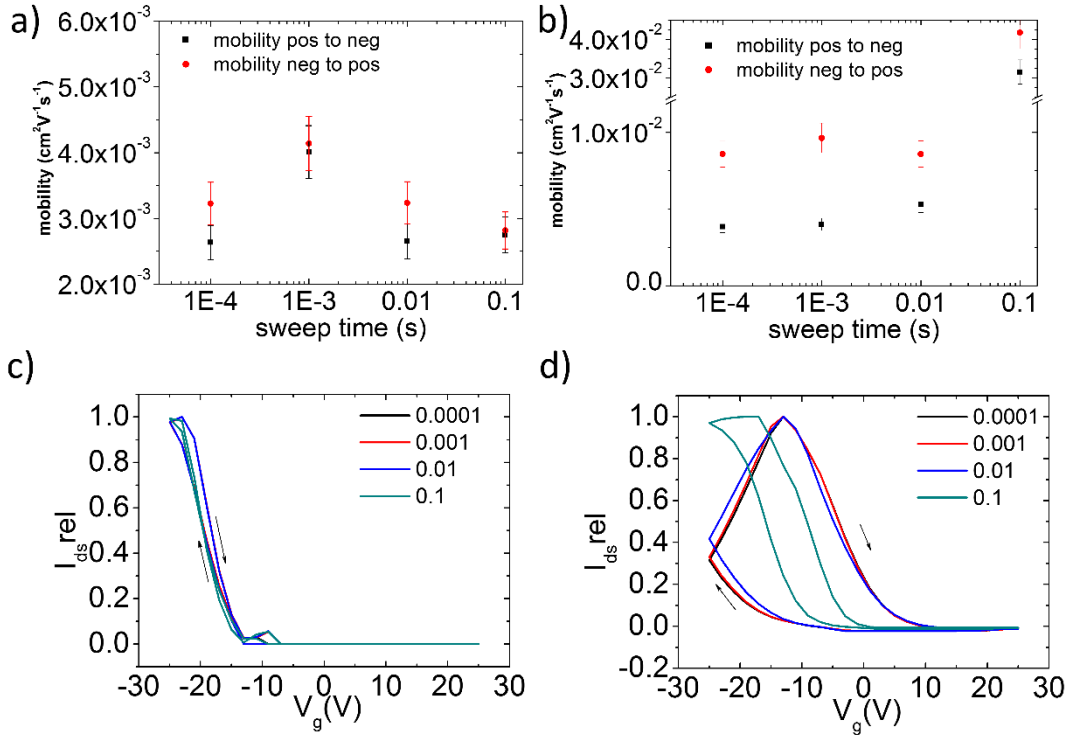

Figure A6.2 IIDDT-C3 electrical hysteresis analysis: (a) mobility values extracted from negative to positive curves and positive to negative curves for pristine OTFTs, (b) mobility values extracted from negative to positive curves and positive to negative curves graphene enhanced IIDDT-C3 based transistors, (c) hysteresis normalized curves at different sweep time for IIDDT-C3 based transistors, and (d) for graphene enhanced IIDDT-C3 based transistors.

Table A.64 Graphene enhanced IIDDT-C3 based transistors electrical hysteresis: mobility and Vth shift

Sweep time	LPE-G/IIDDT-C3 mobility positive to negative sweep direction ($cm^2 V^{-1} s^{-1}$)	LPE-G /IIDDT-C3 mobility negative to positive sweep direction ($cm^2 V^{-1} s^{-1}$)	Relative mobility variation	V_{th} value positive to negative sweep direction (V)	V_{th} value negative to positive sweep direction (V)	V_{th} Shift
0.0001	0.004	0.008	0.44	-7.5	10.55	-18.25
0.001	0.004	0.009	0.41	-7.5	9.9	-17.4
0.01	0.005	0.008	0.61	-7.5	10.3	-17.9
0.1	0.03	0.04	0.75	-5.8	-0.25	-6

Hysteresis for both pristine semiconducting polymers is extremely low if not absent. When the polymers are spin-coated on the LPE-G treated SiO_2 it is possible to observe a dramatic increase in the hysteresis, both in mobility variation and V_{th} shift.

8. Light-driven morphology of AZO/PMA polymeric LC for bi-stable memories.

8.1 INTRODUCTION

Azobenzene polymers are well-known and established photochromic systems that can form photo-responsive materials.[1] Their properties have been widely explored for macroscopic applications like fabrication of surface gratings[2-4] and photomechanical deformations[5,6] and as well for microscopic modifications aimed at optical data storages[7], photo-induced phase transition[8,9] and photo-oriented polymer morphology.[10,11] The main feature of these polymers is that a photochemical reaction which occur in small molecules bonded to of the polymeric backbone can be induced to occur in the whole macromolecule.[12] In this regard, azobenzene (AZO) moieties are a class of diazene capable of undergoing reversible photochemical isomerization between a *trans* and a *cis* conformations.[13] In particular, UV-irradiation triggers *trans*-to-*cis* isomerization,[14] while *cis*-to-*trans* is achieved upon irradiation with a blue-violet wavelength or by thermal relaxation.[15] On the other hand, polymethylmethacrylate (PMMA) and polymethacrylate (PMA)[16] are well-established polymer dielectrics for electronic application.[17,18] AZO-P(M)MA polymers have been studied because of their photomechanical properties[19], behavior in sol-gel systems,[20] rheological response[21] and morphology modifications[22]. With particular regards to this last aspect, they have been successfully employed as optical input/output memories. For such application, various systems have been developed in which surface gratings or bi-rifrangence on AZO-P(M)MA thin film could be modified mainly using lasers[23-25] or temperature,[26] in order to store an optical information. Such information could be easily read with other optical techniques, as birefringence,[24,26] anisotropy[23] analysis and SHIM microscopy.[27]

In this chapter we use AZO-P(M)MA polymer as active element in light-input, electrical-output memories (LI/EO memories). In other words, the light-induced modification in the polymer are detected electrically via a difference in the conductance of the film. In this framework, our group has demonstrated the possibility of efficient light control on electric

output in different AZO based devices, tuning charge injection,[28] charge transport,[29] work function modification,[30] diode emission efficiency[31] and vertical junctions tunneling.[32,33]

Here we employ azo-modified derived polymers of P(M)MA as optically driven, electrically detectable memories by gauging their conductance, *i.e.* measuring athwart transmitted current difference before and after irradiation. In order to achieve this goal, we make use of a simple two-terminal device geometry in which the azo-polymer is sandwiched between two metallic electrodes, and we record different electrical resistance depending on the polymer meso-group isomerization. To gain a comprehensive understanding, we have studied how film thickness affects electrical switching ratio and how inducing isomerization in meso AZO units can be related to change in conductance. We decided to work in this study with two AZO-polymer, nominally poly 2-(metha-hexyloxy-2-methyl-4'-pentyloxy-azobenzene) called PMA-AZO1 and poly 2(methyl-metha-hexyloxy-4'-ethoxyazobenzene) called PMMA-AZO2 whose chemical formula are reported in **Figure 8.1a.** As well standard PMMA for a comparison has been investigated. PMA-AZO1 is a poly-methyl-acrylate side chain AZO copolymer which is in liquid crystalline (LC) phase at room temperature (RT).[34] PMMA-AZO2 is a poly-methyl-meta-acrylate side chain AZO copolymer which is at RT is in its glass phase.[35] This choice has been made in order to better discriminate contribution from morphological rearrangement or from intrinsic changes like dipole moment[36] of employed polymers to electric conductance. Optical properties and morphological structures were investigated in order to understand changes in conductance. We proved how with appropriate light irradiation is possible to control nano-structured surface features to trigger a mesoscopic reorganization of the polymers. Furthermore, morphological modifications have been directly correlated to conductance switches, when the same films were contacted with a soft liquid compliant top electrode to be studied as memory elements.

8.2 MATERIALS AND METHODS

Substrates: thin film preparation: Solution 2.5 mg/ml of each polymer in chloroform have been prepared and stirred 2h to ensure complete solubilisation. Quartz samples of 2.5 cm side have been purchased from AdValueTech. They have been cleaned by sonication in isopropanol for 20 minutes and dried under a gentle nitrogen flow. These substrates have been coated with a high vacuum evaporated 3 nm thick chromium interlayer, and a top 15 nm tick gold layer. 520 µl of solution of each polymer has been spincoated on such electrodes at 1000 rpm for 30 sec, acceleration time of 500 $Rpm \cdot s^{-2}$. The samples have then been warmed at 35 C° for 30 min. These parameters allowed us to obtain 12 nm thick film. Different thicknesses have been achieved by varying the spincoating parameters. The film thickness has been evaluated by AFM and it is reported in **Table 7.1**.

The same procedure has been followed to prepare flexible substrates on PET with comparable thickness.

Table 7.1. Spincoating parameter for different film thickness

Film Thickness (nm)	Solution casted (µl)	Rpm	$Rpm \cdot s^{-2}$	Time (s)
3	520	1000	2000	30
8	520	1000	1000	30
12	520	1000	500	30
22	520	500	500	30
55	1040	500	500	30

Samples irradiation procedure for AFM and E-GaIn junctions measurements: irradiation was performed using fiber coupled LED (ThorLabs) with wavelength centered at 365 and 455 nm, respectively. Irradiation distance was of 1 cm with an angle of 45° with respect to the surface. Irradiation power was 0.52 $mWcm^{-2}$ for 365 nm LED and 0.45 $mWcm^{-2}$ for 455 nm. Irradiation cycles to promote the *trans* to *cis* isomerization were performed by illumination for 15 min with 365 nm LED. Irradiation cycle to trigger the back *cis* to *trans* isomerization was performed by irradiation for 30 min with 455nm LED. All the measurements have been performed in dark and after irradiation.

Flexible film preparation and bending: PET foils were fabricated and purchased by DuPont®. They were cleaned with nitrogen. 3 nm of chromium were evaporated on it followed by 15 nm of gold. A thin film of PMA-AZO1 of 12 nm has been deposited on it as previous described. Bending of 1 cm of radius has been achieved by mechanically adapting the sample on a metallic cylinder of 2 cm diameter.

8.3 RESULTS AND DISCUSSIONS

8.3.1 Optical Characterization

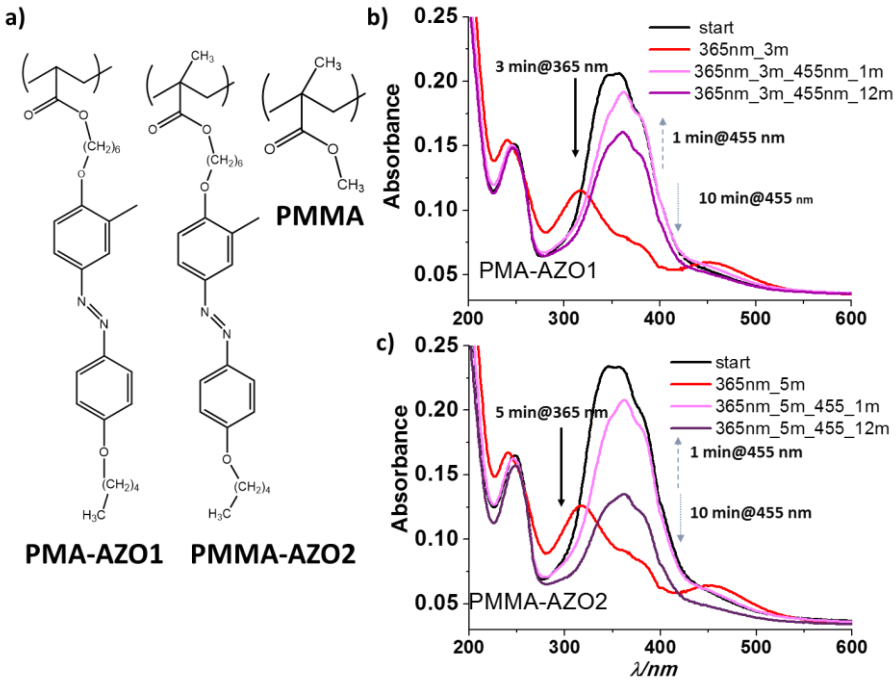

Figure 8.1 a) chemical structure of PMA-AZO1, PMMA-AZO2 and PMMA. Changes in absorption spectra of a thin film of b) PMA-AZO1 and c) PMMA-AZO2 by irradiation with 365 nm and 455 nm. Initial *trans* spectrum is reported in black line, *cis* spectrum obtained after 365 nm is reported in red line (*cis*-form). Magenta lines represent successive recovery after 455 nm irradiation after 1 min and dark magenta line is the spectrum after continued irradiation at 455 nm as discussed in the text.

In order to investigate the *trans-cis* photo-isomerization of PMA-AZO1 and PMMA-AZO2 we recorded changes in the absorption spectra of their thin solid films. As reported in **Figure 8.1b,c** (spectrum depicted in black lines), the films showed a band at around 360 nm, typical of π-π* transition of AZO moieties in *trans* form. For both polymers, the irradiation with UV light (365 nm, 5 min) caused a decrease of this band, and the increase of a new band, centered at 450 nm, which is addressed to n-π* transition of the *cis* form (**Figure 8.1b,c** the red line) Noteworthy, after irradiation at 455 nm (1-3 min) to perform back-isomerization from *cis* to *trans*, both the polymer films show a not completed recovery to initial absorbance features (**Figure 8.1b,c** magenta spectra) and the absence of classic isosbestic point.[37] Moreover, a prolonged irradiation with 455 nm caused a decrease of general absorbance (see **Figure 8.1b,c**, dark magenta line).. As previously reported for very similar systems[38] , the change in the shape of the absorbance bands during the irradiation time can be can be accounted to the formation of out of plane aggregates In particular, the irradiation at 455 nm favorites J aggregates formation (centered at 380 nm) than the H-aggregate ones (band at 340 nm). Interestingly, , irradiation with 365 nm (time ?) seems not alter the morphology of the films since the absorbance spectra superimpose one obtained after the first cycle spectrum reported with a red line (*cis*-form).

8.3.2 Morphological characterization through Atomic Force Microscopy

After demonstrating that both AZO-polymers can undergo isomerization from *trans* to *cis* and *vice-versa* upon irradiation at well-defined wavelengths, we explored if the azobenzene isomerization in the polymer matrix would induce changes in morphology. We prepared three films about 12 nm thick for pristine PMMA, PMMA-AZO2 and PMA-AZO1 on gold deposited on quartz. PMMA and PMMA-AZO2 films AFM images revealed a very flat surface with low roughness (R_q 0.35 and 0.32 respectively) as shown in **Figure 8.2a.**

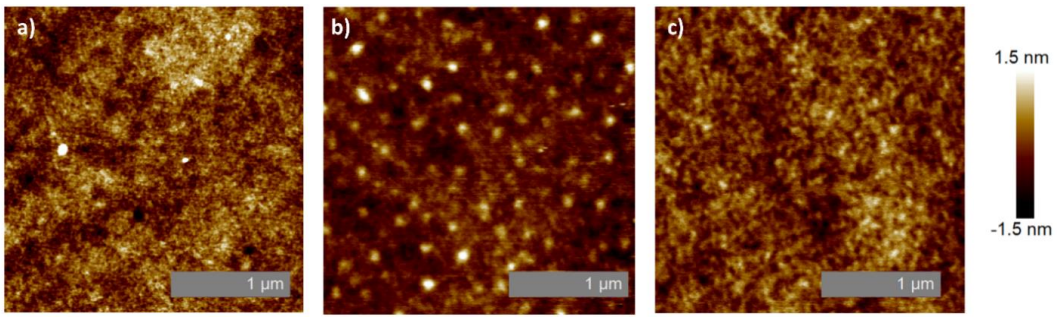

Figure 8.2 AFM topographical images recorded in tapping mode before the films irradiation of the samples a) PMMA, b) PMA-AZO1, c) PMMA-AZO2.

On the other hand, PMA-AZO1 sample in **Figure 8.2b** shows the presence of nanostructures protruding out of the surface and appearing as nano-hills on the film surface. These features are 2 nm tall and about 60-80 nm wide, and are randomly distributed over the whole surface. R_q has been found to be of 0.51 nm (image size). This higher values is addressed to the presence of nano-structures.

8.3.3 AFM nano-structures modulation by light

In order to gain deep knowledge on the nature of these protrusions, we further investigated the film morphological changes upon light irradiation.

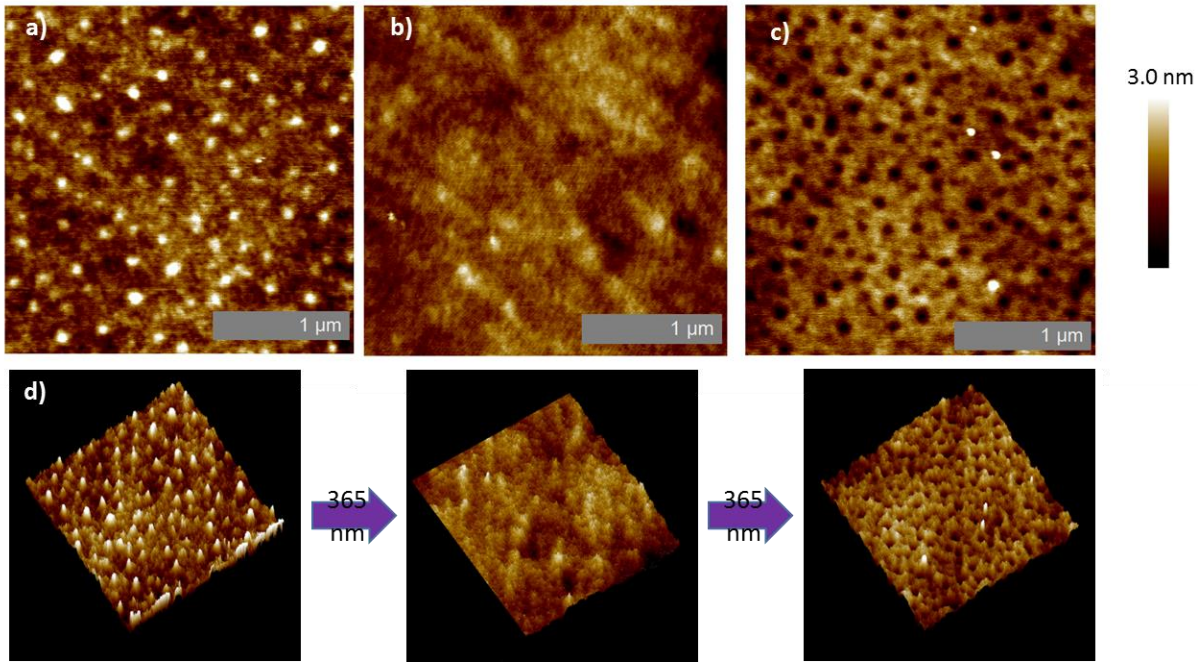

Figure 8.3 a) PMA-AZO1 AFM image of the polymer film before irradiation, b) after 5 min 365 nm irradiation, c) after 15 min 365 nm irradiation. d) 3D rendering of a,b,c pictures highlighting change in morphology from nano-hills to nano-wells passing through an intermediate state.

In **Figure 8.3a** initial state is portrayed exhibiting the same area with nano-hills showed in **Figure 8.2b**. Irradiation for 5 min at 365 nm caused morphological changes in structural features. In particular the nano-hills disappeared and the surface became less rough, decreasing from R_q = 0.51 to R_q = 0.4. (**Figure 8.3b**). Further light exposure at the same wavelength for further 10 min (total irradiation time of 15 min), led to a complete different morphology, now characterized by wells on the sample surface (**Figure 8.3c**). As highlighted in **Figure 8.3d** in a 3D rendering of above pictures, initial hills disappeared, and by passing through an intermediate situation with any appreciable feature, a morphological change on the surface was observed, leading to the formation of nano-wells that were 1.5 to 2 nm deep and 60 to 70 nm wide. The formation of nano-structures on the surface of AZO/PMMA polymers have already been reported,[39,40] as well with the formation of an intermediate phase of reorganization.[41] Fundamental condition for structured protrusions to exist and change is for the polymer to be

in liquid crystalline phase.[42,43] With regard to our system, PMMA-AZO2 has a T_g =79° C and hence is a glass at RT,[35] whereas PMA-AZO1 has a T_g at 19° C, being in a nematic LC phase at our experimental conditions.[34] It is worth underlining experiments were carried out in a conditioned room with fixed temperature of 22.5°C. This allowed the material to change conformation under irradiation and rearrange itself as proved for more dramatic reorganization.[44] We can assume that polymer chains are curled around liquid crystalline rod-like structures composed by AZO moieties clenched together, immersed in a matrix of different oriented or amorphous PMA chains as for similar polymers.[22,39,45,46] Switching from *trans* to *cis* can therefore trigger a structural re-organization within these areas[47] in light of different orientation of the two isomers even not using polarized light.[48-50]

8.3.4 Temperature effect on nano-structures morphology

To provide evidence of the role played by temperature on the film's morphology, the same experiment was carried out by keep the sample at 0 °C, in order to have also PMA-AZO1 polymer in its glass phase.

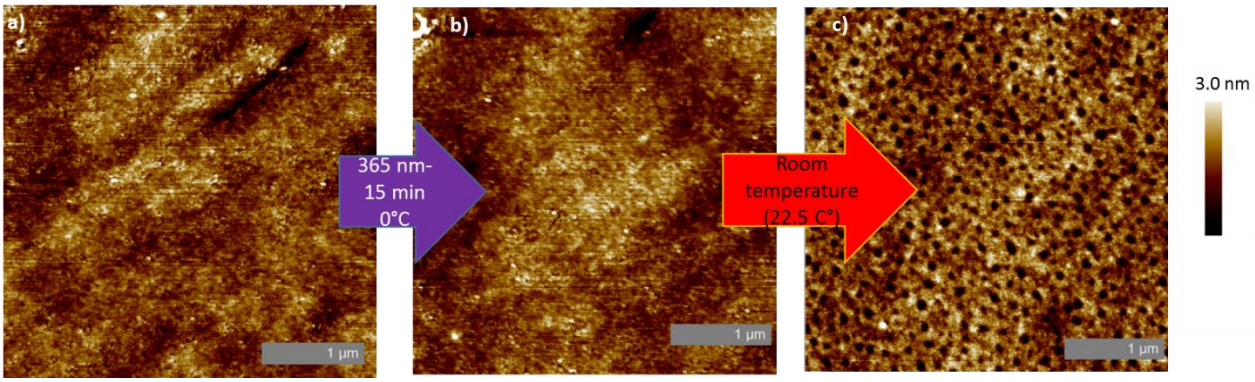

Figure 8.4 PMA-AZO1 surface morphology at 0°C a) before and b) after 15 min 365 nm irradiation. After slowly warming sample to 22.5°C, c) AFM image of the same area shows formation of nano-wells typical of *cis* AZO

Dry ice was put on AFM metallic plate. PMA-AZO1 sample (previously stored in a fridge at 7°C for 12h) was left there cooling down for 1 hour. Temperature was controlled with a thermometer. When it reached 0°C we recorded an AFM image, and, as shown by **Figure 8.4a**, no characteristics nano-features were found. We assumed that this is an indication of glass state. We irradiated with 365 nm light for 15 minutes. No change in morphology was recorded with the sample displaying still a flat surface (**Figure 8.4b**). We left the sample to warm up gently to room temperature by removing dry ice from sample holder and we waited 2 hours. When the temperature reached 22 C°, another AFM image was recorded in the same exact spot. As shown in **Figure 8.4c** we observed the presence of nano-wells on film surface. This experiments provides unambiguous evidence that temperature plays a major role in morphological change and that PMA-AZO1 must be in liquid crystalline state to achieve structural modifications upon irradiation. Also we verified that AZO-groups isomerize when irradiated even in glass state,

but they do not have enough energy for reorganizing the polymer on the long scale. When the polymer reaches its LC phase it gains enough mechanical mobility and thus it rearranges and nano-structures are formed.

8.3.5 Irradiation cycles

We further characterized morphological changes by performing 3 irradiation cycles on another sample.

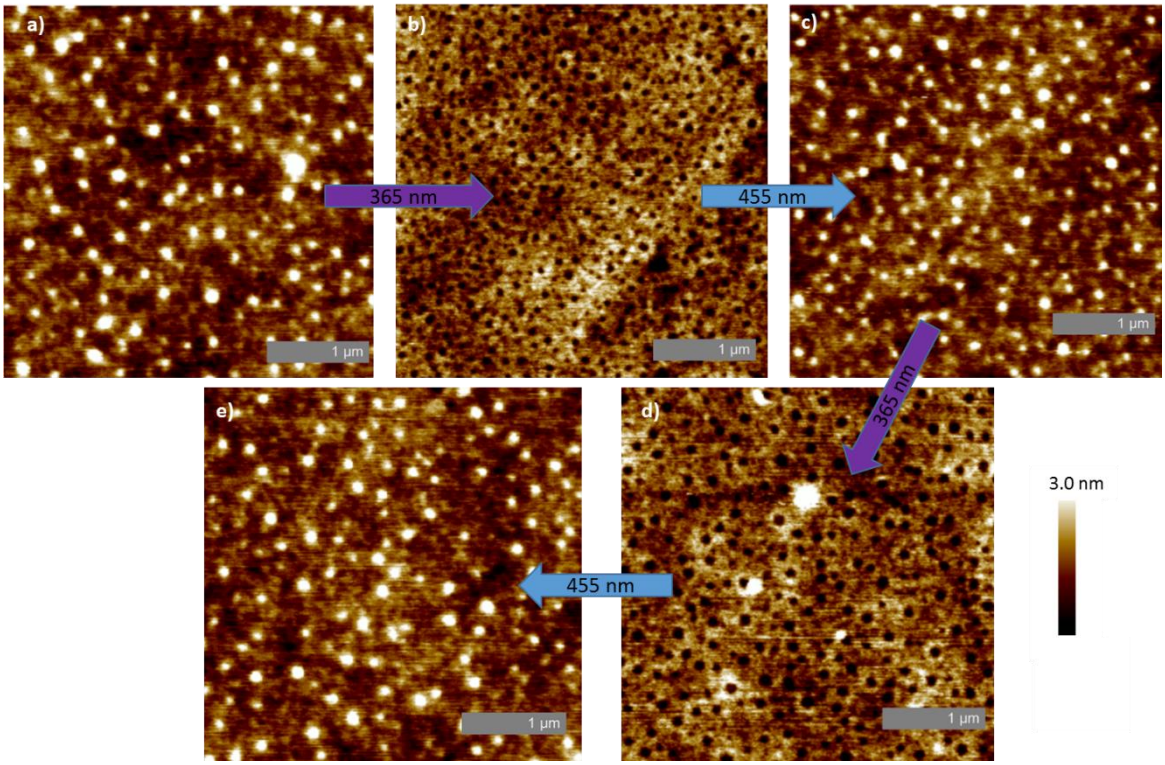

Figure 8.5 a) PMA-AZO1 film morphology before irradiation. b) PMA-AZO1 film morphology after 15 min 365 nm irradiation, showing typical nano-wells addressed to *cis*-AZO. c) PMA-AZO1 film morphology after 30 min irradiation at 455 nm, with nano-hills on surface addressed to *trans*-AZO. Further cycle: d) PMA-AZO1 film morphology after 365 nm irradiation and e) after further irradiation at 455 nm

As showed in **Figure 8.5a** before irradiation a different film had the already analyzed nano-hills. After irradiation of the sample (**Figure 8.5b)** with 365 nm light for 15 minutes we were able to induce morphological conformation change from nano-hill to nano-wells indicating achieved isomerization to *cis* form. Irradiation with 455 nm for 30 min (**Figure 8.5c)** allowed to switch back to *trans* form: surface nano-wells were then present. Hence we proved reversibility of morphological changes of nano-structure by irradiation. This cycle has been repeated again (**Figure 8.5d,e)**, confirming the same morphological changes when the film is irradiated at the specific wavelengths.

8.3.6 Irradiation effect on film thickness

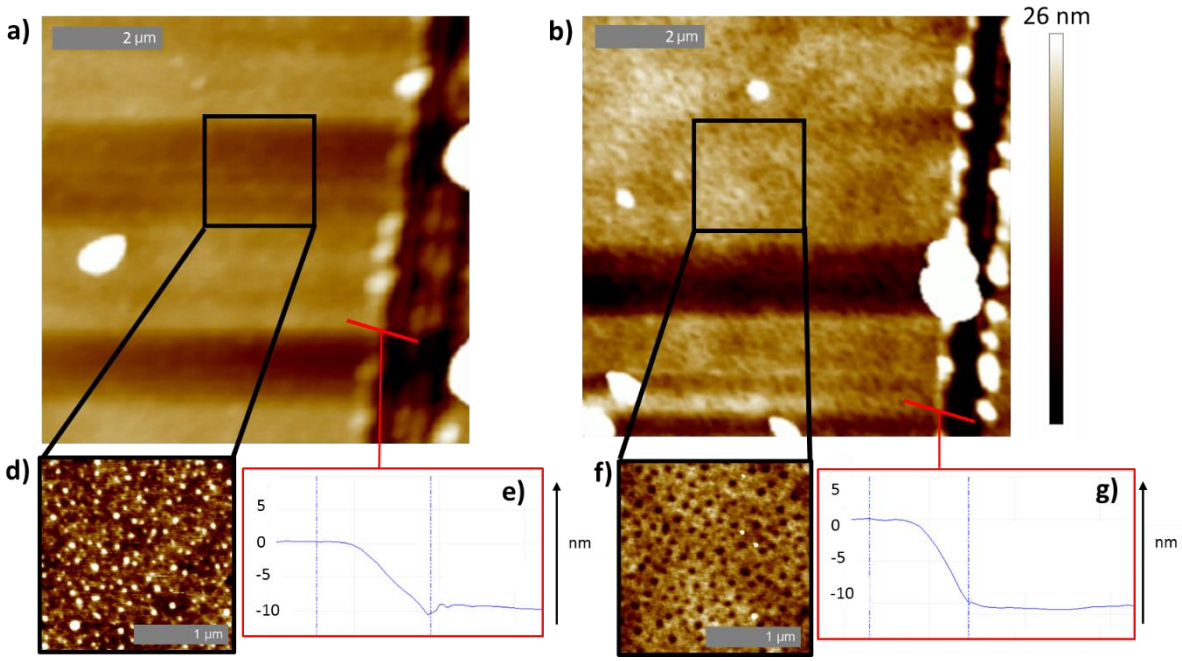

Figure 8.6 AFM picture of a) pre-irradiation and b) after 365 nm irradiation of PMA-AZO1 film with a scratch made to analyze thickness. Red line indicates where profile height was reported in e) and g) respectively. e) and g)are the profile extracted from a) and b) respectively. Zoom-in of black squares are reported in d) for not irradiated and in f) for irradiated film with a Z scale of 3 nm as for other Figures .

While the results that were just presented above provide an insight into surface morphology and how it is modified upon irradiation, what happen to the bulk of deposited thin film when irradiated and, more important, what happened to whole film structure when surface nanostructure are switched from *trans* to *cis*. In order to cast light onto this aspect, we scratched a PMA-AZO1 film and we evaluated thickness as shown in **Figure 8.6a**. Thickness was quantified where the red line is reported and was found to amount to 10 nm (**Figure 8.6e)**. The scratch caused an accumulation of its edge, making difficult to discern nano-structures on the film surface. Therefore we zoomed in emphasized of **Figure 8.6a** area to show that nano-hills were present on pre-irradiated film as **Figure 8.6d** reports**.** We then irradiated at 365 nm for 15 min to induce AZO isomerization. We analyzed the same scratch in about the same area. It was not possible to image exactly the same point due to necessity of irradiating with a known power and distance. Anyhow the very same film in the about the same area after irradiation showed (**Figure 8.6b)** nano-wells that are again highlighted in **Figure 8.6f.** Thickness was again taken where red line is placed and was found to be 10 nm (**Figure 8.6g**). Reported analysis showed that overall film thickness is not affected by irradiation. We therefore can consider the presence of a matrix with a thickness depending on spincoating parameters in which are embedded nano-structures composed of AZO aggregates that react to light by morphological reorganization in hills and wells. .

8.3.7 E-GaIn vertical junctions

In light of these findings, we measured the current passing through PMMA, PMMA-AZO2 and PMA-AZO1 thin films.

First, we fabricated a 12 nm thick film for each polymer as shown in **Table 7.1**. We tested these samples (PMA-AZO1, PMMA-AZO2 and PMMA) using a vertical junction made with a soft drop of Gallium/Indium eutectic (E-GaIn). E-GaIn electrode has already been proved to be an ideal way to explore tunneling resistance in self-assembled monolayer,[51,52] and as well across polymeric thin film.[53] A small oxide layer is formed when the eutectic is in contact with air, which helps to retain its form. E-GaIn does not diffuse in the sampled layer and therefore allows to achieve reproducible high-throughput, non-destructive current density–voltage (J–V) measurements.[54] In addition, E-GaIn vertical junction has been already used to record current difference between different isomers of photochromic molecules.[33]

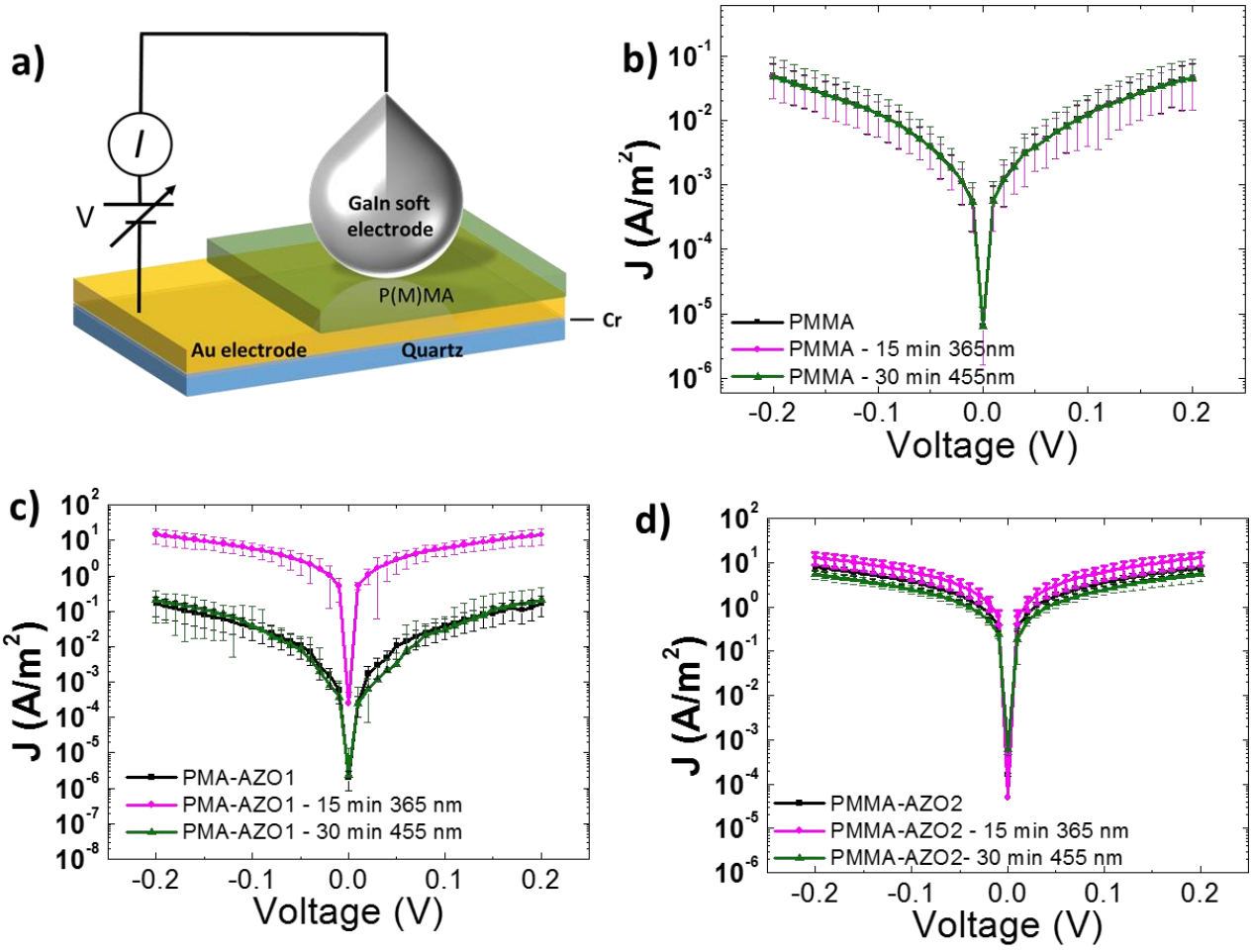

Figure 8.7 a) Schematic representation of vertical junction architecture memristor employed, showing top E-GaIn electrode contacted on summit of polymeric thin film. Au electrode on quartz is grounded, while potential is applied through top (soft) electrode for a) PMMA, b) PMA-AZO1 and c) PMMA-AZO2. In black are reported initial measurements, in violet after 15 min 365nm irradiation and in green after consequently 30 min 455 nm irradiation

In **Figure 8.7a** E-GaIn drop makes a contact with the upper layer of a polymer film. This film has been previously spincoated on a gold electrode evaporated over a quartz slide, with a thin

chromium layer in between to improve adhesion. The gold was grounded while the potential was swept between -0.2 and 0.2 V through the top electrode and therefore current passing athwart the polymer was recorded. Current density J was extracted from recorded current by dividing for surface area contact of E-GaIn. For each sample 5 contacts have been made and at least 5 cycles of 20 sweeps have been recorded for at least 500 measurements *per* each sample configuration. We report here averaged current density curves and their respective standard deviation. In **Figure 8.7b,c,d** are reported in black results for all PMMA, PMA-AZO1 and PMMA-AZO2, respectively. Pristine PMMA junctions presented the lowest current, while for PMA-AZO1 was slightly higher and for PMMA-AZO2 was one of order of magnitude higher. We then proceeded with ex-situ irradiation at 365 nm for 15 minutes in order to trigger the isomerization of the *trans* form of AZO meso-group into *cis* to provide a proof of principle on the light driven memristors. Density curves after irradiation are reported in violet. While for PMMA no change in current density is observed, as expected, PMA-AZO1 exhibits an increase of conductance of almost 2 orders of magnitude after light irradiation. We can hence consider the *trans* state of PMA-AZO1 (with nano-hills on the surface) as the high resistance state, and the *cis* state (with nano-wells on the surface) as the low resistance state of the memristor. PMMA-AZO2 behave as PMMA with no changes in current density. We performed further irradiation with 455 nm light to switch back to *trans* AZO moieties. In this case while again, no change were observed for PMMA and PMMA-AZO2, while for PMA-AZO1 current density was switched back to original value demonstrating possibility of light modulable based memory element.

In light of these findings and previous morphological analysis, we assumed that differences are due to the formation and switching under irradiation of nano-structures, which change distance between E-GaIn top electrode and gold bottom electrode.

8.3.8 Film thickness effect on current light modulation

To prove our assumptions we have prepared different films of PMA-AZO1 with different thicknesses and analyzed them with our vertical junction configuration. Samples prepared were (3, 8, 12, 22, 55) nm thick. We reported in **Figure 8.8** current density recorded for each different thickness. 3 nm-thick sample's current is the highest recorded. This came as no surprise since the distance between the two electrodes is the lowermost. **Figure 8.8a** reports in black initial averaged J and in violet curve averaged J after 15 min irradiation. In this case we obtained an increase in current of more than 150 times on average. After irradiation with an LED source with λ centered at 455 nm, current density shifted back to initial values. In the case of 8 nm sample starting current density is 10 times lower with respect previous sample (**Figure 8.8b**).

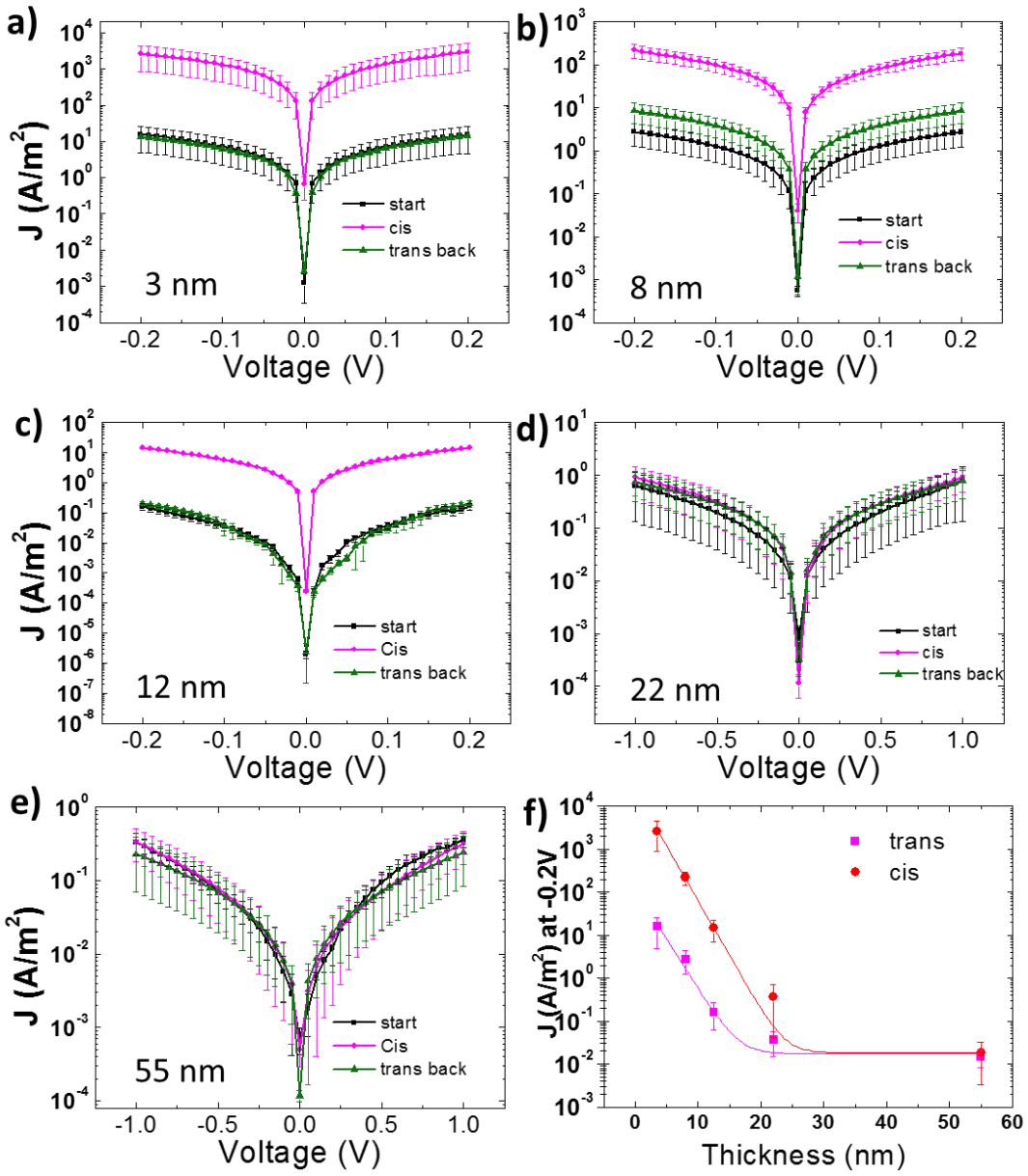

Figure 8.8 J-V curves for PMA-AZO1 vertical junction of different film thickness. a) 3nm, b)8 nm, c)12 nm , d)22 nm, e) 55 nm. f) Plot of J value in *trans* (magenta) and *cis* (red) at -0.2V v plotted vs. film thickness and both single exponential fitting thereof.

Irradiation with UV lead to an intensification of more than 95 times of current density and again after 455 nm irradiation for 30 minutes, current density values becomes equal to starting ones. The 12 nm (**Figure 8.8c**) sample has been already discussed before. In this case the conductance increase due to isomerization is about 90-fold. For thicker samples we decided to sweep voltage between -1 V and 1 V since in 0.2 V interval currents were too low and thus too noisy. A 22 nm thick sample (**Figure 8.8d**) had an initial current at -0.2 V 300 times lower with respect 3 nm sample. Irradiation at 365 do not change much current density, with variations lower than standard deviation. Lastly, 55 nm thick sample (**Figure 8.8e)** showed the lowest current density recorded and no changes after irradiation have been observed.

To better analyze our data we plotted in **Figure 8.8f** current density values at -0,2V for different thickness. Initial values for *trans* configuration are reported in violet. It is evident how current decrease for increasing polymer thickness following a single exponential trend that reach a plateau at 22 nm. It can be explained considering that tunneling current contribution to recorded current decreases exponentially with increasing thickness up to complete suppression.[55] In red are plotted current density values after UV irradiation for *cis* forms. Again we can observe an exponential decrease of current with increased thickness with same parameter exponential parameter of *trans* ones. More important for memory application a linear decrease of switching ratio from 250 to 1 is observed going from thin to thick samples.

We can schematize these assumptions by a simplified model shown in **Scheme 7.1**

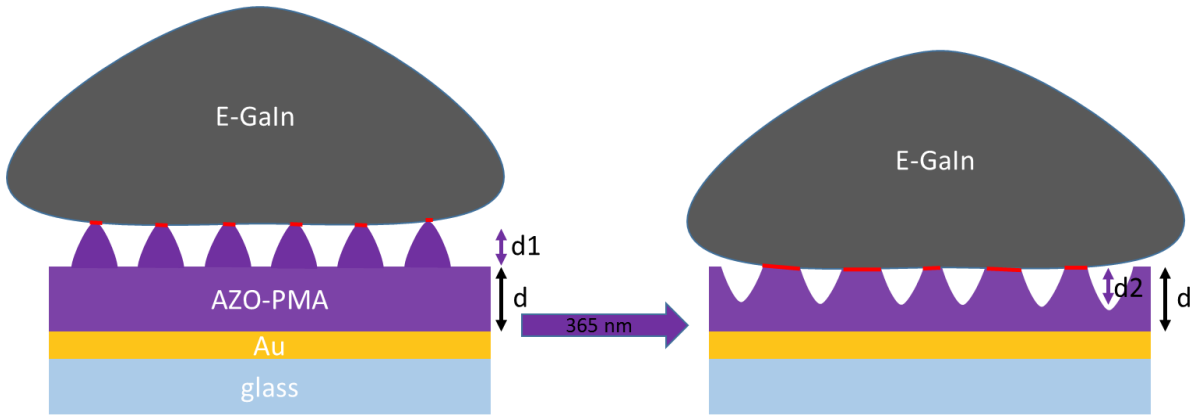

Scheme 7.1 Schematic representation of morphology modification induced by light. In red is highlighted contact area in *trans* and *cis* configuration respectively.

Although E-GaIn contact surface is more complex than a complete flat area and composed by small spikes[56] this simplified model can be considered consistent since the nanoscale of the structure and the microscopic scale of the tip. When in *trans* configuration distance between two electrodes is $d+ d_1$, where d is the bulk film thickness and d_1 which represent nano-structures height.

When irradiated, the active layer morphological surface conformation of film changes to wells. In this case the distance between the tip and Au bottom electrode corresponds just to the bulk thickness *d*. In the case of 3 nm film thickness we can estimate a distance of 5 nm in *trans* form (3 nm bulk thickness plus 2 nm height of nano-structures) and 3 nm in *cis* form between the two electrodes (3 nm bulk thickness). Therefore a change of 60% in distance leads to a current variation of 250 times as reported in **Figure 8.8f at** -0.2V applied bias. The effect on increasing bulk thickness is the decreases of the effect of nanostructures morphological change on total film thickness, and thus to conductance. In the case of 8 nm film thickness, a change of 25% in distance (8 nm bulk plus 2 nm of nano-hills) corresponds to a change of 95 times in conductance. For 22 nm thick film, changes in distance is 9% and light-triggered hills-wells switch becomes of no account in altering conductance. This means that the thinner film possible

is needed to optimize difference between the two electrical states of the memory. Importantly, the film conductance in the *cis* form is higher than what one would expect for the same thickness of the film on *trans* form. This can be clarified with geometric contact reason as reported. In fact when the surface of film is cover with nano-hills the effective contact area between the PMA and the eutectic electrode is composed mainly by top nano-hills surface as highlighted in red in **Scheme 7.1.** On the other configuration, the contact is made by the whole film surface less the nano-wells. Hence from a large contact area a larger J passes athwart the sample.

In light of these finding we can consider the whole sample like a light programmable bi-stable memory. Performing a contact with a top soft junction in any point of the surface permits an easy scanning of the programmed memory state.

Finally we explored the possibility of modifying the conductance with direct in situ irradiation. We irradiate from the bottom a 3 nm sample, leaving the E-GaIn drop in contact with the film during irradiation. No changes in current density have been recorded. These findings can be explained in two ways: *(i)* PMA-AZO1 is not able to lift E-GaIn electrode, *(ii)* on the side in contact with quartz nano-structures cannot form and thus no morphological changes happen on that side. This could imply that direct irradiation on the free surface is needed to achieve nano-structured isomerization.

8.3.9 AZO-PMA on a flexible substrate

Finally we tested the possibility of employing this vertical soft junction memristor on a flexible substrate.

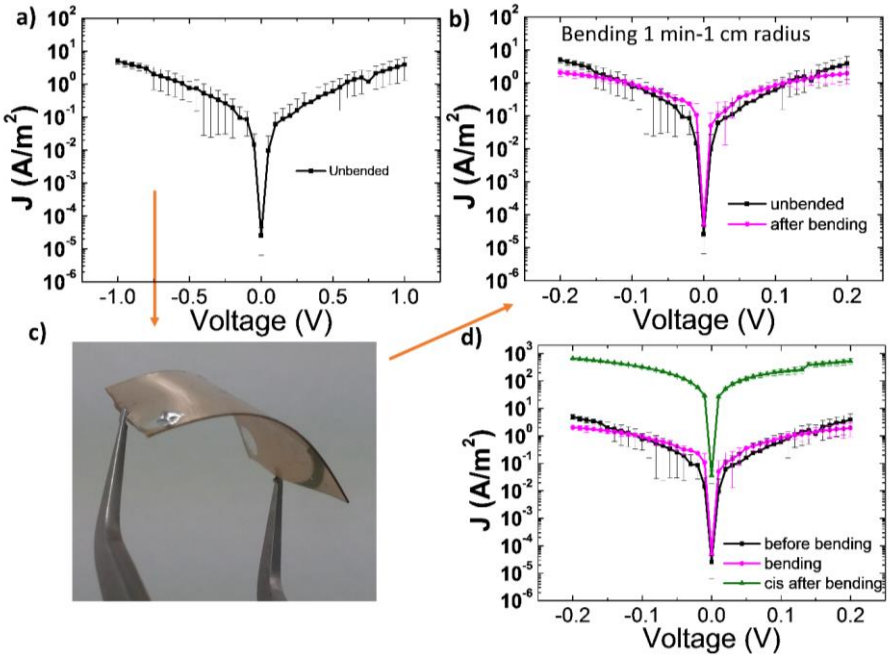

Figure 8.9 a) Characteristics of mean log current density as a function of junction bias for PMA-AZO1 film - 12 nm deposited on unbent PET. After c) 1 min bending at 1 cm radius characteristics of mean log current density as a function of junction bias are reported before b) and c) after 365 nm irradiation.

A 12 nm thick film has been deposited on PET substrate. Current density has been recorded obtained values comparable with quartz substrates as shown in **Figure 8.9a**. The sample has been bent for 1 minute at 1 cm bending radius (**Figure 8.9c**). After bending we recorded again current density which showed no change. After irradiation with 365 nm for 20 min **(Figure7.9d**), we observed an increase in current density of almost 100 times, in perfect agreement with the analogue measurements performed on a film supported on a rigid quartz substrate.

8.4 CONCLUSIONS

In summary, we have demonstrated the possibility of light driven memory elements, in which conductance is modulated via light irradiation at specific wavelength and the state of the system is read by electrical measurements. This was made possible as a result of the strict correlation between light irradiation and surface's nano-structures morphological modification of PMA-AZO1 polymer. We have proved how addressing these structures with light implies modulation of the electrical conductance. The change in overall thickness of the film, i.e. of the distance between electrodes, is the main physical reason in the observed variance of current. The fundamental condition for obtaining a light driven memristor based on AZO—PMA is that the polymer assembles in its liquid crystalline phase into aggregates. These nanostructures, in virtue of the liquid nature of the LC phase, does not require a great energy to rearrange under light. More important we demonstrated that morphological changes are restricted to surface nanostructures and that bulk film is not affected by them. This allows for a perfect control on the switching ratio which is possible to achieve by controlling film thickness. Finally, conductance variation mechanism has been investigated for different thickness proving actual possibility of light tuning of film conductance. We found that to maximize difference between programmed states the thinner film possible is needed. This allowed us to consider the whole film as the active switchable layer of the memristor, meaning that a punctual and reproducible read of the memory state can be done using a top soft junction. This concept could be further expanded by employing a transparent not- invasive top contact like a 2D material flakes for nanometric scaled memory elements. Our findings open new possibility in implementation of light controlled bi-stable memory elements in integrated circuit. While previous reported optical memory need a transducer, a light-input, electrical-output read memory based on the presented working principle directly addresses by light electrical properties, paving the way towards optical multi-responsive integrated memory devices.

8.5 REFERENCES

1. Natansohn, A.; Rochon, P., Photoinduced Motions in Azo-Containing Polymers. *Chem. Rev.* **2002,** *102*, 4139-4176.

2. Gao, J.; He, Y.; Liu, F.; Zhang, X.; Wang, Z.; Wang, X., Azobenzene-Containing Supramolecular Side-Chain Polymer Films for Laser-Induced Surface Relief Gratings. *Chem. Mater.* **2007,** *19*, 3877-3881.

3. Ishow, E.; Lebon, B.; He, Y.; Wang, X.; Bouteiller, L.; Galmiche, L.; Nakatani, K., Structural and Photoisomerization Cross Studies of Polar Photochromic Monomeric Glasses Forming Surface Relief Gratings. *Chem. Mater.* **2006,** *18*, 1261-1267.

4. Barrett, C. J.; Mamiya, J.-i.; Yager, K. G.; Ikeda, T., Photo-mechanical effects in azobenzene-containing soft materials. *Soft Matter* **2007,** *3*, 1249-1261.

5. Ikeda, T.; Ube, T., Photomobile polymer materials: from nano to macro. *Mater. Today* **2011,** *14*, 480-487.

6. Ikeda, T.; Mamiya, J.-i.; Yu, Y., Photomechanics of Liquid-Crystalline Elastomers and Other Polymers. *Angew. Chem. Int. Ed.* **2007,** *46*, 506-528.

7. Wang, Y.; Han, P.; Xu, H.; Wang, Z.; Zhang, X.; Kabanov, A. V., Photocontrolled Self-Assembly and Disassembly of Block Ionomer Complex Vesicles: A Facile Approach toward Supramolecular Polymer Nanocontainers. *Langmuir* **2010,** *26*, 709-715.

8. Ikeda, T., Photomodulation of liquid crystal orientations for photonic applications. *J. Mater. Chem.* **2003,** *13*, 2037-2057.

9. Sato, M.; Nagano, S.; Seki, T., A photoresponsive liquid crystal based on (1-cyclohexenyl)phenyldiazene as a close analogue of azobenzene. *Chem. Commun.* **2009**, 3792-3794.

10. Bobrovsky, A.; Ryabchun, A.; Shibaev, V., Liquid crystals photoalignment by films of side-chain azobenzene-containing polymers with different molecular structure. *J. Photochem. Photobiol. A* **2011,** *218*, 137-142.

11. Shishido, A., Rewritable holograms based on azobenzene-containing liquid-crystalline polymers. *Polym J* **2010,** *42*, 525-533.

12. Kumar, G. S.; Neckers, D. C., Photochemistry of azobenzene-containing polymers. *Chem. Rev.* **1989,** *89*, 1915-1925.

13. Bandara, H. M. D.; Burdette, S. C., Photoisomerization in different classes of azobenzene. *Chem. Soc. Rev.* **2012,** *41*, 1809-1825.

14. Rau, H., 1 - Photoisomerization of Azobenzenes. In *Photoreactive Organic Thin Films*, Knoll, Z. S., Ed. Academic Press: 2002; pp 3-47.

15. Rau, H.; Lueddecke, E., On the rotation-inversion controversy on photoisomerization of azobenzenes. Experimental proof of inversion. *J. Am. Chem. Soc.* **1982,** *104*, 1616-1620.

16. Hayashida, K., Dielectric properties of polymethacrylate-grafted carbon nanotube composites. *RSC Advances* **2013,** *3*, 221-227.

17. Wunsche, J.; Tarabella, G.; Bertolazzi, S.; Bocoum, M.; Coppede, N.; Barba, L.; Arrighetti, G.; Lutterotti, L.; Iannotta, S.; Cicoira, F.; Santato, C., The correlation between gate dielectric, film growth, and charge transport in organic thin film transistors: the case of vacuum-sublimed tetracene thin films. *J. Mater. Chem. C* **2013,** *1*, 967-976.

18. Na, M.; Park, H.; Ahn, M., Dielectric Properties of Polymer Thin Films for the Organic Gate Dielectric Layer. *Mol. Cryst. Liq. Cryst.* **2009,** *510*, 223/[1357]-1231/[1365].

19. Mahimwalla, Z. S.; Ngai, Y.; Barrett, C. J. In *Photomechanical effect of azobenzene thin polymer films measured with an AFM cantilever based sensor*, 2010; pp 771217-771217-771210.

20. Ueda, M.; Kim, H. B.; Ikeda, T.; Ichimura, K., Photoisomerization of an azobenzene in sol-gel glass films. *Chem. Mater.* **1992,** *4*, 1229-1233.

21. Andreozzi, L.; Faetti, M.; Giordano, M.; Zulli, F.; Galli, G.; Samaritani, S., Fragility and Glass Transition Temperature in the Rheological Response of Azobenzene Copolymers. *Mol. Cryst. Liq. Cryst.* **2006,** *450*, 173/[373]-182/[382].

22. Liu, J.-H.; Chiu, Y.-H., Behaviors of self-assembled diblock copolymer with pendant photosensitive azobenzene segments. *J. Polym. Sci. A Polym. Chem. A* **2010,** *48*, 1142-1148.

23. Ramanujam, P. S.; Hvilsted, S.; Ujhelyi, F.; Koppa, P.; Lörincz, E.; Erdei, G.; Szarvas, G., Physics and technology of optical storage in polymer thin films. *Synth. Met.* **2001,** *124*, 145-150.

24. Hagen, R.; Bieringer, T., Photoaddressable Polymers for Optical Data Storage. *Adv. Mater.* **2001,** *13*, 1805-1810.

25. Hill, R. A.; Dreher, S.; Knoesen, A.; Yankelevich, D. R., Reversible optical storage utilizing pulsed, photoinduced, electric-field-assisted reorientation of azobenzenes. *Appl. Phys. Lett.* **1995,** *66*, 2156-2158.

26. Lee, M.-J.; Jung, D.-H.; Han, Y.-K., Photo-responsive Polymers and their Applications to Optical Memory. *Mol. Cryst. Liq. Cryst.* **2006,** *444*, 41-50.

27. Gindre, D.; Boeglin, A.; Fort, A.; Mager, L.; Dorkenoo, K. D., Rewritable optical data storage in azobenzene copolymers. *Optics Express* **2006,** *14*, 9896-9901.

28. Crivillers, N.; Orgiu, E.; Reinders, F.; Mayor, M.; Samorì, P., Optical Modulation of the Charge Injection in an Organic Field-Effect Transistor Based on Photochromic Self-Assembled-Monolayer-Functionalized Electrodes. *Adv. Mater.* **2011,** *23*, 1447-1452.

29. Raimondo, C.; Crivillers, N.; Reinders, F.; Sander, F.; Mayor, M.; Samorì, P., Optically switchable organic field-effect transistors based on photoresponsive gold nanoparticles blended with poly(3-hexylthiophene). *Proc. Natl. Acad. Sci.* **2012,** *109*, 12375-12380.

30. Crivillers, N.; Osella, S.; Van Dyck, C.; Lazzerini, G. M.; Cornil, D.; Liscio, A.; Di Stasio, F.; Mian, S.; Fenwick, O.; Reinders, F.; Neuburger, M.; Treossi, E.; Mayor, M.; Palermo, V.; Cacialli, F.; Cornil, J.; Samorì, P., Large Work Function Shift of Gold Induced by a Novel Perfluorinated Azobenzene-Based Self-Assembled Monolayer. *Adv. Mater.* **2013,** *25*, 432-436.

31. Lazzerini, G. M.; Mian, S.; Di Stasio, F.; Merari Masillamani, A.; Crivillers, N.; Reinders, F.; Mayor, M.; Samorì, P.; Cacialli, F., Increased efficiency of light-emitting diodes incorporating anodes functionalized with fluorinated azobenzene monolayers and a green-emitting polyfluorene derivative. *Appl. Phys. Lett.* **2012,** *101*, 153306.

32. Mativetsky, J. M.; Pace, G.; Elbing, M.; Rampi, M. A.; Mayor, M.; Samorì, P., Azobenzenes as Light-Controlled Molecular Electronic Switches in Nanoscale Metal−Molecule−Metal Junctions. *J. Am. Chem. Soc.* **2008,** *130*, 9192-9193.

33. Ferri, V.; Elbing, M.; Pace, G.; Dickey, M. D.; Zharnikov, M.; Samorì, P.; Mayor, M.; Rampi, M. A., Light-Powered Electrical Switch Based on Cargo-Lifting Azobenzene Monolayers. *Angew. Chem. Int. Ed.* **2008,** *47*, 3407-3409.

34. Andreozzi, L.; Faetti, M.; Giordano, M.; Palazzuoli, D., Physical Aging in Side-Chain Liquid Crystal Polymers: A DSC Investigation of the Enthalpy Relaxation. *Macromolecules* **2002,** *35*, 9049-9056.

35. Angiolini, L.; Barberá, J.; Benelli, T.; Giorgini, L.; Paris, F.; Salatelli, E.; Tejedor Rosa, M., Photoinduced supramolecular chirality in glassy nematic linear and star shaped methacrylic azopolymers obtained by ATRP. *e-Polymers* **2009,** *9*, 553.

36. Lutsyk, P.; Janus, K.; Sworakowski, J.; Generali, G.; Capelli, R.; Muccini, M., Photoswitching of an n-Type Organic Field Effect Transistor by a Reversible Photochromic Reaction in the Dielectric Film. *J. Phys. Chem. C* **2011,** *115*, 3106-3114.

37. Williams, I.; Williams, N., *Advances in Physical Organic Chemistry*. Elsevier Science: 2014.

38. Moritsugu, M.; Kim, S.-n.; Kubo, S.; Ogata, T.; Nonaka, T.; Sato, O.; Kurihara, S., Photoswitching properties of photonic crystals infiltrated with polymer liquid crystals having azobenzene side chain groups with different methylene spacers. *React. Funct. Polym.* **2011,** *71*, 30-35.

39. Deng, W.; Brûlet, A.; Albouy, P.-a.; Keller, P.; Wang, X.-g.; Li, M.-h., Morphology study of a series of azobenzene-containing side-on liquid crystalline triblock copolymers. *Chin. J. Polym. Sci.* **2012,** *30*, 258-268.

40. Zhao, Y.; He, J., Azobenzene-containing block copolymers: the interplay of light and morphology enables new functions. *Soft Matter* **2009,** *5*, 2686-2693.

41. Camorani, P.; Cristofolini, L.; Galli, G.; Fontana, M. P., Photoinduced Morphological Changes and Optical Writing in a Liquid Crystalline Polymer on the Micron and Sub-Micron Scale. *Mol. Cryst. Liq. Cryst.* **2002,** *375*, 175-184.

42. Matsuzawa, Y.; Tamaoki, N., Photoisomerization of Azobenzene Units Controls the Reversible Dispersion and Reorganization of Fibrous Self-Assembled Systems. *J. Phys. Chem. B* **2010,** *114*, 1586-1590.

43. Zhao, Y., New photoactive polymer and liquid-crystal materials. *Pure Appl. Chem.* **2004,** *76*, 1499-1508.

44. Yu, Y.; Nakano, M.; Ikeda, T., Photomechanics: Directed bending of a polymer film by light. *Nature* **2003,** *425*, 145-145.

45. Shiwaku, T.; Nakai, A.; Hasegawa, H.; Hashimoto, T., Ordered structure of thermotropic liquid-crystal polymer. 1. Characterization of liquid-crystal domain texture. *Macromolecules* **1990,** *23*, 1590-1599.

46. Cai, Y.; Lu, J.; Zhou, F.; Zhou, X.; Zhou, N.; Zhang, Z.; Zhu, X., Cyclic Amphiphilic Random Copolymers Bearing Azobenzene Side Chains: Facile Synthesis and Topological Effects on Self-Assembly and Photoisomerization. *Macromol. Rapid Commun.* **2014,** *35*, 901-907.

47. Bogdanov, A. V.; Vorobiev, A. K., Photo-Orientation of Azobenzene-Containing Liquid-Crystalline Materials by Means of Domain Structure Rearrangement. *J. Phys. Chem. B* **2013,** *117*, 13936-13945.

48. Han, M.; Ichimura, K., Tilt Orientation of p-Methoxyazobenzene Side Chains in Liquid Crystalline Polymer Films by Irradiation with Nonpolarized Light. *Macromolecules* **2001,** *34*, 82-89.

49. Stumpe, J.; Geue, T.; Fischer, T.; Menzel, H., Photo-orientation in LB multilayers of amphotropic polymers. *Thin Solid Films* **1996,** *284–285*, 606-611.

50. Shimamura, A.; Priimagi, A.; Mamiya, J.-i.; Ikeda, T.; Yu, Y.; Barrett, C. J.; Shishido, A., Simultaneous Analysis of Optical and Mechanical Properties of Cross-Linked Azobenzene-Containing Liquid-Crystalline Polymer Films. *ACS Appl. Mater. Interfaces* **2011,** *3*, 4190-4196.

51. Chiechi, R. C.; Weiss, E. A.; Dickey, M. D.; Whitesides, G. M., Eutectic Gallium–Indium (EGaIn): A Moldable Liquid Metal for Electrical Characterization of Self-Assembled Monolayers. *Angew. Chem.* **2008,** *120*, 148-150.

52. Masillamani, A. M.; Crivillers, N.; Orgiu, E.; Rotzler, J.; Bossert, D.; Thippeswamy, R.; Zharnikov, M.; Mayor, M.; Samorì, P., Multiscale Charge Injection and Transport Properties in Self-Assembled Monolayers of Biphenyl Thiols with Varying Torsion Angles. *Chem.–Eur. J.* **2012,** *18*, 10335-10347.

53. Pasquier, A. D.; Miller, S.; Chhowalla, M., On the use of Ga–In eutectic and halogen light source for testing P3HT–PCBM organic solar cells. *Sol. Energy Mater. Sol. Cells* **2006,** *90*, 1828-1839.

54. Lilly, G. D.; Whalley, A. C.; Grunder, S.; Valente, C.; Frederick, M. T.; Stoddart, J. F.; Weiss, E. A., Switchable photoconductivity of quantum dot films using cross-linking ligands with light-sensitive structures. *J. Mater. Chem.* **2011,** *21*, 11492-11497.

55. Simmons, J. G., Generalized Formula for the Electric Tunnel Effect between Similar Electrodes Separated by a Thin Insulating Film. *J. Appl. Phys.* **1963,** *34*, 1793-1803.

56. Simeone, F. C.; Yoon, H. J.; Thuo, M. M.; Barber, J. R.; Smith, B.; Whitesides, G. M., Defining the Value of Injection Current and Effective Electrical Contact Area for EGaIn-Based Molecular Tunneling Junctions. *J. Am. Chem. Soc.* **2013,** *135*, 18131-18144.

9. Conclusions and outlooks

In this thesis it has been explored how interfaces in nanostructured multicomponent materials can be tailored in order to tune and enhance fundamental physical and chemical properties in supramolecularly engineered organic electronic devices as well as to confer them new functions.

We first focused on AuNPs because by a straightforward blending approach, they can easily generate hybrid interfaces in a polymeric semiconducting matrix. The properties of AuNPs depend on their sizes. Their electrical conductivity makes no exception. Moreover, AuNPs are necessarily coated by a layer of surfactant to avoid occurrence of coalescence. The type of molecular coating was found to hold a fundamental importance as it makes it possible to tune the aggregation capacity of the AuNPs and the way they interact with other components such as polymeric matrixes. The aggregation behavior of nanostructures holds a primary role since they determine the physical and chemical properties of the materials, including their electrical characteristics when integrated in field-effect transistors. The subtle nature of these interactions governs a large number of basic physical processes such as formation of ordered interfaces and energetic alignment for efficient electronic cross talking between the components. Our findings provide a solid background on the possibility of integrating AuNPs in organic electronic devices. We have also showed that when the AuNPs, which can be seen as nanostructured scaffolds, are coated with a functional molecule conferring them a responsive nature, multifunctional organic/hybrid devices can be realized.

In this framework photochromic molecules have been used as light-responsive components, when coating AuNPs in order to trap reversibly charge carriers. In particular, true bi-stable optical switches such as photochromic diarylethene molecules have been chemisorbed on AuNPs. Diarylethenes can undergo reversible isomerization from the open to the closed form upon illumination with light at specific wavelengths. The two isomers exhibit markedly different physical properties, including their conductivity. When diarylethenes are coating AuNPs they mediate interfacial electronic interactions between the AuNPs and the semiconducting polymer matrix. Two are the physical processes that are brought into play, *i.e.* change in the tunneling resistance of the coating layer and variation of the ionization energy of the whole nanoparticle. In particular, light modulation was found to activate the capacity of the hybrid interface to trap charges, as evidenced by a marked threshold voltage shift.

Nowadays graphene is an established functional system possessing exceptional optical, mechanical, thermal and electrical properties. We have produced here graphene via liquid phase exfoliation (LPE) and used it to fabricate a bi-component field-effect transistors using a two-

steps deposition procedure. To avoid graphene aggregation and its phase segregation in two components blend, first a diluted solution of the LPE graphene has been spun to form graphene nano-patches on SiO_2. Then a polymeric semiconductor has been deposited on its top. In this way, polymers' crystallinity was mildly affected by graphene presence on the gate dielectric surface. We proved for the first time that by thermal annealing it is possible to attain a complete control of the ionization energy of LPE-G and therefore of the energy interactions between graphene and the active polymeric layer. Combining this aspect with different dielectric surface coverage we added different working regime to OFETs, both for p- and n-type polymeric semiconductors, and we realized, for the first time, a memory flash device with no need of a dielectric layer separating the charge-storing graphene layer from the active channel.

Finally, we directly took advantage of photochromic molecules to impart multifunctional aspects to organic devices. Diarylethenes were used to functionalize gold source and drain electrodes in high performance n-type device, and by varying their conjugation with light it was possible to modulate charge injection resulting in output current (and mobility) variation of 70%, being the highest value ever achieved in this kind of system. This approach adds just one-step to the fabrication process and it allows switching between the two DAEs isomers with a short time irradiation. The introduced barrier at the interface constituted by DAEs had a small impact on overall performances and we obtained devices with mobility exceeding 0.1 $cm^2V^{-1}s^{-1}$, being very close to the maximum ever obtained for multifunctional devices.

On the other hand, side chain azobenzene – PMMA has been studied as two terminal memory elements. For the first time the possibility to modulate electrical properties of this material with light was proved, taking advantage of morphology rearrangement induced upon irradiation. These rearrangements affect directly the interface with the soft junction, and the overall output current still depends on overall film thickness. Therefore we demonstrated that this kind of materials are a suitable active layer for a memory elements programmed by light and read by electric measurements.

The hybrid approach presented in this thesis, relying on the combination of organic/polymeric semiconducting matrix with either nanoparticles or graphene nano-flakes enables the formation of functional interfaces for multifunctional devices and logic operations. The main advantages can be summed up as: (*i*) easy processability and fabrication of the hybrid devices, (*ii)* straightforward introduction of multifunctional properties, and *(iii)* programming of the assembly and aggregation by relying on the different supramolecular interactions as an effective way for tailoring electrical properties.

All those aspects are critic for industrialized production of hybrid device. We used solution processed deposition for obtaining multifunctional devices in a simple manner, without the need of orthogonal solvents and laborious lithography steps. Moreover just by self-assembly or blending we transferred molecular functions directly two the hybrid device.

Anyhow, some concerns should be noticed. The first is that blending approach does not offer a control over the nanoparticles position in the channel and introduces disorder in the device. This is directly reflected in the loss of performances with respect to pristine devices. The second problem is about fabrication process, that although very simple, it is time consuming. Both annealing of graphene and growth of the SAMs requires over 12 hours.
Moreover it is evident that the introduced complications must be compensated by the benefits brought about by the functionalization. This has not been always the case, but the results achieved here are and will be helpful to discriminate when integrating a (functionalized) interface in an organic based device is worth the effort. In addition, we demonstrated that even with a deep knowledge of both materials before the introduction in the hybrid device it is not always possible to predict the outcome of the bi-component active layer electrical properties. This is particularly true when gold nanoparticles are present.

If we look on a short time scale, i.e. in the future (2-5 years), the major open question on the topic of this thesis work is how one can limit the disorder introduced combining different component. Polymers forming very tight and stacked aggregates will be needed, by increasing rigidity of the core. This should lead to higher performances polymers by reducing paracrystallinity. At the same time tightly packed aggregates are less sensitive to disorder and thus they should decrease the effect of introducing nanoparticles in the polymer matrix.

For photochromic-functionalized nanoparticles the direct development is the design of high effective light controlled memory device, combining a multifunctional memory effect together with an increase in overall performances. This could be achieved by tuning the AuNPs size for a more convenient energetic level alignment between the NPs and the chosen semiconductor. Moreover also a study on how the terminal group of t-DAE molecules affect aggregation and quenching is of fundamental importance to gain a greater understanding of the system and its supramolecular interactions.

On the other hands, electrodes functionalized with photochromic moieties/molecules, should be designed to attain fast response to the optical stimuli, bringing the timescale on the millisecond or shorter. This has already been achieved for multifunctional devices based on a blend of DAEs with semiconductors. For DAE growth as SAM on gold, beside the intrinsic property of the photochromic system, the interfacial level it is key how the photochromic molecules are packed to allow tight assemblies yet not sterically or electronically hindering an efficient isomerization. The choice of irradiation method is also important. Employing more powerful light sources, like lasers, response time could be diminished of many order of magnitude. Anyhow a balance should be need, since a too powerful irradiation can damage the SAM and the semiconductor, detriming both switching and electrical performances. Because of the final aim of integrating the switch in real applications it is important that the presence of the SAM on the electrodic surface does not disturb much the overall performances of the device,

and finally for memory applications they high retention time for each programmable state is needed.

Our graphene based memories with tunable OTFTs working regime are already promising devices. The challenge is the deposition of a single flake in a small interelectrodic channel to scale down the whole device. In the specific case of our findings, a deep study is also needed to understand the reason of shifting of ionization energy and the role of NMP and temperature. This could allow to have a complete picture of how annealing affects graphene properties, not only ionization potential, but also sheet resistance, transparency and chemical reactivity of the edges. Therefore, the annealing method could be useful to obtain graphene with desired properties with a simple thermic treatment. It could be applied to various applications, like electrodes (for solar cells or any kind of device needing high-conductive transparent electrodes), charge storage systems, catalyst, etc.

The use of side-chain azobenzene polymers, in which the main chain is a dielectric macromolecule, as an active layer for an electronic device is a complete new application in electronics, and thus the next step should be the integration of this material in a junction with a transparent electrode, like graphene. Such a junction has potential as "memristor-like" element programmable by light irradiation for logic applications.

On the long term (5-20 years), with the emergence of OTFTs as a real technology, the use of nanostructured systems like AuNPs holding tunable physical and chemical properties which can be leveraged also via their exploitation as scaffold when decorated by suitably designed functional molecules to confer to the hybrid system new properties. One application is that of nano-memories and as single nanoparticles based light sensors. These are obvious developments once direct manipulation of nano-objects will be achieved. The second is towards photovoltaic applications. AuNPs SPR band acts as light antenna for light. When AuNPs are embedded in a polymeric semiconducting matrix they increase generated photocurrent. In other words, by combining this intrinsic properties of AuNPs with a photochromic molecules it could be possible to design efficient high-responsive light harvesting system, ideally tunable for collecting specific wavelengths, for high-efficiency photovoltaic elements.

The electrodes functionalization is a highly promising approach to introduce additional light current modulation in transistors. The biggest and more fascinating challenge would be to introduce light-controlled devices in integrated circuits to work not just on a binary system but with an additional light-controlled state. The electrode SAM functionalization with DAE is a particularly well-fitted design for this objective because they present two well defined states. This is extremely important because a clear discrimination between the different bit states is fundamental for logic applications. Such a large shift in the working paradigm of computer would permit to design and build exponentially more powerful computer, a possibility whose effects are unpredictable.

Graphene, in virtue of its exceptional properties, is presently the focus of a great research effort. This thesis proved that it is possible to use it to redesign an established concept as transistor-based memories. The graphene based memories developed in the framework of this thesis, in view of its easy processability relying on successive deposition methods and a simple layout, if properly scaled down, could lead to a more efficient, by production cost and/or performances, storage devices for different applications, especially if requirements are transparency and flexibility. By combining lithography and controlled single flake deposition, it would be possible to create a short-channel device over a single charging element composed by just one graphene flake, a super-efficient memory element that could be produced at industrial scale. Their applications could range from gadgets needing a low-cost but effective memory, to be an actual and technological candidate in replacing SSD memories in computers.

List of Contributions

Publications

- The Role of Size and Coating in Au Nanoparticles Incorporated into Bi-Component Polymeric Thin-Film Transistors

Thomas Mosciatti, Emanuele Orgiu, Corinna Raimondo, Paolo Samorì

Nanoscale, 2014, 6, 5075-5080 – HIGLIGHTED on the Cover Page - Nanoscale, 2014,6, 4946

- A Multifunctional Polymer-Graphene Thin-Film Transistor with Tunable Transport Regimes

Thomas Mosciatti, Sébastien Haar , Fabiola Liscio , Artur Ciesielski, Emanuele Orgiu, and Paolo Samorì

ACS Nano, 2015, 9 (3), pp 2357–2367

- Tunable charge injection in high performance polymeric thin-film transistors

Thomas Mosciatti, Maria del Rosso, Martin Herder ,Johannes Frisc, , Oliver Fenwick, Norbert Koch, Stephan Hect, Emanuele Orgiu, Paolo Samorì – In preparation

- Light controlled charge trapping in photo-chromic AuNPs/polymeric bi-component n-type OFET.

Thomas Mosciatti, , Johannes Frisc, Martin Herder, Norbert Koch, Stephan Hect, Emanuele Orgiu, Paolo Samorì – In preparation

- Light-driven Morphology of AZO/PMA Polymeric LC for bi-stable Memories

Thomas Mosciatti, Sara Bonacchi, Marco Gobbi, Loris Giorgini, Emanuele Orgiu, Paolo Samorì – In preparation

- Graphene/azobenzene nanocomposites: light-enhanced liquid-phase exfoliation and photoswitching current in hybrid material

Markus Döbbelin,Sébastien Haar, Silvio Osella, Matteo Bruna,Andrea Minoia, **Thomas Mosciatti**, Fanny Richard, Eko Adi Prasetyanto, Luisa De Cola, Vincenzo Palermo, Raffaello Mazzaro, Vittorio Morandi, Roberto Lazzaroni, Andrea C. Ferrari David Beljonne, Artur Ciesielski1 and Paolo Samorì. – Submitted

Talks

- Gold Nanoparticles blended in organic field effect transistor: size and coating effects

Presented at: E-MRS Lille 2015

- A novel multifunctional polymer-graphene thin-film transistor device with tunable transport regimes

Presented at : E-MRS Lille 2015

Posters

- Unraveling the role of coated AuNP in P3HT-based OFET”

Thomas Mosciatti, Emanuele Orgiu, Corinna Raimondo, Paolo Samorì

9-13/06/2013, Grenoble, France, ICOE.

- “Unraveling the role of coated AuNP in P3HT-based OFET”

Thomas Mosciatti, Emanuele Orgiu, Corinna Raimondo, Paolo Samorì

26-28/06/2013, Strasbourg, France, SUPERIOR CONFERENCE.

- “Unraveling the role of coated AuNP in P3HT-based OFET”

Thomas Mosciatti, Emanuele Orgiu, Corinna Raimondo, Paolo Samorì

9-13/09/2013, Sevilla, Espagne, EUROMAT.

- “Unraveling the role of coated AuNP in P3HT-based OFET”

Thomas Mosciatti, Emanuele Orgiu, Corinna Raimondo, Paolo Samorì

9-13/09/2013, Sevilla, Espagne, EUROMAT.

- "Gold Nanoparticles blended in organic field effect transistor: size and coating effects"

Thomas Mosciatti, Emanuele Orgiu, Corinna Raimondo, Paolo Samorì

11-13/06/2014, Modena, Italie, ICOE. - best poster prize award

- “Tuning the electrical properties of polymer-based TFTs via controlled deposition of liquid-phase exfoliated graphene on the gate dielectric”

Thomas Mosciatti, Sébastien Haar , Fabiola Liscio , Artur Ciesielski, Emanuele Orgiu, and Paolo Samorì

24-29/08/2014, Strasbourg, France, ELECMOL 2014.

- “Liquid-phase exfoliated graphene nano-flakes acting as floating gate elements for polymer-based OTFT memories

Thomas Mosciatti, Sébastien Haar , Fabiola Liscio , Artur Ciesielski, Emanuele Orgiu, and Paolo Samorì

21-25/09/14, Strasbourg, France, GDR-I GNT 2014.

Statement of Work

All the synthesis, experiments and data analysis have been carried out by myself except for the followings:

- **Chapter 4 and 5**: t-DAEs synthesis was made by Dr. Martin Herder under the supervision of Prof. Hect at Humbolt University in Berlin. TEM images were taken by Dr. Simona Moldovan at IPCMS.
- **Chapter 6**: t-DAEs synthesis was made by Dr. Martin Herder under the supervision of Prof. Hect at Humbolt University in Berlin. SAM optical absorption spectra and XPS spectra and analysis were carried out by Ms. Maria del Rosso. UPS experiments and data analysis were carried out by Dr. Joannes Frisc at Humbolt University in Berlin.
- **Chapter 7**: LPE-G was exfoliated by Mr. Sebastien Haar. XRD measurements and analysis were performed by Dr. Fabiola Liscio (Università di Bologna) at synchrotron facilities in Trieste. XPS measurements were performed by Dr. Fanny Richard.
- **Chapter 8**: AZO-P(M)MA were provided by Prof. Loris Giorgini of Università di Bologna. Absorbance spectra were recorded by Dr. Sara Bonacchi.

Dr. Emanuele Orgiu helped with useful discussions on experimental design and data analysis, Dr. Oliver Fenwick and Dr. Marco Gobbi helped with experimental designs and data analysis respectively, Dr. Chiara Musumeci and Mr. Marco Squillaci helped with technical support on instruments.

Acknowledgments

Paolo Samorì really did more than merely doing his job as PhD Advisor in these three (ah-ah!) years towards me, and looking back to the first days I realize how being part of his group has really been an intriguing and particularly formative experience, by all points of view.

Emanuele Orgiu had a fundamental part in all the work presented in this thesis, by helping me, guiding me and bringing me out of the swamps of bad science when needed, never failing to provide a hint, a suggestion, an inspiration, especially when problems were too complexes and pernicious to be overcome just by myself.

Marco Gobbi and Oliver Fenwick both helped me a lot to figure out what was going on with my stuff, especially from a physics point of view, when numbers come into play and nobody wants to deal with them.

Many other colleagues helped me, taught me something, or just shared a smile. Karl, Markus, Chiara, Marco, Laura, Agostino, Alexander, Sebastién, Sara, Nicolas, Anna, Marc-Antoine, Andrea, Artur ,Gareth, Song Lin, Corinne,.

I have to admit my good luck in finding in Tim a great office mate, a great person and finally, a friend.

As PIs put their name last in a scientific paper, to underline their importance and at the same time their humility, Maria get the last name in this work, as the person who provided me energy, happiness, serenity and love. Non aggiungo altro ché non c'è nulla io possa dirti tu non sappia già.

prego,

Strasbourg, 25/05/2015

Thomas

Thomas MOSCIATTI

Interfaces hybrides nanostructurées pour l'électronique supramoléculaire

Résumé

Cette thèse a exploré comment, en introduisant des interfaces nanostructurées dans des systèmes supramoléculaires pour l'électronique, il est possible de moduler, ajouter et étudier les propriétés des nano-objets. Sur ces applications de fonctionnalisation auto-assemblée des limites, le contrôle thermique sur les propriétés intrinsèques, la modulation lumineuse des structures chimiques et physiques ont été trouvés comme étant des techniques adaptées pour affecter le système supramoléculaire fonctionnalisé nano-structuré pour l'électronique organique. Des nanoparticules d'or ont été utilisées pour générer des interfaces qui ont été fonctionnalisés afin d'étudier l'effet de transport de charge dans un transistor à couche mince organique. Par conséquent, cette approche a été intensifiée en employant des molécules photochromiques et par le contrôle du piégeage de charge par irradiation de lumière. Le même principe a été utilisé pour moduler l'injection de charge dans les transistors à haute performances, par fonctionnalisation des électrodes appropriées avec des diaryléthènes. Enfin, une approche différente pour contrôler le dépôt de flocons de graphène sur surface diélectrique a été employée avec succès pour concevoir de nouveaux éléments de mémoire par ajustement de l'alignement des niveaux énergétiques du graphène après recuit thermique.

Mots-clés: Interfaces, nanoparticules d'or, molécules photochromiques, transistors à couches minces organiques.

Résumé en anglais

This thesis explored how, by introducing nanostructured interfaces in supramolecular system for electronics, is possible to modulate, tune, add and study properties arising from nano-objects. On these purposes self-assembled functionalization of boundaries, thermal control on intrinsic properties, light modulation of chemical and physical structures have been found as tailored techniques to affect nano-structured functionalized supramolecular system for organic electronics. Gold nanoparticles have been used to generate interfaces that have been functionalized in order to study charge transport effect in organic thin film transistor. Therefore this approach has been stepped up employing photochromic molecules and controlling charge trapping with light irradiation. The same principle has been used to modulate charge injection in high performance transistors, by functionalizing electrodes with appropriate diarylethenes. Finally, a different approach of controlling deposition of graphene flakes on dielectric surface has been successfully employed to design new memory elements by tuning energetic level alignment of graphene with thermal annealing.

Keywords: Supramolecular electronics, Interfaces, Gold Nanoparticles, Photochromic molecules.